Université de Toulouse

THÈSE

En vue de l'obtention du

DOCTORAT DE L'UNIVERSITÉ DE TOULOUSE

Délivré par :
Université Toulouse III Paul Sabatier (UT3 Paul Sabatier)

Discipline ou spécialité :

Nanochimie

Présentée et soutenue par :
Gurunatha Kargal Laxminarayana

le : Jeudi 5 Juillet 2012

Titre :

Approches colloïdale et bio-inspirée en nanoplasmonique.

Ecole doctorale :
Sciences de la Matière (SDM)

Unité de recherche :
Centre d'Elaboration de Matériaux et d'Etudes Structurales

Directeur(s) de Thèse :

Dr. Erik Dujardin

Rapporteurs :

Pr.Anna Mitraki	Université de Heraklion (Crète,Grèce)
Pr.Thibaud Coradin	Collège de France (Paris, France)

Membre(s) du jury :

Pr.Raphael Levy	Université de Liverpool (Liverpool, Grande Bretagne)
Pr.Peter Faller	LCC CNRS UPR 8241 (Toulouse, France)
Pr.Philippe Minard	Université de'Orsay, IBBMC UMR 8619 (Paris, France)

ACKNOWLEDGEMENTS

This thesis represents not only my work but also depicts one of the first attempts to use artificial proteins with inorganic interface. I have been given this unique opportunity to work in this interdisciplinary field and I successfully taken advantage of them to learn a new aspect in the field of science. At first, I would like especially to thank to my advisor Erik Dujardin who chose me to work in this project, continually conveying a spirit of adventure in regard to a research and also helping me personally during my entire stay in Toulouse. I would greatly acknowledge his contribution in the successful completion of my thesis. I would also like to thank Dr. Tapas Kumar Maji and Dr.M. Eswaramoorthy, Assistant professor at JNCASR, Bangalore for referring me for this position. I am especially grateful to Prof. Anna mitraki, Prof. Thibaud Coradin, Prof. Raphael Levy, Prof. Philippe Minard and Prof. Peter Faller as the thesis jury members.

This thesis would not have been possible without the help, support and successful collaboration with Prof.Philippe Minard group at IBBMC, Orsay Paris. My sincere thanks to Prof Philippe Minnard, Dr.Agathe Urvoas, Marielle Valerio Lepiniec and Asma Guellouz who accommodated me in their lab for short term during my PhD and helping me to learn many biological techniques. I am also indebted to Dr. Valérie Marchi-Artzner and Cyrille Hamon at University of Rennes, for helping me to learn some experimental techniques which I successfully performed at CEMES. I would like to express my deepest appreciation to my group members, my colleagues and administrative staff at CEMES for their helpful hands and selfless support during the entire period of my thesis. My very sincere thanks to CNRS and ERC for the scholarship and financial aid for my doctoral study. I would like to give my gratitude to my lovely roommates, and friends for the time with laughter, mutual encouragement, and love I had and also for their care and love despite my current location. Also I would like to acknowledge my friends those who helped me to understand the pure biological terms and helped me a lot during the writing of this thesis.

Finally, I take this opportunity to express the profound gratitude from my deep heart to my beloved parents, and my siblings for their love and continuous support both spiritually and materially, whose love enabled me to complete this work.

SYMBOLS AND ABBREVIATIONS.

SPR: Surface plasmon resonance.

LSPR: Localized surface plasmon resonance.

DDA: Discrete dipole approximation.

ε_m: Medium dielectric constant

ε_0: Permittivity of free space

ε_r: Real part of the metal dielectric function.

L: Depolarization factor.

K_B: Binding constants.

K_D: Dissociation constant.

ΔH: Enthalphy.

Alpha Helix : A common motif in the secondary structure of proteins, the alpha helix (α-helix) is a right-handed coiled or spiral conformation, in which every backbone N-H group donates a hydrogen bond to the backbone C=O group of the amino acid.

β-strand: A beta strand (also β strand) is a stretch of polypeptide chain typically 3 to 10 amino acids long with backbone in an almost fully extended conformation

β-sheet: The β sheet (also β-pleated sheet) is the second form of regular secondary structure in proteins, only somewhat less common than the alpha helix. Beta sheets consist of beta strands connected laterally by at least two or three backbone hydrogen bonds, forming a generally twisted, pleated sheet. β-barrel is a closed β sheet.

β-propeller: A beta-propeller is a type of all β protein architecture characterized by 4 to 8 blade-shaped beta sheets arranged toroidally around a central axis. Each sheet typically has four antiparallel β-strands twisted so that the first and fourth strands are almost perpendicular to each other.

β-hairpin: Protein structural motif involving two beta strands that look like a hairpin.

Fibronectin: Fibronectin is a high-molecular weight (~440kDa) glycoprotein of the extracellular matrix that binds to membrane-spanning receptor proteins called integrins.

ScFv: A single-chain variable fragment (scFv) is a fusion protein of the variable regions of the heavy and light chains of immunoglobulins, connected with a short linker peptide of ten to about 25 amino acids.

Complementarity determining regions (**CDRs**)**:** These are the regions within antibodies (also known as immunoglobulins) or T cell receptors where these proteins *complement* an antigen's shape. CDRs determine the protein's affinity and specificity for specific antigens. The CDRs are the most variable part of the molecule, and contribute to the diversity of these molecules, allowing the antibody and the T cell receptor to recognize a vast repertoire of antigens.

N-cap and C-cap: The external repeats at each end of most repeat proteins are referred to as N- and C-cap repeats.

Lipocalins: The lipocalins are a family of proteins which transport small hydrophobic molecules such as steroids, bilins, retinoids, and lipids. They share limited regions of sequence homology and common tertiary structure architecture.

Pfam : Pfam is a database of protein families that includes their annotations and multiple sequence alignments generated using hidden Markov models.

PBS HEAT-like repeat: These proteins contain a short bi-helical repeat that is related to HEAT. Cyanobacteria and red algae harvest light energy using macromolecular complexes known as phycobilisomes (PBS), peripherally attached to the photosynthetic membrane. The major components of PBS are the phycobiliproteins.

BLAST: Basic **L**ocal **A**lignment **S**earch **T**ool, or **BLAST**, is an algorithm for comparing primary biological sequence information, such as the amino-acid sequences of different proteins or the nucleotides of DNA sequences. A BLAST search enables a researcher to compare a query sequence with a library or database of sequences, and identify library sequences that resemble the query sequence above a certain threshold.

SMART: SMART (Simple Modular Architecture Research Tool) is a protein domain database that returns predicted protein functional domains for a protein sequence or accession number submitted by the user.

Mth187: Mth187 is a protein derived from Methanobacterium thermoautotrophicum micro organism.

PDB: The **Protein Data Bank** (**PDB**) is a repository for the 3-D structural data of large biological molecules, such as proteins and acids. The data typically obtained by X-ray crystallography or NMR spectroscopy and submitted by biologists and biochemists from around the world.

UniProtKB identifier: UniProt is a comprehensive, high-quality and freely accessible database of protein sequence and functional information. It contains a large amount of information about the biological function of proteins derived from the research literature.

TABLE OF CONTENTS

Table of contents

INTRODUCTION

La conception, la synthèse et de structuration de matériaux hybrides fonctionnels composés de briques colloïdales a attiré une attention renouvelée avec l'avènement de la physique nanométrique. Dans ce contexte, le confinement et le guidage de l'énergie lumineuse à l'échelle nanométrique a été rendue possible par la structuration de films de métaux nobles jusqu'à quelques centaines de nanomètres en utilisant des techniques conventionnelles. Pourtant, afin de poursuivre cette réduction d'échelle de manière efficace, cette quête en cours pourrait bénéficier de la richesse des structures métalliques colloïdales dont la taille latérale est typiquement de quelques dizaines de nanomètres. Toutefois, une telle approche colloïdale nécessite un contrôle précis (i) de la morphologie des nano-particules, (ii) de leur organisation spatiale dans les architectures à plus grande échelle et (iii) du couplage entre les colloïdes métalliques et des molécules optiquement actives. Si ces trois objectifs sont réunis, de nouvelles synergies entre propriétés optiques pourraient émerger du couplage précis entre des entités colloïdales et moléculaires.

Ce travail de thèse a poursuivi chacun de ces trois objectifs en mettant en œuvre une synthèse innovante de nanoparticules métalliques permettant d'assurer un contrôle morphologique, en développant une nouvelle plate-forme de protéines artificielles pour induire l'auto-assemblage des nanoparticules et en testant une approche bio-inspirée du contrôle de l'interaction métal-fluorophore afin d'améliorer les propriétés optiques moléculaires.

Le chapitre 1 est une introduction au contexte de cette thèse et est subdivisé en trois sections consacrées aux trois aspects de ce travail, à savoir: la nanoplasmonique, la morphosynthèse des nanoparticules et l'auto-assemblage induit par des biomolécules.
Dans la première section, nous donnons un aperçu de la physique des plasmons et de leurs applications, appelée "plasmonique". En particulier, nous insistons sur le fait que les colloïdes métalliques complètent avantageusement les structures et dispositifs conventionnels produits par des techniques de lithographie. La chimie des nano-particules métalliques produit désormais un grand nombre de formes et de tailles et permet ajustement efficace de leurs propriétés optiques. Nous détaillons ensuite l'influence de l'auto-assemblage des nano-particules sur le comportement collectif des plasmons couplés. Pour conclure cette section, nous donnons un bref aperçu du phénomène d'exaltation de fluorescence par les métaux, qui se produit quand une molécule fluorescente est mise dans le proche voisinage d'une structure métallique. Ce dernier point est essentiel pour l'interfaçage des nanostructures plasmoniques avec des entités moléculaires.
Dans la deuxième section, nous nous concentrons sur les nanostructures anisotropes de métaux nobles qui possèdent les propriétés plasmoniques les plus prometteuses mais qui posent aussi la question du contrôle morphologique lors de la synthèse colloïdale. Nous comparons les méthodes classiques de synthèse avec les synthèses les plus récentes utilisant des biomolécules, comme l'ADN ou des peptides, comme agents de contrôle de forme.
La dernière section passe en revue la littérature récente sur l'auto-assemblage de nanoparticules induit par reconnaissance entre biomolécules, qui est un autre moyen de contrôler efficacement les propriétés plasmoniques de colloïdes. Deux principales méthodes sont décrites, à savoir l'auto-assemblage par effet template dans lequel les nanoparticules sont assemblées sur une surface, et le couplage direct dans lequel les biomolécules attachées aux colloïdes dirigent l'interaction particule-particule.

Chapitre 2 rassemble les principales techniques expérimentales et instrumentales qui ont été employées au cours de cette thèse. La synthèse standard de nanoparticules or ou d'argent

monodisperses ainsi que le calcul de leur concentration utilisée dans ce travail sont inclus. Certaines descriptions expérimentales spécifiques ont été laissées dans les chapitres correspondants.

Comme un premier aperçu, une approche innovante pour le contrôle du couplage plasmon-molécule est décrite au **chapitre 3.** Contrairement à la plupart des approches rapportées ces dernières années, nous avons développé une approche inverse dans laquelle le fluorophore est au cœur d'une structure multicouche, entouré par un espaceur diélectrique, qui est lui-même utilisé pour lier des nanoparticules métalliques. Les nano-bâtonnets ordonnés et de taille finie de porphyrines fluorescentes appelés J-agrégats sont utilisés comme support à la minéralisation d'une coquille de silice. Cette encapsulation par la silice est étroitement contrôlée afin de créer une gaine d'épaisseur bien définie dans la gamme pertinente au passage du régime de suppression (quenching) à celui d'exaltation de l'émission. Cette coquille minérale procure une stabilité mécanique à l'assemblage supramoléculaire et devient aussi un template pour l'adsorption de nanoparticules d'Au ou d'Ag. De nouvelles propriétés apparaissent lorsque le couplage exciton-plasmon est optimisé pour un espaceur diélectrique spécifique. Après les étapes successives de synthèse, ce chapitre décrira l'ensemble de la caractérisation spectroscopique et microscopique.

Le chapitre 4 est un lien entre la chimie des matériaux et les aspects biologiques de ce travail de thèse puisque les deux derniers chapitres décriront nos tentatives d'utiliser des protéines artificielles pour diriger le morphosynthèse de colloïdes d'or puis l'auto-assemblage de nanoparticules d'or préformés par interaction entre protéines.

Nous donnerons donc une introduction générale sur la production et la structure des protéines génétiquement modifiées (protéines artificielles) et l'exploitation de leurs propriétés. Les étapes de la synthèse des protéines artificielles, qui consistent en la sélection, d'amplification et de purification, sont exposées. Nous résumerons ensuite comment des structures protéiques ont été largement utilisées dans l'ingénierie de la reconnaissance moléculaire pour des applications en biologie. L'analyse des structures et propriétés des structures les plus réussies nous conduira à envisager plus en détail une famille en particulier, les protéines à répétitions HEAT.

Il nous est apparu que de telles structures de protéines pourraient être exploitées pour la synthèse et l'auto-assemblage de nano-matériaux, en général, et de colloïdes métalliques, en particulier. Si un tel objectif est assez exotique pour la communauté des biologistes

moléculaires étudiant les protéines génétiquement modifiées, nous avons eu la chance de rencontrer l'enthousiasme du Professeur Philippe Minard et de son équipe du laboratoire IBBMC (Orsay, France), qui est l'un des rares spécialistes de l'ingénierie des protéines à répétitions HEAT. Il a conçu un programme de recherche dédié à la construction de protéines spécifiques, appelées protéines à motif α-hélicoïdal répété (α-Rep), à la conception de leur séquence, à la construction de bibliothèques de protéines homologues, à la sélection des meilleurs individus basé sur une méthode dite de "phage display" et à la caractérisation biophysique de ces protéines artificielles.

Au cours d'une étroite collaboration, nous avons exploré les potentialités de cette famille de protéines α-Rep en tant qu'agents directeurs de forme pour la croissance de nanoparticules d'or (chapitre 5) et en tant que partenaires de nouvelles paires de protéines qui interagissent en provoquant l'auto-assemblage de nanoparticules d'or (chapitre 6). Nous consacrons donc la dernière partie de ce chapitre à la description détaillée des protéines α-Rep, qui sont dérivés de bactéries thermophiles et montrent une grande stabilité thermique avec une structure 3D extrêmement bien définie. Enfin, nous décrivons comment l'équipe du professeur Minard a créé des protéines α-Rep, appelés "homorepeats", contenant un nombre différent de copies de la séquence unitaire d'hélice α et aussi une brève introduction à la construction de paires de protéines αRep par le même groupe.

Le chapitre 5 est consacré à notre deuxième défi: le contrôle de la morphologie des nanostructures métalliques. Pour une première tentative, nous avons utilisé des protéines α-Rep homorepeat non sélectionnés pour diriger la réduction de Au(III). Les principaux avantages de ces protéines artificielles sont leur bonne stabilité thermique et leur structure 3D bien définie et robuste, qui peut être modulée par la concaténation d'une partie de la séquence, tout en préservant une certaine variabilité pour certains sites d'acides aminés. Le chapitre explorera successivement l'influence des paramètres de synthèse qui peuvent influencer à la fois la morphologie des nanoparticules, mais aussi l'intégrité des protéines: la concentration en Au (III), le pH, le rapport molaire protéine : Au(III), la présence d'un co-réducteur doux. Les nanostructures obtenues seront étudiées avec plusieurs techniques spectroscopiques, les analyses microscopiques et thermiques des produits hybrides aideront à identifier les mécanismes de formation sous-jacents. Enfin, nous allons discuter de l'influence de ces paramètres ainsi que l'effet du nombre de motifs répétés sur la forme et la taille des nanoparticules.

Enfin, au **chapitre 6,** nous abordons notre dernier objectif qui est l'exploration de contrôler l'auto-assemblage de nano-particules avec une distance interparticulaire correspondant à un couplage fort entre les plasmons de surface localisés. La stratégie suivie par le groupe du Prof Minard consiste d'abord à concevoir des paires de protéines α-Rep qui ont une forte affinité mutuelle par la technique de "phage display". Nous fournirons également des données sur l'affinité des paires de protéines. La deuxième partie, qui a été réalisée au cours de ce travail, consiste à attacher les protéines partenaires à la surface de nanoparticules d'or. Lors du mélange des populations de nanoparticules fonctionnalisées, l'affinité des protéines génétiquement modifiées conduira à la formation de paires de protéines et donc organisera spontanément les nanoparticules. La chimie de surface sera particulièrement détaillée car c'est un point crucial pour l'efficacité de l'auto-assemblage. Notre système a été caractérisé par analyse détaillée de la spectroscopie d'absorption UV-visible, diffusion dynamique de la lumière (DLS), électrophorèse sur gel, microscopie électronique à transmission et à balayage.

CHAPITRE 1

NANOPLASMONIQUE, DES COLLOIDE ET AUTO-ASSEMBLAGE

Résumé

Le contrôle de l'interaction entre la lumière et la matière est fondamental pour la science et les technologies, et de nouveaux matériaux optiques peuvent être obtenus par des techniques de fabrication nanométriques. Traditionnellement, la lumière ne peut être contrôlée sur des échelles de longueur plus petites que la longueur d'onde de la lumière (quelques centaines de nanomètres), mais le contrôle de la lumière à l'échelle nanométrique reste un défi, à cause de la limite habituelle de résolution des microscopes optiques. Toutefois, un nouveau paradigme appelé plasmonique a émergé : c'est une approche basée sur l'utilisation des résonances plasmon de surface de métaux nobles pour contrôler la lumière en dessous de la limite de longueur d'onde, jusqu'à des échelles nanométriques. Dans ce contexte, nous proposons une nouvelle approche dans le but de synthétiser de nouveaux matériaux fonctionnels avec des propriétés optiques contrôlées, principalement en contrôlant la morphologie et l'organisation spatiale à grande échelle des nanostructures plasmoniques, mais aussi le couplage entre colloïdes plasmoniques et molécules optiquement actives.

Dans cette section, nous donnons un aperçu de la physique des plasmons et de leurs applications, appelée plasmonique. Ensuite, nous considérons une approche différente mise en place pour obtenir des matériaux nanométriques avec des propriétés optiques intéressantes.

CHAPTER 1

NANOPLASMONICS, COLLOIDS AND SELF-ASSEMBLY

Controlling the interaction between light and matter is fundamental to science and technology and creation of new optical materials can be achieved by nanoscale fabrication techniques. Traditionally, light can only be controlled on length scales down to about half the wavelength of light, i.e. a few hundred nanometers for visible light. Therefore controlling light at nanoscale remains a challenge for conventional optical microscope techniques. However, a new paradigm called plasmonics has been emerging, which is an approach based on using the localized surface plasmon resonances of metal particles to control light below the diffraction limit, down to nanometer length scales. Hence, in this context we bring our new chemical approach to synthesize new functional materials with controlled optical properties by addressing the morphology control and large scale spatial organization of metallic nanostructures and by adjusting the coupling between the plasmonic colloids and optically active molecules. To this end we will first exploit bioinspired principles applied to the templated synthesis of fluorophore/dielectric/metallic nanoparticle constructs. In chapter 4-6

we will show how new proteins can be engineered to control the growth of metal nanoparticles and their self assembly into higher order architectures.
In this first chapter, we thus wish to introduce two scientific palms at the interface of which our work tries to constitute the engineering of localized surface plasmon in metal nanoparticle using biomolecules on the other side.

1.1. Plasmonics, colloids and self-assembly.

In this section we give an overview of the physics of plasmon and their applications, so-called plasmonics. After we illustrate different approaches already established to obtain nanoscale materials with tailored optical property followed by their respective applications.

1.1.1. Plasmons and Plasmonics.

Physical properties of macroscopic systems and materials differ from those properties of their individual atoms and constituents. In particular nanostructured metals show complex optical properties. Among the striking phenomena encountered in these structures are the collective oscillations of the conduction electrons at the surface of some metals termed as ***surface plasmon***. Plasmon polariton (SPP) oscillations exist in different geometries and mostly in noble metals such as gold and silver. ***Plasmonics*** is a relatively new term which encompasses all studies of these particular light-matter interactions, and covers all areas of research and technology concerned with the study, fabrication, and applications of plasmon supporting structures.[1,2] However, with recent advances that allow controlled fabrication and manipulation of metallic structures on the nanoscale, researchers have demonstrated the new potential of the *localized surface plasmon* (LSP) confined in those structures. Indeed, surface plasmons confined in nanometer-sized structures oscillate around the nanoparticle with a resonance frequency that is known as *localized surface plasmon resonance* (LSPR). [3-6]

When a nanoparticle is much smaller than the wave length of light, the coherent oscillations of the valence band electrons induced by their interaction with an electromagnetic field leads to strong light scattering and absorption and an enhancement of the local electromagnetic field. *Figure I.1* illustrates the difference between propagating and localized surface plasmons. Surface plasmon polaritons (SPP), (*Fig I.1a)* propagate in the *x*- and *y*-directions along the metal-dielectric interface, for distances on the order of tens to hundreds of microns. It usually loses energy to the metal and the nearby dielectric environment due to absorption in

the *z*-direction. [7] Surface plasmons are thus very sensitive to the interfacial medium and adsorbed molecular layer leads to marked shifts in the plasmon resonance wavelength, which can be observed in three modes: (*a*) angle resolved, (*b*) wavelength shift, and (*c*) imaging.

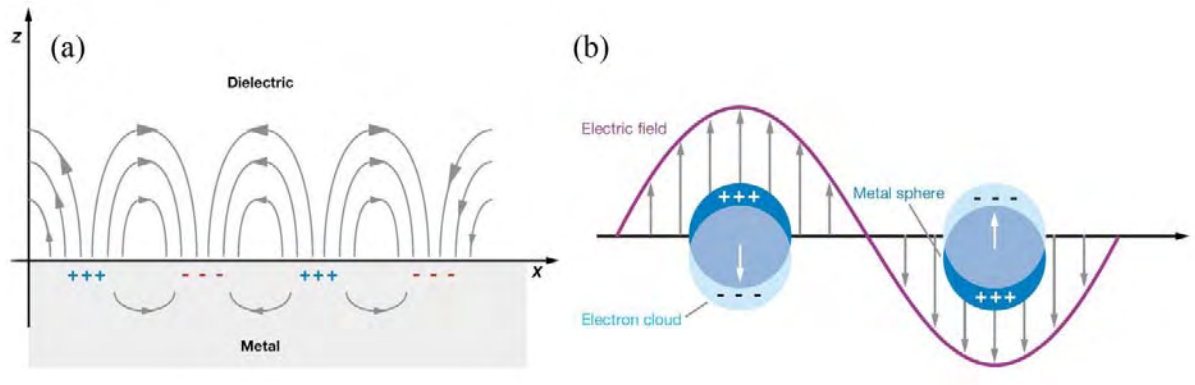

Fig I.1: *Schematic diagrams illustrating (a) surface plasmon polariton (or propagating plasmon) and (b) localized surface plasmon.[8] Image is extracted from the reference, Annual Review of Physical. Chemistry. 2007, 58,267-97.*

In the first two modes, one measures the reflectivity of light from the metal surface as a function of either angle of incidence (at constant wavelength) or wavelength (at constant angle of incidence). The third method uses light of both constant wavelength and incident angle to interrogate a two-dimensional region of the sample, mapping the reflectivity of the surface as a function of position.[9] In the case of localized surface plasmons, light interacts with particles much smaller than the incident wavelength (*Figure I.1b*). This leads to a plasmon that oscillates locally around the nanoparticle with a frequency known as LSPR.[3] Similar to the SPR, the LSPR is sensitive to changes in the local dielectric environment.[10] Typically changes in the local environment can be ascertained through an LSPR wavelength-shift measurement, although a variant of angle resolved sensing for the LSPR is also possible.[11]

Mie originally calculated the surface plasmon resonance by solving Maxwell's equations for small spheres interacting with an electromagnetic field[12]. In the Mie formulation, the incident plane wave as well as the scattering field is expanded into radiating spherical vector wave functions. By enforcing the boundary condition on the spherical surface, the expansion coefficients of the scattered field was computed. For particles much larger or much smaller than the wavelength of the scattered light there are simple and excellent approximations that are sufficient to describe the behavior of the system. Gan was able to extend this theory to apply to ellipsoidal geometries. Modern methods using the discrete dipole approximation

(DDA) allow one to calculate the surface plasmon resonance absorption for arbitrary geometries.[10,13,14]

1.1.2. Applications of Plasmons.

Plasmonics concerns the main possible applications of SPP and LSP modes, which of can be separated into three groups. (1) Applications based on surface plasmon or localized surface plasmon resonances, (2) application based on surface wave propagation and guiding, (3) applications based on local field enhancements.

The sharpness and large sensitivity of SPP resonances to environmental parameters on planar interfaces make them well suited for biological and chemical sensing applications. [15-27] Plasmonic materials can already be found in commercial instruments, such as the BIAcore ®, which monitors the thermodynamics and kinetics of biological binding processes using SPR spectroscopy. In these experiments, a thin (~50-nm) metal film constitutes the sensing platform. The local change in refractive index on the upper side of the film (upon adsorption of analytes) modifies the reflection angle of the monitoring beam placed on the lower side.

However, the controlled fabrication of metallic structures on the nanoscale, by standard lithographic means require better quality metal surfaced to minimize dissipation and improve spatial resolution and hence LSPR borne by colloidal crystal have gained more interest.

The most relevant plasmonic applications are based on the large local field enhancements arising in patterned rough films in most surface enhanced spectroscopy, [28-32] and in particular, surface-enhanced fluorescence. Based on similar principles numerous applications have been proposed in which plasmonic structures are used to engineer and enhance the optical properties of light emitters. For example to cite just a few recent reports the directionality of emission or the quantum yield of solid state emitters and absorbers such as semiconductor quantum dots,[33] quantum wells,[34] light-emitting diodes[35] and solar cells[36] have been enhanced by plasmon engineering.

1.1.3. Nanofabrication techniques.

In order to tailor nanoscale and molecular properties, a precise control of spatial organization of structures with nanometer dimension into complex hierarchy is required. Techniques addressing this challenge encompass two complementary approaches: (1) top-down approach, and (2) bottom up approach. In the top-down approaches bulk material is directly patterned using a number of lithographic techniques using light, electrons, or ions but also embossing, molding, stamping and nanofluidics. The main short coming in top down approaches is the

imperfection of surface structure crystallographic quality of the processed patterns and either each of spatial resolution or excessive process time. These imperfections in turn, lead to dissipation and device failure. But this approach leads to the bulk production of nano device. Bottom-up nanofabrication is the transfer of nanocomponents such as atoms, molecules, clusters, nanoparticles, nanotubes and nanowires etc, from their stock solution to the substrate where they are integrated and evaluated. Supramolecular and colloidal chemistry are two of the main techniques used in this approach. Often the choice of the nanofabrication method is a compromise between the effectiveness, cost and technology available.

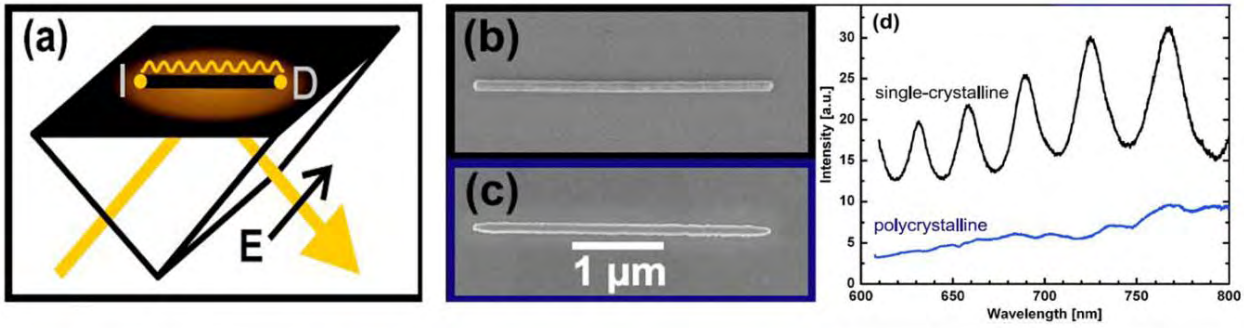

Fig I.2: *Scattered light spectra of 3.3 µm long silver nanowires, diameter 90 nm. (a) Sketch of optical excitation on nanowires. (b), (c) Scanning electron micrographs of a chemically and an electron-beam lithographically fabricated silver nanowire respectively. (d) Scattered light spectra from the distal nanowire end face of the chemically fabricated wire (single crystalline, upper curve) and the lithographically fabricated wire (polycrystalline, lower curve). Image extracted from the reference, Physical Review Letters 95, 257403, 2005.*

Fig I.2 clearly demonstrates the advantage of bottom up approach.[37] Here micrometer long silver nanowires are synthesized by chemical (bottom-up) as well as lithographic technique (top-down). Light scattered from both nanowires end faces is measured as a function of wavelength.[37] The scattered light intensity is modulated as a function of wavelength in single crystalline nanowires which indicates the multiple reflection of the surface plasmon wave whereas no regular signal modulation is observed in case of polycrystalline nanowires synthesized by lithographic technique. Hence bottom up approach can potentially produce nano structures with less defects and more homogeneous chemical composition.

1.1.4. Noble metal nanostructures.

In noble metals the new optical properties emerge as size of the metal nanoparticles gets small enough. The origin of properties can be traced to the confinement of the oscillation of free electrons on the particle surface which gives rise to oscillating modes displaying resonance behavior. These resonance modes are very sensitive to the nanoparticle size and shape.

Therefore synthetic protocols, which deliver well-defined shapes and sizes, are highly desired. Several classes of synthesis routes exist, which lead to products that display different characteristics. Bottom up synthetic approaches include templated chemistry, chemical, electrochemical, sonochemical, thermal and photochemical reduction techniques of a starting metal salt.[38] Nanoparticles synthesis usually employs an agent able to stop growth of the particle at the nanoscale. These capping molecules, such as surfactants or polymers are used for example to prevent aggregation and precipitation of the metal nanoparticles. The two archetypal examples are the single phase, water based reduction of a gold or silver salt by citrate, introduced by Turkevich et al.[39,40] and refined by Frens,[41] which produces almost spherical particles over a tunable range of sizes. The kinetics of the Turkevich process and the mechanism of gold nanoparticle formation have been explained with sequential nucleation and growth process. [42] [43]

In the second example which involves two step process, gold (III) salt is reduced into highly monodispersed nanorods.[44] Growth of nanorod begins with the synthesis of metallic 'nanospheres' (seeds) by the reduction of Au(III) salt with a strong reducing agent (sodium borohydride) in the presence of a capping agent to prevent particle growth. The gold or silver spheres thus generated can serve as seeds for the growth of anisotropic nanostructures. Hence in the second step, these seeds are added to a solution containing more metal salt in presence of mild reducing agent (ascorbic acid), and a rod like micellar template (cetyltrimethylammonium bromide, CTAB). The seeds serve as nucleation sites for nanorod and nanowires growth with CTAB preventing the growth of a subset {100} of facet in favor of another subset {111}. The choice of the reduction technique, time, and capping molecule[45,46] determines the size and shape of the nanoparticles. For example in the case of the nanorods synthesis, the gold ions are complexed by cetyltrimethylammonium (CTA) and not directly reduced by ascorbic acid. Upon adding the gold particle seeds the autocatalytic growth of crystallographically oriented rods is allowed under the kinetic control of excess CTA. This passivation leads to a large variety of different shapes. spheres,[38,47,48] rods,[45] cubes,[49] disks, [50] wires, [51,52] triangular prisms,[53] and tetra hexahedral nanocrystals,[54] made of gold(*Fig I.3*), silver (*Fig I.4*) which were obtained with different reduction techniques and capping materials.

In spite of many synthetic protocols available in morphosynthesis, these as synthesized objects have lack of advantage since the capping molecules firmly stick to their surface and it is hard to do any post functionalization afterwards. Moreover these results are based on the

serendipity and mostly results in low yield of the product. In this regard there is a large space for the design of new synthetic strategy to obtain desired metal nanostructures.

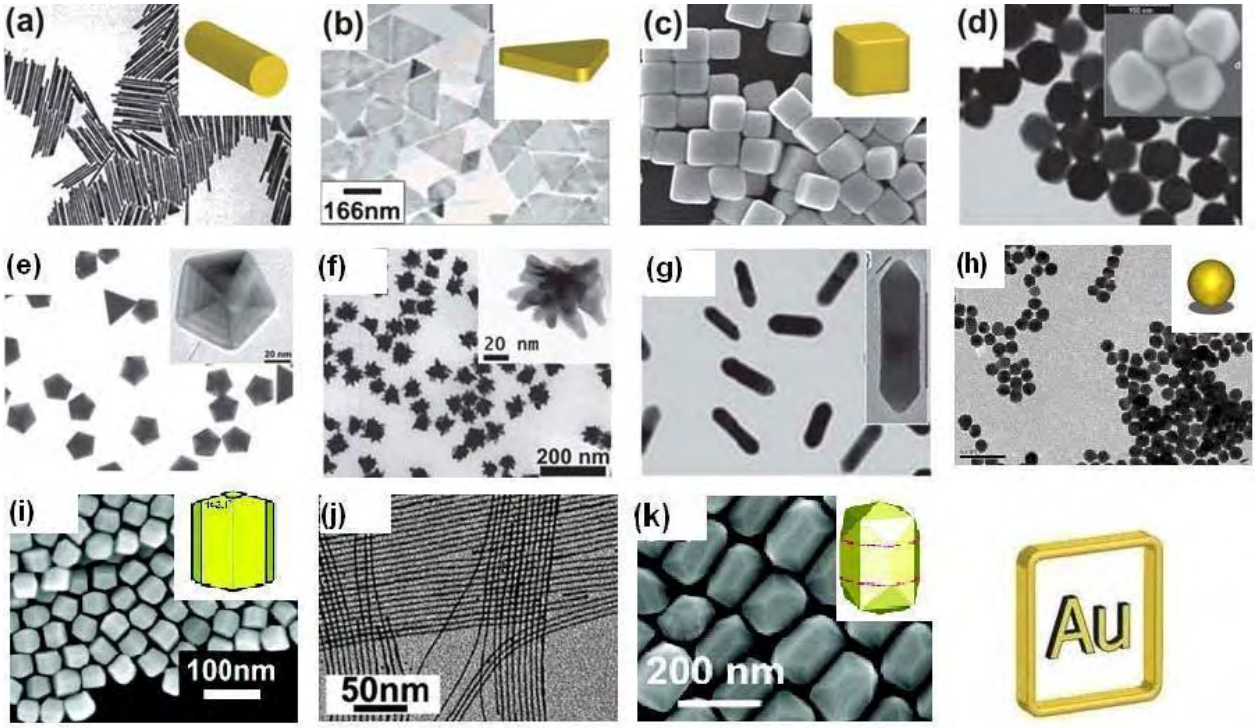

Fig I.3: *Anisotropic nanostructures of Au. (a) Rods (b) triangular (c) cubic (d) octahedral NPs (e) decahedra (f) nanostars (g) nanorods with sharp tips (h) spherical gold nanoparticles truncated ditetragonal prisms (j) nanowires (k) tetra hexahedral gold nanocrystals.* [54-56] *Image is extracted from the reference Nanoscale, 2011, 3, 1304.*

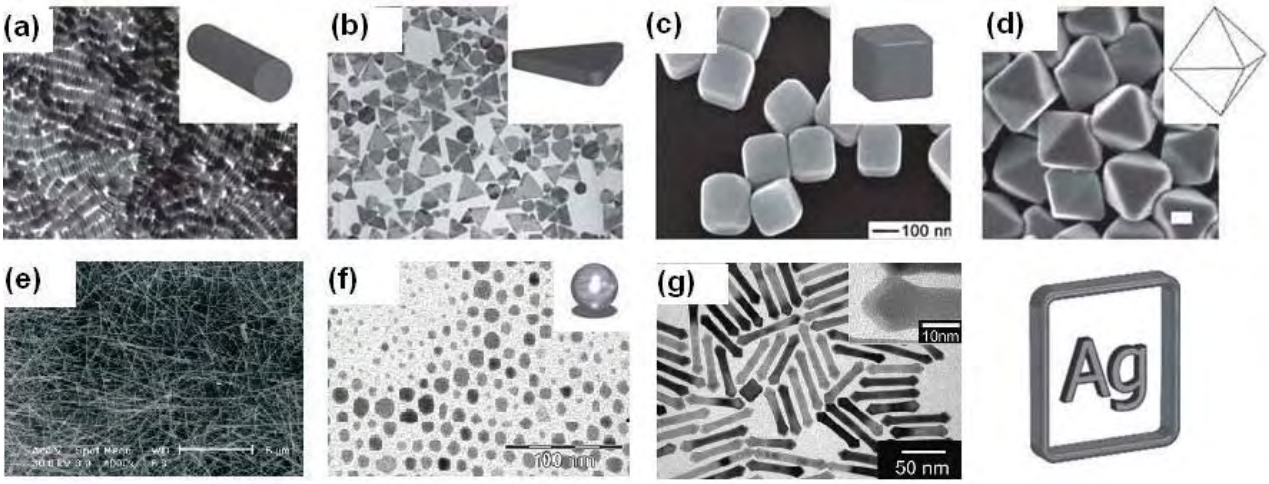

Fig I.4: *Anisotropic nanostructures of Ag. (a) Nanorods (b) triangular (c) cubic (d) bi pyramidal (e) nanowires (f) spherical nanoparticles and (g) bimetallic rods with sharp tips*[55,57]*. Image is extracted from the reference Nanoscale, 2011, 3, 1304.*

1.1.5. Effect of size, shape, and assembly of metal nanoparticles on optical properties.

Effect of size.

The spectral and spatial properties of local surface plasmon borne by nanoparticle strongly depend on size, shape/geometry, composition and local environment. Hence controlling these parameters allows the tunability of both the plasmon resonance frequency (the color) as well as the strength of the plasmonic enhancement (the intensity). Many applications could be envisioned thanks to the large enhancement of the surface electric field on the metal nanoparticles surface and, in addition, anisotropic shapes have plasmon resonance absorptions that are even stronger, leading to increased detection sensitivity.

As the size of the nanoparticle increases, the number of free which is directly proportional to the volume electrons increases,[10] causing a shift in the electric field density on the surface and this is strictly valid in the dipolar limit. As the size of the nanoparticle approaches the wavelength of light, the nanoparticle can no longer be homogeneously polarized by the light, resulting in the excitation of higher-order oscillation modes. However for a nanoparticle in the size range of few tens of nanometer, it is sufficient to consider that the nanoparticle behave as a single dipole (dipole approximation) and to assume that the electric field of light is constant (quasistatic approximation).[58]

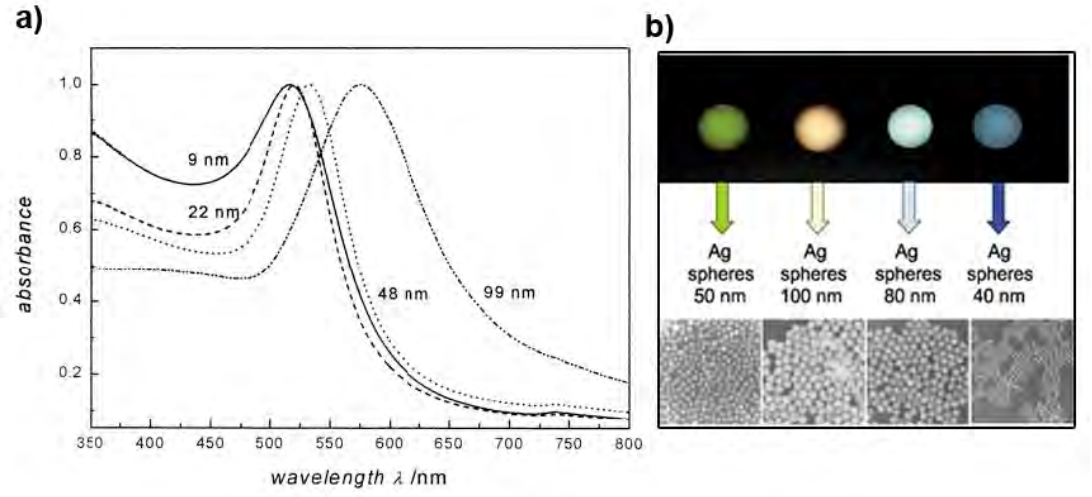

Fig I.5: *a) UV-vis extinction spectra of Au nanospheres of different size ranging from 9- 99 nm [58].b) The influence of size on the light-scattering, and resultant colors, of silver nanoparticles[59]. Image is extracted from the reference a) J. Phys. Chem. B 1999, 103, 4212, and b) Small 2005, 1, 1.*

Fig I.5a clearly demonstrates the red-shift and broadening of the plasmon resonance band of gold nanoparticles, as the size of the nanoparticles are increased (9 to 99nm). [58] In addition, as the particle size increases, there is increased emission by the plasmon oscillations (radiative

damping) which results in an increase in the scattering contribution, but also reduces the plasmon lifetime (increased plasmon line width)[10] comes from electromagnetic retardation which results from the depolarization of the light field across the particle surface.[58] Gold nanoparticles can be easily synthesized with a good size control and low size dispersion in the 10-60 nm range.

On the contrary, when the size of the nanoparticle is reduced down to ~2nm it approaches the Fermi wavelength of electrons (i.e., the electron the de Broglie wavelength at the Fermi level: ~0.5nm for Au and Ag), the continuous density of states breaks up into discrete energy levels leading to the observation of dramatically different optical, electrical and chemical properties compared to nanoparticles[60] including fluorescence.

Effect of Shape.

For nanoparticles of anisotropic shape (e.g., triangles or nanorods), the coulombic restoring force on the electron cloud is weaker along the light polarization direction as compared to a sphere. This results in the emergence of lower resonance frequency modes.

In general, the polarizibility of a nanoparticle of any general shape is given as:

$$\boldsymbol{\alpha} = \frac{\boldsymbol{\varepsilon_0 V}}{\boldsymbol{L}} \left(\frac{\boldsymbol{\varepsilon - \varepsilon_m}}{\boldsymbol{\varepsilon + \left(\frac{1-L}{L}\right)\varepsilon_m}} \right) \qquad \textbf{(1)}$$

Where L is a depolarization factor, which depends on the shape. Here ε_0 is the permittivity of vacuum and ε_m is the dielectric constant of the surrounding. ε is the dielectric function of the metal which is a complex and frequency dependent. For a sphere, which is isotropic in all three dimensions, L=1/3, which reduces eq (2) to eq (1)[61,62]. The plasmon resonance condition from eq (3) is given as [62]:

$$\boldsymbol{\varepsilon_r = -\left(\frac{1-L}{L}\right)\varepsilon_m} \qquad \textbf{(2)}$$

This condition summarizes the effect of the nanoparticle shape (through *L*) on the surface plasmon resonance frequency.

Fig I.6 clearly shows the influence of shape on the optical property of noble metal nanoparticles. Spherical silver and gold nanoparticles have single plasmon absorption bands at ~400 and ~520 nm, respectively. Anisotropic gold and silver nanorods have two main principle plasmon absorption peaks; one at shorter wavelength corresponding to absorption

and scattering of light along the short axis of the nanorod (transverse plasmon band), and the other band at longer wavelength corresponding to absorption and scattering of light along the long axis of the nanorod (longitudinal plasmon band).

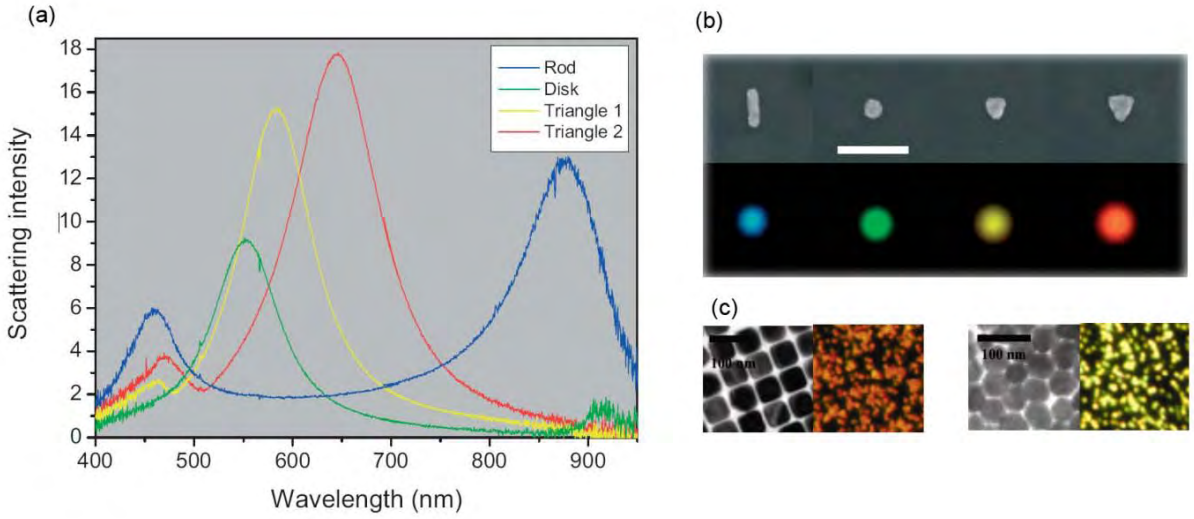

Fig I.6: *(a) Dark-field spectra of several metallic nanoparticles made by e-beam lithography. (b) Scanning electron micrographs (top), dark-field images (down), and from left to right the shapes are, a rod, a disc, and two triangles (the right hand one being the larger of the two).(The scale bar in the top figure is 300 nm).*[63] *(c) Transmission electron micrographs and dark field microscopy image of gold nanocubes (left) and gold nano hexagons (right), taken on solutions dried down on a microscope slide. Scale bars 100 nm and the field of view is 1 mm.*[47]

The longitudinal plasmon absorption bands are widely tunable with nanorod aspect ratio from the visible to the near-IR.[64] Triangular nanoparticles have been generated by photochemical means[65] and chemical growth.[66] The edges and corners are very important for triangular nanoparticles. Snipping of the edges produces a visible blue shift in the plasmon resonance,[65] which can be modeled theoretically.[13] Disks also display a similar dependence of the plasmon resonance absorption dependence on their aspect ratio.[67] Thus the anisotropy of metal nanostructures has been shown to allow a large control over the optical absorbance for different types of shapes generated.[10]

Effect of assembly.

While the optical properties of a metal nanoparticle are primarily determined by its surface plasmon resonance, there is a dramatic change in the optical absorption spectrum position of resonances when nanoparticles come into close proximity.[13 68,69] This is due to the coupling of the plasmon oscillations of the interacting particles. The plasmon oscillation generates an enhanced electric field localized on the nanoparticle surface, decaying with the distance away

from the nanoparticle. The near-field of particles present in close proximity can interact with each other.

Thus the electric field E' felt by each particle is the sum of the incident light field E and the perturbation due to the presence of the electric dipole present on the neighboring particle:

$$E' = E + \xi \frac{\mu}{4\pi\varepsilon_0\varepsilon_m d^3} \quad (3)$$

where μ is the dipole moment due to the particle plasmon and ξ is an orientation factor.[70] Because of the near-field coupling of the plasmons, there is a change in the frequency of the surface plasmon oscillation of the coupled nanoparticle system with respect to the isolated particle.[61]

For example, the assembly or aggregation of spherical Au nanoparticles into a close packed structure results in a red shift (*Fig I.7a, b)* of the SPR wavelength with decrease in the intensity of absorption.

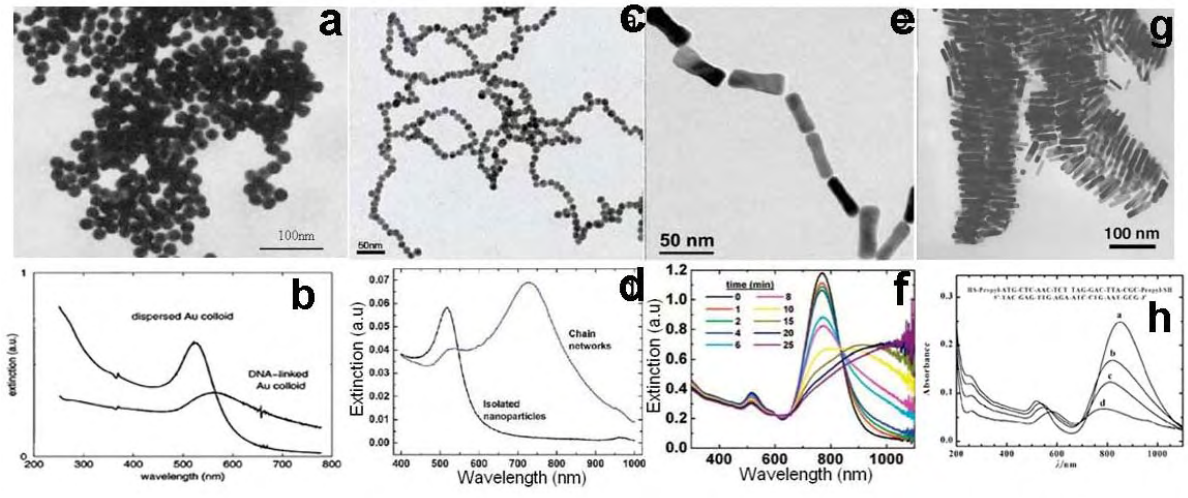

Fig I.7: *Self-assembly of gold nanostructures by linker molecules. a) aggregation of spherical Au nanoparticles into a close packed structure with DNA,[71] c) formation of branched chain network of gold nanoparticle 3 days after addition of 2-mercaptoethanol (MEA), [72] e) End-to-end assembled gold nanorods using cysteine amino acid at pH 1.0. The assembly is due to the attachment of both thiol and amine groups of cysteine to the tips of adjacent nanorods.[73] g) Side by side uniaxial assembly of gold nanorods triggered by DNA duplex[74]. Figures b), d), f) and h) depict the UV-visible spectral changes before and after nanostructure self-assembly corresponding to the images a, c, e and g respectively. Picture taken from the reference Journal of Nanosciences. Letter. 2012,2,10.*

The chain like assembly of nanoparticles also show red shift of 520nm plasmon band with decrease in the absorption intensity along with uprising longitudinal band at longer wavelengths (*Fig I.7c, d).*[75] The extent of the coupling-induced red shift increases with

decreasing inter-particle distance and increasing number of particles in the assembly. In case of side by side uniaxial assembly of nanorods, *(Fig I.7 g, h)* there is a clear blue-shift of the longitudinal plasmon band is observed and can be attributable to the coupling of the plasmons of the two interacting nanorods.

In contrast the coupling of the transverse plasmon oscillations in side-by-side assembled nanorods leads to a red-shifted resonance. In case of end to end assembly of nanorods (*Fig I.7 e, f*) a large red-shift of the longitudinal plasmon band is observed whereas the transverse plasmon resonance does not show any appreciable shift. The detailed mechanism and theoretical calculations are performed which is well in agreement with experimental values.[76,77] The shift in the surface plasmon resonance wavelength maximum resulting from the electromagnetic coupling between the nanoparticles allows the use of far-field absorption or scattering-based measurements to probe the near-field coupling.

1.1.6. Metal enhanced fluorescence (MEF) and metal-fluorophore coupling.

The efficient tuning of the optical features of plasmons can be achieved by controlling morphology and organization of nanoparticles as explained above. The finely tuned coupling of this localized plasmon with luminescent molecules results in an effective modulation of a fluorescence.[78] Therefore, the study of molecular fluorescence in association with metal plasmon for sensing and microscopy applications has gained a lot of importance in the past few decades.

When chromophores are placed near plasmon-bearing surfaces, their optical properties and fluorescence are significantly modified. In most cases, the quenching (i.e. strong suppression) of fluorescence is observed when the chromophores are placed in direct contact with metals whereas it is un-altered when the molecule is placed far from the metal surface. Surprisingly, when the chromophore is placed within a very narrow range of intermediate distances from the metal, the fluorescence appears to be strongly amplified. This effect is now known as metal-enhanced fluorescence that has potential applications in sensing, imaging technology. The quenching of the fluorescence is usually related to the opening of non radiative decay channels, where energy is dissipated in the vibration of the metallic material.[79] On the other hand, the enhancement of the fluorescence can be induced by either an enhanced absorption into the excited state due to the local increase of the incident electric field by plasmon resonances, or an increased radiative decay rate due to the modified photon density of states near the metal surface. The dependency of quenching vs. enhancement on the molecule-metal

distance is quite strong. Chromophores placed within less than 5 nm of the metal nanoparticle surface (*Fig I.8a*) have their fluorescence quenched while chromophores placed at distances of about 10 nm have their fluorescence enhanced up to 100-fold.

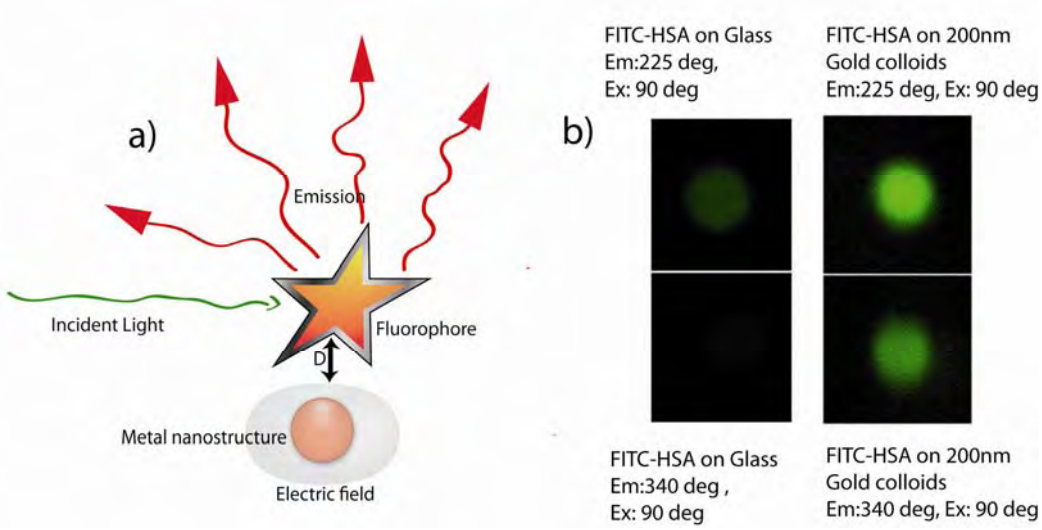

Fig I.8: *a) Schematic illustration depicting the processes in close proximity to metals (< 10nm) involved in metal enhanced fluorescence, enhanced absorption and coupling to surface plasmons). b) Real-color photographs of fluorescence emission of FITC-HSA on glass and 200 nm gold colloids taken through an emission filter (488 nm) at an excitation angle 90 deg and fluorescence emission was observed at 225 and 340 degrees.*[80,81]

The quantum yield and photo stability of weakly fluorescing species are dramatically increased in the vicinity of strong electromagnetic field generated at the surface of metal nanoparticles.[82] Hence metal-enhanced fluorescence has become a powerful tool for applications in drug discovery, high-throughput screening, immunoassays and protein-protein detection. [83,84] As an illustration, *Fig 1.8b* shows real color photographs of the emission of fluorescein isothiocynate (FITC) placed on a glass or on 200nm gold colloid. The fluorescence emissions on 200 nm gold colloids at both emission angles (225deg, 340deg) are much brighter than that of the glass substrate. More comprehensive understanding of this inherently nanoscale process can be acquired by studying the efficiency of the molecular fluorescence enhancement and its dependency on plasmon resonance energy and nanoparticle scattering.

An increased understanding of this interaction will ultimately lead to design strategies for optimizing molecular fluorescence enhancement with adjacent metallic nanostructures, a highly useful goal with direct relevance in many molecule-based measurement or device applications.

1.1.7. Approaches and methodology of fluorophore/dielectric /metal systems.

Over the past two decades, several approaches have been adopted to study the coupling between molecular and plasmonic resonances. One of the first reported observations of fluorescent signal enhancement by nanoparticles was by Thomas and Kamat.[85] 1-Methylaminopyrene was attached onto gold clusters (with diameters ranging from 5 to 8 nm), weakly stabilized by tetraoctylammonium bromide moieties. In the resulting system, an intense emission was detected, while the nanoparticles themselves are non fluorescent and the 1-methylaminopyrene in the buffer used was only weakly luminescent. It was hypothesized that the interaction of the amino lone pair electrons of the fluorophore with the metal decreases the donating ability of the fluorophore and hence suppresses the photo-induced electron transfer responsible for the main non-radiative decay process.

The study of metal-fluorophore interactions has also been extended to large scale structures formed by the finite ensemble of fluorophore molecules generally called as J-aggregates that exhibit intense narrowband absorption and emission bands from the coherent excitation of tens of thousands of aligned molecules. Such structures will be studied in Chapter 3. This gives an opportunity to study the collective fluorescence of a supramolecular structure containing a finite, albeit large, number of fluorophores. Kometani et al[86] observed resonant coupling effects in molecule-coated plasmonic nanostructures. They observed an absorption dip in the extinction spectra of silver and gold nanoparticles coated with J-aggregate. Wiederrecht et al,[87] explained that this observation arise from coherent coupling between molecular excitons and electronic polarizations of noble metal nanoparticles. The effects of resonant coupling as a function of spectral overlap were experimentally reported by Wurtz et al, who used J-aggregate molecules on metallic nanowires assemblies with tunable LSPR.[88] They observed the formation of hybrid plasmonic - excitonic states in assemblies of aligned gold (Au) nanorods surrounded by a shell of J-aggregates (*Fig I.9a)*.

Halas et al. later extended these ideas to solution-bound gold nanoshells and J-aggregates, Fofang et al,[89] observed similar behavior in both dipolar and quadrupolar plasmonic resonances. More recently this group has investigated the near-infrared fluorescence enhancement of Indocyanine green (ICG) molecules as a function of distance from the surface of Au nanoshells.[90] The shape of metallic nanostructure can also influence the quantum yield and life time of a fluorophores molecule [91](*Fig I.9c)*. Recently, a hybrid nanostructure formed by spin-coating a thin layer of J-aggregated molecules onto a array of holes in a metal film

was studied in transient absorption experiments (*Fig I.9b*) by Salomon et al.[92] The strong coupling between excitons and surface plasmon polaritons in a hybrid structure is observed and the energy splitting between coupled hybrid states is found to be several 100 meV. Such large splitting shows that the local enhancement of the near-field in these structures can result in very strong coupling effects with molecules.

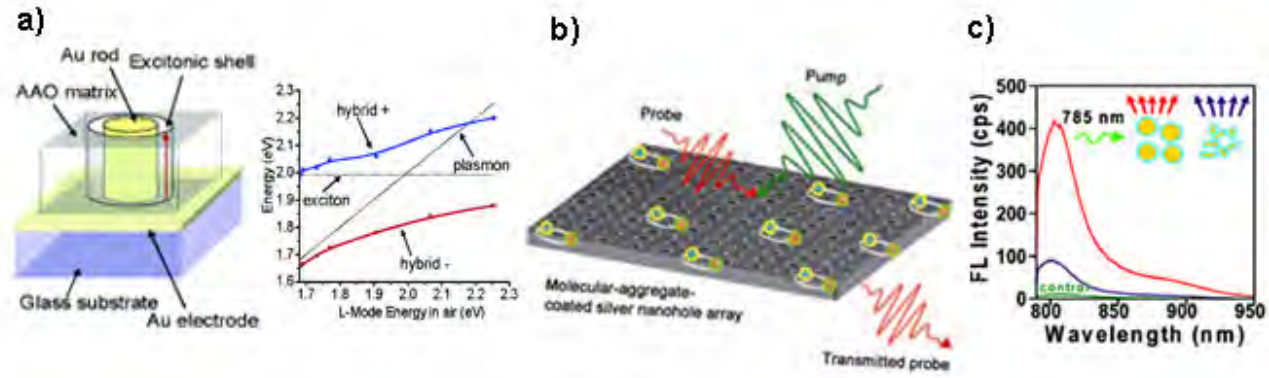

Fig I.9: *Schematic illustration and experimental data depicting different approaches employed to study metal enhanced fluorescence. a) Assembly of aligned Au nanorods supported by a transparent substrate and energy diagram showing the anti crossing of the plasmonic (diagonal solid black line) and the excitonic (horizontal dotted black line).[88] b) Diagram illustrating J-aggregated molecules onto a metallic nanostructure fabricated by perforating a 100 nm thick silver film with a hexagonal array of holes 230 nm in diameter. The dynamics of coupled exciton-SPP hybrid modes is studied in a transient absorption experiment.* [92] *c) Fluorescence spectra showing enhancement by Au nanoshells and nanorods on conjugation with conjugation of HSA_IR800 protein-fluorophore complex to nanoshells (NSs) and nanorods (NRs).*[91]

From these studies, it is clear that the extinction spectra of nanoparticles covered with resonant molecules are not a simple sum of absorption contributions, but rather strongly influenced by the strength of resonant coupling, which is maximized at the spectral overlap of the resonances. In order to achieve efficient resonant coupling there is a need to ease the processing of metal nanoparticle surface as well as fluorophore and to control the distance between them. So far most of the approaches employed in this domain have used the surface modification or processing of metal nanostructures. Yet, in these methods, it is difficult to quantify the amount of molecules on metal surface.

Hence in our study described in Chapter 3, we propose a reverse approach where we create a fluorophore / dielectric / metal system through a unique templating process. This method gives us an opportunity to study the evolution of the fluorescence of the fluorophore when the

molecule / dielectric interface is created as well as the final effect of adding a plasmon material on the emission of the fluorophore.

1.2. Bio-inspired Morphosynthesis.

In standard growth of inorganic material, crystal shape is usually limited to the macroscopic expression of the geometric rules encompassed in the space groups of unit cells. On the contrary, biominerals produced by living organisms usually exhibit exquisitely complex structures that are not simply inherited from the symmetries of the bulk material. The main reason for this difference is that biomineralization occurs under the kinetic control of the mineral growth by organic matrices. Shape emerge from the interaction of these matrices with the growing inorganic materials (morphogenesis) via several possible mechanism: templating, confinement of the reaction field, anisotropic diffusion, etc.[93] The careful observation of biomineral growth and the understanding of the natural biomineralization mechanisms have led to bio-inspired principles which are now used to produce new nanomaterials with controlled shape with non-natural ingredients and condition. This synthetic control of morphology has been named as morphosynthesis.

Our second aim, during this thesis work, is to propose new ways to synthesize anisotropic metal nanoparticles with designable surface chemistry for subsequent derivatization. In this section, we therefore expose the conventional methodologies used for the synthesis of anisotropic noble metal nanostructures and will point out their shortcoming. We then review some unconventional approaches to generate specific shape of inorganic materials including noble metals using biomolecules.

1.2.1. Conventional synthesis of noble metal anisotropic nanostructures.

In general, nanoparticle growth can happen either in a thermodynamically controlled or kinetically controlled manner. Thermodynamic growth often results in uniform growth of all crystal facets having low surface energy. The formation of nanoparticles starts with nucleation (formation of nuclei as seeds), followed by growth stages[94]. Like other face-centered cubic (fcc) metals with intrinsically high symmetry, gold and silver seeds mainly express facets bounds by {111} and {100} planes due to their lower surface energies [95]. When the gold or silver precursor is reduced to generate metal atoms at a high rate, thermodynamic control will take over in both nucleation and growth stages, so that the metal atoms will add homogeneously to all facets of the seeds to form particles with thermodynamically favored

shapes, mostly spherical or near-spherical structures (truncated cubes). In the case of kinetically controlled growth, preferential and directional growth happens that in turn results in the anisotropic growth. Here when the rate of reduction is quite slow, gold or silver atoms will preferentially add to facets with higher surface energies, which can be promoted by selectively lowering the surface energies of other facets with the help of capping agents. As a result, some facets of the seeds will grow more rapidly than other facets, yielding particles with shapes different (twins) from those generated under thermodynamic control. The synergistic effects of both thermodynamic and the kinetic aspects play a critical role in determining nanoparticle shape. The formation of anisotropic Au nanostructure (for example gold nanorods) by electrochemical[96] or photochemical reduction methods [97] in a surfactant solution has been demonstrated. Two types of templates have been mainly used: a hard template and a soft template. Mesoporous alumina or silica and carbon nanotubes are examples of hard templates that have cylindrical. Au ions are introduced into the pores where their reduction produces colloidal particles or small enough nanoparticles are diffused in the pores and attached to the surface of a hard template.[98,99] It is possible to prepare final products of uniform size by using a hard template, but the quality of the metallic nanostructure cannot exceed that of the template which is usually as rough as lithographically patterned motives. Moreover, reactant diffusion in the pores usually limits the length of the nanorods. Among the recently reported soft templates, let us mention the case of Au nanowires obtained by mixing aqueous solution of Au (I) to oleylamine solution in hexane or toluene which results in the formation of ultrathin nanowires of micrometer length.[51,100] The cooperative interaction between the gold precursor and the oleylamine leads to a meso structure formation followed by slow in situ reduction and mesostructures of the Au+-oleylamine complex serve as growth template and govern the anisotropic growth in nanoscale.

A major breakthrough in the synthesis of noble metal nanoparticles was the splitting between nucleation and growth steps which led to the discovery of famous seed mediated synthesis of Au nanorods. In the first step, the seed particles are generated with a strong reducing agent such as sodium borohydride. These seeds are small (2-5 nm) and generally pseudo-spherical or decahedral. In the second step, these seeds are then added to a growth solution that consist of fresh metal salt, surfactant cetyltrimethylammonium bromide, (CTAB) that directs the growth of nanoparticles to nanorods and a weaker reducing agent (often ascorbic acid) that simply pre-reduces Au(III) into Au(I). The final reduction occurs auto-catalytically at the surface of the nanoparticles. Counter ions and additives have also been found to play a role in

directing growth and final shape of nanoparticles obtained. However, a general mechanism for the formation of these morphologies has not been fully understood yet. It is believed that surfactant-capped seed becomes part of the soft template and introduction of seed to the growth solution results gold atoms into the template. Quaternary ammonium has an affinity for Au surface but can be better packed into self assembled monolayer (SAM) when attaching to {100} facets. Since penta twins are present in the seed solution they can accommodate CTAB on {100} then growth is restricted and only {111} can grow (*Fig I.10*). [47] [101]

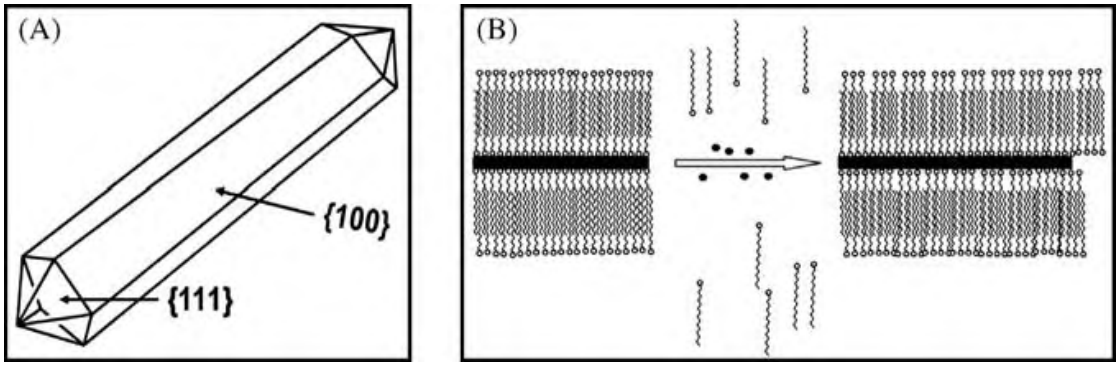

Fig I.10: *Cartoon representation of (A) 3-D morphology showing (111) end-faces and (100) side-faces. (B) Illustration of 'zipping' mechanism for the formation of the bi-layer of CTAB (squiggles) on the NR (black rectangle) surface may assist NR formation as more gold ion (black dots) is introduced. Reproduced with permission from Reference.*[47]

Hence a preferential adsorption of capping molecules to specific facets can hinder the crystal growth of some crystallographic planes and promote the growth in selected directions. It has been established that the morphology of final nanoparticles is mainly determined by the number of twin defects present in the initial seed as shown in the schematic illustration *Fig I.11.* External agents such as halide ion can either reduce the redox potential of the Au and thus increase the rate of the reaction or modify the relative facet growth even in the presence of the cetyltrimethylammonium. By adding iodide ions in a growth solution typically used in nanorod synthesis, the shape of the resultant nanoparticles can be changed into triangular nanoprisms.[102] Here, the iodide ion adsorption appears to suppress the crystal growth along the Au (111) direction, resulting in Au (111)-faced triangular nanoprisms. When the counter anions of the surfactant cetyltrimethylammonium bromide (CTAB) were replaced with chloride ions, a drastic change in the morphology from rod to rice-shape was observed, which demonstrates the effectiveness of the adsorption of halide ions.

Gold and silver nuclei usually incorporate twin boundary defects as they lead to a lower surface energy. As the growth proceeds, changes in the defect structure of the nuclei become

too costly relative to the available thermal energy and they remain trapped in a given morphology. As illustrated by *Fig I.11*, this process results in various kinds of seeds such as multiply twinned, singly twinned, and single-crystal seeds, with the fivefold symmetry. Multiply twinned decahedra are the naturally abundant seed morphology and are also the most reactive. Metal atoms preferentially add to the twin defects of decahedra, leading to the formation of nanowires (NWs).

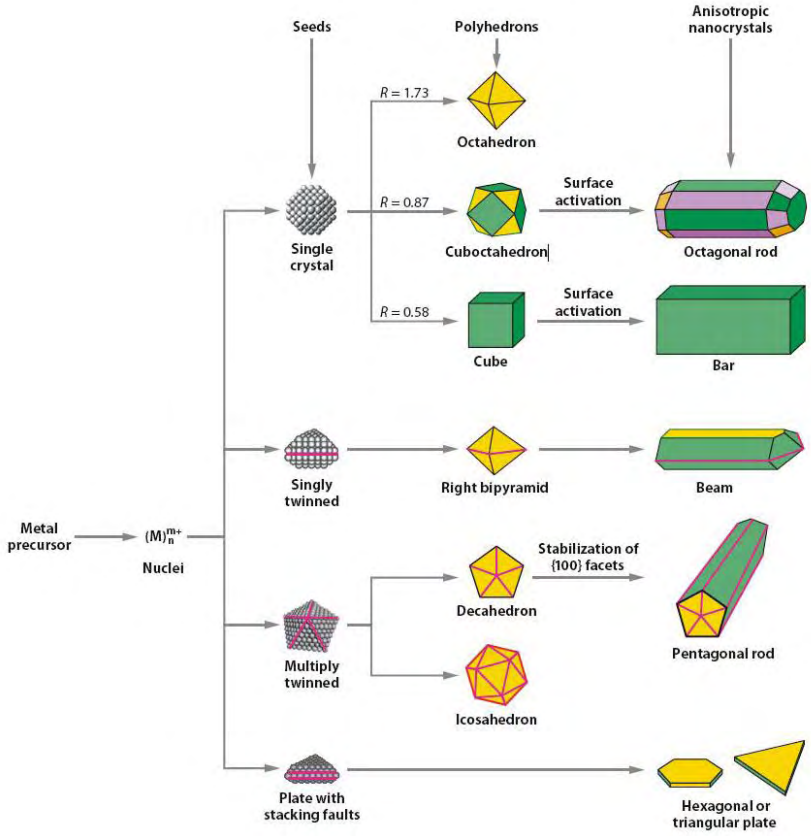

Fig I.11: *A schematic illustrating various stages of the reaction that leads to the formation of noble-metal nanoparticles with different shapes. After the formation of nuclei (small clusters), they become seeds with a single-crystal, singly twinned, or multiply twinned structure. Stacking faults in the seeds results in plate-like structures. Green, orange, and purple represent the (100), (111), and (110) facets, respectively. The parameter R is defined as the ratio between the growth rates along the (100) and (111) directions. Twin planes are delineated in the drawing with magenta lines. Image extracted from the reference Annual Review of Physical Chemistry, 167, 60, 2009.* [103]

Among the various solution-phase methods, polyol (alcohol containing multiple hydroxyl groups) reduction is probably the best established for generating Ag nanoparticles with controllable shapes and optical properties in addition by using this method various shapes of Au nanostructures can also be synthesized. Polyol synthesis was developed in 1989 by Fievet et al[104] ,Viau et al.[105], Sun et al.[106] and Wiley et al.[107] made a number of modifications to the

conventional protocol. The polyol synthesis involves the reduction of an inorganic salt precursor by polyol at an elevated temperature. Many precursor salts can easily dissolve in polyol. Apart from this, temperature dependent reducing power and relatively high boiling points makes it suitable solvents for making anisotropic nanoparticles.

From these example, it appears that plasmonic nanoparticles of desired shape can nowadays be prepared if one controls precisely the internal structures of the seeds, the structure directing and/or stabilizing agent, the reduction rate and the precursor nature. Thus solution-based chemical route produces a number of structural architectures from rods, [45] cubes,[49] disks, [50] wires,[51,52] triangular prisms,[53] and tetra hexahedral nanocrystals[54] of Au and Ag nanoparticles (*Fig I.5 and Fig I.4*) in high yield at room temperature in the presence of a single surfactant in aqueous solution. Molecules that bind strongly to the surface of the nanoparticles are efficient to stabilize crystalline facets and thus promote anisotropy. However, this efficiency has an adverse consequence since strongly binding molecules have a tendency to passivate the nanoparticle surface and therefore to prevent subsequent surface reactions. Hence post functionalization of these nanoparticles are very difficult in order promote sensing and bio imaging applications. For example in case of gold nanorods, the functionalization of CTA-coated nanorods remains challenging and therefore there is a strong necessity to explore new synthetic methods for the generation of anisotropic gold and silver nanoparticles.

1.2.2. Bio-inspired approaches for morphosynthesis.

More than 50 years of observation of biominerals has resulted in the understanding that some biomolecules have emerged with the ability to strongly affect crystal growth and therefore to control the shape of minerals. In living organisms, minerals almost never grow in the thermodynamically stable form but in some metastable form, the shape or property of which is important for the organism. For example hard, wear-resistant material with highly ordered micro/nano architecture consisting of hydroxyl apatite crystallites that assemble into woven rod structure has been found in mouse enamel (*Fig I.12c*) and a fiber like biologically synthesized complex materials were observed in sponge spicule of Rosella which has a layered silica with excellent optical and mechanical properties (*Fig I.12d*). It has been found that biological systems are also capable of making functional superstructures of inorganic nanomaterials such as amorphous silica, magnetite (magneto tactic bacteria) (*Fig I.12b*), and calcite.[108]

Such observations have been extrapolated to the concepts of biomimetism or bio-inspiration. In particular, this has opened the way to use and design biomolecules as a morphosynthetic

agent for non-natural mineral, including noble metals. Concerning the mechanisms of the biological control over morphology and microstructure, the apatite-gelatin system can be seen as a simplified model because of its close chemical correspondence and remarkable analogy to structural aspects of dentine and enamel composites.[109] (*Fig I.12c*) The formation of this self-assembled aggregate occurs with the complex organization of minute apatite crystals together with proteins. The growth of subsequent mineral layers is controlled by an epitaxially linked composite of fluorapatite and the organic component.

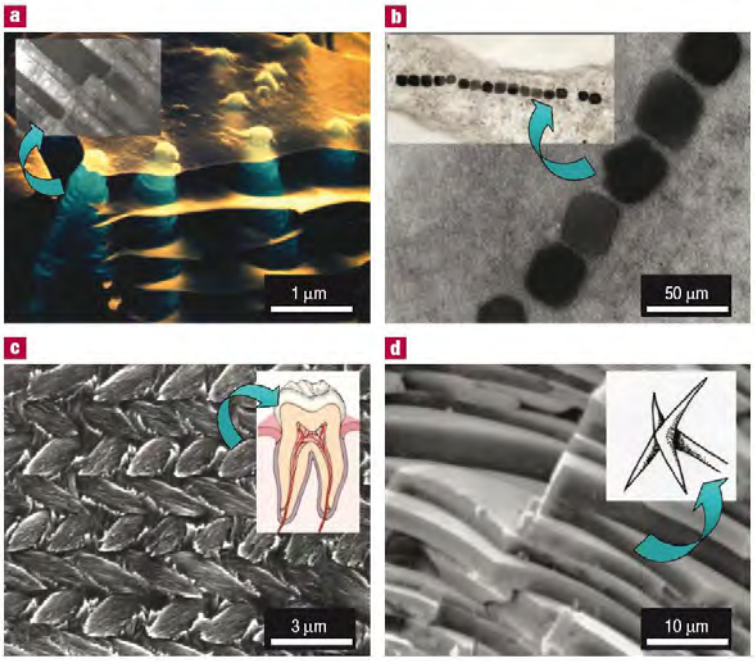

Fig I.12: *Early examples of biologically synthesized complex materials. a) Scanning electron microscope (SEM) image of a growth edge of abalone displaying aragonite platelets (blue) separated by organic film (orange) that eventually becomes nacre (mother-of pearl). b) TEM image of magnetite nanoparticles formed by magneto tactic bacterium (Aquaspirillum magnetotacticum), c) SEM image of mouse enamel (inset: schematic cross-section of a human tooth). d) SEM image of sponge spicule (with a cross-shaped apex shown in inset. Image extracted from the reference, nature materials, 2, 2003.*

In biological systems, shape-controlled synthesis of nanomaterials can be achieved by using template-directed synthesis, where nanostructures are directly synthesized on the organic matrix. The size and shape of the final structure is dictated by the geometry of the template. Numerous biological systems, such as proteins,[110-113] polysaccharides,[114-116] DNA[117] or combinatorial phage display peptide libraries,[118] have already been used to direct the growth of nanoparticles. In addition, the morphology control of nanomaterials can also be achieved through functional molecules such as polypeptides that bind specifically to crystallographic

planes of inorganic surfaces. As a model system of the crystal habit modification, the formation and characterization of CdS nanoparticles grown in the sub phase of Langmuir-Blodgett (LB) films have been studied systematically.[119] Mann et al. pioneered the use of self-assembled bacteria S-layers to synthesize cadmium sulfide super lattices.[110] Here S-layer protein arrays acts as templates for the in-situ nucleation of ordered two-dimensional arrays of 5-nm CdS nanocrystals. The nucleation of the inorganic phase is confined to the pores between subunits in the S-layers. Two-tier stacks of nanoparticles can be formed in the presence of double-layered protein crystals.[110] Double-stranded DNA, an ubiquitous biomolecule with cylindrical double-helical structure, has also been explored in templated-synthesis of gold and copper nanoparticle-nanowires.[120] However, small DNA oligonucleotides are unable to accurately determine the shape of nanocrystals but rather result in spatially organizing in spate the nucleation of spherical particles. DNA origami can develop robust and well folded 3D template structure of DNA but it remains that DNA has not shown an effective ability to binding to arbitrarily chosen materials.

Serendipitous approaches have led to several other examples where biomolecules have been chosen for their chemical properties that conferred them a selective affinity towards specific crystallographic faces. The main issue that arose then was how to rationalize these methods to design the best match between biomolecules, inorganic material and crystallographic facets. Different ways for selecting biomolecules with desired specific affinity to inorganic surface have therefore been explored. One way is by a molecular theoretical approach similar to that used for pharmaceutical drugs.[121,122] Another possibility is to extract biomolecules from the biological source followed by their isolation, purification and cloning.[123] A third approach has met a much larger application field and consist in using combinatorial biology techniques in which a large library of peptides with the same number of amino acids, but of randomly different sequences, is used to determine specific sequences that strongly bind to a chosen inorganic surface.[111,124] The specific aspect of phage display libraries will be discussed in detail in Chapter 4, however, we give a brief overview of the power of this approach through the work of A. Belcher and colleagues. These authors pioneered in the use of genetically engineered phage viruses for the synthesis and multi-length scale ordering of quantum dots (QD). In this system a peptide with specific recognition to ZnS crystal surface was isolated through screening of a phage population exposed to a target made of ZnS. The selected peptide, which is initially expressed as a fusion protein in the M13 virus was then confirmed to have an affinity with ZnS crystal surface. The purified viruses are then resuspended in ZnS

precursor solution to form highly ordered QD of micrometer length.[125]

Such screening techniques have revealed that polypeptides could act on the morphology of silver and gold crystals. Compared to biopolymers and oligonucleotides, short peptide sequences offer simultaneously four unique advantages in developing biomolecule-material interfaces: molecular recognition, self-assembly, genetic manipulation and diverse chemical reactivity. It is conceivable, that molecular recognition leads to nucleation, growth and morphogenesis of inorganics under favorable synthesis conditions. Once a peptide recognizes a material, it could also further self arrange on the surface to form supramolecular architectures. S. Brown's [126] and M. Sarikaya's [111] groups have extensively investigated the peptide-mediated control of crystal growth including for gold.[127]

Typically, gold binding polypeptides were selected and used in a gold precursor solution in presence of mild reducing agent. Small concentration of gold and reaction at low temperature allows particle formation at a slower rate, giving the protein time to interact with surfaces during growth which results in the formation of and flat, triangular or pseudo hexagonal particles (*Fig I.13a*).[127]

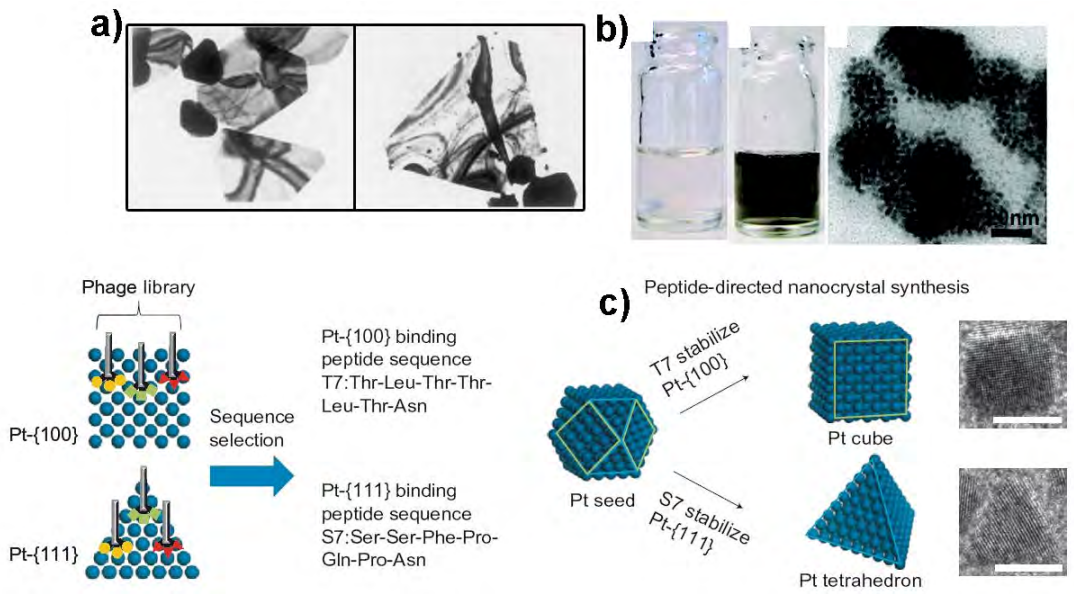

Fig I.13: *Biomolecule mediated synthesis of anisotropic nanostructures. (a) Gold crystals formed by polypeptides,[127] (b) initial and final color of the platinum nanocrystals solution synthesized by peptide regulation and corresponding TEM images of the nano clusterss[128]. (c) Schematic illustration of facet-specific peptide sequence selection and nano crystal synthesis. Facet-specific peptides are used to direct the synthesis of platinum nano crystal cubes and tetrahedrons, respectively and TEM images of platinum nanocubes obtained from the T7-regulated reaction and platinum nano tetrahedrons obtained from the S7-regulated reaction, respectively; scale bars 5 nm[129].*

Very recently C.-Y. Chiu et al. have reported the synthesis of platinum nanocrystals selectively shaped using facet-specific peptide sequences. This is one of the first rational approaches to the predictable control of nano crystal structure using biomolecular specificities. Peptide sequences that recognize Pt-{100} and Pt-{111} planes have been identified by phage display screening and used in directing the shape for the formation of platinum nanocrystals in a colloidal synthetic process[129]. Although the fundamental mechanism of the recognition of a material surface by a short peptide is far from clear, quantitative binding experiments and modeling give some clues of how this might be possible[118]. While peptides selected for a specific crystallographic affinity provides a way to engineer their amino acid sequence, they will lack the 3D folding of proteins which would provide a much more reliable way to organize the chemical moieties in space in order to favor a peptide-mineral epitaxial relation. Some attempts to use natural proteins have been reported[112] but modifications of their amino acids sequence had to be done, in order to improve their affinity for the target materials, which is a long process that often destabilizes the overall structure resulting in the protein denaturation.

Hence the concept of artificial proteins that have been introduced recently in molecular biological sciences are appealing candidates which could be used effectively to overcome the specific problems encountered at the biomolecule-inorganic material interface. Artificial proteins possess a stable, folded three dimensional structure with variable positions in their amino acid sequence that can be used to modulate their chemical activity. If these proteins can be partially engineered for improving their affinity towards a target materials (for example, in this work, gold) without disrupting the folded 3D structure there would be an opportunity to create a new class of artificial proteins with well-folded 3D scaffold that would ensure a reliable spatial positioning of some amino-acids that could then be optimized for the chemical and structural matching with mineral surface atoms. In such a protein, one surface could be engaged with the metal binding or shape control while other surfaces could be used for further chemical reactions or molecular recognition. In our work we propose to use artificial proteins called as α-Rep proteins, which will be introduced separately in Chapter 4, and which are highly thermo stable and possess a well-defined 3D folded structure, as a morphosynthetic agents for the creation of anisotropic Au nanoparticles.

Noteworthingly, some of the template-directed synthesis described above could simultaneously give rise to templated self-assembly of nanoparticles with in-situ growth

process. While syntheses where self-assembly occurs simultaneously with the reduction of the precursors by available chemical moieties, the best organization of nanoparticles has been obtained from the assembly of pre-synthesized colloids, which is another way to create higher order architectures relevant for nano plasmonics if metal nanoparticles are considered. In the next section, we give a brief overview of these principles.

1.3. Biomolecule driven self assembly.

In section 1.1.5 we have pointed out the marked evolution of the optical properties of nanoparticles when they are brought in close vicinity so that their respective LSPR are coupled. Since the coupling of plasmonic nanoparticles appears to be another efficient route to the engineering of plasmonic architectures, we describe in this section chemical methods used to assemble nanoparticles spontaneously into higher-order structures. After a brief overview of the classical self-assembly approaches, we introduce some recent strategies exploiting the unique organization capabilities of biomolecules. We are then able to define the characteristics that self-assembling molecular systems should possess.

Self-assembly is a process by which molecules, nanoparticles or other discrete components spontaneously organize into ordered structures characterized by a minimum in the system's free energy. In order to successfully exploit nanoparticle self-assembly in technological applications and to ensure efficient scale up, a high level of direction and control will be required.

1.3.1. Conventional methods for self assembly.

Simple chemical molecules can be used to induce the self-assembly of nanoparticles and a vast literature is available that cannot be exhaustively surveyed here. Some essential principles will therefore be illustrated from a personal selection of published results. One can distinguish two orthogonal approaches. Self-assembly can be mediated by a substrate. In this case the particles will be precisely positioned with respect to anchoring groups but there will be little control on the interparticle distance. On the other hand, functionalized particles can be driven to assemble by direct interparticle coupling. This will result in the effective control of the interparticle distance yet the aggregates will remain in suspension and the challenge will be to position this assembly onto a substrate, especially if device fabrication is targeted. To illustrate the first approach, let us consider the formation a monolayer of Au nanoparticles on a silicon substrate reported by Hsuen-Li et. al.[130] In this method, a self-assembled

monolayer (SAM) of a dithiol is formed on oxidized silicon substrate when the surface modification is carried out by 3-mercaptopropyl trimethoxysilane (MPS), which is then immersed into a Turkevitch's solution containing citrate and $HAuCl_4$ for 10 to 50 min at elevated temperature. *Fig I.15a,b* show the resulting dense monolayer of nanoparticles formed directly on the surface but that have no specific in plane ordering.[130] Such dense monolayer of nanoparticles can also be obtained by carefully controlling the dewetting conditions as illustrated in *Fig I.15b*. Here, the aqueous suspension of nanoparticles is injected between a cover glass and a template substrate. Upon drying, the water front line moves backward and the particles are concentrated near the edge of the meniscus. The capillary force drags and presses and eventually traps the particles onto the template substrate[131]. Interestingly, such nanoparticle arrays show optical properties different from usual thin gold film used in SPR detection devices, such as shifted plasmon angles, broadened spectrum and increased minimum reflectivity.

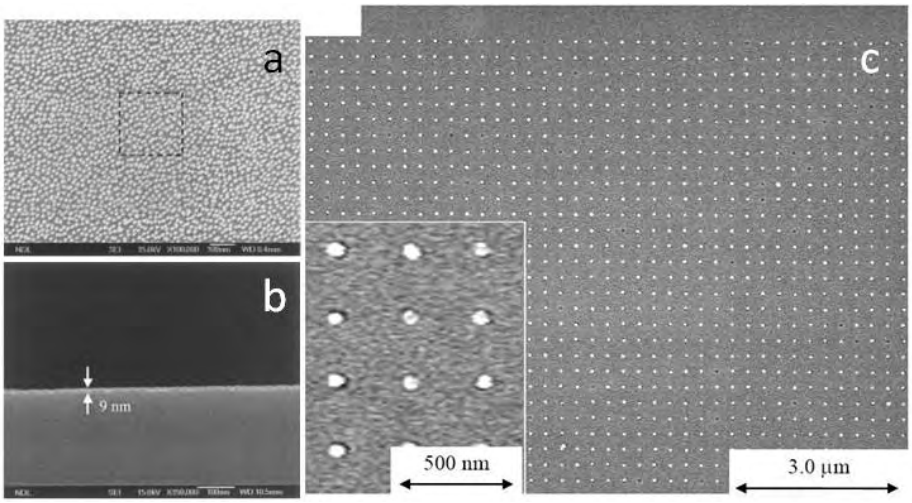

Fig I.15:*(a) Top view and (b) cross-section SEM images of gold nanoparticle film on silicon substrate.*[130] *c) SEM image of self assembled 60nm Au nanoparticles by template assisted self assembly.*[131]

A fine immobilization of Au nanoparticles into a layer by layer patterns has also been accomplished by using directed self-assembly on templates fabricated from phase-separated mixed Langmuir-Blodgett (LB) films containing a silane coupling agent[132]. The patterns of the mixed LB films can be tuned by adjusting the intermolecular interactions between the film-forming molecules and the fabrication conditions. However, it is clear from these examples that the template can only accurately set the interparticle spacing to very large or touching conditions but they fails to adjust it precisely in the regime where localized surface

plasmons interact efficiently, i.e. in the 1-20 nm range. For this, the direct interparticle self-assembly is more effective.

As an example, we consider the use of mercaptoethanol (MEA) for the self assembly of Au nanoparticles into chain like structure. When mercaptoethanol (MEA) is added to 13nm Au nanoparticle solution at a typical molar ration of 5000: 1, the initially light red colored solution turned to purple as monitored by UV-Vis spectra.[72] The initially single plasmon band at 520 nm slowly decreases in intensity without energy shift and a shoulder emerges at 700 nm which is stabilized in a period of 24 hr *(Fig I.4b).* The assembly of nanoparticles occurs when a permanent dipole is created on citrate-stabilized Au nanoparticles by spatial partitioning of the neutral MEA and charged citrate capping ligands (*Fig I.14a*).

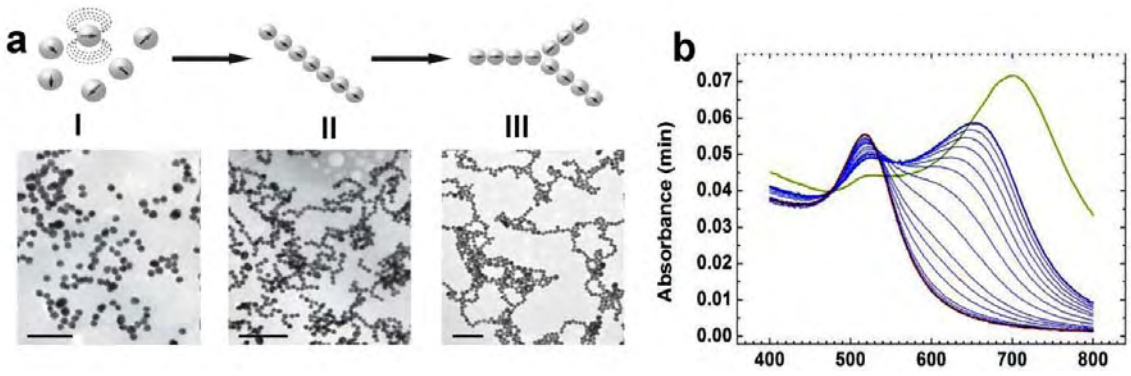

Fig I.14: *a) Au nanochains formation mechanism within the dipolar fluid interpretation. TEM images of (I) isolated gold nanoparticles, (II) short linear chains, and (III) fully formed branched PNN. Scale bars are 100 nm*[133]*.b) Evolution of UV-Vis absorbance spectra showing rise of longitudinal band with the formation of chains.*

A further evolution of the system results in the final highly branched networks (Figure *Fig I.14d*). One should point out that the studies of the plasmonic properties of these networks impose to deposit and spread them onto substrates which can be a limiting step.[134] The main drawback observed with dipole-induced assembly is the dipole-dipole interaction diminishes quickly as the particle dimensions increases. One way to obviate this limitation is to covalently bind neighboring nanoparticles. This was implemented for the end-to-end self-assembly of Au nanorods that was induced by the addition of cysteine amino acid at pH 1.0. The assembly is due to the simultaneous attachment of both thiol and amine groups of cysteine to the tips of adjacent nanorods[73] (*Fig I.7 e, f*). Such chains show a striking variation of the initial optical properties even though the linear segments of the chains are formed of only a small number of nanoparticles (typically 10-20). This assembly process depends on the linker concentration and leads to large networks composed of 100-500 nm-long linear chains.

Such short linear chains are too small to be envisioned as basic structures for nano plasmonic devices if one considers the current spatial resolutions of near-field and far-field optical characterization techniques, which exceed 100 nm minimal feature size.

Through these examples, we have seen that self-assemblies of nanoparticles obtained by conventional methods are becoming more elaborate but face two limitations. In most of the cases, templated approaches do not produce precisely coupled plasmonic particles. Direct self-assembly approaches can control the particle spacing much more effectively but lead to superstructures that are either too small or very complex and difficult to deposit on a substrate for future device fabrications. This points towards more challenges posed by the nano plasmonic context to the self-assembly technology. We will see in the next section that biomolecule-driven self-assembly opens new routes to try and address these issues.

1.3.2. Biomolecule driven self assembly.

In supramolecular chemistry, intermolecular interactions are tailored to create programmed assemblies of molecules. When similar concepts are applied to molecules tethered to the surface of nanoparticles, the molecular interactions drive the self-assembly of colloidal superstructures, in conjunction with the specific force fields of the supporting nanoparticles (hard sphere, electrostatic, magnetic .etc). Among all possible interacting molecular systems, the ones that have emerged in nature provide a wealth of efficient self-assembling molecular tools that are highly relevant in nanosciences. In this section, we will restrict our introduction to the main categories of biomolecules used as self-assembling agents of noble metal nanoparticles but the exposed principles would apply to many other materials.

DNA.

In the past decade, DNA strands of very short (oligonucleotides) or longer length (plasmid and lambda DNA) have received an increasing attention. The main reason is that the genomic projects have generated highly efficient tools to produce oligonucleotides via cheap and fast automated procedure and that sequencing speed and accuracy has gained orders of magnitude. DNA offers two intuitive ways to assembled nanoparticles. The highly negative phosphate backbone is an ideal electrostatic template for the attachment of cationic nanostructures. More interestingly, the base-pairing interactions provide a means of simple yet robust and expandable programming of interactions. Moreover, double strand formation is a convenient way to incorporate different chemical functionalities, including those required for attracting nano objects of diverse nature. Two of the first examples of using DNA to drive the direct

interparticle interaction were demonstrated by the groups of Mirkin and Alivisatos in 1996 [135,136] (*Fig I.19 a, b, c)* Alivisatos and co-workers have conjugated a short oligonucleotide to the surface of nanoparticles. The addition of a long DNA single strand bearing several repeats of the complementary sequence of the oligonucleotides would induce the threading of several nanoparticles along the DNA strand.

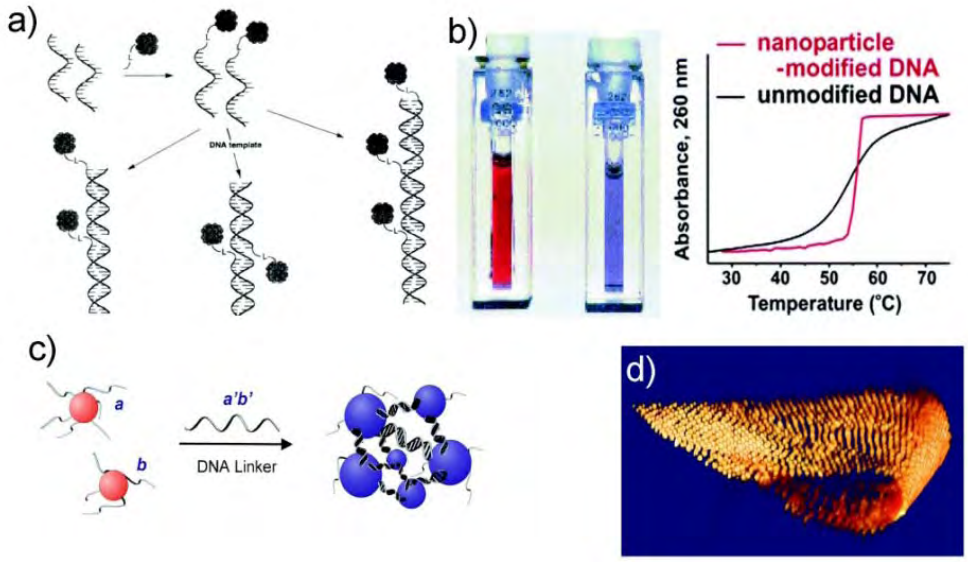

Fig I.19: *Nanostructure assembly induced by sequence-specific DNA binding events: (a) discrete clusters of Au NPs synthesized using a single DNA strand as a template,[136] (b) solution color change from red to purple due to plasmon coupling upon DNA-templated assembly of Au NPs and change in absorbance of DNA duplexes upon thermal dissociation shows a sharp melting transition for assembled DNA-AuNP conjugates,[135](c)polyvalent DNA_AuNP conjugates organized into extended aggregates via the addition of multiple DNA linking strands,[135] (d) 3D STEM tomography reconstruction of a folded nanoparticle super lattice sheet.[137]*

In a slightly different approach, Mirkin and co-workers attached many oligonucleotides strands to the nanoparticle surface, creating a polyvalent DNA-Au NP conjugate. They synthesized two populations of functionalized particles bearing different DNA sequence. Upon addition of a free DNA strand half complementary to each population they drove the macroscopic self- assembly of nanoparticles which can be thermally reverted above the "melting" temperature of the double stranded DNA. Over the years, this concept has been extensively studied and developed. high throughput assembly of nanoclusters by stepwise encoding of DNA.[138] Using the polyvalent DNA-nanoparticle as a building block, many different assemblies have been achieved. For example, and discrete “satellite” structures has been accomplished, where a number of smaller nanoparticles surround a large DNA-functionalized particle.[139,140] On the other side, extended crystallization of colloidal

nanoparticles could be guided by DNA pairing.[141] Nanoparticle-streptavidin-biotin constructs have also been created that utilize single-stranded DNA as a template.[142] DNA was used as a dry ligand in a micro hole confined self-assembly process mediated by drying effect that yielded micrometer-long, free-standing monolayer's of nanoparticle super-lattice sheets [137] *(Fig I.19d).* Anisotropic nanorod assembly has been achieved by direct DNA pairing [74] and, more recently, using DNA origami templates. [143] Well-ordered and oriented Au nanorods and nanorods-nanoparticle hybrid architectures have been self-assembled onto a triangular DNA scaffold showing that templated assembly can also possible to some extent with controlled interparticle positioning.

Through this very limited set of examples, it is already obvious that DNA molecules count among the most efficient, reliable and flexible candidates to achieve self-assembly of nanoparticles.

Peptide and Natural Proteins.

Peptides and natural proteins have a much more varied chemistry due to their amino-acid composition but, in the context of self-assembly, they possess a unique asset, compared to DNA, since they exhibit varying degrees of spatial order. Some polypeptide sequences spontaneously form structures such as α- helices, β-sheets, or even more complex 3D arrangements that resemble folded proteins. Natural proteins are of course the most advanced form of peptide folding which result in highly structured 1, 2, and 3D scaffold. Similarly to DNA, self-assembly driven by peptides or proteins can be achieved by either templated self-assembly or by direct interparticle interaction. Rosi and co-workers have shown that amphiphilic peptides can assemble into several supramolecular architectures, including helicoidal threads that have been used for the templated assembly of unique chiral plasmonic nanostructures (*Fig I.20a).*[144]

Recently, Matsui and co-workers have reported the assembly of gold nanoparticles into micrometer sized 3D arrays using collagen fibers. [145] The peptide structure is modified to incorporate biotin moiety, which are used to bind streptavidin coated gold nanoparticles. The resulting cubic structures, the size of which could be tailored from 100 nm to 2 μm in diameter by altering the relative concentrations of peptides and nanoparticles. Some natural proteins are organized into large and highly ordered arrays, which are favorable for the 2D organization of nanoparticles. An early example of the assembly of metallic structures based

on protein arrays was shown by McMillin et al., where chaperonin proteins spontaneously form 2-D arrays on top of which nanoparticles could be effectively organized (*Fig I.20 b).*[146]

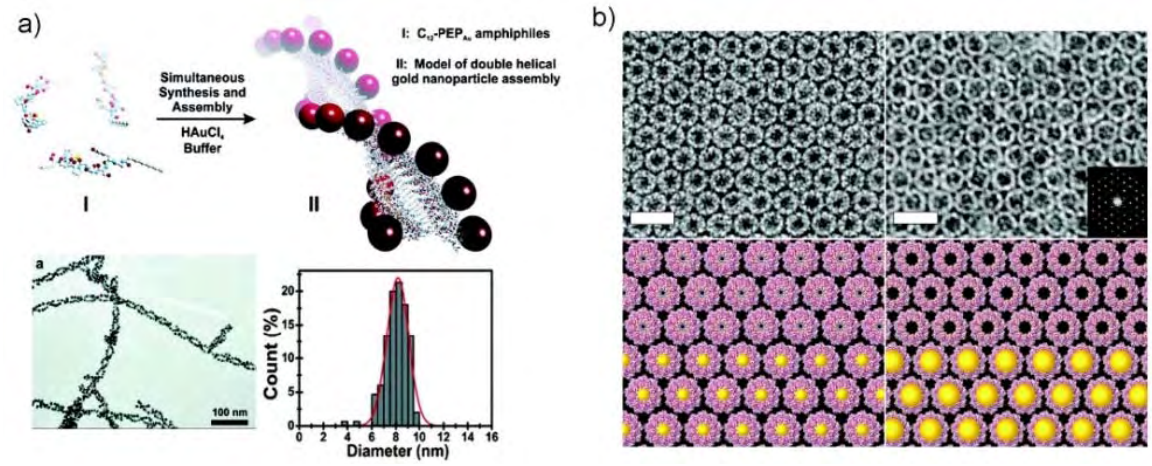

Fig I.20: *a) Schematic illustration of the formation of helical peptide supramolecular architectures that template the formation of ordered Au NPs, TEM images showing the helical morphology and size histogram of Au NPs*[144]*. b) Arrays of chaperonin proteins serving as binding sites for different sizes of particles. Top: TEM images, with the electron diffraction pattern inset, bottom: schematics of protein arrays and Au NP binding sites. Scale bars are 30 nm*[146]*.Images are extracted from the references.*[144,146]

In this work, the proteins were modified with cysteine residues at selected points on their surface and then exposed to gold nanoparticles with diameters of 5, 10, or 15 nm, resulting in large hexagonally close packed nanoparticle arrays. Interestingly, the size of the cysteine rings that bind the nanoparticles has a distinct impact on the diameter of Au NPs that could associate with the template. The 3 nm rings bind only 5 nm Au NPs, while the 9 nm rings bind only 10 nm Au NPs. Similar to this approach, a periodic 2D structure formed by S-layer protein has been utilized to form site specific organization of gold nanoparticle by Mann and co-workers[147].

Antibody.

Among the most evolved molecular recognition systems in nature, antibodies are the dominant strategy. Antibodies can recognize antigen with a very high selectivity, a strong affinity and constitute a very large family of proteins that provide a virtual infinity of protein pairs. One of the first examples of application of antigen-antibody recognition to the 3D assembly of metallic nanoparticles was provided by Mann and co-workers. [148] In the same year, Fitzmaurice and coworkers attached disulfide-biotin analogues to gold nanoparticles and subsequently assembled the particles by adding streptavidin, a molecule known to bind up to

four biotins with some of the highest known affinity. [149] Murphy and colleague have applied this archetypal biotin-streptavidin pair to self-assemble long 1D arrays of nanorods joined in an end-to-end fashion after the attachment of thiolated biotin on the tips of the nanorods. Finally, Kotov and collaborators have recently developed a method to template end-to-end or side-to-side assembly of nanorods using the specific interaction between an antibody and a smaller molecule.[150]

Virus.

Stepping up in complexity, proteins can themselves self-assemble into 2D arrays as stated before or into more complex structures such as viruses which usually comprise a protein capsid protecting their genetic code (RNA or DNA). Viruses are discrete nanoscale objects of predictable sizes and shapes that can be considered, from the material chemist viewpoint, as a complex 3D amino-acid surface able to template the self-assembly of materials.

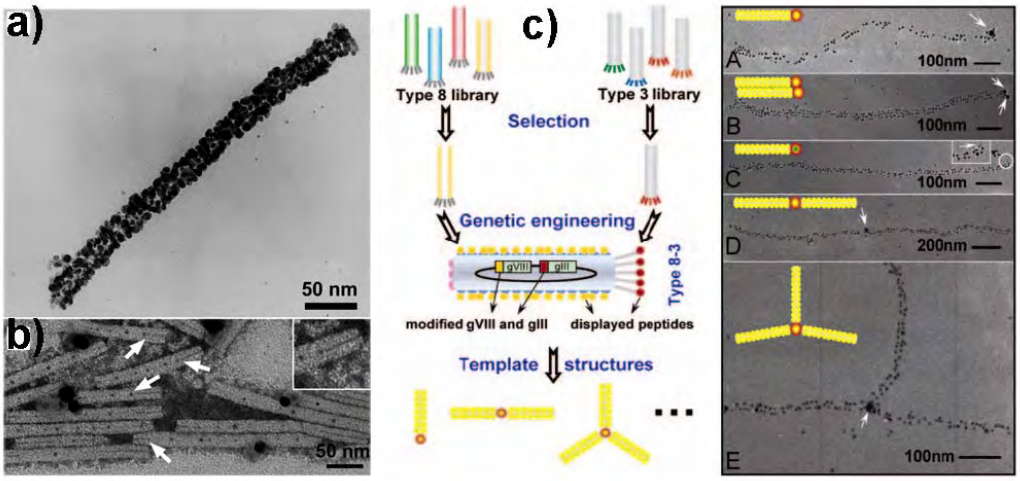

Fig I.21: *(a) Selective deposition of metal on the outside surface or inner channel of tobacco mosaic virus templates, TEM image of $AuCl4^-$ ions reduced at low pH where they have associated primarily with the positively charged outer coat, (b) TEM image of Ag^+ ions photo reduced at high pH where they have migrated into the internal cavity. (c)Scheme for engineering the type 8-3 phage and right, TEM images of various nano architectures templated by clone.*

Some of the early examples are the mineralization of hollow spherical chlorotic cowpea mottle virus (CCMV) [151] and of tobacco mosaic virus (TMV).[152] CCMV is a spherical virus of about 26nm in diameter with a 20nm hollow cavity defined by coat proteins. TMV is a rod-shaped supramolecular viral protein assembly approximately 300 nm long and 18 nm wide with a hollow ~4 nm inner channel.[151] Kern and co-workers first generated a plasmonic

nanostructure using this template through simple reduction of $AgNO_3$ with formaldehyde, forming Ag NPs along its length.[153] Simultaneously, Mann and co-workers have shown the spatially selective deposition of Au and Pt nanoparticles or Ag nanoparticles on or inside TMV scaffolds by adjusting the protein surface charge with the solution pH (*Fig I.21*). [154] For example, at pH 3, Au (III)Cl_4^- precursor ions adsorbed primarily on the positively charged amines of the viral template surface and formed a dense coating of Au NPs after reduction with hydrazine. On the other hand, at alkaline or neutral pH, the surface charge was mitigated with neutral amines but deprotonated carboxylates. Consequently, Ag^+ ions spontaneously associated with the negatively charged inner channel, forming well-defined linear nanoparticle arrays after photo reduction. Belcher and co-workers have worked extensively with a filamentous bacteriophage virus known as M13 that can also be coupled to Au nanostructures. This group has developed and popularized the M13 bacteriophage display techniques to the design of phage-borne peptides able to specifically adsorb onto chosen inorganic materials, including Au and Ag (*Fig I.21*).[125,155,156] Owing to their aspect ratio, M13 phages can be driven into a liquid crystalline phase and therefore attached nanoparticles can be organized into 2D films in between phage layers.

In spite of the various examples presented above, one should point out that some limitations for the self-assembly processes are still encountered for both small synthetic molecules (oligonucleotides or polypeptides) and larger entities (DNA, proteins, antibodies, viruses). For example, in the case of DNA, nucleic acids lack the chemical wealth of peptides. All nucleic acids are built on polyanionic phosphate-ribose backbone with a limited side-motif diversity (4 types of base). Nevertheless, 3D assembly was demonstrated very recently by using DNA origami and could be a promising route to complex organization. Short peptides do not fold into stable 3D structures and the structure obtained from long peptides is difficult to predict and control, which is currently a strong limitation towards 3D space patterning. Antigen-antibody and very few other biomolecule interaction have been reported so far that show a strong recognition to their counter parts but construction beyond the one-to-one complex is not straightforward. The synthesis and self-assembly using natural or modified viruses lacks the control on interparticle distance since it proceeds through templating and their engineering requires the implementation of site-directed mutagenesis, which is a difficult and time consuming technique that cannot provide arbitrary structure based on protein stability considerations. Therefore, some opportunities seem to exist for a new strategy based on genetically engineered proteins derived from an artificial but optimized scaffold in order to

self-assembled nano plasmonics and metamaterials. This is the underlying proposal of Chapters 5 and 6 in this thesis

1.3.3. Modified protein engineering.

The proteins bear the potential for 3D-structured molecular recognition from their sophisticated yet robust and well-defined secondary and tertiary structures. These capacities are specific to proteins but have been little exploited in the field of nano-constructions with non-biological materials, in spite of the remarkably successful use of simple unfolded (poly) peptides in such hybrid conjugates.

Here, we propose to extend the methods of directed evolution of short peptides to fully folded proteins in order to produce new artificial proteins having interaction affinities with materials, surfaces or nano-objects which could constitute useful elements in multi-functional, multi-scale nano constructions. Moreover, these genetically engineered proteins show very important features like well-defined 3D structures with high thermal resistance. Their structure and their modularity appear particularly well suited to the recognition of surfaces and materials which will be exploited in Chapter 5. In addition these artificial protein pairs are good candidates for driving self-assembly processes as they allow for the search for high affinity protein pairs continue with an aim to reach streptavidin-biotin affinities ($Kd \sim 10^{-14}M$). We will examine this approach in Chapter 6.

References:

(1) Ozbay, E. *Science* **2006**, *311*, 189-193.

(2) Pacifici, D. *Nature Photonics* **2007**, *1*, 689-690.

(3) Haes, A. J.; Haynes, C. L.; McFarland, A. D.; Schatz, G. C.; Van Duyne, R. R.; Zou, S. L. *Mrs Bulletin* **2005**, *30*, 368-375.

(4) Haes, A. J.; Stuart, D. A.; Nie, S. M.; Van Duyne, R. P. *Journal of Fluorescence* **2004**, *14*, 355-367.

(5) Willets, K. A.; Van Duyne, R. P. In *Annual Review of Physical Chemistry*; Annual Reviews: Palo Alto, 2007; Vol. 58, p 267-297.

(6) Yonzon, C. R.; Jeoungf, E.; Zou, S. L.; Schatz, G. C.; Mrksich, M.; Van Duyne, R. P. *Journal of the American Chemical Society* **2004**, *126*, 12669-12676.

(7) Pitarke, J. M.; Silkin, V. M.; Chulkov, E. V.; Echenique, P. M. *Reports on Progress in Physics* **2007**, *70*, 1-87.

(8) Barnes, W. L.; Dereux, A.; Ebbesen, T. W. *Nature* **2003**, *424*, 824-830.

(9) Brockman, J. M.; Nelson, B. P.; Corn, R. M. *Annual Review of Physical Chemistry* **2000**, *51*, 41-63.

(10) Kelly, K. L.; Coronado, E.; Zhao, L. L.; Schatz, G. C. *Journal of Physical Chemistry B* **2003**, *107*, 668-677.

(11) Hamamoto, K.; Micheletto, R.; Oyama, M.; Umar, A. A.; Kawai, S.; Kawakami, Y. *Journal of Optics a-Pure and Applied Optics* **2006**, *8*, 268-271.

(12) Wiscombe, W. J. *Appl. Optics* **1980**, *19*, 1505-1509.

(13) Hao, E.; Schatz, G. C.; Hupp, J. T. *Journal of Fluorescence* **2004**, *14*, 331-341.

(14) Draine, B. T.; Flatau, P. J. *Journal of the Optical Society of America a-Optics Image Science and Vision* **1994**, *11*, 1491-1499.

(15) Anker, J. N.; Hall, W. P.; Lyandres, O.; Shah, N. C.; Zhao, J.; Van Duyne, R. P. *Nature Materials* **2008**, *7*, 442-453.

(16) Aslan, K.; Lakowicz, J. R.; Geddes, C. D. *Analytical Biochemistry* **2004**, *330*, 145-155.

(17) Kumar, S.; Harrison, N.; Richards-Kortum, R.; Sokolov, K. *Nano Letters* **2007**, *7*, 1338-1343.

(18) Homola, J.; Vaisocherova, H.; Dostalek, J.; Piliarik, M. *Methods* **2005**, *37*, 26-36.

(19) Mitchell, J. S.; Wu, Y. Q.; Cook, C. J.; Main, L. *Analytical Biochemistry* **2005**, *343*, 125-135.

(20) Yu, F.; Tian, S. J.; Yao, D. F.; Knoll, W. *Analytical Chemistry* **2004**, *76*, 3530-3535.

(21) Mitchell, J. S.; Wu, Y.; Cook, C. J.; Main, L. *Steroids* **2006**, *71*, 618-631.

(22) Piliarik, M.; Vaisocherova, H.; Homola, J. *Methods in molecular biology (Clifton, N.J.)* **2009**, *503*, 65-88.

(23) Wark, A. W.; Lee, H. J.; Qavi, A. J.; Corn, R. M. *Analytical Chemistry* **2007**, *79*, 6697-6701.

(24) Kabashin, A. V.; Patskovsky, S.; Grigorenko, A. N. *Optics Express* **2009**, *17*, 21191-21204.

(25) Lin, T.-J.; Lou, C.-T. *Journal of Supercritical Fluids* **2007**, *41*, 317-325.

(26) Taranekar, P.; Baba, A.; Park, J. Y.; Fulghum, T. M.; Advincula, R. *Advanced Functional Materials* **2006**, *16*, 2000-2007.

(27) Wright, J. D.; von Bultzingslowen, C.; Carter, T. J. N.; Colin, F.; Shepherd, P. D.; Oliver, J. V.; Holder, S. J.; Nolte, R. J. M. *Journal of Materials Chemistry* **2000**, *10*, 175-182.

(28) Tao, A.; Kim, F.; Hess, C.; Goldberger, J.; He, R. R.; Sun, Y. G.; Xia, Y. N.; Yang, P. D. *Nano Letters* **2003**, *3*, 1229-1233.

(29) Moskovits, M.; Suh, J. S. *Journal of Physical Chemistry* **1984**, *88*, 5526-5530.

(30) Brosseau, C. L.; Casadio, F.; Van Duyne, R. P. *Journal of Raman Spectroscopy* **2009**, *42*, 1305-1310.

(31) Cotton, T. M.; Kim, J. H.; Chumanov, G. D. *Journal of Raman Spectroscopy* **1991**, *22*, 729-742.

(32) Lu, L. H.; Randjelovic, I.; Capek, R.; Gaponik, N.; Yang, J. H.; Zhang, H. J.; Eychmuller, A. *Chemistry of Materials* **2005**, *17*, 5731-5736.

(33) Dabbousi, B. O.; RodriguezViejo, J.; Mikulec, F. V.; Heine, J. R.; Mattoussi, H.; Ober, R.; Jensen, K. F.; Bawendi, M. G. *Journal of Physical Chemistry B* **1997**, *101*, 9463-9475.

(34) Okamoto, K.; Niki, I.; Shvartser, A.; Narukawa, Y.; Mukai, T.; Scherer, A. *Nature Materials* **2004**, *3*, 601-605.

(35) Vuckovic, J.; Loncar, M.; Scherer, A. *Ieee Journal of Quantum Electronics* **2000**, *36*, 1131-1144.

(36) Pillai, S.; Catchpole, K. R.; Trupke, T.; Green, M. A. *Journal of Applied Physics* **2007**, *101*.

(37) Ditlbacher, H.; Hohenau, A.; Wagner, D.; Kreibig, U.; Rogers, M.; Hofer, F.; Aussenegg, F. R.; Krenn, J. R. *Physical Review Letters* **2005**, *95*.

(38) Daniel, M. C.; Astruc, D. *Chemical Reviews* **2004**, *104*, 293-346.

(39) Enustun, B. V.; Turkevich, J. *Discussions of the Faraday Society* **1951**, 55-75.

(40) Enustun, B. V.; Turkevich, J. *Journal of the american chemical society* **1963**, *85*, 3317.

(41) Frens , G. *Nature physical science* **1973**, *20*, 241.

(42) Chow, M. K.; Zukoski, C. F. *Journal of Colloid and Interface Science* **1994**, *165*, 97-109.

(43) Polte, J.; Ahner, T. T.; Delissen, F.; Sokolov, S.; Emmerling, F.; Thuenemann, A. F.; Kraehnert, R. *Journal of the American Chemical Society* **2010**, *132*, 1296-1301.

(44) Murphy, C. J.; Jana, N. R. *Advanced Materials* **2002**, *14*, 80-82.

(45) Jana, N. R.; Gearheart, L.; Murphy, C. J. *Journal of Physical Chemistry B* **2001**, *105*, 4065-4067.

(46) Nikoobakht, B.; El-Sayed, M. A. *Chemistry of Materials* **2003**, *15*, 1957-1962.

(47) Murphy, C. J.; San, T. K.; Gole, A. M.; Orendorff, C. J.; Gao, J. X.; Gou, L.; Hunyadi, S. E.; Li, T. *Journal of Physical Chemistry B* **2005**, *109*, 13857-13870.

(48) Wiley, B.; Sun, Y.; Xia, Y. *Accounts of Chemical Research* **2007**, *40*, 1067-1076.

(49) Zhang, J.; Langille, M. R.; Personick, M. L.; Zhang, K.; Li, S.; Mirkin, C. A. *Journal of the American Chemical Society* **2010**, *132*, 14012-14014.

(50) Huang, P.; Maillard, M.; Brus, L. E. *Abstracts of Papers of the American Chemical Society* **2004**, *227*, U489-U489.

(51) Lu, X.; Yavuz, M. S.; Tuan, H.-Y.; Korgel, B. A.; Xia, Y. *Journal of the American Chemical Society* **2008**, *130*, 8900.

(52) Jana, N. R.; Gearheart, L.; Murphy, C. J. *Chemical Communications* **2001**, 617-618.

(53) Millstone, J. E.; Hurst, S. J.; Metraux, G. S.; Cutler, J. I.; Mirkin, C. A. *Small* **2009**, *5*, 646-664.

(54) Ming, T.; Feng, W.; Tang, Q.; Wang, F.; Sun, L.; Wang, J.; Yan, C. *Journal of the American Chemical Society* **2009**, *131*, 16350.

(55) Romo-Herrera, J. M.; Alvarez-Puebla, R. A.; Liz-Marzan, L. M. *Nanoscale* **2011**, *3*, 1304-1315.

(56) Feng, H.; Yang, Y.; You, Y.; Li, G.; Guo, J.; Yu, T.; Shen, Z.; Wu, T.; Xing, B. *Chemical Communications* **2009**, 1984-1986.

(57) Park, K.; Vaia, R. A. *Advanced Materials* **2008**, *20*, 3882.

(58) Link, S. E.-S., M. A. *Journal of Physical Chemistry B* **1999**, *103*, 4212-4217.

(59) Mirkin, C. A. *Small* **2005**, *1*, 14-16.

(60) Wilcoxon, J. P.; Abrams, B. L. *Chemical Society Reviews* **2006**, *35*, 1162-1194.

(61) Jain, P., K. Dessertaion, Georgia Institute of Technology, 2008.

(62) Bohren, C. F. H., D. R. **1983.**

(63) Murray, W. A.; Barnes, W. L. *Advanced Materials* **2007**, *19*, 3771-3782.

(64) Eustis, S.; El-Sayed, M. A. *Chemical Society Reviews* **2006**, *35*, 209-217.

(65) Jin, R. C.; Cao, Y. W.; Mirkin, C. A.; Kelly, K. L.; Schatz, G. C.; Zheng, J. G. *Science* **2001**, *294*, 1901-1903.

(66) Metraux, G. S.; Mirkin, C. A. *Advanced Materials* **2005**, *17*, 412.

(67) Pileni, M. P. *Nature Materials* **2003**, *2*, 145-150.

(68) *Hand book of nanophysics: Nanoparticles and Quantum dots*; Sattler, K., D. , Ed., 2010; Vol. CRC Press Taylor & Francis Group.

(69) Shaw, C. P.; Fernig, D. G.; Levy, R. *Journal of Materials Chemistry* **2011**, *21*, 12181-12187.

(70) Jain, P. K.; Huang, W.; El-Sayed, M. A. *Nano Letters* **2007**, *7*, 2080-2088.

(71) Storhoff, J. J.; Elghanian, R.; Mucic, R. C.; Mirkin, C. A.; Letsinger, R. L. *Journal of the American Chemical Society* **1998**, *120*, 1959-1964.

(72) Li, M. J., Sara Guo, Hongtao Dujardin, Erik Mann, Stephen *Advanced Functional Materials* **2011**, *21*, 851-859.

(73) Sethi, M.; Joung, G.; Knecht, M. R. *Langmuir* **2009**, *25*, 1572-1581.

(74) Dujardin, E.; Hsin, L. B.; Wang, C. R. C.; Mann, S. *Chemical Communications* **2001**, 1264-1265.

(75) Mucic, R. C.; Storhoff, J. J.; Mirkin, C. A.; Letsinger, R. L. *Journal of the American Chemical Society* **1998**, *120*, 12674-12675.

(76) Shibu Joseph, S. T.; Ipe, B. I.; Pramod, P.; Thomas, K. G. *The journal of physical chemistry. B* **2006**, *110*, 150-7.

(77) Thomas, K. G.; Barazzouk, S.; Ipe, B. I.; Joseph, S. T. S.; Kamat, P. V. *Journal of Physical Chemistry B* **2004**, *108*, 13066-13068.

(78) Geddes, C. D. *John Wiley & Sons,Inc.* **2010**.

(79) *Metal-Enhanced Fluorescence*; Geddes , C. D., Ed.; John Wiley & Sons: New Jersy, 2010.

(80) Aslan, K.; Malyn, S. N.; Geddes, C. D. *Journal of Fluorescence* **2007**, *17*, 7-13.

(81) Aslan, K.; Wu, M.; Lakowicz, J. R.; Geddes, C. D. *Journal of Fluorescence* **2007**, *17*, 127-131.

(82) Thomas, K. G.; Kamat, P. V. *Accounts of Chemical Research* **2003**, *36*, 888-898.

(83) Geddes, C. D.; Cao, H.; Gryczynski, I.; Gryczynski, Z.; Fang, J. Y.; Lakowicz, J. R. *Journal of Physical Chemistry A* **2003**, *107*, 3443-3449.

(84) Aslan, K.; Holley, P.; Geddes, C. D. *Journal of Immunological Methods* **2006**, *312*, 137-147.

(85) Thomas, K. G.; Kamat, P. V. *Journal of the American Chemical Society* **2000**, *122*, 2655-2656.

(86) Kometani, N.; Tsubonishi, M.; Fujita, T.; Asami, K.; Yonezawa, Y. *Langmuir* **2001**, *17*, 578-580.

(87) Wiederrecht, G. P.; Wurtz, G. A.; Hranisavljevic, J. *Nano Letters* **2004**, *4*, 2121-2125.

(88) Wurtz, G. A.; Evans, P. R.; Hendren, W.; Atkinson, R.; Dickson, W.; Pollard, R. J.; Zayats, A. V.; Harrison, W.; Bower, C. *Nano Letters* **2007**, *7*, 1297-1303.

(89) Fofang, N. T.; Park, T.-H.; Neumann, O.; Mirin, N. A.; Nordlander, P.; Halas, N. J. *Nano Letters* **2008**, *8*, 3481-3487.

(90) Bardhan, R.; Grady, N. K.; Halas, N. J. *Small* **2008**, *4*, 1716-1722.

(91) Bardhan, R.; Grady, N. K.; Cole, J. R.; Joshi, A.; Halas, N. J. *Acs Nano* **2009**, *3*, 744-752.

(92) Salomon, A.; Genet, C.; Ebbesen, T. W. *Angewandte Chemie-International Edition* **2009**, *48*, 8748-8751.

(93) *Biomineralization* Mann, S., Ed.; Oxford University Press, USA, 2002.

(94) Cushing, B. L.; Kolesnichenko, V. L.; O'Connor, C. J. *Chemical Reviews* **2004**, *104*, 3893-3946.

(95) Murphy, C. J.; Gole, A. M.; Hunyadi, S. E.; Orendorff, C. J. *Inorganic Chemistry* **2006**, *45*, 7544-7554.

(96) Abdelmoti, L. G.; Zamborini, F. P. *Langmuir* **2010**, *26*, 13511-13521.

(97) Dong, S.-A.; Zhou, S.-P. *Materials Science and Engineering B-Solid State Materials for Advanced Technology* **2007**, *140*, 153-159.

(98) Sander, M. S.; Tan, L. S. *Advanced Functional Materials* **2003**, *13*, 393-397.

(99) Evans, P.; Hendren, W. R.; Atkinson, R.; Wurtz, G. A.; Dickson, W.; Zayats, A. V.; Pollard, R. J. *Nanotechnology* **2006**, *17*, 5746-5753.

(100) Huo, Z.; Tsung, C.-k.; Huang, W.; Zhang, X.; Yang, P. *Nano Letters* **2008**, *8*, 2041-2044.

(101) Johnson, C. J.; Dujardin, E.; Davis, S. A.; Murphy, C. J.; Mann, S. *Journal of Materials Chemistry* **2002**, *12*, 1765-1770.

(102) Ha, T. H.; Koo, H.-J.; Chung, B. H. *Journal of Physical Chemistry C* **2007**, *111*, 1123-1130.

(103) Lu, X.; Rycenga, M.; Skrabalak, S. E.; Wiley, B.; Xia, Y. In *Annual Review of Physical Chemistry* 2009; Vol. 60, p 167-192.

(104) Fievet, F.; Lagier, J. P.; Blin, B.; Beaudoin, B.; Figlarz, M. *Solid State Ionics* **1989**, *32-3*, 198-205.

(105) Viau, G.; FievetVincent, F.; Fievet, F. *Solid State Ionics* **1996**, *84*, 259-270.

(106) Sun, Y. G.; Yin, Y. D.; Mayers, B. T.; Herricks, T.; Xia, Y. N. *Chemistry of Materials* **2002**, *14*, 4736-4745.

(107) Wiley, B.; Sun, Y. G.; Mayers, B.; Xia, Y. N. *Chemistry-a European Journal* **2005**, *11*, 454-463.

(108) Yu, S.-H. In *Biomineralization Ii: Mineralization Using Synthetic Polymers and Templates*; Naka, K., Ed. 2007; Vol. 271, p 79-118.

(109) Busch, S.; Schwarz, U.; Kniep, R. *Chemistry of Materials* **2001**, *13*, 3260-3271.

(110) Shenton, W.; Pum, D.; Sleytr, U. B.; Mann, S. *Nature* **1997**, *389*, 585-587.

(111) Sarikaya, M.; Tamerler, C.; Jen, A. K. Y.; Schulten, K.; Baneyx, F. *Nature Materials* **2003**, *2*, 577-585.

(112) Xie, J.; Zheng, Y.; Ying, J. Y. *Journal of the American Chemical Society* **2009**, *131*, 888.

(113) Nikitin, M. P.; Zdobnova, T. A.; Lukash, S. V.; Stremovskiy, O. A.; Deyev, S. M. *Proceedings of the National Academy of Sciences of the United States of America* **2010**, *107*, 5827-5832.

(114) Brayner, R.; Coradin, T.; Fievet-Vincent, F.; Livage, J.; Fievet, F. *New Journal of Chemistry* **2005**, *29*, 681-685.

(115) He, J. H.; Kunitake, T.; Nakao, A. *Chemistry of Materials* **2003**, *15*, 4401-4406.

(116) Sarma, T. K.; Chattopadhyay, A. *Langmuir* **2004**, *20*, 3520-3524.

(117) Warner, M. G.; Hutchison, J. E. *Nature Materials* **2003**, *2*, 272-277.

(118) Sarikaya, M.; Tamerler, C.; Schwartz, D. T.; Baneyx, F. O. *Annual Review of Materials Research* **2004**, *34*, 373-408.

(119) Nabok, A. V.; Richardson, T.; Davis, F.; Stirling, C. J. M. *Langmuir* **1997**, *13*, 3198-3201.

(120) Patolsky, F.; Weizmann, Y.; Lioubashevski, O.; Willner, I. *Angewandte Chemie-International Edition* **2002**, *41*, 2323-2327.

(121) McConney, M. E.; Anderson, K. D.; Brott, L. L.; Naik, R. R.; Tsukruk, V. V. *Advanced Functional Materials* **2009**, *19*, 2527-2544.

(122) Slocik, J. M.; Naik, R. R. *Chemical Society Reviews* **2010**, *39*, 3454-3463.

(123) Ogasawara, W.; Shenton, W.; Davis, S. A.; Mann, S. *Chemistry of Materials* **2000**, *12*, 2835.

(124) Tamerler, C.; Sarikaya, M. *Acta Biomaterialia* **2007**, *3*, 289-299.

(125) Lee, S. W.; Mao, C. B.; Flynn, C. E.; Belcher, A. M. *Science* **2002**, *296*, 892-895.

(126) Brown, S. *Nature Biotechnology* **1997**, *15*, 269-272.

(127) Brown, S.; Sarikaya, M.; Johnson, E. *Journal of Molecular Biology* **2000**, *299*, 725-735.

(128) Li, Y.; Whyburn, G. P.; Huang, Y. *Journal of the American Chemical Society* **2009**, *131*, 15998.

(129) Chiu, C.-Y.; Li, Y.; Ruan, L.; Ye, X.; Murray, C. B.; Huang, Y. *Nature Chemistry* **2011**, *3*, 393-399.

(130) Chen, H.-L.; Cheng, H.-C.; Ko, T.-S.; Chuang, S.-Y.; Chu, T.-C. *Japanese Journal of Applied Physics Part 1-Regular Papers Brief Communications & Review Papers* **2006**, *45*, 6984-6986.

(131) Ozaki, T.; Sugano, K.; Tsuchiya, T.; Tabata, O.; Ieee In *Mems 2008: 21st Ieee International Conference on Micro Electro Mechanical Systems, Technical Digest* 2008, p 1048-1051.

(132) Watanabe, S.; Shibata, H.; Sakamoto, F.; Azumi, R.; Sakai, H.; Abe, M.; Matsumoto, M. *Journal of Materials Chemistry* **2009**, *19*, 6796-6803.

(133) Lin, S.; Li, M.; Dujardin, E.; Girard, C.; Mann, S. *Advanced Materials* **2005**, *17*, 2553.

(134) Bonell, F.; Sanchot, A.; Dujardin, E.; Pechou, R.; Girard, C.; Li, M.; Mann, S. *Journal of Chemical Physics* **2009**, *130*.

(135) Mirkin, C. A.; Letsinger, R. L.; Mucic, R. C.; Storhoff, J. J. *Nature* **1996**, *382*, 607-609.

(136) Alivisatos, A. P.; Johnsson, K. P.; Peng, X. G.; Wilson, T. E.; Loweth, C. J.; Bruchez, M. P.; Schultz, P. G. *Nature* **1996**, *382*, 609-611.

(137) Cheng, W.; Campolongo, M. J.; Cha, J. J.; Tan, S. J.; Umbach, C. C.; Muller, D. A.; Luo, D. *Nature Materials* **2009**, *8*, 519-525.

(138) Maye, M. M.; Nykypanchuk, D.; Cuisinier, M.; van der Lelie, D.; Gang, O. *Nature Materials* **2009**, *8*, 388-391.

(139) Sadasivan, S.; Dujardin, E.; Li, M.; Johnson, C. J.; Mann, S. *Small* **2005**, *1*, 103-106.

(140) Sebba, D. S.; Mock, J. J.; Smith, D. R.; LaBean, T. H.; Lazarides, A. A. *Nano Letters* **2008**, *8*, 1803-1808.

(141) Nykypanchuk, D.; Maye, M. M.; van der Lelie, D.; Gang, O. *Nature* **2008**, *451*, 549-552.

(142) Niemeyer, C. M.; Burger, W.; Peplies, J. *Angewandte Chemie-International Edition* **1998**, *37*, 2265-2268.

(143) Pal, S.; Deng, Z.; Wang, H.; Zou, S.; Liu, Y.; Yan, H. *Journal of the American Chemical Society*, *133*, 17606-17609.

(144) Chen, C.-L.; Zhang, P.; Rosi, N. L. *Journal of the American Chemical Society* **2008**, *130*, 13555.

(145) Kaur, P.; Maeda, Y.; Mutter, A. C.; Matsunaga, T.; Xu, Y.; Matsui, H. *Angewandte Chemie-International Edition* **2010**, *49*, 8375-8378.

(146) McMillan, R. A.; Paavola, C. D.; Howard, J.; Chan, S. L.; Zaluzec, N. J.; Trent, J. D. *Nature Materials* **2002**, *1*, 247-252.

(147) Hall, S. R.; Shenton, W.; Engelhardt, H.; Mann, S. *Chemphyschem* **2001**, *2*, 184-186.

(148) Shenton, W.; Davis, S. A.; Mann, S. *Advanced Materials* **1999**, *11*, 449.

(149) Connolly, S.; Fitzmaurice, D. *Advanced Materials* **1999**, *11*, 1202-1205.

(150) Wang, L.; Zhu, Y.; Xu, L.; Chen, W.; Kuang, H.; Liu, L.; Agarwal, A.; Xu, C.; Kotov, N. A. *Angewandte Chemie-International Edition* **2010**, *49*, 5472-5475.

(151) Douglas, T.; Young, M. *Advanced Materials* **1999**, *11*, 679-+.

(152) Fowler, C. E.; Shenton, W.; Stubbs, G.; Mann, S. *Advanced Materials* **2001**, *13*, 1266-1269.

(153) Knez, M.; Sumser, M.; Bittner, A. M.; Wege, C.; Jeske, H.; Kooi, S.; Burghard, M.; Kern, K. *Journal of Electroanalytical Chemistry* **2002**, *522*, 70-74.

(154) Dujardin, E.; Peet, C.; Stubbs, G.; Culver, J. N.; Mann, S. *Nano Letters* **2003**, *3*, 413-417.

(155) Whaley, S. R.; English, D. S.; Hu, E. L.; Barbara, P. F.; Belcher, A. M. *Nature* **2000**, *405*, 665-668.

(156) Nam, K. T.; Kim, D. W.; Yoo, P. J.; Chiang, C. Y.; Meethong, N.; Hammond, P. T.; Chiang, Y. M.; Belcher, A. M. *Science* **2006**, *312*, 885-888.

CHAPTER 2

MATERIALS AND METHODS

In this chapter we briefly explain general experimental and instrumental techniques which we used during the course of this thesis.

2.1. Reagents.

2.1.1. Starting materials

Sodium salt of tetrakis(4-sulfonatophenyl) porphyrin (H_2TPPS^4, F.W. 1239.1) , silver nitrate ($AgNO_3$,F.W.169.88), sodium citrate ($C_6H_5Na_3O_7$,F.W. 294.1), gold(III) chloride trihydrate ($HAuCl_4.3H_2O$, F.W.393.83), 3-mercaptopropyltrimethoxysilane ($HS(CH_2)_3Si(OCH_3)_3$, F.W. 196.34), sodium phosphate monobasic (NaH_2PO_4,F.W.119.98), sodium phosphate dibasic (Na_2HPO_4 ,F.W141.96), pottasium chloride (KCl, F.W.74.55), boric acid (H_3BO_3, F.W.61.83), sodium chloride (NaCl, F.W. 58.44), sodium hydroxide (NaOH, F.W.39.9) and aminopropyltriethoxysilane (APTES) (F.W.221.37) were purchased from Aldrich Chemicals and CASTER and all chemicals were used as received.

2.1.2. Biomolecules.

α-Rep proteins are synthesised by A.Urvaoas, M.Lepiniec and P.Minnard in IBBMC (Orsay, CNRS ,UPR8619, Paris) and finally stored in 50mM sodium phosphate buffer pH 7.0 with 100mM NaCl.A purification is described later in this chapter.

Negatively charged peptide, Cys-Cys-Cys-21-amino-4,7,10,13,16,19-hexaoxaheneicosanoyl-Asp (C_3E_6Asp) (> 90% purity, theoretical M.W 778.0) and neautral petide Cys-Cys-Cys-21-amino-4,7,10,13,16,19-hexaoxaheneicosanoyl-NH_2($C_3E_6NH_2$) (>95% purity, theoretical M.W 661.9) are purchased from PolyPeptide Group and used as received. To cleave disulphide bond in artificial proteins, DL-dithiothreitol ($C_4H_{10}O_2S_2$, F.W.154.25) has been used which was purchased from Sigma aldrich. Brilliant blue R ($C_{45}H_{44}N_3NaO_7S_2$) dye for coloring gel has been used as received from Sigma.

2.1.3. Water purification.

All water used for experiments was ultrapure de-ionized water using ELGA PURELAB classic M2 fitted with deionization cartridge, UV lamp (185/254nm) and ultra filtration membrane which gave final water resistivity 18.2 MΩ-cm.

2.1.4. Synthesis of citrate-stabilized Au and Ag nanoparticles.

Turkevich method.

Turkevich method[1, 2] is a standard protocol to prepare water suspension of Au nanoparticles by reduction of a gold or silver salt with sodium citrate. Introduced by Turkevich et al. [1] it was later refined by Frens,[3] this protocol produces almost exclusively spherical or decahedral particles over a tunable range of sizes. In this procedure, sodium citrate acts as a reducing as well as stabilizing agent, which forms a uniform layer on nanoparticle surface with negative charge on the surface. The kinetics of the Turkevich process and citrate stabilization mechanism has been addressed by Chow and Zukoski. [4]

Briefly, the synthesis is based on the rapid injection of citrate solution to a boiling solution of $HAuCl_4$ or $AgNO_3$ under continuous stirring.[5] All seeds are formed at the same time and grow until the entire metal salt is consumed, resulting particles are mostly monodisperse. The diameter of these objects is determined by the molar ratio between citrate and the metal salt. The large amount of citrate introduced, small was the diameter of the final particles. In addition, the amount of metal salt determines the final concentration particles in the solution.

2.1.5. Experimental protocol for the synthesis of Au nanoparticles.

All glass wares was washed thoroughly with aqua regia (HCl: HNO_3 = 3:1) before the experiment, rinsed with deionized water and dried at 120°C. Typically, 100mL of 1mM tetrachloroaurate (III) solution was brought to a rolling boil with stirring. Once boiling, the solution was allowed to reflux for 10 minutes before a 10 mL solution of tri-sodium citrate (38.8mM) was rapidly added while still stirring the solution vigorously. The mixed solution was further refluxed for another 15 min. The pale Au (III) yellow solution initially turned colorless Au (I) solution before becoming an intense burgundy color indicating the formation of colloidal gold. The suspension was naturally cooled to room temperature under stirring. The gold nanoparticle suspension was then stored in a clean glass bottle in the dark.

2.1.6. Experimental protocol for the synthesis of Ag nanoparticles.

In typical experiment, 100 ml of 1mM $AgNO_3$ was heated to boiling. To this solution, 10 ml of 6 μM trisodium citrate was added drop by drop vigorously. The solution was heated until the color change from colorless to pale yellow was visible. Then it was left with stirring. During the process, the solution was stirred vigorously. The solution was heated until color change is evident (pale yellow). Then it was left to cool naturally to room temperature while maintaining the stirring.

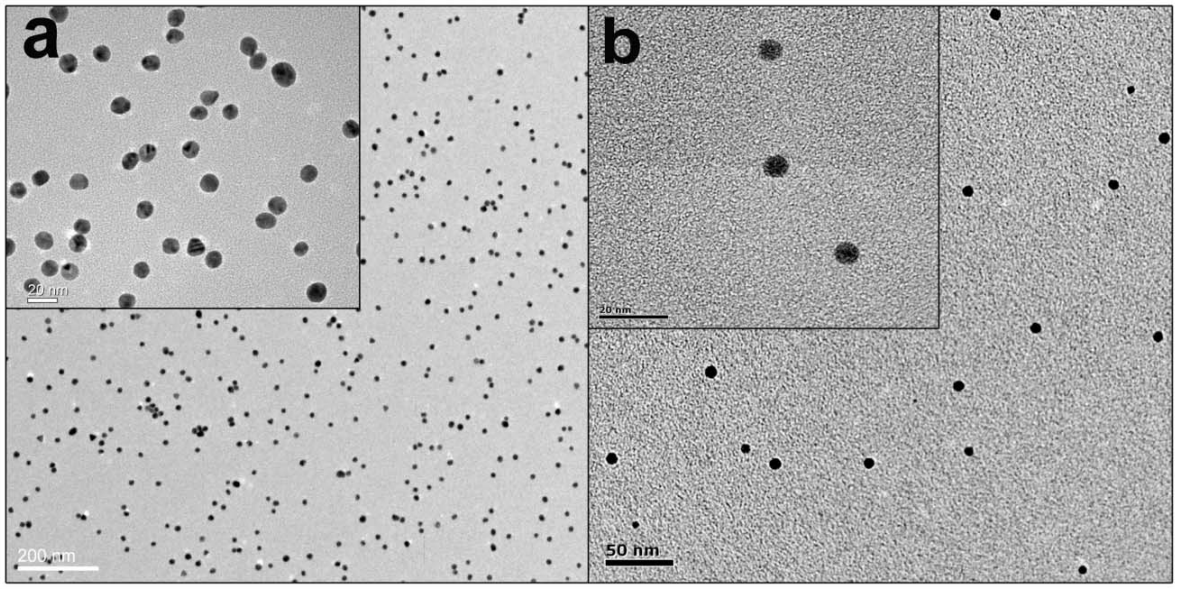

Fig II.1: *Transmission electron micrograph images of (a) Au and (b) Ag nanoparticles. Inset show the close view of nanoparticles. Monodispersed particles of Au (13 ± 2 nm) and Ag (8 ± 2 nm) nanoparticles are obtained.*

2.1.7. Calculating concentration of nanoparticles.

It was very important to calculate the concentration and surface area of metal nanoparticles to quantify number of proteins to be attached to metal nanoparticle. Here we illustrate the procedure by taking gold as an example. For this calculation, the mass of $HAuCl_4.3H_2O$ used in the reaction, final volume of the gold nanoparticle suspension and the mean particle diameter measured from TEM micrographs were taken into consideration. The diameter of ~200 nanoparticles was measured by "Image J" software on TEM micrograph and average distance was taken into account. Three main approximations were made for the calculation. First, we assumed that the density of the gold nanoparticle was equal to the density of bulk gold (19300 kgm^{-3}), secondly the nanoparticles were considered as perfect spheres and finally we assumed that all the gold salt Au (III) was completely reduced to Au (0).

$$m_{Au} = \frac{m_{HAuCl4.3H2O}}{M_{HAuCl4.3H2O}} \; X \; M_{Au} \quad (I)$$

Where $\mathbf{m_{Au}}$ = Total mass of Au

$\mathbf{m_{HAuCl43H2O}}$ = mass of $HAuCl_43H_2O$

$\mathbf{M_{HAuCl4.3H2O}}$ = Molecular weight of $HAuCl_43H_2O$

$\mathbf{M_{Au}}$= Atomic mass of Au

Next, we consider that the density of gold nanoparticles particles $\rho_{Au\text{-}NP}$ is equivalent to that of the bulk of solid gold $\rho_{Au\text{-}Bulk.}$

$\boldsymbol{\rho_{Au\text{-}NP} = \rho_{Au\text{-}Bulk}}$

$$m_{Au} = \rho_{Au.} V_{NP} \cdot N_{NP} \qquad \textbf{(II)}$$

Where m_{Au} is $_{mass}$ of one particle,

Volume of one particle $\mathbf{V_{NP}} = \frac{4}{3}\,\boldsymbol{\pi r^3}$ where 'r' is the radius of gold nanoparticle.

Combining equation (I) and (II)

$$\mathbf{N_{NP}} = \frac{m_{HAuCl4}}{M_{HAuCl4}} \cdot \frac{M_{Au}}{\rho_{Au}.V_{NP}}$$

Where N_{NP} is the number of particles in the total volume of the solution.

Hence,

$$\mathbf{C} = \frac{N_{Np}}{N_a V_{Tot}}$$

Where $N_{A=}$ Avagadro number.

Hence the concentration of the assynthesised Au nanoparticles and Ag nanoparticles is measured to be

Au C = 1.33 x 10^{16} particles/L or (2.208x10^{-8}) M

Ag C = 3.88 x 10^{17} particles/L. or (64.419 x 10^{-9}) M.

2.1.8. Determination of extinction coefficient.

The UV / Visible spectrophotometer measures the attenuation of the intensity of a light beam of wavelength λ, which passes through a solution of concentration C, over a length ℓ. From the Beer-Lambert law which states that there is a logarithmic dependence between the transmission, T, of light absorption coefficient of the substance, ε, and the distance the light travels through the material (i.e., the path length), $\boldsymbol{\ell}$.

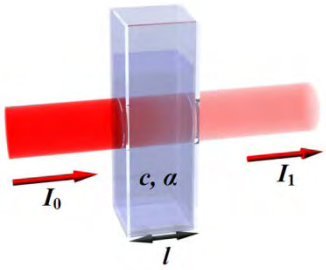

$$A = log\frac{I_0}{I_l} = \varepsilon lc \qquad \textbf{(III)}$$

$$\mathbf{A} = \frac{\mathbf{1}}{\boldsymbol{T}} \qquad \textbf{(IV)}$$

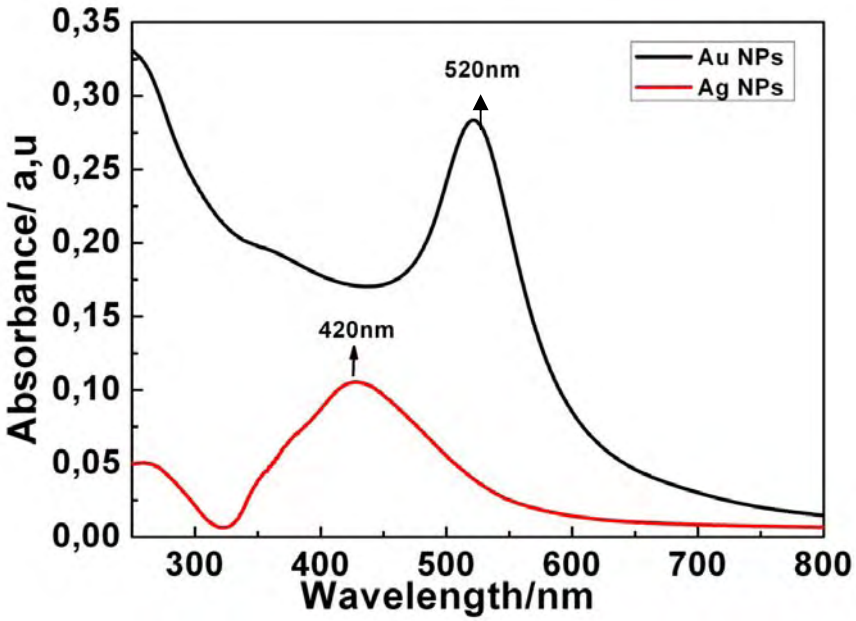

Fig II.2: *UV-Vis absorption spectra of as synthesized Au and Ag nanoparticles.*

For gold and silver nanoparticles with a diameter between 10 nm to 20 nm, the absorbance decreases continuously in the visible with the exception of a peak, which is the signature of the plasmon resonance. The absorption frequency for asynthesised gold and silver nanoparticle is 520nm and 420nm respectively. Hence from the equation (IV) we can determine the extinction coefficient for gold and silver nanoparticle as 7.80×10^{-9} cm^{-1} $mol^{-1}L$ and 6.13×10^{-8} cm^{-1} $mol^{-1}L$ at their respective plasmon absorption.

2.2 Colloidal characterization techniques.

2.2.1. pH measurements.

pH measurements were carried out using a Consort C533 multi-parameter analyzer calibrated in the range of pH 4-10 using standard buffer solutions.

2.2.2. UV/Vis spectrometry.

UV/Vis spectroscopic measurements were carried out using a Cary-5000 UV-Vis NIR spectrophotometer instrument operated by Carry UVWinLab (Version 1.1) software. Typical spectra were recorded in the range 200-800nm and at 600nm/min scan rate. A matched pair of Hellma QS 284 precision cells made of QUARTZ SUPRASIL (path length 1mm working volume 250µL) was used to hold both the sample and reference solutions.

2.2.3. Fluorescence measurements.

Luminescence spectra as well as excitation spectra were recorded on Hitachi F-4500 spectrophotometer operated by FL_mnu software. The sample solutions were placed in quartz cells of path length 1cm and emission spectra was measured in the range of 300 to 600nm.

2.2.4. Dynamic light scattering and Zeta potential.

The effective hydrodynamic radius of nanoparticles was measured in ZETASIZER Nanoseries instrument operated by Zetasizer software version 6.12. The temperature was maintained 25°C with an equilibration time of 120sec.Each experiment was recorded 6 times and averaged. The measurement was monitored along with Auto-Correlogramme as well as Cumulant fit. Disposable cuvettes DTS0012 of 10mm size have been used for measurements. For zeta potential measurements we maintained the same condition except that we used DTS1060C clear disposable zeta cells. The setup was used in University of Rennes (collaboration with Valérie Marchi-Artzner) as well as at CEMES Toulouse.

2.3. Protein characterization technique.

2.3.1. Protein expression and purification.

The gene coding for each α-Rep protein was sub cloned into the vector (pQE-31, Qiagen). The corresponding plasmid was transformed into the expression E. coli strain (Qiagen). Cells were grown at 37 °C in a culture medium. Protein expression was induced by addition of Isopropyl β-D-1-thiogalactopyranoside (IPTG) to 1 mM and the cells were further incubated for 4 h. The cells were harvested, suspended in Tris Buffered Saline (TBS), submitted to three freezing/thawing cycles and treated with lysozyme and benzonase for 30 min. After centrifugation, the His-tagged proteins were purified from the supernatant using nickel-affinity chromatography (Ni-NTA agarose, Qiagen) followed by Size exclusion chromatography. For each protein, the purity of the final sample was checked by SDS-PAGE with an overloaded gel showing one well-resolved band with no visible contamination.

2.3.2. Circular Dichroism.

Circular dichroism (CD) refers to the differential absorption of left and right circularly polarized light. Circular Dichroism is exhibited by biological molecules, because of their dextrorotary and levorotary amino acids components. The far-UV (ultraviolet) CD spectrum of proteins can reveal important characteristics of their secondary structure[6]. CD spectra can be readily used to estimate the fraction of a product that is in the alpha-helix conformation, the beta-sheet conformation, the beta-turn conformation, or some other (e.g. random coil) conformation[6] .

CD spectra were recorded from 185 nm to 260 nm with a data pitch of 0.2 nm, a scan speed of 50 nm/min, a response time of 0.5 s and a bandwidth of 1 nm using quartz cells with a 1 mm path length, on a Jasco dichrograph equipped with a thermostatically controlled cell-holder and connected to a computer for data acquisition. Each spectrum was recorded five times and averaged. Measurements were done at 25 °C and at 95 °C. The CD signal was corrected by buffer subtraction and converted to mean residue ellipticity. Data were acquired from 10 μM samples in 50 mM sodium phosphate buffer, pH 7.0, in quartz cells with a 1 mm path length.

2.3.3. Differential Scanning Calorimetry (DSC).

Thermal stability of proteins and protein reduced nanostructures were studied by differential scanning calorimetry (DSC) with a MicroCal VP-DSC instrument with αRep proteins (0.23 – 1.25 mg mL-1) in 50 mM sodium phosphate buffer, pH 7. Each measurement was preceded

by a baseline scan with the standard buffer. Scans were done at 1K min^{-1} between 20 °C and 110 ^{0}C. The heat capacity of the buffer was subtracted from that of the protein sample before analysis. These corrected data were analyzed using a cubic spline as a baseline in the transition. Thermodynamic parameters calorimetric enthalpy, ΔHcal, and the van't Hoff enthalpy ΔHvH were determined by fitting the following equation to the data,

$$\Delta C_p(\mathrm{T}) = \frac{\mathrm{K_d(T)}\Delta H_{cal}\Delta H_{VH}}{[1+\mathrm{K_d(T)}]^2\,\mathrm{RT^2}} \quad \textbf{(V)}$$

where K_d is the equilibrium constant for a two-state process, ΔH_{vH} is the enthalpy calculated on the basis of a two-state process and ΔH_{cal} is the measured enthalpy.

2.3.4. Analytical size exclusion chromatography (SEC).

Analytical SEC was done with an ÄKTA Purifier (GE Healthcare) system using a Superdex™ 75 10/300 GL column (flow-rate 0.8 mL min^{-1}) equilibrated in 50mM sodium phosphate buffer pH 7.0. For all the proteins analyzed, 100 μL of 3 mg mL^{-1} protein were injected onto the column. A solution containing standard globular proteins was injected as a control. As molar extinction coefficients were different for each protein, data were normalized relative to the maximum absorbance at 280 nm of each elution profile.

2.3.5. Acrylamide gel electrophoresis (AcGEP).

Acrylamide gel was performed with the Mini-PROTEAN Tetra cell and external PowerPac™ basic power supply along with casting frame, gel Cassette assembly, Casting stand, Buffer dam, electrode assembly, mini tank and lid.

For the preparation of acrylamide gel, resolving gel buffer 1.5M Tris-HCl pH 8.8, 0.5M Tris-HCl buffer pH 6.8,10X Tris/Glycine/SDS buffer, Precision plus protein standard N,N,N',N'-tera-methyl-ethylenediamine (TEMED),40% acrylamide/bis solution, 37.5:1(2.6%C), ammonium per sulfate were purchased from BIO-RAD. Glycerin($C_3H_8O_3$), 2-mercapto ethanol ($C_2H_6O_3$) and staining solution Brilliant Blue R ($C_{45}H_{44}N_3NaO_7S_2$) were purchased from Sigma.

Preparation of 4% acrylamide Gel: Briefly, two glass plates were washed with distilled water, and fixed to the gel casting stand. The gel was prepared in two steps. First the inferior portion of gel was prepared by mixing 1.5M Tris-HCl pH 8.8, 40% Acrylamide/Bis solution, with water and then ammonium per sulfate with Tetramethylethylenediamine (TEMED). The

solution was shaken for 5-10 seconds and then poured into the glass plates slowly up to 3/4th volume of glass plates and allowed to dry for 20 min. The gel upper portion was prepared by same procedure using 0.5M Tris-HCl pH 6.8 buffer instead of using 1.5M Tris-HCl pH 8.8. The rest of the volume between glass plates was filled by this solution and the combs were inserted slowly and left for dry for 20 min. The Gel was stored at 4^{o}C and used for running protein samples by removing the comb.

Protein samples were mixed with β-mercaptoethanol, and Laemli sample buffer heated at 40^{0}C for 5 min, 20% glycerol was added to the sample and loaded to the gel placed in the buffer dam. Voltage of 50V/cm was applied to the gel for 30 min along with careful observation of the sample. The gel was then carefully removed from the glass and then stained with Brilliant blue for 45min and destained with methanol and acetic acid mixture.

2.3.6. Agarose gel electrophoresis (AGEP).

To perform agarose gel electrophoresis of Au nanoparticles conjugated with peptide and protein, Enduro Gel XL with standard casting set, gel tank with safety lid and power supply, 120V (E0160) w/ FREE UPS was purchased from Labnet.International Inc. For the preparation of the gel agarose, boric acid (H_3BO_3) was purchased from Sigma-Aldrich.

Preparation of 4% acrylamide Gel: 10x Tris borate buffer pH 8.3 was prepared by mixing 0.2M KCl, 0.2M H_3BO_3, 0.2M NaOH, and 1mM NaCl in 500mL deionized water. About 500mg of agarose was weighed and 100mL of 1x tris borate buffer was added. The solution was heated at 85 ^{0}C with stirring until all agarose dissolved in a buffer then the solution was slowly cooled down until 50 ^{0}C and poured into gel tray and the comb was inserted the above solution was allowed to cool down for 30 min. It can be used by placing the gel in a buffer dam.

For running samples, they were first mixed with 30% glycerol solution and slowly injected in a well. A current of 100mA is applied across the gel for 30min.

2.4. Microscopy.

2.4.1. Transmission electron Microscopy (TEM).

TEM measurements of the samples were carried out on 300mesh carbon coated copper grids using PHILIPS CM20FEG operating at 200kV accelerating voltage in bright field mode. The filament source is a Schottky field emission gun (FEG). The microscope is equipped with a SC100 Orius CCD camera (11 megapixels) mounted on 35mm port, which offers a large field

of view. The microscope comprises a Energy-Dispersive X-ray spectroscopy (EDX) add-on from Quantax System BRUKER with a silicon drift detector (SDD). Microscope images were recorded on Gatan Digital Micrograph software.

2.4.2. TEM staining protocol.

Most of the biological components were composed of low atomic number elements and thus exhibit poor diffraction efficiency, which makes it difficult to analyze them in TEM. Staining biological samples with high atomic number stains enhances the contrast of the sample. There are mainly two types of staining namely, positive and negative staining. Negative staining is an easy, rapid, qualitative method for examining the structure of isolated organelles, individual macromolecules and viruses. Ideally, the negative stain should not react with the specimen in a 'positive staining' manner (i.e. it should not bind to the specimen).

We mainly used uranyl acetate (UO_2 (CH_3COO) $_2 \cdot 2H_2O$), ammonium molybdate $(NH_4)_2$ MoO_4 (99.8%) and sodium phosphotungstate dibasic hydrate ($2Na_2O.P_2O_5$ $12WO_3.18H_2O$) as a negative staining agents purchased from Sigma Aldrich.

In general 3% of staining solution was prepared by dissolving metal salts in deionized water and then pH was adjusted to pH 7. The dried grid was taken and a drop of staining solution was added and left undisturbed for 3-5min, washed single time with distilled water and then TEM grid was dried and taken into the microscope.

In case of uranyl acetate, the pH of the solution maintained at pH 4.2 to 4.5 because the stain has a low pKa it is not recommended for use with specimens that are unstable in acidic conditions. Also, the stain precipitates at physiological pH and in the presence of many salts and great care is needed when using it.

2.4.3. Atomic Force Microscopy (AFM).

The AFM images presented in this manuscript were acquired on a microscope Veeco dimension 3000. This unit operates in air and has two main functions which are imaging (reconstitution of the surface topography) and the measurement of adhesion forces. This microscope is isolated from ambient vibrations by a table on a cushion of air and a phonic cap. Moreover, a motorized stage can move in the three axes (X, Y, and Z). The AFM can be used in two modes: contact and intermittent mode. In this thesis, we have used the AFM in tapping mode. The tips used (Bruker, OTESPA) are made of silicon. They are terminated by rectangular cantilever silicon, the thickness is between 3.6 and 5.6μm, and length between 140 and 180μm. The rear face of the cantilever is covered with a 50nm aluminum layer

reflective. The resonance frequency of these tips is between 290 kHz and 345 kHz and their spring constant between 12 and 103 Nm^{-1}.

The sample were typically dried onto silicon-silica or mica substrates and scanned in the tapping mode with a point probe silicon tip (Otespa) 011303 on mica wafer at an oscillation frequency of 350 kHz. Topographic images of 1μm x 1μm and 100 nm were produced at a scan rate of 1Hz, containing 512 x 512 data points with Nanoscope V531r1 software.

2.4.4. Scanning Electron Microscopy.

Routine SEM analysis was carried out on Carl Zeiss 1540XB FIB Dual Beam/SEM. it combines a high-resolution scanning electron microscope and a focused ion beam the source of which is gallium and energy of the barrel is between 8keV and 30keV. This unit can be used for structuring or characterization of nanomaterials with a precision up 20 nanometer scale. The beam column of which the electron beam (GEMINI®) has a barrel-type Schottky the acceleration voltage is between 5 kV and 30 kV. The resolution of the SEM is estimated at about 1.1nm at 20kV and 1kV to 2.5Nm. Silicon-silica substrates are used to prepare samples.

References:

(1) Enustuna, B. V.; Turkevich, J. *Discussions of the Faraday Society* **1951**, 55-75.

(2) Enustuna, B. V.; Turkevich, J. *Journal of the american chemical society* **1963**, *85*, 3317.

(3) Frens, G. *Nature physical science* **1973**, *20*, 241.

(4) Chow, M. K.; Zukoski, C. F. *Journal of Colloid and Interface Science* **1994**, *165*, 97-109.

(5) Chi, H.; Liu, B.; Guan, G.; Zhang, Z.; Han, M.-Y. *Analyst*, *135*, 1070-1075.

(6) Sreerama, N.; Venyaminov, S. Y.; Woody, R. W. *Protein Science* **1999**, *8*, 370-380.

CHAPITRE 3

AGREGATS /SiO_2/METAL

Résumé

Dans ce chapitre, nous explorons une méthode colloïdale afin de construire couche-par-couche des agrégats modèles de type fluorophore / diélectrique / métal. Dans ce domaine, la plupart des approches consistent à greffer une molécule fluorescente sur la surface de nanoparticules métalliques, éventuellement recouvertes d'un diélectrique. Bien que cette méthode soit bien adaptée pour des boîtes quantiques semi-conductrices (QD), les molécules sont généralement exposées à l'environnement qui peut altérer leur photophysique. De plus, il est souvent difficile de contrôler la quantité précise de molécules déposées et donc de quantifier l'éventuelle modification de fluorescence induite par la présence des nanoparticules. Par conséquent, nous proposons d'utiliser une approche appelée « inside-out » où le fluorophore est au cœur de la structure et recouvert d'un matériau diélectrique qui joue un double rôle. D'une part, il agit classiquement comme un espaceur entre le métal et la molécule fluorescente et d'autre part il permet d'encapsuler et de protéger le fluorophore.

Cette méthode permet d'étudier non seulement l'influence de l'interface diélectrique-fluorophore sur l'intensité de fluorescence, un point qui est en général éludé, mais également la seule influence du métal pour une configuration fluorophore/diélectrique intacte.

Concernant le choix de la molécule fluorescente, les agrégats J de porphyrine solubles dans l'eau ont attiré une attention considérable car l'agrégation peut être aisément contrôlée en écrantant la répulsion des charges de la force ionique par un contrôle du pH. À cet égard, les agrégats J de $TPPS_4$ sont des structures auto-assemblées intéressantes, formées par un nombre fini de molécules de colorant, permettant d'obtenir des rubans de longueur micrométrique. D'un point de vue optique, ils sont caractérisés par une bande d'absorption relativement fine et décalée vers le rouge par rapport à la bande associée au monomère. Cet effet résulte de la délocalisation de l'exciton sur les assemblages moléculaires constituant l'agrégat. Cette agrégation des molécules de porphyrine commence à se produire pour un pH inférieur à 4. La protonation des atomes d'azote conduit alors à la formation d'un macrocycle di-cationique (*Fig III.2*). Notons que les groupements sulfonatés restent chargés négativement même lorsque le pH de la solution inférieur à 1. La molécule $TPPS_4$ globale est alors dianionique qui s'agrège par interaction entre les charges opposées localisées.

Le mécanisme de formation de J-agrégats peut être expliqué en supposant que le modèle 'spread deck of cards' est valide. Dans ce modèle, lorsque le pH de la solution est abaissé, les anneaux de la porphyrine s'empilent (*Fig III.3b*) pour former une structure en rubans (*Fig III.3c-I*). Les groupes latéraux chargés peuvent alors être importants pour la stabilisation des agrégats. Cet auto-assemblage supramoléculaire peut être observé en AFM et en TEM sous forme de 'stries' aplaties (*Fig III.3c*). La *Fig III.4* résume notre stratégie pour étudier l'interaction entre plasmons et molécules fluorescentes. Tout d'abord, les molécules de porphyrine sont auto-assemblées en J-agrégats fluorescents ayant une forme cylindrique en contrôlant le pH de la solution (étape 1). Ensuite, les J-agrégats sont encapsulés dans une coquille de silice diélectrique d'épaisseur bien contrôlée. Le défi de cette étape réside dans la fabrication d'un revêtement uniforme très mince (1-20nm) constituant un renforcement mécanique et un espaceur précis pour le couplage (étape 2). Enfin, des nanoparticules d'or et d'argent sont conjuguées aux agrégats J protégés par la coque de silice en utilisant des interactions covalentes ou électrostatiques (étape 3). L'objectif de cette approche 'inside-out' est d'améliorer les propriétés fluorescentes des J-agrégats en les encapsulant dans une

matrice de silice puis en décorant celle-ci avec des nanoparticules d'or ou d'argent. Ici, le revêtement de silice joue un rôle multiple. En effet, il assure la robustesse mécanique du noyau contenant les agrégats, permet d'optimiser la distance avec les particules métalliques afin de maximiser l'émission de lumière via le couplage plasmon/exciton, et sert de modèle pour fixer des nanoparticules d'or ou d'argent sur la surface en utilisant une interaction électrostatique ou une liaison covalente (*Fig III.4*, étape 3).

La dépendance au pH de l'absorbance optique de la molécule porphyrine est mise en évidence dans la *Fig III.5*. Le *tableau III.1* résume la position des pics d'absorption UV-visible de monomère TPPS et des agrégats en fonction du pH. Initialement, la solution de monomère de porphyrine est de couleur rose (*Fig III.6*), mais celle-ci devient verte lors de l'addition d'HCl 1 M. Ce changement de couleur est caractérisé par spectroscopie UV-Visible. Le décalage vers le rouge observé sur les spectres résulte d'une diminution des intensités de la Soret (413 nm) et Q (516, 552, et 590 nm) des bandes du monomère $[H2TPPS]_4^-$ et de l'apparition de bandes à 434, et 594 et 645 nm. Les spectres de fluorescence correspondants du monomère de porphyrine, lorsqu'il est excité 413 nm (bande de Soret), révèlent deux pics très intenses à 640 nm et 702 nm (*Fig II.7* noir). Lorsque la solution agrégée est excitée à 490 nm, le maximum d'émission apparaît à 720nm (*Fig III.7* bleu), alors qu'une excitation à une plus grande longueur d'onde (706nm) conduit à une émission à 728nm. Une émission à 720 nm peut être complètement obtenue en abaissant le pH de la solution.
Le *tableau III.2* résume les longueurs d'onde d'excitation et d'émission pour la molécule de porphyrine, le monomère dianion et les J-agrégats. La caractérisation TEM et AFM des agrégats J a révélé la longueur des nanorubans qui varie de 0,5 à 5μm ainsi qu'une largeur et une hauteur uniformes de 17 ± 2 nm et 11 ± 1 nm, respectivement.

Lors de la deuxième étape, nous avons encapsulé les nanorubans d'agrégats J avec de la silice en utilisant un mélange de APTES / TEOS. La *Fig III.10* montre des images TEM et AFM des agrégats enrobés par différentes épaisseurs de silice. La morphologie est similaire à celle de J-agrégats formés en l'absence de silice mais les dimensions de ces structures sont légèrement différentes.
Le protocole a été optimisé pour obtenir une gaine de silice ayant une épaisseur comprise entre 2 et 10 nm (*Fig. III.11*). Ces épaisseurs sont pertinentes pour pouvoir suivre la modification (inhibition ou exaltation) de l'intensité de fluorescence des J-agrégats due la

présence de nanoparticules métalliques. Nos expériences indiquent que la meilleure façon de contrôler l'épaisseur de la silice est de faire varier la quantité de précurseur plutôt que d'autres paramètres comme le pH, le temps de réaction, la température ou le rapport volumique entre APTES/TEOS, qui ont également été testés. Pour une solution typique contenant une concentration de la couche de 50μM de TPPS, l'épaisseur de silice peut être ajustée à 2.2, 4.5, 6.7, 9.0 et 11.2 nm (± 1 nm) en ajoutant respectivement 10, 20, 30, 40 ou 50μL de APTES/TEOS, respectivement. La relation entre épaisseur et concentration est rigoureusement comme cela est montré sur la *Fig III.11* et a été observée à la fois pour la largeur (données TEM) et l'épaisseur (AFM données), la variation d'épaisseur est essentiellement représentée par la polydispersité résiduel du template de départ (les agrégats eux-mêmes).

En fin, la conjugaison de nanoparticules métalliques à des agrégats J encapsulés par de la silice a été réalisée. Lorsque des nanoparticules métalliques sont conjuguées directement aux agrégats non encapsulés, la morphologie en ruban est détruite au profit de petits agrégats sphériques comme en témoigne l'analyse par TEM (*Fig III.17*). De plus, une inhibition de fluorescence a été observée lors de ce changement de forme. Les nanoparticules métalliques induisent l'assemblage des molécules libres de TPPS4 ainsi que des molécules provenant des agrégats J préalablement formés. Les agrégats J sont alors désasemblés en petits agrégats qui se fixent à la surface des nanoparticules métalliques. Ces petits J-agrégats sont en contact direct des nanoparticules métalliques, ce qui résulte en l'inhibition de la fluorescence par dissipation non-radiative. Ainsi, la diminution de fluorescence de ces structures provient non seulement du changement de forme (désassemblage partiel) des agrégat J observé en TEM mais aussi de l'inhibition de fluorescence des molécules de J-agrégat issue de désexcitations non radiatives vers le métal. Par conséquent, le revêtement de silice des J-agrégats semble être essentiel pour obtenir un couplage exciton-plasmon optimal en vue de l'émission de lumière par ce type d'architecture. Il sert également de template pour le greffage des nanoparticules sur la surface en utilisant une interaction électrostatique comme décrit ci-après.

Les agrégats J encapsulés par de la silice et couplés a des nanoparticules d'or et d'argent sont présentés dans la section 3.4.2. Il est intéressant de noter que la morphologie des agrégats J n'a pas été modifiée avec la conjugaison de nanoparticules et de nanoparticules Au et Ag sont décorées le long de ces agrégats de type bande.

Chapter 3 Résumé

Le greffage des nanoparticules métalliques de la coque de silice est mis en évidence par TEM (*Fig III.19* et *Fig III.21*), SEM (*Fig III.21*) et EDXA (*FigIII.20*). Le spectre d'absorption des agrégats J n'est pas modifié par la fixation de nanoparticules métalliques. En particulier, l'intensité des bandes à 490 nm et 434 nm restés inchangée, quelle que soit la quantité de nanoparticules. La fixation de nanoparticules d'Au ou d'Ag fraîchement préparées sur la surface extérieure de silice modifie sensiblement l'intensité d'émission des agrégats J encapsulés (*Fig III.21* et *Fig III.22*).

En conclusion, dans ce travail, nous avons montré que l'encapsulation peut être contrôlée dans une gamme de épaisseurs de1-10 nm, avec une très bonne précision (± 2 nm) soit l'équivalent de 1-2 couche de silicates. Cela nous a permis de sonder le régime de couplage fort entre les agrégats J encapsulés et les nanoparticules plasmonique. Nous avons observé les trois régimes de fluorescence attendus : l'inhibition, l'exaltation et le découplage.
Dans notre système, la fluorescence exaltée par la présence de particules métalliques pourrait être optimisée pour dépasser les x 300% que nous avons observé. L'encapsulation de nanoparticules fluorescentes ou d'agrégats supramoléculaires par une coquille de silice présente plusieurs avantages en termes de stabilité mécanique et optique, ainsi que de biocompatibilité, qui sont d'une grande importance pour les applications de bio détection. Nous pensons que notre approche bottom-up pourrait permettre de concevoir des sondes optiques pour la détection et l'imagerie, mais aussi d'intégrer efficacement des absorbeurs et des émetteurs moléculaires dans des dispositifs plasmoniques pour le traitement optique de l'information, qui nécessitent un réglage fin du couplage entre les fluorophores et les nanostructures métalliques.

CHAPTER 3

J-AGGREGATE /SiO_2/METAL.

In this chapter we aim at exploring well-stabilized methods inherited from biomineralisation and bioinspired templated chemistry to fluorophore-metal nanoparticle coupling. Most approaches in this field put the metal inside and molecule on the surface of nanoparticle (outside) and this method is well suited for quantum dots (QD). However, in these approaches, molecules are exposed and it is difficult to control the amount of molecules i.e. to quantify metal enhanced fluorescence (MEF).

Hence, we propose to use an inside-out approach where a dielectric plays a dual role i.e. on the one hand it acts as a dielectric spacer between metal and a fluorophore molecule and on the other hand it gives a protective shell for the fluorophore. Therefore, this method allows for studying the influence of the dielectric–fluorophore interface on the fluorescence intensity and influence of the metal for an identical fluorophore /dielectric system. For this, we applied our knowledge of templated chemistry.

3.1. J-aggregates.

3.1.1. Porphyrins and porphyrin aggregates.

J-Aggregates are self assembled structures that are formed by a finite number of molecular dyes. Peculiar classes of aggregating dyes are represented by cyanine and porphyrin dyes which are large macrocyclic dye molecules with a large degree of aromaticity. They are highly colorful compounds and have been used for centuries as pigments.[1] Different aggregation patterns of these dyes in different media have been proposed.[2] These aggregates are characterized from their spectral shifts mainly arising from the electronic coupling of monomers. The bathrochromically shifted J-bands (J for Jelly)[3] and hypsochromically shifted H-bands (H for hypsochromic) of the aggregates have been explained in terms of molecular exciton coupling theory, i.e., coupling of transition moments of the constituent dye molecules. The aggregates that exhibit J-bands in their absorption spectrum are called J-aggregates and H-aggregates exhibit these H-bands. It is known that the aggregation of dyes is important in biological and artificial photosynthetic systems.[4] Thus, J-aggregates are studied due to their potentially useful application in fluorescent cell imaging, opto-electric conversion and nonlinear optics.

In particular, water-soluble porphyrin J aggregates attracted considerable attention because aggregation can be conveniently controlled by screening the charge repulsion by changes in the ionic strength and pH. Many relevant physicochemical properties of this class of compounds, including photo physical features, are strictly dependent on their aggregation state. These are well suited building blocks because, depending on their electronic and steric properties.[5] The J-aggregates of $TPPS_4$ have previously been studied by various spectroscopic techniques and much is known about the excitonic interactions.[6-8]

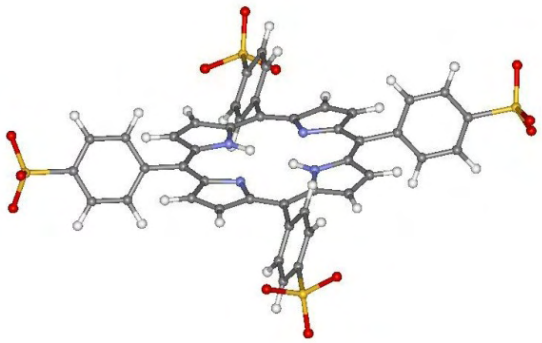

Fig III.1: *Computer generated optimized diagram of $TPPS_4$ molecule.*

The sodium salt of Meso-tetrakis (4-sulfonatopenyl) porphyrin ($TPPS_4$) is one of the few porphyrins that are capable of forming J-aggregates in dilute aqueous solution.[9-12] Many porphyrins are hydrophobic but in the case of $TPPS_4$, the four sulfonato groups attached at the meso-positions make it polar enough to be highly soluble in water. They are characterized by a red shifted and sharp absorption band relative to the monomer band, a result of exciton delocalization over the molecular building blocks of the aggregates.[13-15] A sharp absorption band at 490nm arising from the formation of J-aggregates is well suited for an effective coupling with plasmon band of Au and Ag nanoparticles.

Aggregation of porphyrin molecules starts to occur when the pH of the porphyrin solution is lowered below pH 4. The acid protonates the central nitrogen atoms and lead to the formation of a di-cation with respect to the macrocyclic ring (*Fig III.2*). The sulfonato groups remain negatively charged even down to pH 1 and so the $TPPS_4$ molecule is a dianion overall.

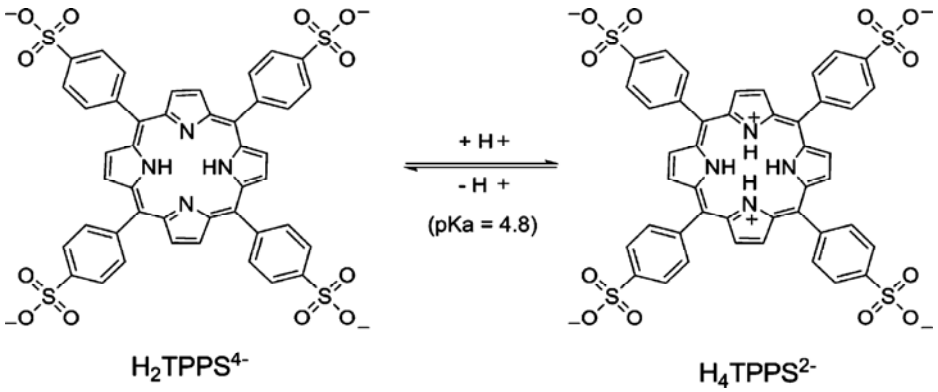

Fig III.2: *Protonation of $H_2TPPS_4^{4-}$ to $H_4TPPS_4^{2-}$ with acidification by HCl.*

In these conditions the molecules start to aggregate. This is observed by a dramatic change in the absorption as well as fluorescence spectrum of the solution. The proposed mechanism for the aggregation is that molecules are connected by electrostatic interaction between the negatively charged sulfonato groups and the positive centre of the porphyrin ring. The molecules are thought to stack, first into dimers and then to higher order structures. Analysis of the absorption spectra also rules out side-by-side linear dimer formation. The possibility of a structure in which one molecule is at an angle with respect to the other is also unlikely since the spectroscopic data does not support a structure with non- parallel dipole transitions. Hence the mechanism of formation of J-aggregates can be explained by assuming the "spread deck of cards" model.[16-18]

In this suggested model, the porphyrin rings stack face to face but the planes were shifted relative to one another. One of the sulfonato groups, which lie perpendicular to the plane of the ring, was positioned over the centre of the macrocycle of another monomer to form a thread like structure (*Fig III.3c-I*). The remaining charged side groups may be important in the stabilization of the aggregates.

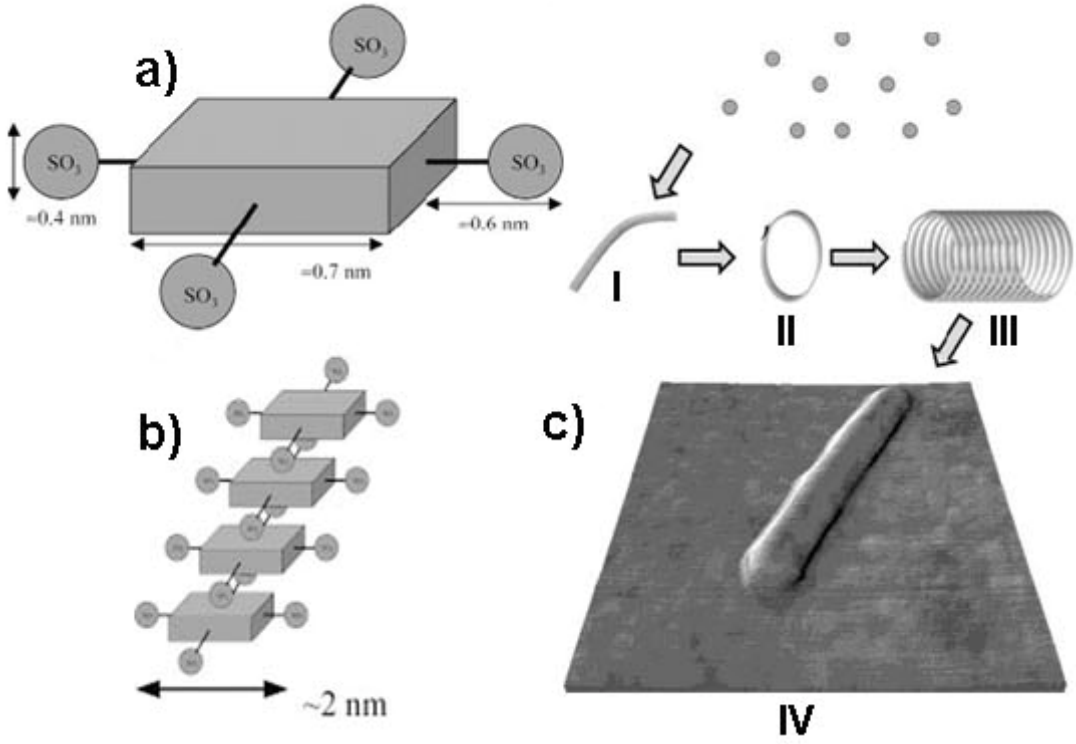

Fig III.3: *a) Schematic diagram of $TPPS_4$ assuming the spread card deck model. (b) The negatively charged sulfonic group's interact strongly with the positively charged protonated nitrogen's of porphyrin molecules to form stacked arrangement. (c) $TPPS_4$ molecules aggregate and form linear one-dimensional aggregates (I). These aggregates result in ring-shaped structures (II).Rings stack together and form nanotubes (III), which is flattened on the surface (IV) and can be observed directly (by means of AFM and TEM).Figure extracted from the reference J. Phys. Chem. B 2004, 108, 2833-2838.*

These thread like structures promote one-dimensional rings of approximately 20 nm in diameter (*Fig .III.3*). Further on, such rings stack together and form a nanotape (*Fig II.3a-III*), can be observed by AFM and TEM as flattened stripes (*Fig III.3c*). The ring should contain 60-70 molecules of $TPPS_4$ (approximately calculated from the geometrical "spread deck of cards" assumption).[16] Recently the porphyrin aggregation mechanism has been discussed in detail by Hollingsworth et al.[17] Mechanism of silicification of J-aggregates and change in morphology, variation in the optical properties on silicification will be discussed in section 3.3.3.

3.1.2. Method and scheme description.

Meso-tetrakis (4-sulfonatopenyl) porphyrin ($TPPS_4$) exhibit sharp absorption peaks with very high absorption coefficient which can be efficiently used to couple with plasmon band of metal nanoparticles. Hence the use of this molecule to study the effect of plasmon on molecular fluorescence helps in understanding the mechanism of metal-molecule interaction.

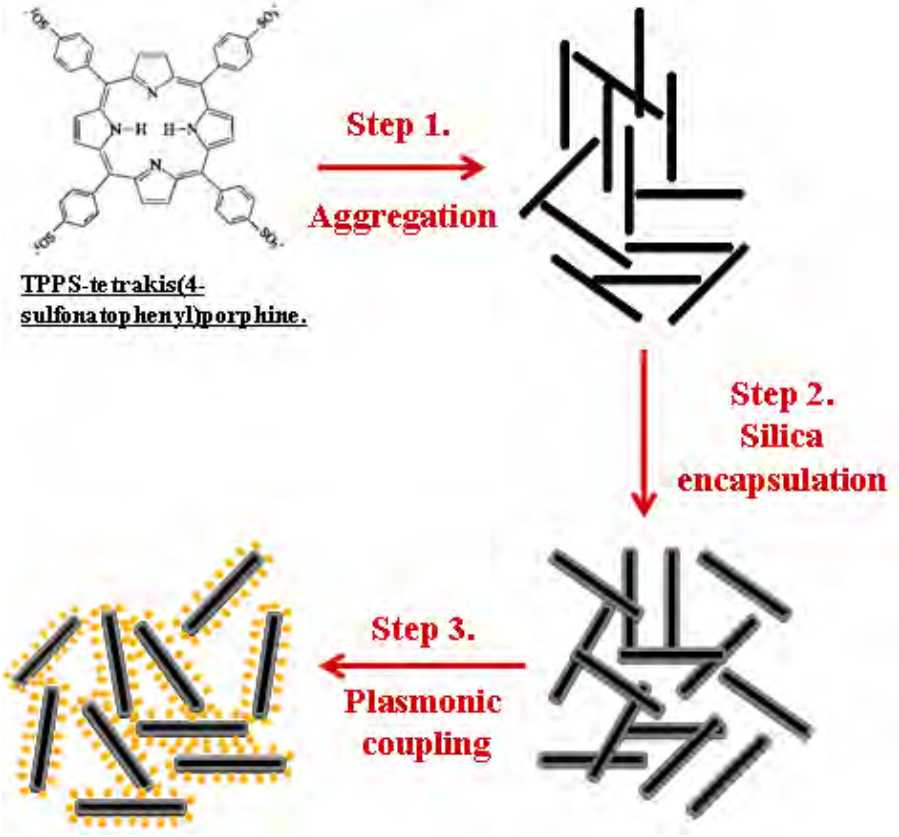

***Fig III.4**: Scheme describing the 3-step bottom-up synthesis of fluorophore-metallic conjugates with finely tuned coupling by templated growth of silica. (1) J-aggregation of $TPPS_4$ porphyrins into rod-shaped ensemble of well-defined morphology. (2) Templated silica encapsulation of the J-aggregates which provides a mechanical reinforcement and a dielectric sheathing of controlled thickness. (3) Attachment of Au or Ag nanoparticles at a controlled distance from the fluorophore in order to enhance the intensity of the local electromagnetic field.*

Fig III.4 summarizes our strategy. $TPPS_4$ porphyrins are self-assembled into fluorescent, rod-shaped J-aggregates in first step by changing the pH of the solution (*Step 1*). The J-aggregates are encased inside a dielectric silica shell of well-controlled thickness. The challenge is to reach very thin (1-20nm) uniform coating which provide mechanical reinforcement and a precise coupling spacer (*Step 2*). And finally gold and silver nanoparticles are conjugated to the silicified J-aggregate rods using either covalent or

electrostatic interactions (*Step 3*). Hence our inside-out approach goal is fluorescence enhancement of J-aggregates by the decoration of the silica-coated aggregates with gold or silver nanoparticles.

Therefore, here we defined an original mineralization approach where we encapsulate TPPS J-aggregates themselves in a silica shell of controlled thickness in the 1-20 nm regimes relevant to optimal plasmon-exciton coupling (*Fig II.4, step 2*). The silica coating plays a multiple role, it ensures the mechanical robustness of the aggregate core, it provide a dielectric spacer for optimal exciton-plasmon coupling and it serve as template for binding Au or Ag nanoparticles onto the surface using electrostatic interaction or covalent bonding (*Fig III.4, step 3*).

3.2 Synthesis and characterization of J-aggregates.

3.2.1. Synthesis of J-aggregates.

J-aggregation of *tetrakis* (4-sulfonatophenyl)-porphyrin (TPPS) was induced by addition of a small amount of 1M hydrochloric acid to a dilute aqueous solution of porphyrin. Acidification to pH values below 4 immediately produced a pink to bright-green colour change due to protonation of $[H_2TPPS]^{4-}$ ions and formation of $[H_4TPPS]^{2-}$ monomers (*Fig II.6*).

Protocol: TPPS J-aggregates were prepared by following the method described elsewhere.[19] Typically, 10 mL of a 50 μM, (5×10^{-5} M) solution of $TPPS_4$ in deionized water were acidified below pH 4 by addition of aliquots of 1 M hydrochloric acid. A gradual color change from pink to a green was observed as the J-aggregates formed.

3.2.2. UV-Vis spectroscopy.

The pH dependency of optical absorbance of the porphyrin dye molecule is shown below. Initially, the porphyrin monomer solution was pink in color (*Fig III.6*) but changed to green on addition of 1M HCl acid. *Fig III.5* showed the evolution of the UV-Vis spectra of a porphyrin solution with increasing acid concentration. After 1hour, an intense green color was observed. This change was monitored in UV-Vis absorption spectrum. The red shift translate in the spectrum by decrease in the intensities of the Soret (413 nm) and Q (516, 552, and 590 nm) bands for monomeric $[H_2TPPS]^{4-}$, and appearance of corresponding bands at 434, nm, and 594 and 645 nm, respectively. With further acidification, the 413 nm peak and the monomer Q bands diminished completely as the porphyrin was fully converted into the diacid, $[H_4TPPS]^{2-}$, through protonation of all four nitrogen atoms in the macrocycle.

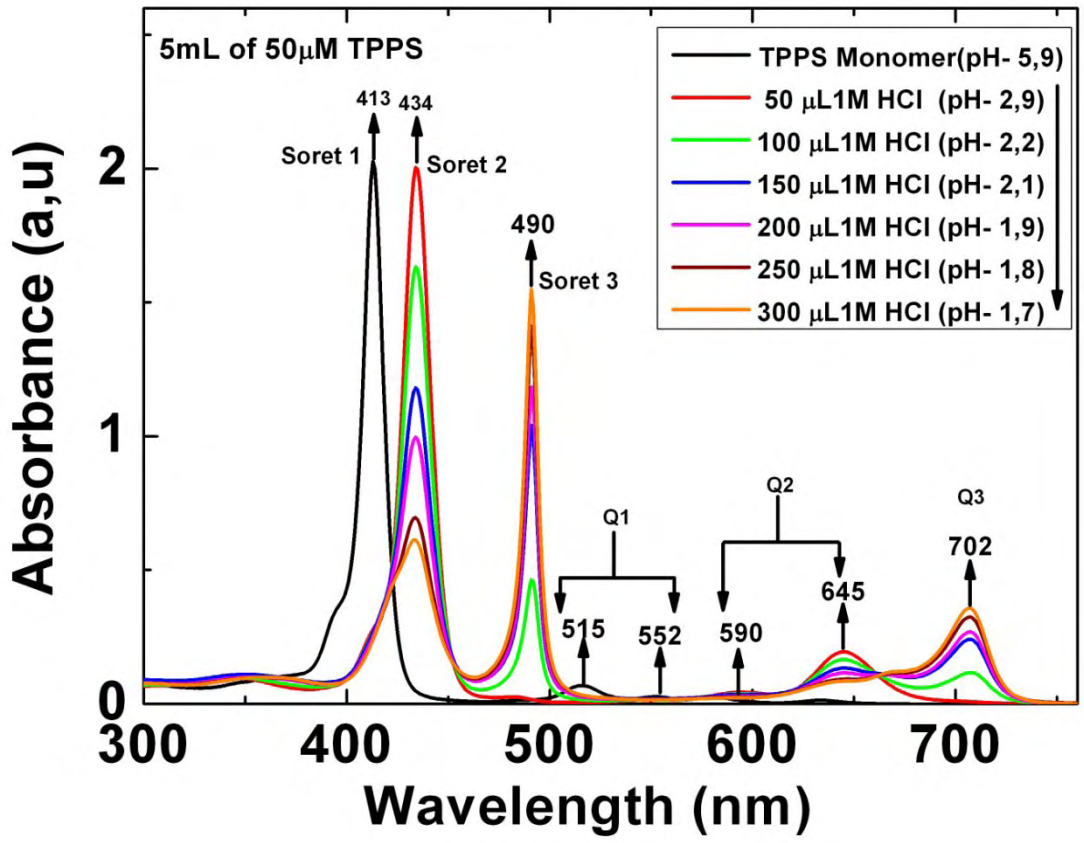

Fig III.5: *Evolution of $TPPS_4$ absorption spectra with the amount of acid added.*

Fig III.6: *Photograph of TPPS solution of concentration A) 9mM (9 X 10^{-3} M), B) TPPS solution of concentration 50µM (5 X 10^{-5} M), C) J-aggregates at pH >2, D)- J-aggregates at pH < 2.*

UV	$[H_2TPPS]^{4-}$ (pH 7) Pink	$\Leftrightarrow [H_4TPPS]^{2-} \Leftrightarrow$ (pH < 4) Green	J-aggregates (pH < 2) Darker green
Soret	413 nm	434 nm	490 nm
Q bands	515, 552, 590 nm	594, 645 nm	645, 668, 706 nm

Table III.1 *Table summarizing a position of UV-visible absorption peaks of TPPS monomer and aggregates as a function of pH.*

Within 20 min, self- aggregation of the $[H_4TPPS]^{2-}$ anions produced a darkening of the green solution, and UV-Vis spectra showed the gradual appearance of an intense red-shifted soret band at 490 nm along with a broad peak at 645, 668 and 706 nm due to formation of J-aggregates in equilibrium with the $[H_4TPPS]^{2-}$ monomer. Subsequently, a cloudy, green suspension was observed which precipitated over a period of 24 hours.

The rates of formation of J-aggregates were dependent on the volume of acid added. After 30 minutes, slowly developing J-aggregate Q-band at 706 nm was most intense for sample with the highest acid concentration. Dilution of J-aggregate suspensions was found to significantly reduce the relative intensities of the 490 and 706 nm bands probably because slight increase in pH causes a shift in the equilibrium towards small aggregates and protonated monomers.

3.2.3. Fluorescence spectroscopy

The fluorescence of TPPS molecules and their aggregates has been well-established[12 13]. $TPPS_4$ are known to exhibit a strong fluorescence which can be altered by their aggregation state. We have investigated the emission properties of native TPPS monomer and J-aggregates as a reference by preparing the solution with the same protocol.

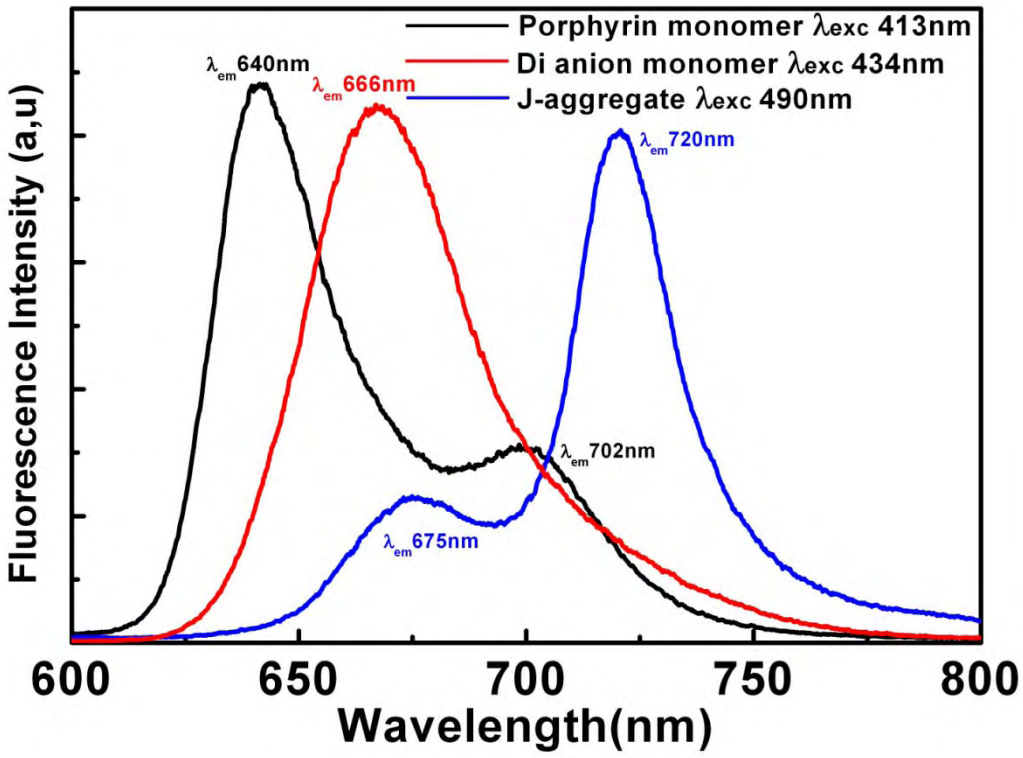

Fig III.7: *Fluorescence spectra of TPPS monomer-black (λ_{exc} 413nm), dianion monomer –red (λ_{exc} 434nm) and J-aggregates-blue (λ_{exc} -490nm).*

The fluorescence spectra obtained from a 50µM solution of the porphyrin monomer when excited at λ_{exc}413 nm (Soret-band) showed two peaks with very intense fluorescence at 640nm and 702nm (*Fig III.7 black*). The same result was obtained when we excite the monomer at Q-band, i.e. at 515nm.When the pH was decreased just below pH4, the change in the colour was observed and if solution when the solution was excited at 434 and 645 nm

wavelengths, the emission occurred which corresponds to the emission peak at 675nm by the dianion monomer (*Fig III.7 red*). When the pH of the solution was further lowered to pH < 2, J-aggregates were formed. Maximum emission at 720nm and minimum at 675nm was obtained by excitation at 490nm (*Fig III.7 blue*), whereas excitation at longer wavelength 706nm gave emission at 728nm.The emission at 720nm can be fully achieved by lowering the pH of the solution. Below, the table summarizes the excitation and emission wavelength for freebase, dianion monomer and J-aggregates.

Fluorescence	λ_{exc} (nm)	λ_{em} (nm)
TPPS monomer	413 515	640, 702
Dianion monomer	434 645	675
J-aggregates	490 706	675,720 728

Table III. 2: *Table summarizing a position of fluorescence emission peaks (λ_{em}) of TPPS monomer, di-anion and its aggregates and their corresponding most efficient excitation (λ_{exc}) wavelength.*

In order to investigate the influence of the metal particles on the molecular fluorescence of the J-aggregates, we have first identified the most relevant excitation wavelength and then systematically monitored the emission at all stages of our templated construction. They were usually excited using the Soret and Q-bands observed in the absorption or excitation spectrum (*Fig III.5*). Emission of the TPPS monomer at 640 and 702 nm can be produced with similar spectral features by exciting either the Soret band (413 nm) or the lower Q-band (515 nm), the latter one being more efficient than the former (*Fig. III.7 and Table III. 2*)

3.2.4. Structural characterization by TEM and AFM.

Samples for TEM were prepared by casting a drop of freshly prepared sample of J-aggregates on 300 mesh TEM grid and left for drying overnight. TEM images of unstained samples of J-aggregates showed large numbers of needle-like particles (*Fig III.8).* These needles were very sharp and long enough to be viewed under transmission electron microscope. In general, the length of the needles varied greatly, ranging from 500nm to 5μm but the width contrast was found to be uniform. Closer inspection of the larger aggregates revealed that they were in fact made up of bundles of finer fibres. This made the actual widths of individual fibres in the range of 17.5±2.5nm (*Fig III.8a*).

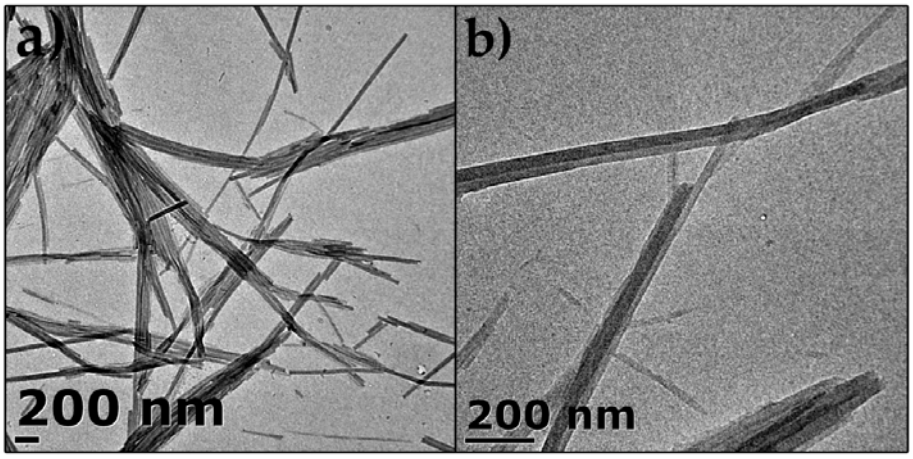

Fig III.8: *Low and high magnification TEM images of assynthesised $TPPS_4$ J-aggregates.*

J-aggregate sample for AFM was prepared by drying a drop of freshly prepared sample solution of J-aggregates onto silicon-silica (Si-SiO_2) substrates. Height measurements of J-aggregates deposited on silicon-silica substrates yielded a uniform filament thickness of 11 ± 1 nm as shown by the profiles in *Fig III.9*. The height profile measured across many aggregates showed the regular height above the background, and a few peaks of double that value when two aggregates were overlapping.

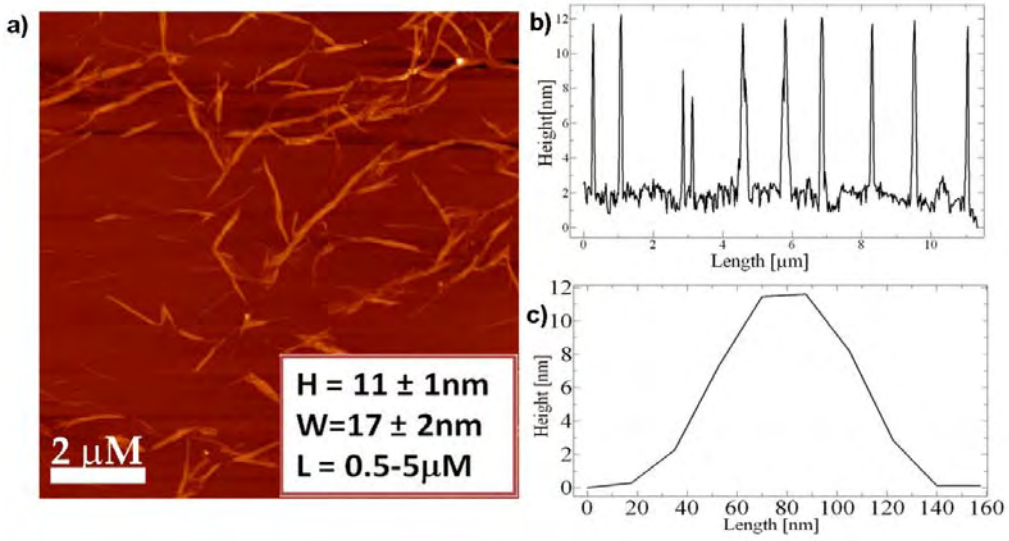

FigIII.9: *a) AFM images of $TPPS_4$ J-aggregates. b) And c) height profile of J-aggregates along several rods and along the single rod respectively.*

The profile along one filament confirmed a height along the length, right to the ends, which were abrupt. AFM could not be used accurately to measure widths due to tip convolution

effects which were important because of the small difference between the size of the tip and the aggregate. The statistical analysis on width and height on these aggregates have been performed (*Fig III.9b, c*).The combined results from AFM, which measures height and TEM, which assess a width, indicated that the TPPS superstructures were assembled in the form of high aspect ratio nanotapes, *ca.* 11 x 17 nm in thickness and width, respectively and the length of the J-aggregates varies from 0.5-5 μM.

3.3. Silica Encapsulation of J-aggregates.

3.3.1. Silicification of J-aggregates.

Tetraethoxysilane (TEOS), 3-Mercaptopropyltrimethoxysilane (MPTES) and Aminopropyltriethoxysilane (APTES) were used to modify J-aggregate surface to attach gold or silver nanoparticle. TEOS has been used previously to coat gold nanoparticles to make core-shell particles. Furthermore, a mixture of TEOS -APTES was used to coat the Tobacco Mosaic Virus[20,21]. Tetraethoxysilane TEOS is often used in basic conditions but can also be used in acidic condition. The rate of silica coating with TEOS is slow and it is better for thin silica coating. APTES is self-catalysing and silica coating is very fast and hard to control the thickness. In addition, APTES also gets protonated at low pH giving a positive charge, which could interact favourably with the negatively charged porphyrin template and giving a positive surface charge which could attract the negatively charged Au and Ag nanoparticles. Therefore, mixture of TEOS and APTES can bring a controlled silica thickness with functionalised silica surface. APTES Silica-coated TPPS J-aggregate nanofilaments were prepared by mixing TEOS/APTES mixtures, with pH neutral porphyrin solutions followed by rapid acidification with hydrochloric acid to pH 2.

MPTES was also used to coat J-aggregates in order to have a covalent attachment of metal nanoparticles with thiol group of MPTEOS on the surface of J-aggregates. The rate constant for the condensation of MPTEOS was essentially zero at pH 4 and increases as a function of increasing pH. [22]. Therefore, the direct addition of MPTEOS and acidification to pH 2 resulted in a precipitation of the solution. In order to coat mercaptopropyltrimethoxysilane, we have to work at neutral or basic pH. We followed two step methods where in the first step we coat J-aggregates with TEOS at acidic pH and then increase the solution pH to 8 which in turn disassemble J-aggregates. Since it was trapped inside the silica shell and hence in the next step we start conjugating this with mercaptopropyltrimethoxysilane and bring the solution back to pH 2 with vigorous stirring.

The deposition of organosilane molecules onto other surfaces requires two reactions, hydrolysis and condensation reaction. Both hydrolysis and condensation of the molecules must occur as shown in the reactions below. The rates and extent of these reactions depend on number of factors such as the organosilane of interest, the solvent, water availability, solution pH, silane concentration and the surface to be coated. Mainly, the availability of water, solution pH and silane concentration affect the rates of hydrolysis and condensation. [23,24] The rate of hydrolysis is faster than condensation when water is in excess and the pH of the solution is low. The observed kinetics suggest that the hydrolysis of silanes may be a stepwise pseudo first order reaction. The rate of condensation is faster than hydrolysis when a small amount of water is present and the solution pH is high. The rate of condensation has also been shown to increase with increasing organosilane concentration. The possibility that organosilane hydrolysis and condensation occur simultaneously in solution has also been postulated.

The encapsulation of silica (TEOS-APTES) on J-aggregates proceeds mainly with two steps. In the first step, hydrolysis of a reaction takes place in presence of H^+ or OH^- ions. APTES is a self catalyzing agent which is enough to increase the rate of the reaction in presence of TEOS and water.

$$\mathbf{R\,(CH_2)_x\,Si\,(OR')_3 + 3H_2O \longrightarrow R\,(CH_2)_x\,Si(OH)_3 + 3OR'}$$

$$\mathbf{R\,(CH_2)_x\,Si(OH')_3 + R\,(CH_2)x\,Si(OH')_3 \longrightarrow R\,(CH_2)_x\,(OH)_2\,Si\text{-}O\text{-}Si\,(OH)_2\,(CH_2)_x\,R + H_2O}$$

In the second step, the hydrolyzed organosilane molecules can undergo condensation on J-aggregates which acts as a template. Below, we have summarized three protocols we used during our experiment.

3.3.2. Experiemental protocol for the encapsulation of silica on J-aggregates.

Protocol-1: A small volume of 50% v/v APTES-TEOS was added to the 50μM neutral solution of $TPPS_4$ with vigorous stirring. Rapidly this solution was acidified with the addition of 1 M HCl inducing the self assembly of J-aggregates as well as triggering the silica condensation. This solution was vigourosly stirred for 30 min and left undisturbed for 4 hour.

Protocol-2: A small volume of 10% v/v APTES-TEOS was added to the 50μM neutral solution of $TPPS_4$ with vigorous stirring. Rapid addition of 1 M HCl to this solution brings the solution pH to 2 and change in the colour was observed from pink to green.This solution vigourosly was stirred for 30 min and left undisturbed for 4 hour. The volume of silica

precursor solution was varied between 10 and 50 μL, by portions of 10 μL, in order to control the silica sheath thickness.

Protocol-3: A small volume of 10μL TEOS was added to the 50μM neutral solution of $TPPS_4$ with vigorous stirring. This solution was acidified to pH 2 with the addition of 1 M HCl. The change in the colour was observed from pink to green. This solution was vigorously stirred for 30 min and left undisturbed for 6 hour. After 1M NaOH solution was added to bring solution pH to 8. 3μL MPTEOS of 10% volume was added and continuously stirred for 1hr. The solution pH was brought back to pH 2 by adding 1M HCl and the stirring continued for another 1hour.

3.3.3. TEM and AFM characterization and silica thickness optimization.

The reaction by our first protocol i.e. addition of 50% v/v APTES-TEOS mixture to the TPPS solution followed by the rapid acidification with HCl, resulted in the precipitation of J-aggregate solution. This could be from the increased amount of APTES which results in the fast condensation of silica and hence makes it difficult to control the rate of reaction. Therefore, we subsequently reduced the concentration of APTES with TEOS in the next protocol in order to control silica conjugation on J-aggregates.

Samples for TEM and AFM studies from protocol-2 taken 4 hours after the addition of the alkoxysilane reactants, showed the presence of well-defined, high aspect ratio nanofilaments. *Fig II.10* show TEM and AFM image of silicified J-aggregates with different silica thickness. The morphology was similar to that of J-aggregates formed in the absence of silica but with slight differences in the dimensions. Typically, the molar ratio of silica precursors to TPPS was 1:5 which means that the porphyrin was present in four-fold excess. At these low alkoxysilane concentrations negligible levels of non-templated silica were obtained. Width and height measurements from TEM and AFM showed that silicified J-aggregates become approximately equivalent with that of J-aggregates except that silicified J-aggregates were more cylindrical than the flat tapes formed by acidification of the porphyrin. Addition of small amounts of APTES (10 mol %) to the reaction mixture produced nano filaments that were shorter in length and increased in width. TEM images showed that increase in silica amount resulted in decrease of rod length and increase in the width of J-aggregates (*Fig III.10 corresponding histogram in Fig III.11*). Excess of silica has been found in TEM grids which were spherical in shape. AFM showed that the height of the rods increased to 35 - 40 nm.

There was also evidence that the J-aggregates could form twisted bundles as well as aligning in a parallel fashion.

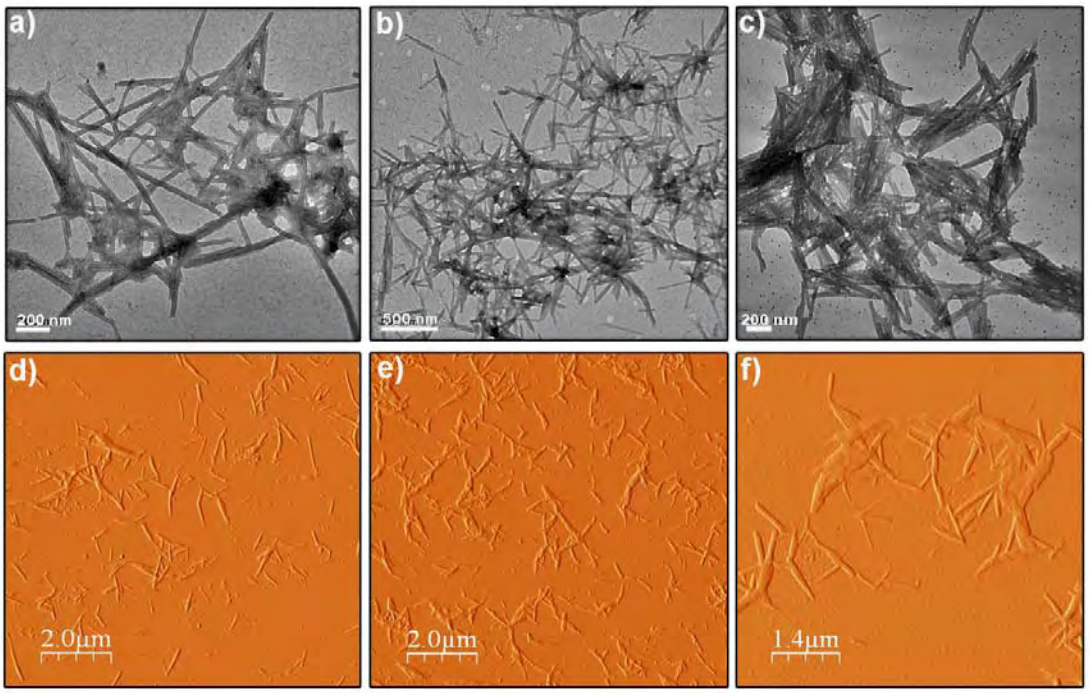

Fig III.10: *TEM and AFM images of J-aggregates with varied silica thickness. Images a) and d) 2.2nm, b) and e) 6.7nm and c), f) 11.2 nm of silica thickness.*

Protocol-3 was optimised to achieve a nanometer precision for the silica sheath thickness in the range of 2-10 nm (*Fig III.11*), which is relevant for metal-enhanced fluorescence (MEF). It appears that the finest thickness tuning is achieved by varying the amount of precursor rather than any other parameters such as pH, reaction time, temperature or APTES / TEOS volume ratio that were also tested[19]. For a typical 10 mL, 50 µM solution of TPPS, the silica coating thickness could be adjusted to 2.2, 4.5, 6.7, 9.0 and 11.2 nm (± 1 nm) by adding 10, 20, 30, 40 or 50 µL of APTES/TEOS solution, respectively. This was in strictly linear correlation, as showed in *Fig III.11* and was observed for both the width (TEM data) and the thickness (AFM data) data, with thickness variation mostly accounted by the template residual polydispersity.

Although the average length of the silica-coated aggregates appeared to be both shorter (ca. 200 nm-1 µm) and less polydisperse, the smooth and linear increase of the silica coating thickness indicates that the encapsulation of porphyrin nanotapes occurs without significant disruption to the supramolecular organization. The reliable templating effect of the J-

aggregates was promoted by the electrostatic interactions between the anionic TPPS moieties and the cationic APTES precursor, which also ensured the acidic auto-catalysis of the silica condensation.

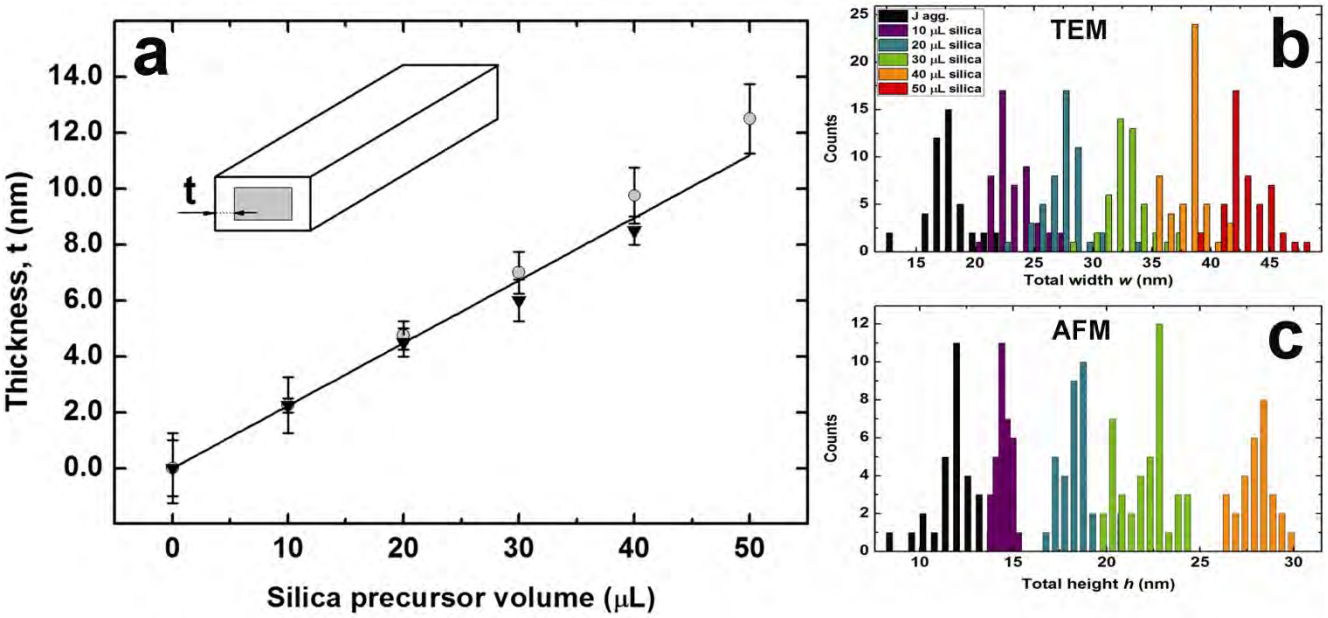

Fig III.11: a) *Variation of the silica coating thickness, t, as a function of the volume of silica precursor, APTES / TEOS, added to the porphyrin solution. Inverted triangle data represent height data measured by AFM and grey circles are derived from width data measured on TEM images. Right side the histogram showing change in the width with of J-aggregates with increasing silica thickness. b) And c) histograms of width and height of J-aggregate nanoribbons measured on TEM images and AFM images. Each histogram corresponds to either native J-aggregates uncoated (black) or coated with a silica sheath using 10 mL (purple), 20 μL (dark cyan), 30 μL (green), 40 μL (orange) or 50 μL (red) of silica precursor solution for a fixed amount of J aggregate suspension.*

3.3.4. UV-Vis and fluorescence spectroscopy coated J-aggregates.

The evolution of the optical properties of the encapsulated samples was studied 2-3 hour after addition of alkoxysilane reactants by UV-Vis absorption using quartz cuvette with a 1 mm light path. The spectrum was monitored as a function of silica sheath thickness. The silica mineralization did not induce major spectral modifications to the four main peaks in the UV-Vis spectra. However, the respective intensities of the bands were affected. As the silica thickness was increased from 2.2 to 11.2 nm, the intensity of the Soret and Q-band at 490 and 708 nm increased with a concomitant diminution in the absorption of the 434 nm and 645 nm bands (*Fig III.12*).

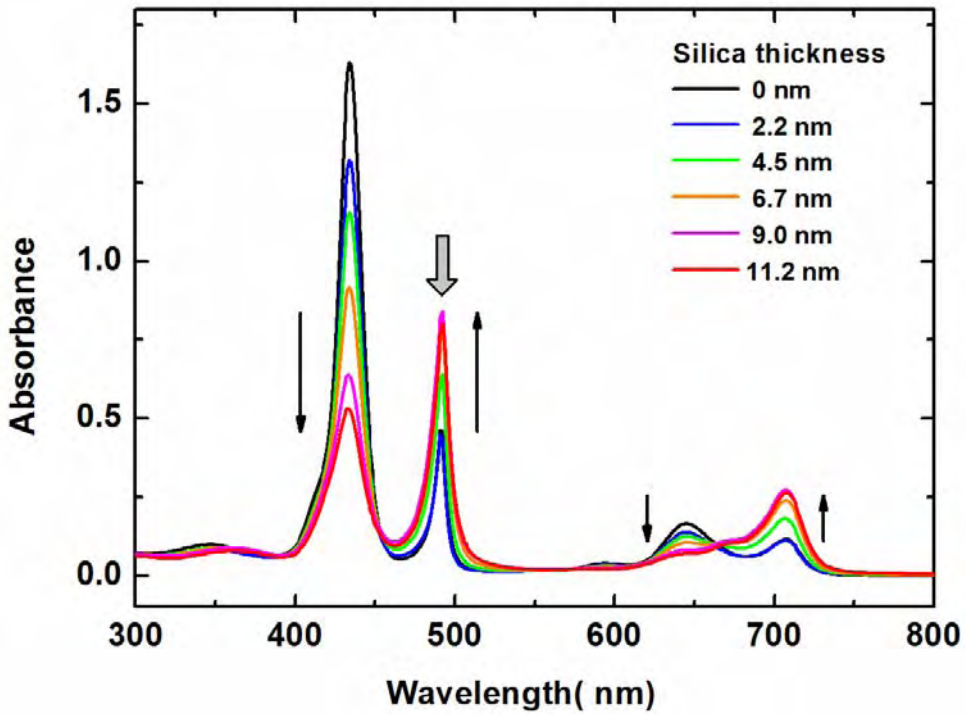

Fig III.12: *Evolution of the J-aggregates absorption spectrum with silica shell encapsulation for thicknesses comprised between 2.2 and 11.2 nm. The anionic precursor absorption peaks (434 and 645 nm) decrease in intensity as the aggregate band (490 and 708 nm) increase. The thick grey arrow indicates the fluorescence excitation wavelength.*

This conversion of the protonated monomer peaks (434 and 645 nm) to the J-aggregate peaks (490 and 708 nm) reflects exactly the evolution of the spectrum upon aggregation by acidification of the TPPS solution below pH 2 although the observed pH for the encapsulated J-aggregates remains constant at 2.06-2.02. This observation along with the TEM and AFM data led us to propose the previously described synergic templating action of silica growth and TPPS assembly (*Fig III.13*). Moreover, the encapsulated nanotapes appear to be more numerous in the TEM and AFM samples compared to uncoated samples, which further confirms that the J-aggregates remain stable upon silica templated growth. AFM and TEM microscopy images showed that the aggregate morphology undergoes very little change upon mineralization, yet the average length of the encapsulated rods was slightly shorter than the pristine J-aggregates.

On the contrary, absorption spectroscopy clearly showed that encapsulation induces further aggregation with no significant pH variation. It therefore appears that $TPPS_4$ molecules are more involved into aggregates in the presence of silica shell and that aggregates are on average, shorter but more numerous. We interpret this observation by the superposition of 2 mechanisms.

Upon mineralization, native aggregates could be partially fragmented when the shell is formed but the silica shell could also prevent the extension of self assembly when the drying droplet of TEM or AFM sample artificially increases the $TPPS_4$ concentration and lowers the pH. When encapsulated, the observed samples remain as they were in the bulk solution. On the other hand J-aggregate nuclei can grow into full size aggregates in the presence of silicates in the growing shell. Indeed a synergic assembly mechanism has been proposed in the case of silica encapsulation of octapeptide nanotubes which can be similarly invoked here.[25] In the earlier work, E. Pouget et. al have investigated the bio-inspired silica mineralization process of well-characterized self-assembled peptide structures. Lanreotide, a dicationic octapeptide which self-assembles in pure water into nanotubes with a monodispersed diameter of 24.4nm and a wall thickness of 1.8 nm, and the presence of two exposed protonable amine groups per octapeptide makes the lanreotide nanotubes a potential template for silica growth. The mineralization of these precisely designed tubes is obtained by cross-diffusion of a lanreotide gel and a tetraethylorthosilicate (TEOS) solution in water within the confined volume of 1.5-mm-diameter glass capillaries.[25]

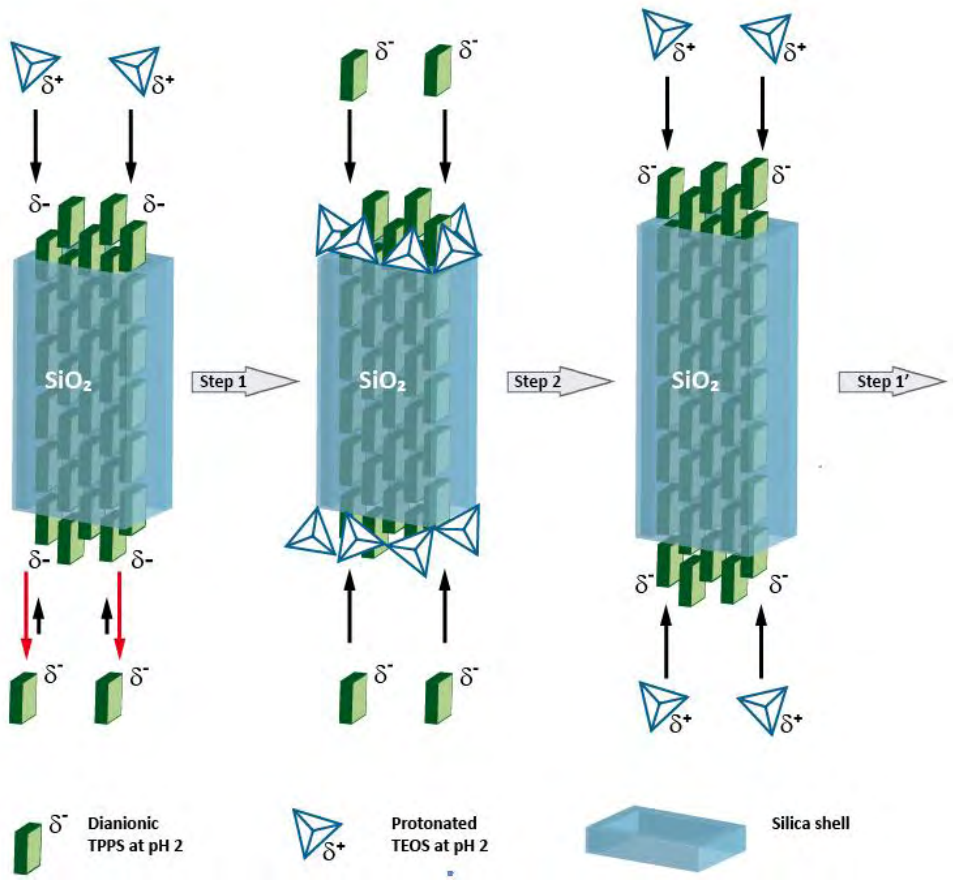

Fig III.13: *Mechanistic scheme of the silica mineralization of TPPS J-aggregates.*

At pH 2, TPPS molecules are still partially anionic, therefore the net surface charge of J-aggregates is negative. The supramolecular assembly equilibrium is limited by the competition between π–π stacking assembly and electrostatic repulsion between porphyrins. On the contrary, TEOS and APTES, the two silica precursors used in this study, are strongly protonated and cationic at pH 2. Therefore, the template effect of J-aggregate efficiently promotes the formation of the silica sheath (*Step 1 -Fig III.13*). In so doing, the negative charge of the template is partially neutralized near the mineralization area, where further TPPS recruitment for self-assembly into the J-aggregate is then favored. The mineralized J-aggregates therefore tend to lengthen as their sides are mineralized (*Step 2*).

The addition of new dianionic resumes the initial situation, in which further self-assembly is repressed but mineralization is better templated, but now on a longer encapsulated J-aggregate rod (*Step 1*').While mineralization can mechanically disrupt preformed J-aggregates, leading to shorter rods on average, the free TPPS molecules, which remain in equilibrium with the supramolecular rods, are efficiently assembled into extra aggregates. The net variation of the absorption spectrum shows an increase in aggregate formation (and a decrease in the concentration of free TPPS), while TEM and AFM evidence their shorter average length.

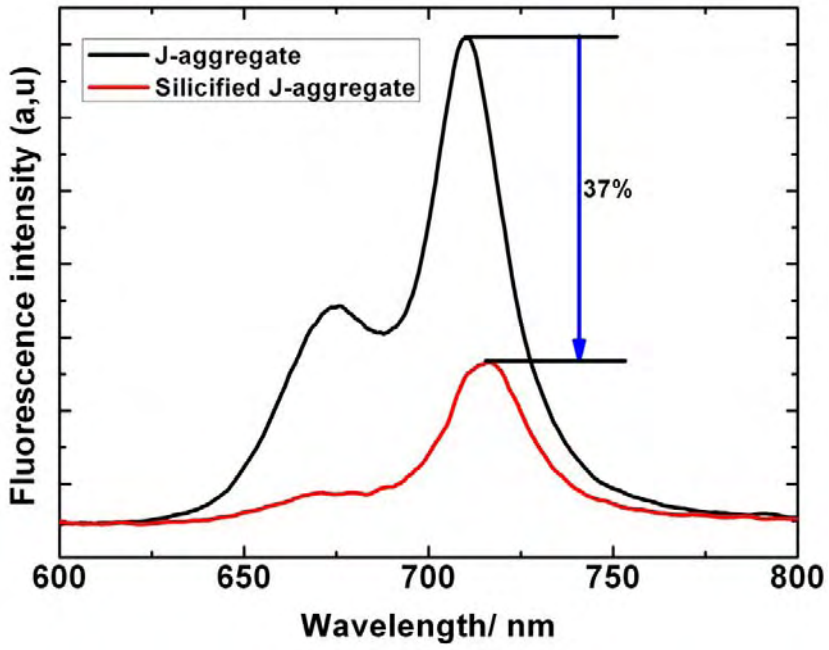

Fig III.14: *Fluorescence spectra of porphyrin J-aggregate and silicified J-aggregates (silica thickness 6.7nm).*

Fluorescence measurements of silica coated J-aggregate showed quite different behavior. The addition of silica on J-aggregates leads to a quenching of fluorescence intensity, reaching as

much as 63% reduction. The fluorescence at 720 nm reaches its minimum value (37% of max) for a silica thickness of about 6-8nm. For thicker silica sheath, there was no further change in the fluorescence (*Fig III.14*). With addition of excess silica and with increased time precipitation was observed, whereas with fewer amounts of silica and extended time no precipitation occurred and fluorescence was preserved.

It is very likely that the very first layers of loosely condensed silica framework wrapping the J-aggregates provide non-radiative paths for the excitonic state, hence reducing the fluorescence intensity. This behavior was generally overlooked in the previous approaches. Hence taking this into account we propose recovering as well enhancing the fluorescence of encapsulated J-aggregates by the conjugation of metal nanoparticles.

3.3.5. Characterization of TEOS-MPTEOS silica coated J-aggregates.

UV-Vis spectra of J-aggregates coated with TEOS-MPTEOS showed the presence of red shifted soret (434 nm) and Q (590 and 645 nm) bands but the intensity of 490nm absorption band was very weak (*Fig III.15)*. The intensity of absorption does not increase even after decreasing the pH below 2.

Fluorescence spectra monitored at λ_{exc} -434nm and λ_{exc} -490nm gave emission band at 675nm which correspond to the emission from dianion monomer and it was less intense when excited at λ_{exc} -490nm. Hence UV-Vis spectra and fluorescence spectra showed no sign of formation of J-aggregates on encapsulation with MPTEOS.

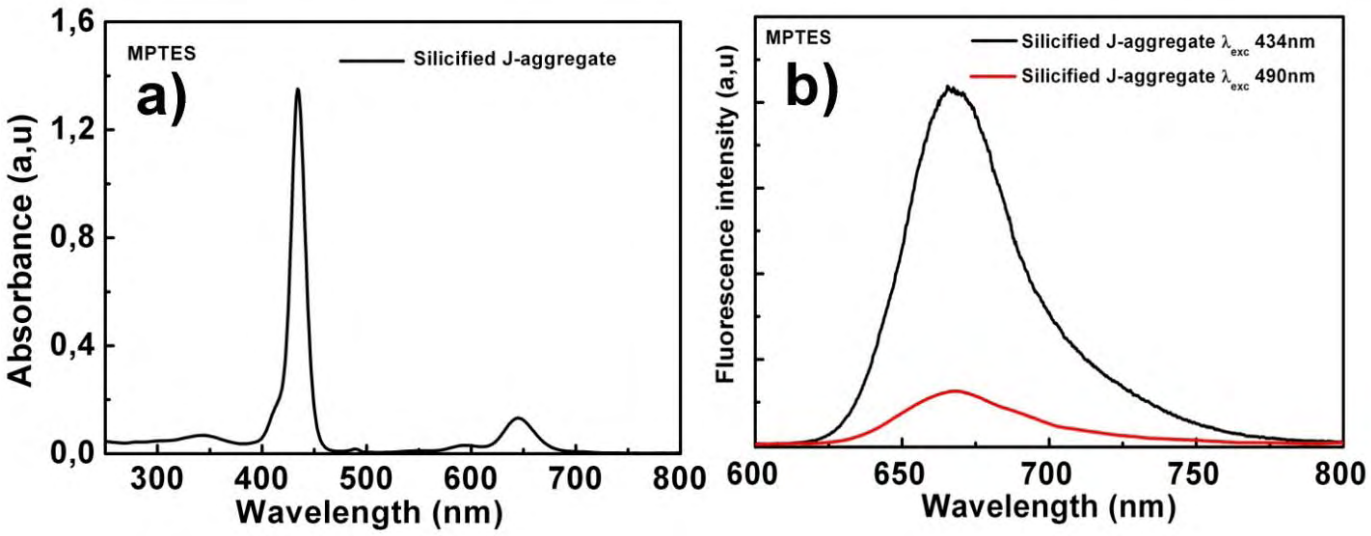

Fig III.15: *a) UV-Vis absorption spectra of TEOS-MPTEOS coated J-aggregates and b) corresponding Fluorescence spectra at λ_{exc} -434nm and λ_{exc} -490nm.*

TEM images of TEOS-MPTEOS coated J-aggregates showed large agglomerated structures with large aggregation of J-aggregates (*Fig III.16*). Tape like structures were completely transformed with the addition of MPTEOS. We still modified this protocol by using ethanol in a reaction mixture but absorption band at 490 nm was always less with the addition of MPTEOS. Although the self assembly of J-aggregates was reversible with change in the pH but once the MPTEOS was added at neutral pH, it appears that ended with the exclusive destruction of J-aggregates Hence conjugation of silica with TEOS-MPTEOS was abandoned.

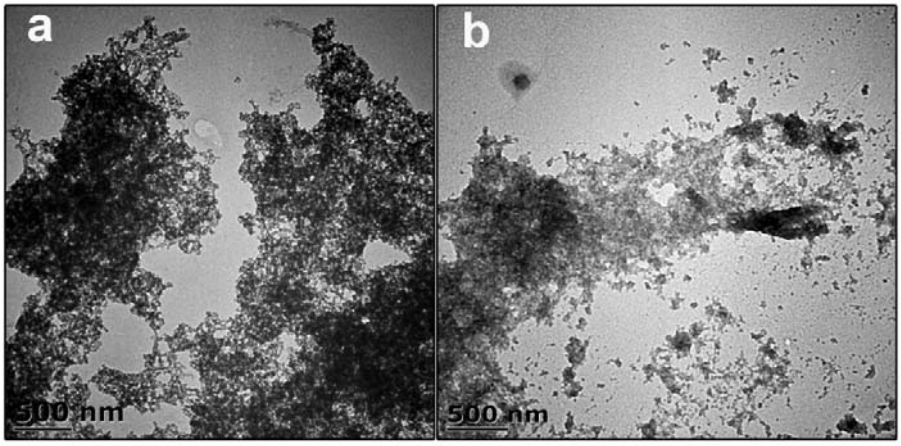

Fig III.16: *TEM images of TEOS-MPTEOS coated J-aggregates. Tapes like structures of J-aggregates were completely transformed into a large bundle like aggregates.*

Thus we managed to control the silica thickness by TEOS-and APTES (protocol-2) mixture with ~2nm accuracy over a range of 2-12nm where silica encapsulation has an adverse effect on fluorescence. In fact this approach gives unique opportunity to study dielectric/fluorophore interface which has not been investigated before. Hence in the next step our aim is to achieve metal enhanced fluorescence by the conjugation of plasmonic nanoparticles on these silicified J-aggregates at different silica thickness.

3.4. Metal Conjugation on J-aggregates and Silicified J-aggregates.

The structural and optical properties of the encapsulated J-aggregates decorated with Au and Ag nanoparticle are presented in this section. The molecular fluorescence was significantly enhanced for an optimal silica thickness while quenching regimes were observed for thinner silica coatings. However, in the beginning, we start by examining the effects of the dierect treatment of Au and Ag nanoparticles to uncoated J-aggregates.

3.4.1. Metal nanoparticle decoration on J-aggregates.

The synthesis and characterization of Au and Ag nanoparticles were discussed in the section 2.1.4. The average size of the nanoparticles of Au and Ag nanoparticles were in the range of 12 ± 2 nm and 10-50 nm respectively. Freshly prepared samples of nanoparticles were treated with J-aggregates and silica encapsulated J-aggregates were characterized by UV-Visible spectroscopy and fluorescence spectroscopy followed by TEM and SEM analysis.

Protocol: About 30μL of freshly prepared nanoparticle solution were added to 1mL of J-aggregates and the solution was subjected to slow stirring for 30 min. The solution was then left undisturbed for 24 hour and finally it was characterized through UV-Vis and fluorescence spectroscopy. The same procedure was followed with silica encapsulated J-aggregates samples of different silica thickness.

The TEM analysis revealed that the tape like morphology of J-aggregates was well conserved presence of metallic nanoparticles (*Fig III.17*). Overall, adding metallic nanoparticles to uncoated J-aggregates left very few intact rods. This apparent disassembly probably contributes to the reduction of the J-aggregate fluorescence (*Fig III.17b*).

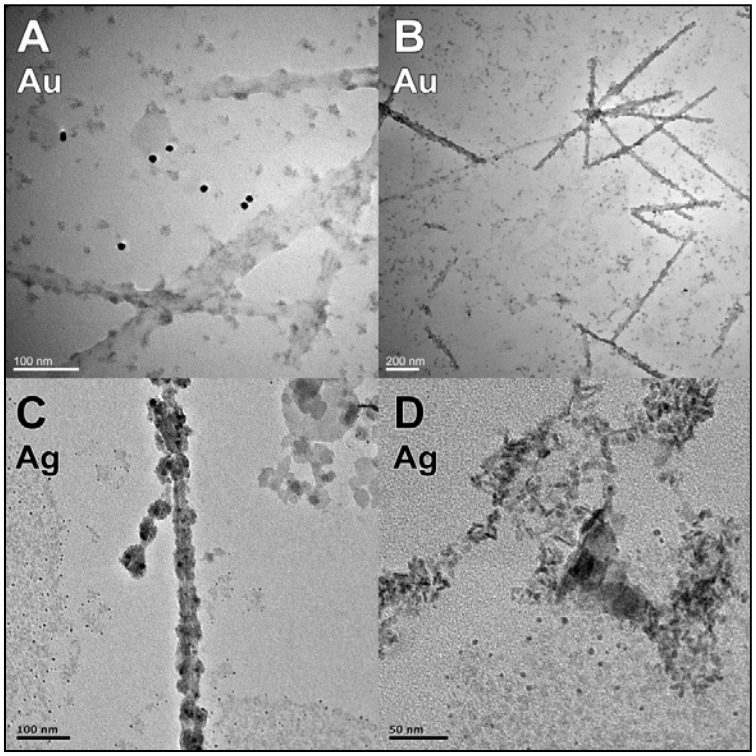

Fig III.17: *TEM images of uncoated J-aggregates in the presence of (A, B) Au and (C, D) Ag nanoparticles.*

However, this cannot be the only mechanism, since the absorption band of J-aggregates increased. Hence, we proposed mechanism of TPPS aggregate reorganization. Indeed, besides disrupted rods, metallic nanoparticles were surrounded by a shell of organic matter. This suggests that the metallic nanoparticles template the TPPS assembly into J-aggregates on their surface with a strong efficiency .This shifts the J-aggregates in favor of particle attached aggregated shells.

The UV-Vis and fluorescent spectra of Au nanoparticle and Ag nanoparticle treated J-aggregates are given in the *Fig III.18.* Upon addition of the metallic nanoparticles, the intensity of the 434 nm Soret absorption band of the monomer decreases as the 490 nm peak increases, indicating further depletion of the free TPPS in solution and a reinforcement of the J-aggregate assembly (*Fig III.18a*). The direct coupling of metallic nanoparticles to the uncoated J-aggregates results in a complex reorganization of the fluorophores. The metallic nanoparticles template the assembly of the free TPPS molecules as well as molecules originating from the pre-formed J-aggregates, which are destroyed, into small surface-bound J-aggregates. The net amount of TPPS molecule engaged in a J-aggregate structure increases. Plasmon-driven field enhancement cannot account for these observations since the 600-750 nm region of the absorption spectrum shows the same trend. Therefore, the variation in the UV-visible spectrum strongly suggests that a net increase of the J-aggregate assembly occurs in the presence of the metallic nanoparticle rather than apparent disassembly seen in TEM.

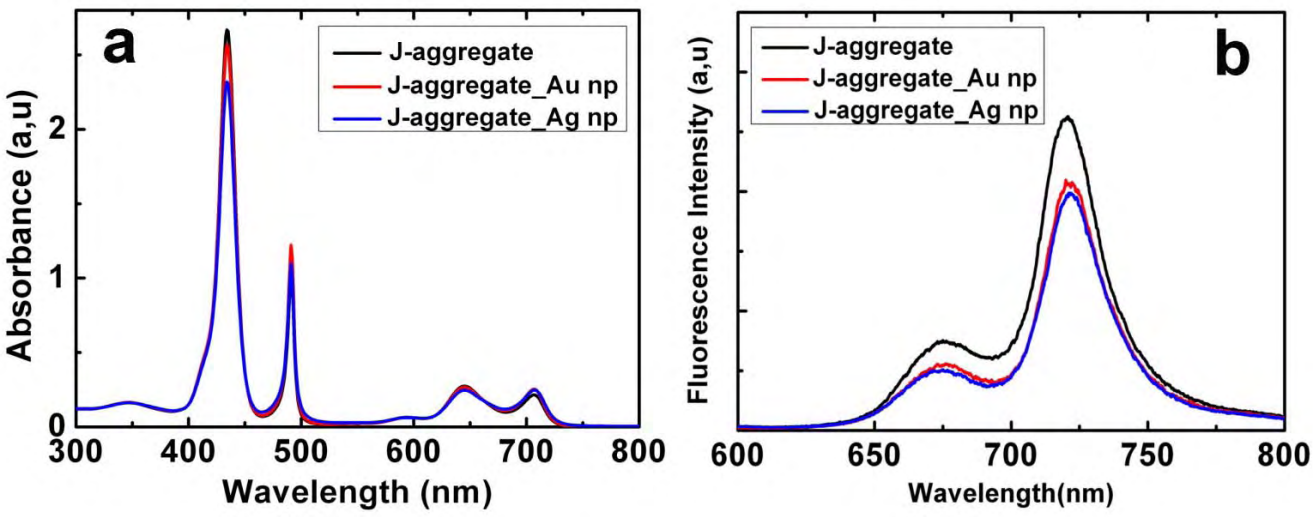

Fig III.18: *a) UV-Vis spectra and b) fluorescence spectra of metal nanoparticle treated J-aggregates and silicified J-aggregates.* λ_{exc} *490nm.*

Although the absorbance and amounts of J-aggregates increases, the observed fluorescence decreases (*Fig III.18b*) by a factor of 20% in the presence of either metal. If assume our previous description of the TPPS reorganization, most J-aggregates lie near the metal surface where plasmon related non radiative excitation paths are open in the near field results in fluorescence quenching. Hence metallic nanoparticles template the assembly of the free TPPS molecules as well as molecules originating from the pre-formed J-aggregates, which are destroyed, into small surface-bound J-aggregates. The net amount of TPPS molecule engaged in a J-aggregate structure increases. Yet, the conversion from self-standing J-aggregates to particle-adsorbed J-aggregates also accounts for the TEM observations and fluorescence measurements. Indeed, the nanoparticle-templated J-aggregates are in the direct vicinity of the plasmonic metallic surfaces, which therefore suppress the fluorescence by non-radiative dissipation. Hence the fluorescence loss results both from the partial disassembly of the original J-aggregates observed in TEM and by the non-radiative quenching of particle-bound aggregates due to the close proximity of the plasmonic material. Therefore silica coating of J-aggregates appears to be an essential step in order to ensure an optimal exciton-plasmon coupling. It also serves as template for binding Au or Ag nanoparticles onto the surface using electrostatic interaction as described here after.

3.4.2. Metal nanoparticle decoration of silicified J-aggregates.

The structural and optical properties of the encapsulated J-aggregates decorated with Au and Ag nanoparticle are presented hereafter. Molecular fluorescence was significantly enhanced for an optimal silica thickness, while quenching and decoupled regimes were observed for thinner and thicker silica coatings respectively. The grafting of the metallic nanoparticles to the silica shell is evidenced by TEM (*Fig III.19* and *Fig III.21*), SEM (*Fig III.21*) and EDXA (*Fig III.20*).

TEM images showed that all Au or Ag metallic nanoparticles were systematically attached to silica shells and the encapsulated aggregate coverage could be varied by adjusting the nanoparticle: aggregate ratio. Interestingly, no morphological change of the encapsulated aggregates was observed upon attachment of the nanoparticles.

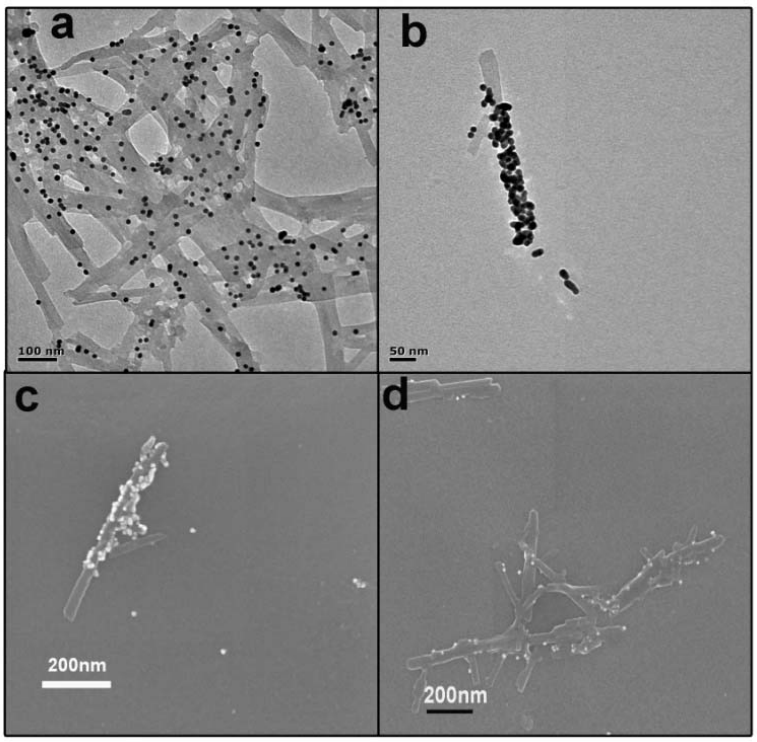

***Fig III.19**: a), b) TEM and c, d) SEM micrographs of silica-encapsulated J-aggregates decorated with Au nanoparticles.*

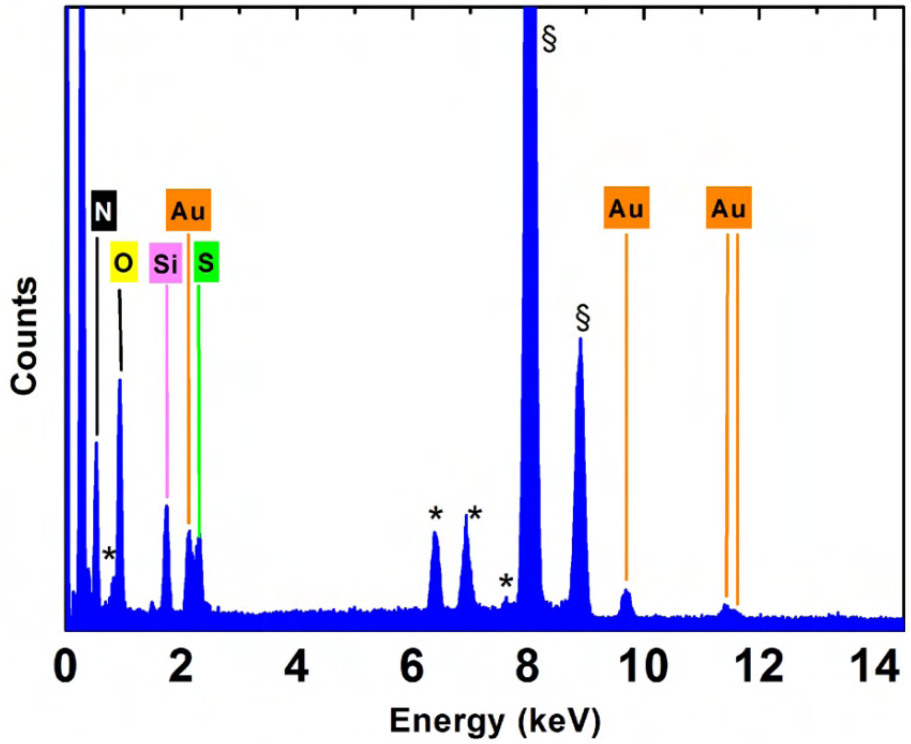

***Fig III.20** EDXA spectrum of Au-decorated silica-encapsulated J-aggregates showing the presence of Au (nanoparticles), Si and O (silica), S and N (TPPS molecule). The symbol (*) indicates the Fe and Co peaks due to the sample holder and the symbol (§) indicate the Cu peaks due to the grid.*

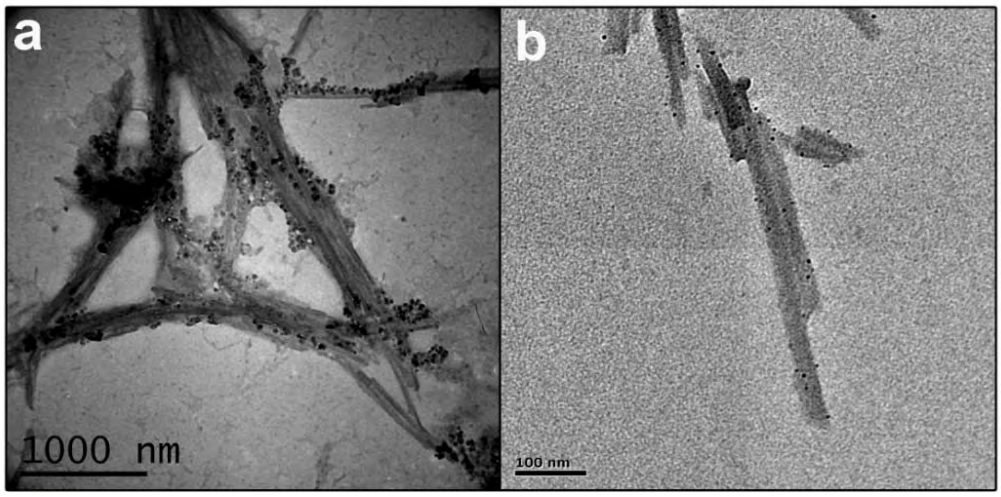

Fig III.21*: TEM micrographs of silica-encapsulated J-aggregates decorated with Ag nanoparticles.*

The absorption spectrum of J-aggregates was almost unaffected by the attachment of metallic nanoparticle. In particular, the intensity of the 490 nm and 434 nm bands were unchanged, irrespective of the amount of nanoparticles. The attachment of freshly prepared Au or Ag nanoparticles on the outer surface of the silica coating significantly modifies the emission intensity of the encapsulated J-aggregates (*Fig III.22* and *Fig III.23*).

Fig II.22 shows the normalised fluorescence intensity of silicified j-aggregates at different silica thickness conjugated with freshly prepared Au and Ag nanoparticles as well as aged Ag nanoparticles. For a silica thickness thinner than 6.7 nm, one observes a further quenching of the fluorescence, (*Fig III.22 Ib, IIb*) which tends to vanish as the silica thickness increases. When the silica thickness reached 9.0nm (*Fig III.22Id, IId*) the fluorescence signal in presence of Au and Ag nanoparticles was increased and with further increase in the thickness very less modulation in the intensity of fluorescence was observed. Since the only parameter that changed was the placement of nanoparticles on the silicified J-aggregate surface, one can consider this observation as a strong indication of MEF.

Interestingly, in the case of aged (naturally oxidized) Ag nanoparticles as illustrated in the *Fig III.22 III*, the quenching observed in the absence of silica sheath was immediately transformed into a strong enhancement (*Fig II.22 IIIa*) of the fluorescence for a silica thickness of 2.2 nm. With further increase in the silica thickness and with the conjugation of aged silver nanoparticle fewer enhancements in the intensity was observed which show no change in the intensity at thicker silica coating.

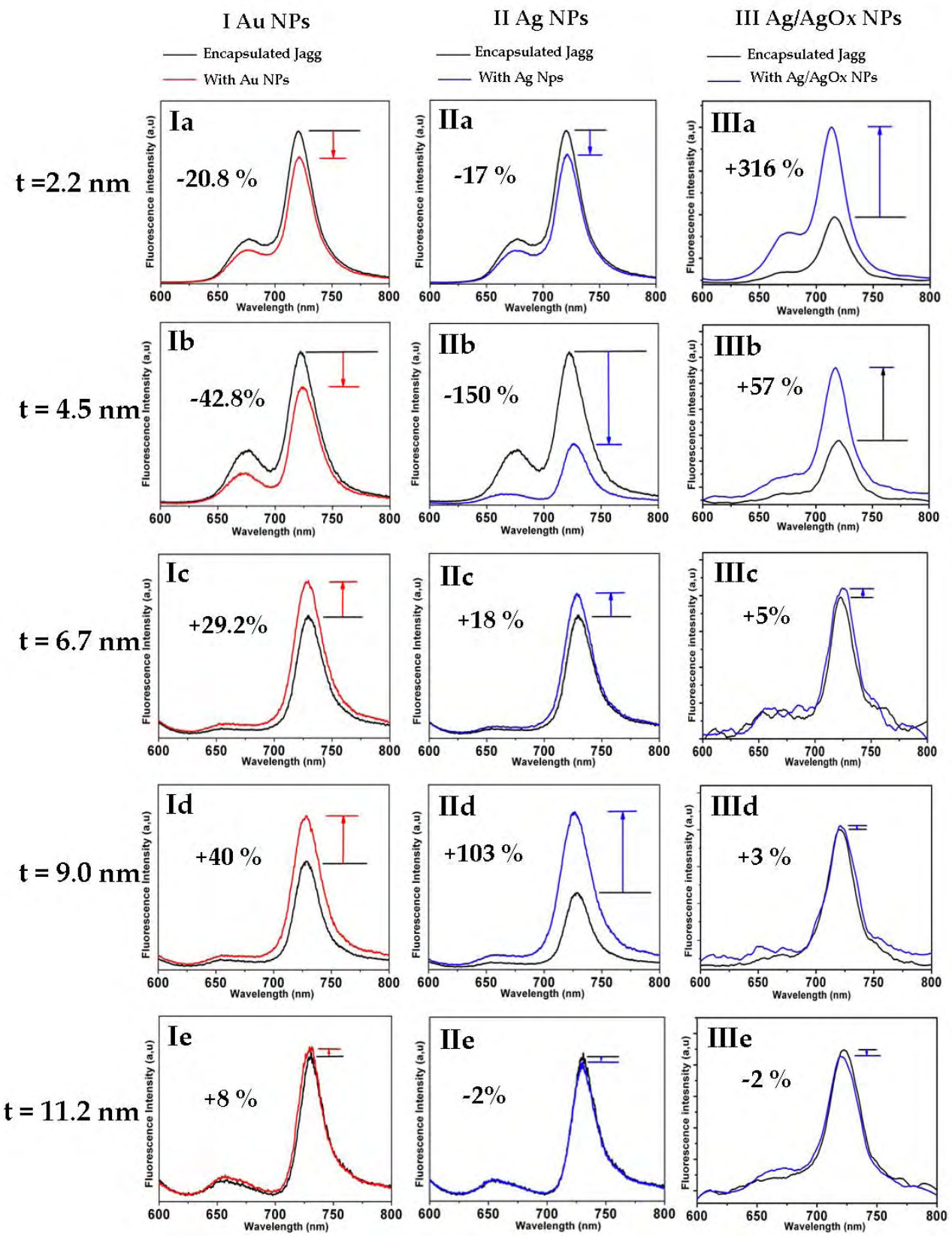

***Fig III.22**: Dependency of the J-aggregate fluorescence intensity on the thickness of the silica sheath in the absence (black squares) of attached metal nanoparticles or with tethered Au (red triangles) or freshly prepared Ag (blue) nanoparticles and aged Ag nanoparticles. Fluorescence intensity at different silica thickness is normalised.*

These observations suggested that thin silica coating combined with AgO_x shell on the aged Ag nanoparticles, constitute a dielectric spacer of effective local index 1.5,[26] which shifts the optimal silica sheath thickness for enhanced fluorescence. For silica thickness beyond 4.7 nm, the additions of Ag nanoparticle do not modify the fluorescence of the encapsulated J-aggregates. *FigIII.23a* shows the corresponding spectra where the uniform enhancement of the J-aggregate fluorescence by fresh non-oxidized Au and Ag nanoparticles to 40% and 103% respectively (red and blue spectra compared to the black spectra of encapsulated J-aggregates). Very efficient fluorescence enhancement was also illustrated in the spectra of *Fig III.23b* with the conjugation of oxidized silver nanoparticles.

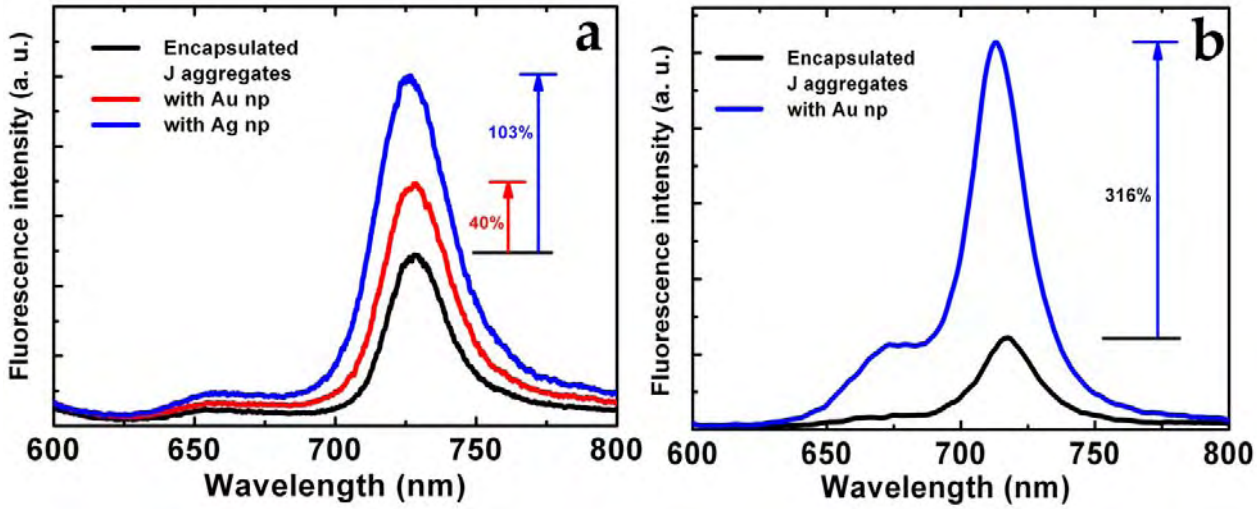

FigIII.23*: a) Fluorescence spectra of J-aggregates encapsulated in silica (black curves) and spectra showing enhanced emission in the presence of attached Au (red curve) or Ag (blue curves) nanoparticles. Here experiments performed with freshly prepared non oxidized nanoparticles at 9.0-nm thick silica shell. b) Fluorescence spectra of J-aggregates encapsulated in silica plots correspond to experiments with oxidized Ag colloids and 2.2-nm silica shell.*

Since the 490 nm Soret band of the J aggregates used to excite the fluorescence is narrow, its spectral overlap with the silver and gold surface plasmon was similar. Yet, the Ag plasmon in nanoparticle was more intense than the resonance in the Au colloids, therefore the local electromagnetic field at 490 nm was more enhanced by the Ag nanoparticles and resulted in more efficient population of the excited state. The optimal enhancement reaches 316% for a much thinner silica shell thickness (2.2 nm) combined with naturally oxidized silver particles (*Fig II.23b*).

Finally one can notice that the emission spectra in *Fig II.23a* and *b* were slightly shifted. We consider that the gradual increase of the silica shell thickness induces a red-shift of the

emission line as illustrated by the two black spectra for silica thickness of 2.2 and 9.0 nm in *Fig II.22*. We correlate this spectral red-shift to the recent observation that mineralization of J aggregates can result in the intercalation of thin inorganic sheets in between TPPS stacks,[27] therefore reducing the molecular overlap in the aggregate, which reduces the energy level of the emitting excitonic state.

3.5. Conclusion and perspective.

In conclusion, in this work, we have shown that templated encapsulation can be controlled in the very thin shell regime (1-10 nm), very good averaged accuracy of ± 2nm i.e. the equivalent of 1-2silicate layer. This has allowed us to probe the strong coupling regime between encapsulated J aggregates and plasmonic nanoparticles. We have observed the three expected regimes of fluorescence quenching, enhancement as well as decoupling.[31]

In our dye-centered system, the metal-enhanced fluorescence could be optimized to exceed 300%. The encapsulation of fluorescence nanoparticle or supramolecular aggregates inside a silica shell presents several advantages in terms of mechanical and optical stability as well as biocompatibility, which are of high relevance for biosensing applications. We think that such bottom-up templated constructions could contribute to the design of optical probes for sensing and imaging application but also to the efficient integration of molecular absorbers and emitters into plasmonic devices for optical information processing, which require a fine tuning of the strong coupling regime between fluorophores and metallic nanostructures.

References:

(1) L.R.Milgrom *Oxford University Press* **1997**.

(2) Pasternack, R. F.; Fleming, C.; Herring, S.; Collings, P. J.; dePaula, J.; DeCastro, G.; Gibbs, E. J. *Biophysical Journal* **2000**, *79*, 550-560.

(3) JELLEY, E. E. *Nature* **1936**, *138*, 1009-1010.

(4) Wang, Y. *Chemical Physics Letters* **1986**, *126*, 209-214.

(5) *The Porphyrins*; White , W. I., Ed.; D. Dolphin (Ed.), 1978.

(6) Micali, N.; Mallamace, F.; Romeo, A.; Purrello, R.; Scolaro, L. M. *Journal of Physical Chemistry B* **2000**, *104*, 5897-5904.

(7) Kitahama, Y.; Kimura, Y.; Takazawa, K. *Langmuir* **2006**, *22*, 7600-7604.

(8) Akins, D. L.; Zhu, H. R.; Guo, C. *Journal of Physical Chemistry* **1994**, *98*, 3612-3618.

(9) Akins, D. L.; Zhu, H. R.; Guo, C. *Journal of Physical Chemistry* **1996**, *100*, 5420-5425.

(10) Snitka, V.; Rackaitis, M.; Rodaite, R. *Sensors and Actuators B-Chemical* **2005**, *109*, 159-166.

(11) Ribo, J. M.; Crusats, J.; Farrera, J. A.; Valero, M. L. *Journal of the Chemical Society-Chemical Communications* **1994**, 681-682.

(12) Ohno, O.; Kaizu, Y.; Kobayashi, H. *Journal of Chemical Physics* **1993**, *99*, 4128-4139.

(13) Maiti, N. C.; Ravikanth, M.; Mazumdar, S.; Periasamy, N. *Journal of Physical Chemistry* **1995**, *99*, 17192-17197.

(14) Rubires, R.; Crusats, J.; El-Hachemi, Z.; Jaramillo, T.; Lopez, M.; Valls, E.; Farrera, J. A.; Ribo, J. M. *New Journal of Chemistry* **1999**, *23*, 189-198.

(15) Maiti, N. C.; Mazumdar, S.; Periasamy, N. *Journal of Physical Chemistry B* **1998**, *102*, 1528-1538.

(16) Rotomskis, R.; Augulis, R.; Snitka, V.; Valiokas, R.; Liedberg, B. *Journal of Physical Chemistry B* **2004**, *108*, 2833-2838.

(17) Hollingsworth, J. V.; Richard, A. J.; Vicente, M. G. H.; Russo, P. S. *Biomacromolecules* **2011**, *13*, 60-72.

(18) Gandini, S. C. M.; Gelamo, E. L.; Itri, R.; Tabak, M. *Biophysical Journal* **2003**, *85*, 1259-1268.

(19) Meadows, P. J.; Dujardin, E.; Hall, S. R.; Mann, S. *Chemical Communications* **2005**, 3688-3690.

(20) Royston, E.; Lee, S. Y.; Culver, J. N.; Harris, M. T. *Journal of Colloid and Interface Science* **2006**, *298*, 706-712.

(21) Fowler, C. E.; Shenton, W.; Stubbs, G.; Mann, S. *Advanced Materials* **2001**, *13*, 1266-1269.

(22) Pena-Alonso, R.; Rubio, F.; Rubio, J.; Oteo, J. L. *Journal of Materials Science* **2007**, *42*, 595-603.

(23) Jiang, H.; Zheng, Z.; Wang, X. *Vibrational Spectroscopy* **2008**, *46*, 1-7.

(24) Scott, A. F.; Gray-Munro, J. E.; Shepherd, J. L. *Journal of Colloid and Interface Science* **2010**, *343*, 474-483.

(25) Pouget, E.; Dujardin, E.; Cavalier, A.; Moreac, A.; Valery, C.; Marchi-Artzner, V.; Weiss, T.; Renault, A.; Paternostre, M.; Artzner, F. *Nature Materials* **2007**, *6*, 434-439.

(26) Tominaga, J. *Journal of Physics-Condensed Matter* **2003**, *15*, R1101-R1122.

(27) Patil, A. J.; Lee, Y.-C.; Yang, J.-W.; Mann, S. *Angewandte Chemie-International Edition* **2012**, *51*, 733-737.

CHAPITRE 4
PLATE-FORME DE PROTEINE ARTIFICIELLE

Résumé

Dans ce chapitre, nous introduisons le concept de protéines artificielles, une famille spécifique parmi elles sera exploitée dans les chapitres 5 et 6, pour l'auto-assemblage et la morphosynthèse de nanoparticules. Nous commençons par un aperçu détaillé des structures, des fonctions et de l'évolution des protéines artificielles. Différents types d'échafaudages protéiques sont décrits suivis par la présentation de la famille particulière des protéines à motifs répétés depuis leur origine jusqu'à leurs fonctions pour lesquelles elles sont utilisées en biologie. Nous détaillons les caractéristiques structurelles des protéines motif répétés spécifiques, notées αRep, qui ont été synthétisées par nos collaborateurs de l'IBBMC (Orsay) puisqu'elles pourraient relever certains défis actuels en sciences des nanomatériaux.

Un échafaudage de protéines est un polypeptide avec différentes fonctions biochimiques présentant une stabilité intrinsèque de conformation. Les immunoglobulines, IgG, qui fonctionnent comme des anticorps, constituent un type naturel d'échafaudage de biomolécules

et souvent considérée comme la seule option disponible quand une protéine de liaison spécifique est nécessaire[7]. Toutefois, la mise en place de sites de liaison est devenue possible dans d'autres types de protéines non liées aux anticorps[8, 9]. Ces échafaudages protéiques apparaissent comme très diversifiés quant à leur taille, leur topologie, leur mode d'interaction et de leur application[8].

Les échafaudages de quelques protéines connues sont généralement classés en fonction de leur structure et des stratégies utilisées pour l'ingénierie de leur site de liaison (tableau IV.1). Il existe environ 50 échafaudages de protéines dans la littérature qui ont été intensément commentés ces dernières années[11, 12]. Les échafaudages protéiques avec une structure de type immunoglobuline avec des *boucles* aléatoires peuvent être comparés aux échafaudages avec une structure compacte avec une *surface plane* aléatoire ou des échafaudages qui possèdent une *cavité* aléatoire. Dans ce chapitre, nous décrivons essentiellement les échafaudages utilisés avec succès pour leurs applications thérapeutiques, notamment les affibody, adnectin, anticalins et protéines à motifs répétés. Notre objectif est d'étendre ces échafaudages à l'interaction avec des surfaces inorganiques et aux applications en science des matériaux.

La conception d'échafaudages protéiques est expliquée dans la section 4.2.6. Ce processus comporte trois étapes: la diversification, la sélection et l'amplification. Dans la première étape, la protéine est choisie dans la base de données de protéines et de séquences d'acides aminés. Elle est comparée à des petits domaines fonctionnels et uniques d'acides aminés qui se trouvent dans des organismes vivants. Un segment de séquence particulier qui correspond au motif répété est identifié. Dans la deuxième étape, l'alignement précis de la séquence d'acides aminés est effectué pour générer une "séquence consensus". La séquence consensus se réfère à un ordre des acides aminés dans un polypeptide ou une protéine donnée. La séquence consensus qui possède les résidus (acides aminés) est essentiellement conservée ou diversifiée dans l'espèce. La séquence consensus devrait donc conduire à une «idéalisation» des protéines. En bref, il y a deux principaux avantages à utiliser la méthode de conception-consensus. Tout d'abord, une conception correcte de consensus a un effet marqué sur la stabilité de la protéine[34]. Deuxièmement la conception-consensus mène à des protéines compatibles, permettant un ajout, la suppression et l'échange d'acides aminés dans leur séquence. En outre, la construction de la séquence consensus peut aider à identifier les principales caractéristiques de l'architecture des protéines, ce qui est important pour l'ingénierie ultérieure. Dans la dernière étape, à l'aide, une bibliothèque appropriée est créée par variation combinatoire des positions variables de la séquence consensus puis la synthèse et la purification de la protéine est entreprise lieu.

Chapitre 4 Résumé

Parmi les différents échafaudages protéiniques possibles, nos collaborateurs se sont particulièrement intéressé à celui des protéines à motifs répété qui forme des architectures 3D robustes. En général, une protéine à motif répété est composée de la répétition de séquences variables couplées à un motif structurel constant, l'ensemble – appelé domaine - comprenant 20 à 40 acides aminés. Ces répétitions sont susceptibles de se produire lors d'un processus d'évolution et des événements de recombinaison. Un domaine est répété pour former la partie caractéristique de la protéine qui est complétée par les structures périphériques (N-cap, C-cap,…). Ces motifs sont repérables par la répétition multiple du domaine et tiennent leur fonction autant de leur séquence que du nombre de domaine répétés et du type de repliement du domaine. Les protéines à motif répété sont subdivisées en classe selon le type de repliement du domaine (hélice1/hélice2, hélice1/helice2/b-sheet, helice1/helice2/b-hairpin,...). Les principales classes sont les protéines à peptide Tetratrico répétés (TPR), les protéines à répétitions riches en leucine (LRR), les ankyrines et les protéines HEAT. En général, chaque protéine à motif répété est composée de la répétition de séquences variables couplées à un motif structurel constant, l'ensemble comprenant 20 à 40 acides aminés. Ces répétitions sont susceptibles de se produire lors d'un processus d'évolution et des événements de recombinaison. Une classe importante de protéines à motif répété comprend les protéines à répétitions Tetratrico (TPR), les répétitions riches en leucine (LRR), les ankyrines et les protéines HEAT.

La synthèse des protéines à motif alpha-hélicoïdaux répétés (α Rep) est décrite dans la section 4.1. Nos collaborateurs de l'IBBMC (Orsay) ont choisi le sous-type spécifique des protéines HEAT pour leur grande stabilité thermique et une nouvelle bibliothèque de protéines a été créée à partir de la séquence consensus modifiée.[64] Mth187*, une protéine naturelle de fonction inconnue,[21] issue de Methanobacterium thermoautotrophicum a été prise comme point de départ pour l'alignement. Cette structure a un domaine C-cap* disponible, mais étant donné que l'extrémité N-cap* n'est pas pliée, une nouvelle l'extrémité N-cap a été conçue. Après la construction de la bibliothèque, la stabilité et l'expression satisfaisante des protéines ont pu être démontrées pour des séquences directement issues de la bibliothèque, sans sélection, et pour un nombre variable de motif répété. Les bibliothèques de protéines αRep possédant des surfaces d'interactiosn de séquence variable ont été produites en faisant varier le nombre de modules entre les extrémités N et C-caps, et, dans chaque module, les 6 positions 18, 19, 22, 23, 26 et 30 - qui sont les plus variables dans la base de données des protéines naturelles – sont choisies au hasard. Parmi les différentes protéines synthétisées qui

diffèrent par le nombre de modules et par leur séquence, nos collaborateurs ont pu cristalliser une protéine α-Rep-N4 et sa structure a été résolue à plus de 2 Å de résolution (figure IV.8). Cette protéine possède quatre module répété et la structure cristalline montre que αRep-N4 est associée sous forme de dimère. Chaque monomère est plié en une succession de paires d'hélices α empilées les unes sur les autres (figure IV.8a). La succession de répétitions forme une super-hélice droite et aplatie. Les structures des répétitions internes sont pratiquement identiques, à l'exception des chaînes latérales variables. Deux conformations différentes (celle obtenue sans et celle avec un PEG lié qui a été utilisé comme agent de précipitation dans la cristallisation) indique une certaine souplesse dans l'échafaudage et à l'interface entre les monomères. La face convexe est une hélice 1 de motifs répétés et la face concave de la protéine est constituée par la succession des surfaces externes des hélices 2. Les chaînes latérales variables sont groupées et créent une surface continue située sur la face concave de la protéine (figure IV.8b) ce qui montre l'environnement chimique variable sur la surface de la protéine.

Les protéines α-Rep produites dans E. Coli par un ensemble de clones contenant 1 à 6 répétitions internes ont été purifiées et caractérisées. Ces protéines sont exprimées de manière très efficace et sont très solubles. Nous avons purifié les protéines possédant 9, 10 et 11 modules de répétition dans leur séquence en utilisant un protocole standard de biologie et l'analyse chromatographique par exclusion de taille. Les spectres en dichroïsme circulaire en UV lointain (CD) (figure IV.9) indiquent que ces protéines sont repliées avec une grande fraction d'hélices alpha, comme attendu[64]. La calorimétrie différentielle à balayage (DSC) (figure IV.9) et les expériences thermiques de dépliement indiquent que ces protéines sont repliées en collaboration, et sont extrêmement résistantes à la dénaturation[64]. La stabilité augmente avec le nombre de modules ce qui suggère que chaque répétition contribue à la stabilité de l'ensemble[64].

En général, l'affinité des protéines artificielles a été démontrée pour des objectifs différents, allant des composés de faible poids moléculaire aux grosses protéines puisque leurs affinités et leurs spécificités peuvent être atteintes de façon comparable à celles des molécules de liaison naturelles. Par conséquent les protéines artificielles sont peu à peu entrées dans des domaines d'applications des anticorps classiques et sont actuellement en cours d'évaluation. À cet égard, nous proposons dans cette thèse que l'utilisation de protéines artificielles peut être étendue à la chimie des matériaux, où elle peut également être utilisée comme un modèle stable pour la synthèse de nanomatériaux inorganiques.

CHAPTER 4

ARTIFICIAL PROTEIN PLATFORM

4.1. Engineering of novel binding proteins.

The appeal of proteins as templates for nanoparticle growth or as self-assembly agents has been introduced in this chapter 1. Recent works have illustrated the strategies to engineer natural proteins to match the needs of non-biological approaches, yet these approaches remain tedious and difficult to generalize. In this chapter, we introduce the concept of artificial proteins, a specific family of which will be exploited for the first time, in chapters 5 and 6, for the morphosynthesis and self assembly of nanoparticles. We start with a detailed overview on the structures, functions and evolution of artificial proteins. Different types of protein scaffolds are described followed by the description of a particular family of repeat proteins from their origin to their functions, for which they are being used in biology. We detail their structural features which could address some current challenges in nanomaterials sciences. Finally we elaborate on the construction of these repeat proteins.

* Terms are explained briefly in symbols and abbreviations.

The rational modification of natural proteins is a challenging aspect but in current decade it is possible to create new proteins and improve or even select their properties by experimentally mimicking natural evolution under a chosen selection procedure. These novel directed evolution techniques initially developed within a biological context can be applied to the selection of new biomolecules with optimized properties.[1] In this context the discovery of robust proteins with a partially variable amino acids sequence is a major breakthrough leading to large designable protein libraries. A protein library contains billions of molecules consisting of common underlying constant scaffold and randomized variable regions that differ from one to another. Because of this enormous variety, achieved by either rational or combinatorial protein engineering, it is possible to isolate library members binding specifically to any new target which is fit for a specific task.

Generally these library frameworks are used to produce new proteins having affinity for natural proteins or other ligands in biological conditions.These selected binding reagents may become valuable candidates to be used in a wide range of biotechnological and biomedical applications, e.g., affinity purification,[2] bioimaging,[3] enzyme inhibition,[4] and potential targeted drug delivery.[5, 6] We propose to apply similar approach but for materials targets. Since these artificial proteins show stable and well-structured spatial tertiary topology their variable surfaces can be selected to interact specifically with metallic, semi-conducting and polymer surfaces. Proteins selected for their affinity for an inorganic surface can be used not only as specific capping agents but also as habit modifiers during the crystal growth of these materials. Moreover we are expanding the impact of artificial proteins to non-biological self assembly applications by the production of new strongly interacting protein pairs beyond the archetypal streptavidin-biotin couple. Proteins will be selected to have high affinity ($K_{D,}$ nM range) and specificity for a chosen protein target in order to produce interacting pairs.
The term ‘artificial protein’ covers a very vast range of biomolecules which has been explored in the past few decades and here we give a brief introduction on different protein scaffolds that have been exclusively investigated for biological applications.

4.2. Protein scaffolds.

A protein scaffold is a polypeptide fold with distinct biochemical functions exhibiting an intrinsic conformational stability. Immunoglobulins, which function as antibodies, constitute a natural type of biomolecular scaffold which is utilized by the immune system of higher

organisms for effective humoral response against their toxins, virus and micro-organisms. Antibodies are often seen as the only available option when a tight binding protein of defined specificity is needed.[7] However, the introduction of binding sites of desired specificity has become feasible in other types of proteins not related to antibodies.[8, 9] These protein scaffolds are appearing to be very diverse in size, topology, mode of interaction and applicability.[8] The basic requirements for these scaffolds are, they should be relatively small, i.e. composed of a single polypeptide chain, and have a highly stable architecture.[10] In particular, high stability independent of disulfide bonds is a clear advantage.

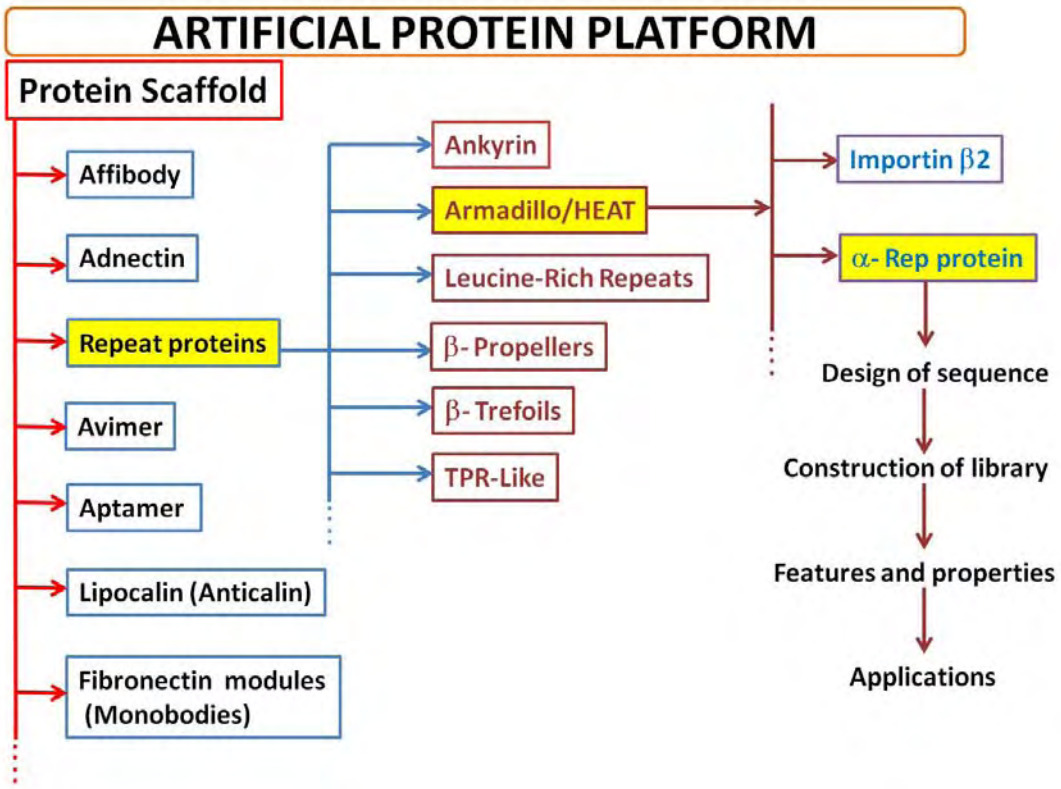

Table IV.1: *Sketch describing different non-immunoglobulin scaffolds followed by the subtype of repeat proteins scaffold.*

The few known protein scaffolds are usually classified according to their structure and strategies used for the engineering of their binding-site (*Table IV.1*). Protein scaffolds whose structures resemble that of immunoglobulin, with engineered loops, can exhibit a compact structure with flat surface or possess a large cavity structures in their topology. There are approximately 50 protein scaffolds reported in the literature which have been intensely reviewed over the last years.[11, 12] Here we describe only the most successfully used scaffolds selected for their structural importance and for therapeutic applications, namely affibody,

adnectin, anticalins and repeat proteins. The principal characteristics of the main families are reviewed below.

4.2.1. Affibodies.

Affibodies are being developed by a Swedish biotechnology company from an immunoglobulin binding domain *Staphylococcus aureus* protein A. In contrast to antibodies, affibody molecules are small, consist of 58 amino acids (6 kDa) and composed of three alpha helices without disulfide bridges *Fig IV.1a.* [13]The scaffold of affibody binding proteins is called Z domain, an engineered variant of a universal sequence found in membrane proteins (marked in red *Fig IV.1a*). Some changes are introduced at gene fragment level during the engineering process to facilitate directional head-to-tail polymerization and to increase the chemical stability of the proteins.[14, 15] Affibody molecules contain a single polypeptide subunit capable of rapid and independent folding. It lacks cysteine residues and shows a capability of high-affinity interaction with binding partner proteins via a defined set of surface-located residues (*Fig IV.1*). They can be easily expressed in soluble and proteolytically stable forms in various host cells on its own or in fusion with other protein partners.

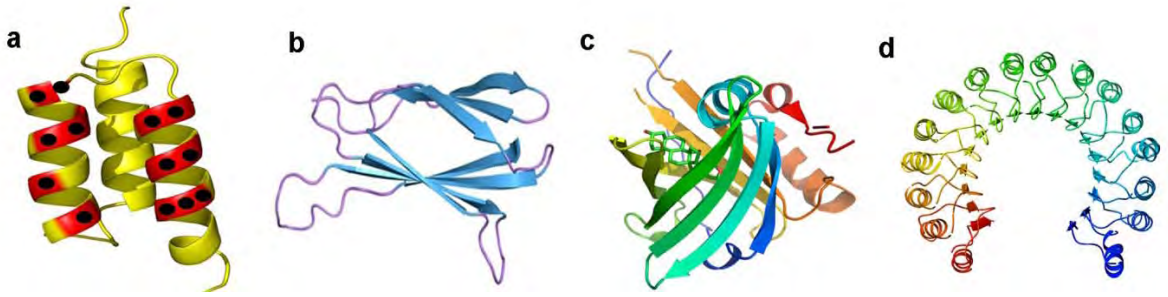

Fig IV.1: *Different protein backbones used as scaffolds for the generation of protein-binding agents,a) thee-helix bundle Affibodies b) The tenth fibronectin* type III domain classified as monobodies c) 3D structure model of an anticalins (ribbon) in complex with digitoxigenin and d) Leucine-rich repeat protein, a porcine ribonuclease inhibitor.*

Affibody molecules have been isolated for therapeutic purposes against a wide range of targets and have proven to be useful tools both for blocking protein-protein interactions and carriers in drug delivery systems.

4.2.2. Monobodies or Adnectins.

Monobodies, also known as adnectin, are genetically engineered proteins that are able to bind to antigens developed by Adnexus, a biotechnological company. Despite their name, they are

not structurally related to antibodies. Monobodies consist of 94 amino acids and have a molecular mass of about 10 kDa, fifteen times smaller than an IgG type antibody and comparable in size to a single variable domain of an antibody. They are based on the structure of human fibronectin*.This domain has a structure similar to antibody variable domains, with seven beta sheets forming a barrel and three exposed loops on each side , out of which three loops are typically directed for diversification (*Fig IV.1b*) and other three corresponds to the Complementarity Determining Regions (CDR).* They are mainly well-investigated as an alternative scaffolds for therapeutic applications such as in treatment of cancer.[16]

4.2.3. Anticalins.

Anticalins are artificial proteins that are able to bind to antigens, either to proteins or to small molecules. They are derived from human lipocalins,* which are a family of naturally binding proteins. They are mainly developed at the University of Technology Munich and currently used in place of monoclonal antibodies owing to their specific recognition with antigens. These anticalins are produced in bacterial cells like E. coli in large amounts.[17] Using phage display technology, anticalins have been generated against a wide range of different targets, from peptides to proteins. They have better tissue penetration than antibodies and are stable at temperatures up to 70°C. This scaffold consists of 180 amino acids and has a mass of about 20kDa. The characteristic of anticalins is their barrel structure formed by eight antiparallel β-strands* pair wise connected by loops and an attached α-helix * (*Fig IV.1c*).[17] They are currently used as research tools, mainly in diagnostics and therapeutic applications, including the use for targeted drug delivery.[18]

4.2.4. Repeat protein scaffold.

Repeat proteins are the scaffolds which contain successive copies of small (about 20–40 amino acid residues) structural units (repeats) that stack together to form adjacent domains. They constitute an abundant class of protein-protein interaction mediators in nature. They are highly interesting and useful scaffolds since they act as a large and standard target with interaction surfaces.[4] A unique feature of such surfaces is that they can be adapted to the target size by adjusting the number of repeats in the protein. These repeat proteins have well-defined folding topology and may contain α-helices,* β-strands,* or both. Hence in comparison with other protein scaffolds repeat proteins show strong interaction surface and

defined structural topology which have specific affinity for material interface or with biological targets and could advantageously be applied to nanomaterials science. Examples of repeats include leucine-rich repeats (LRRs),[19, 20] Ankyrin repeats (ARs),[4] armadillo/HEAT repeats[21] and tetratricopeptide repeats.[22] In a repeat domain, strong interaction between consecutive repeats results in the stable framework of the motif. The structural compatibility of the repeats within a repeat domain is achieved by conserved framework residues that mediate the essential inter-repeat interactions.

Repeat proteins appear even more interesting considering that engineering of the surface of these proteins can be done in order to obtain new synthetic proteins by conserving their structure. For example, the absence of intramolecular cysteines gives the possibility to introduce a unique cysteine for thiol-based conjugation or other chemical modifications.[23] Also repeat proteins are highly versatile binding molecules due to their modular architecture and variable molecular surfaces generated by the assembly of multiple compatible repeats. Protein repeats are discussed in detail the section 4.3.

Repeat name	SMART abbreviation	Repeats	Proteins	Examples
Leucine-rich repeat	LRR	14 722	2 035	Ribonuclease inhibitor,[24] internalins[25]
Ankyrin repeat	ANK	7 958	1 770	IUBK [26], ankyrinR[27]
Tetratricopeptide repeat	TPR	4 883	970	p67phox[28], cyclophilin[29]
Armadillo/HEAT repeat	ARM	1 542	253	L-catenin[30] importin[31]

Table IV.2: *Table summarizes a repeat proteins which are very abundant in nature.*[32]

4.2.5. Scaffold design and engineering.

With this short overview we have a general idea of the different scaffolds available. Yet in order to exploit artificial proteins, one must select a particular scaffold with the different selection technologies and proceed to the construction of library. However, it is a challenge to predict the combination of different amino acid residues which are needed to design a protein with new functionalities and with stable 3D structure. Therefore, the specific objectives involved in the creation of artificial proteins are to have a robust 3D topology, high-level recombinant expression, thermodynamic stability, resistance to aggregation and variable positions in their amino acid sequence which can be successfully modulated to bring

recognition of the proteins for arbitrarily chosen targets. There is a variety of different strategies, employed for the selection and isolation of proteins with new target affinity from a combinatorial protein library.[33] Therefore, it is very important to know how exactly the design of artificial proteins are carried out. In the coming section, we simplify different steps which are usually used for the construction of artificial proteins from a known protein scaffold.

The selection and evolution procedure can be summarized in 3 main steps: ***diversification***, ***selection*** and ***amplification*** (*Fig IV.2*). The diversification (**Step-1**) and selection (**Step-2**) mainly involves a complete statistical and mathematical analysis of amino acid sequences for the construction of new "**consensus sequence**" followed by the synthesis of a new protein library, screening for binding to a defined target molecule and amplification of selected molecules and identification of binding clones (**Step3**). The selection process is typically repeated a number of times, i.e. in cycles, to enrich the population with the molecules with desired binding properties. After selection and identification, the selected novel protein is typically being produced in an organism and characterized in more detail. Depending on the availability and inherent properties of the target protein different selection methods have evolved. The success of a selection strategy depends, to a large extent, on the diversity and quality of the constructed library.

4.2.6. Scaffold diversification and selection (Step-1 and Step-2).

The main part involved in the synthesis of artificial protein is the construction of a consensus sequence. Consensus sequence refers to an order of amino acids in a given polypeptide or protein. The consensus sequence shows which residues (amino acids) are mostly conserved or diversed across the species. It is very difficult to obtain a consensus sequence, which is constructed without taking help of any existing protein and when they are assembled together such proteins rarely produce stable proteins. Hence the design of a protein can be done by taking help of defined consensus sequence from a specific protein of interest selected from particular source based on a protein family. Consensus sequence should hence lead to an 'idealized' protein. Briefly, there are two main advantages in using consensus design method. Firstly, a proper consensus design has a marked effect on the stability of the protein [34]. Secondly consensus design makes proteins, compatible, allowing addition, deletion, and exchange of amino acids in their sequence. Furthermore, the design of full-consensus sequence in proteins can help to unravel principal features of the protein architecture, which is important for subsequent engineering. As mentioned, before the construction of consensus

sequence is performed by taking help of an existing sequence from a particular source. Similar to the crystallographic database there are several protein database, which contains specific information on amino acid sequence. For example, the Domain data base (SMART[35]*, Pfam[36]*) contains information on small amino acid sequences (domains) which has a specific function like recognition, signaling of the molecule. Whereas non redundant (nr) protein database* contains information on unique amino acid sequences of a particular protein in different organisms. Protein Data Bank (PDB)* database is another kind which stores all the structural information of proteins and nucleic acids.

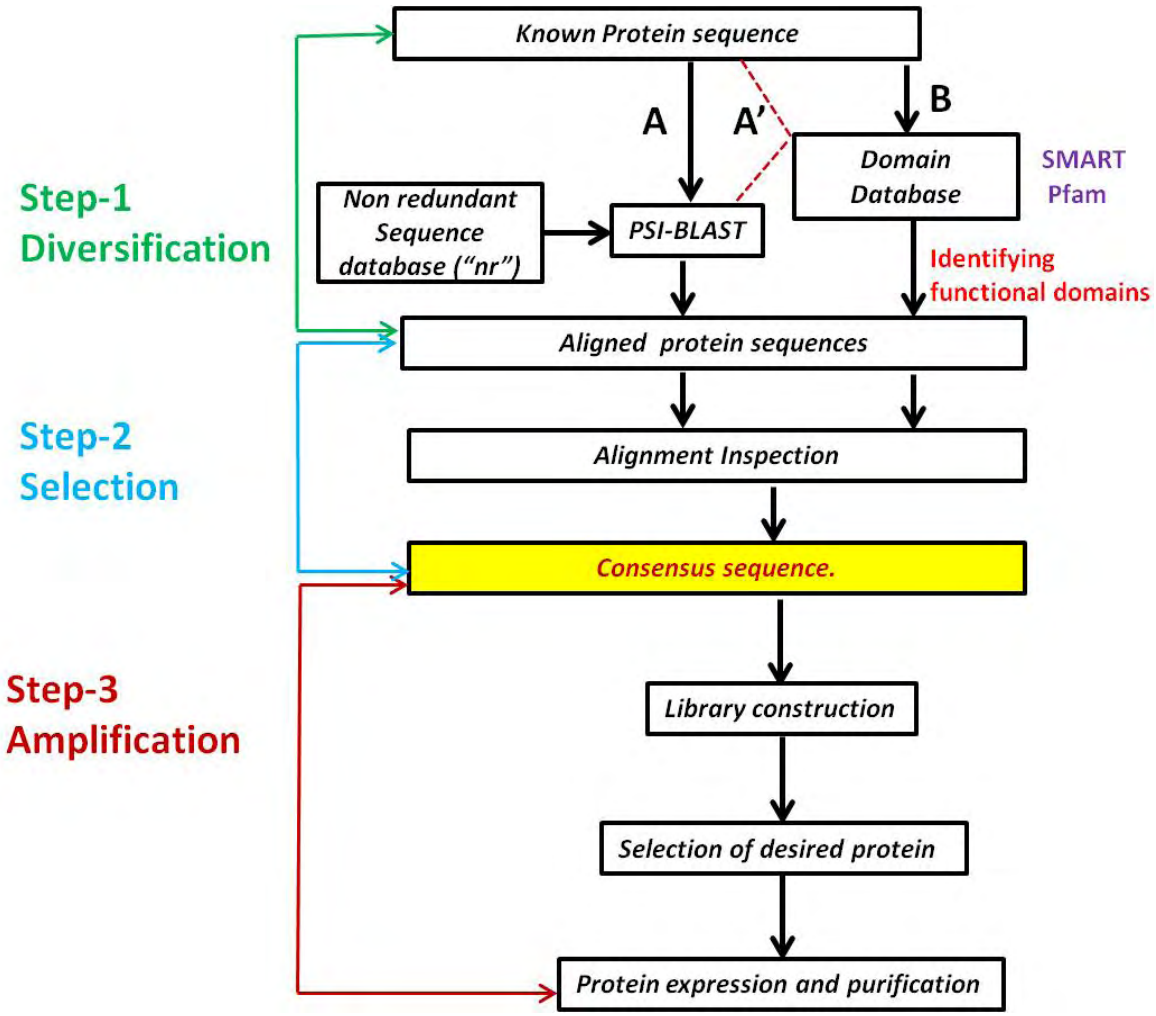

Fig IV.2: *A flowchart illustrating the protocols employed for synthesis of artificial protein. It involves mainly 3 steps. In the first two steps, statistical analysis of known protein sequence with the database is carried and consensus sequence is created. In the third step construction of the protein is performed with a design of library followed by the selection and purification of desired proteins.*

---

* Terms are explained briefly in symbols and abbreviations.

The diversification step can be performed in two ways (*A or B Fig IV.2)*.In the beginning a known amino acid sequence obtained from a protein belonging to a desired type of scaffold (for example repeat protein) is taken as a reference. This sequence is inserted into a domain data base that returns predicted protein functional domains for a protein sequence which on further gives 'aligned protein sequences' (*Fig IV.2**B***). If domain database analysis fails to give any particular domain then method **A** (*Fig IV.2*) is followed. The software called PSI-BLAST[37] compares a known protein sequence with a nr-database and gives aligned sequences (*Fig IV.2A* step-1).

To be more specific with the properties of proteins, PSI-BLAST can also be used with the domain database (*Fig IV.2* ***A'***). In step-2 (method **B**) a number of aligned amino acid sequences are inspected carefully and only a very well conserved sequence among the large sequence is assigned as a consensus sequence. For example, if a particular domain is repeated several times in the obtained sequences this amino acid sequence is assigned as a consensus sequence. The amplification of protein is performed in the next step of the procedure.

4.2.7. Amplification (library construction, selection technologies) (Step-3).

After the design of the Consensus sequence, protein library design enables for the systematic redesign of the proteins to obtain desired functions. To obtain specific binders, one must generate a combinatorial library of the scaffold. This is done at the DNA level by randomizing the codons at appropriate amino acid positions, by using either degenerate codons or trinucleotides.[38] By building different libraries, one can investigate the properties of proteins belonging to each library in terms of solubility, aggregation state, conformational stability and secondary structure formation. It is very important to have the knowledge of the amino acids which are randomized on a particular position in order to make the protein interact with its target. This can be revealed by a crystal structure of the complex between the parental protein and its target which facilitates the residue of choice.[39, 40] This method is used vastly for the generation of most of the scaffold. Several crystal structures of binders selected from libraries of alternative binding proteins (affibodies, designed ankyrin repeat proteins-DARPins and anticalins) in complex with their respective targets show the success of this strategy.

The appropriate protein must be selected from the protein library for its particular characteristics, usually defined as specific binding or inhibition. Hence most of the proteins from the library are unwanted and must be screened. Different selection systems, described

below are employed for isolating the individual proteins. The selection system can be divided into three different categories: cell-dependent display systems, cell-free display systems and non-display systems (*Table IV. 3*). Below we describe the main selection systems from each type. In addition, a large number of methods for expressing affinity proteins from libraries on the surface of different cell types have been investigated. The major advantage with cell surface display systems is the possibility of using fluorescence labeling and powerful flow cytometric sorting for the screening, enabling affinity discrimination in the selection without the need for elution from the target protein. In the cell-dependent display systems, the affinity proteins are displayed on the surface of phage particles or cells, or expressed in a cellular compartment. The most utilized system in this group is phage display,[41] utilizing bacteriophage for display of foreign proteins.

Cell-dependent system	***Cell-free systems***	***Non-display systems***
Phage display	Ribosomal display	Yeast-two-hybrid PCA
E. coli surface display	mRNA display	
Staphylococcal surface display	CIS display	
E. coli display	DNA display	
Yeast display	Covalent DNA display	
	Microbead display	

Table IV.3: *Examples of different selection systems employed in combinatorial protein engineering.*[42]

Phage display is the most widely used selection technology for antibody fragments and was also the basis for many successful selections with alternative binding proteins. Protein DNA code is inserted into phage genes so that viruses are produced that express the protein as one of their coat proteins (eg, PIII) which can interact with targets. In phage display, the phage library (*Fig IV.3a*) is exposed to a target immobilized on a surface molecule and bound phage-target complexes are captured on a solid phase (*Fig IV.3b*), followed by washing for removal of unbound or weakly bound phage (*Fig IV.3c*) and subsequent elution of bound phage (*Fig IV.3d*). The retained phage can be amplified by re-infecting a bacterial host and identical phage particles can be rescued by super infection of helper phage, creating a new phage pool which exhibits a more limited variability due to the selection. The amplification of phages in host such as *E.coli* proceeds via three stages of life cycle includes infection,

replication and release of progenies by the lyses of the host cells. The amplified pool is typically cycled through 3-5 selection rounds to enrich for target-binding clones. Individual clones can be subjected to screening for binding to the target molecule for ranking of binding. The amino acid sequences of the encoded proteins are identified by DNA sequencing.

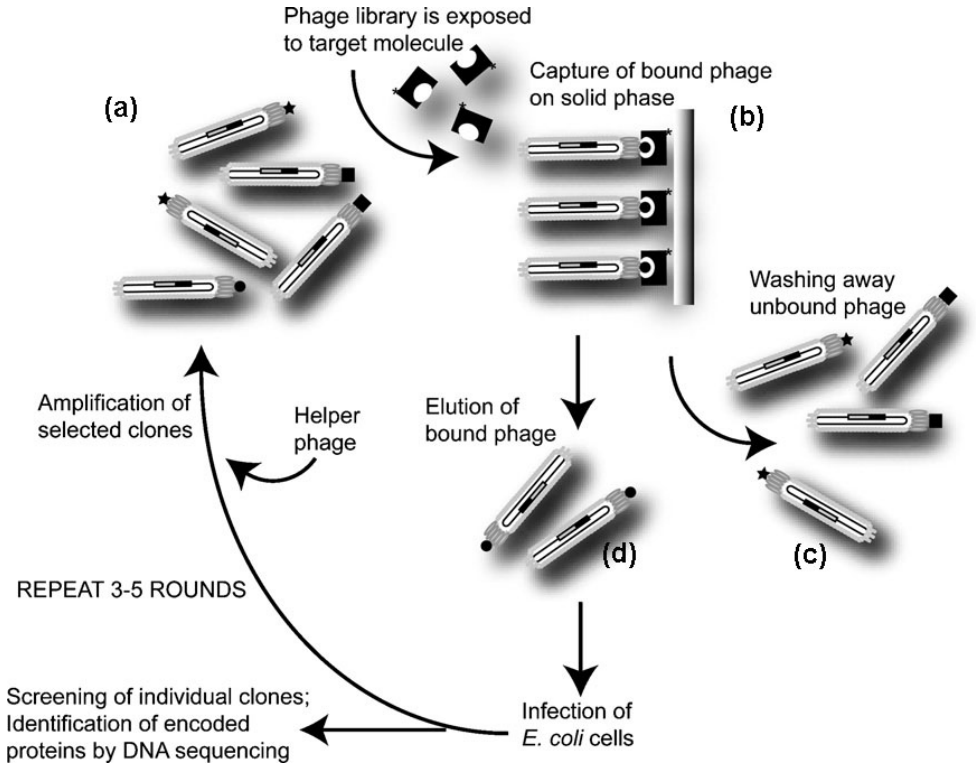

Fig IV.3 *Schematic overview of the phage display selection procedure. Image extracted from the reference.*[42]

Yeast surface display[43, 44] was one of the first developed alternatives to phage display. It is successfully used in combination with Fluorescence Activated Cell Sorting (FACS). The yeast display makes use of a protein complex inserted within the yeast cell wall as a means to fuse the displayed protein in such a way that it is accessible from outside the yeast cell. By comparison with phage display there are many identical proteins, which are displayed on each yeast cell, whereas only few copies of one type of protein is expressed by a given bacteriophage.

However, there are some limitations while using cell-dependent systems. In particular the maximum library size depends on the transformation efficiency of DNA, and the crucial fact that the target protein needs to be available, and preferably in its native form. This has led to the exploration of cell-free systems with the main common feature that they use *in vitro*

transcription and translation for construction of protein libraries. Ribosome display and mRNA display work entirely *in vitro*. They couple the protein with the mRNA non covalently via the ribosome (ribosome display)[45-47]or, after translation in additional steps, covalently via puromycin (mRNA display)[46]. Both have been used in several selections from complex libraries.[45]

In addition, there are other selection systems which are not based on display of libraries and selection by incubation with a target molecule and isolation of binders. These *in vivo* systems commonly rely on the protein interaction between affinity protein and target generating growth survival or fluorescence activity. In these non-display systems, the target protein is co-expressed with the individual library members *in vivo*, and the selection is thus not dependent on an available target protein, but instead the target protein can be expressed in a correctly folded form by the host organism.

4.3. Protein repeats: structures, functions and evolution.

Among the recently discovered protein scaffolds, (section 4.2.4) we have worked with repeat proteins that are described in detail here after. We focus on repeats, the sequence of which occurs tandemly and that form integrated assemblies when viewed as three-dimensional structures. Such repeats are defined by their multiplicity and thus differ from both domains and motifs since these can occur singly. This functional versatility is apparent not only among different repeat types, but also for similar repeats from the same family.

4.3.1. General properties of repeat proteins.

In general each repeat protein is composed of tandem repeats of a basic structural motif with composition of 20–40 amino acids. These repeats are thought to arise via evolutionary process and recombination events. These motifs can range from simple linked structures, for example α-helices in the tetratricopeptide (TPR) motif ,[28, 29] to more complex arrangements like the β-propeller* structure which has blade like β-sheet* arranged toroidally around a central axis[48]. There are few exceptions where these tandem arrays of repeat proteins tend to form elongated non-globular structure by arranging themselves in a stacking manner, which is stabilized by short range interaction from residues close in primary sequence. Sequence alignment of all motifs within a repeat family shows the most conserved positions and on the other hand highly variable positions in the motif. The conserved positions mainly involved in maintaining the stable structure of each motif and/or keeping an adequate interaction with the

neighboring motifs. Variable residues at particular position in the sequence are less likely to contribute to fold stability but they can create a variable macro surface from which interactions with other protein partners can emerge. Thus, in general, sequentially distant residues in the structure do not interact with each other. Specifically, repeat proteins are dominated by short-range and regularly placed interactions, whereas globular proteins tend to have complex interactions.

In order to improve the biophysical or functional properties of repeat proteins, the consensus design is effectively employed which uses statistical analyses of sequence alignments from families of homologous proteins for protein engineering.[49, 50] This approach for obtaining consensus design is particularly well suited for protein scaffolds which are derived from protein families with many homologous members. In the case of repeat proteins (data have so far been reported for ankyrin, leucine-rich and tetratricopeptide repeats), consensus repeat sequences were derived by Ph.Minard and his group (IBBMC Orsay) from the alignment of numerous repeats, which were then used to generate proteins of varying repeat numbers, which both showed high thermodynamic stability with a stable 3D topology and they were well expressed in E. coli in order to amplify the protein[49].

4.3.2. Major repeat proteins.

TPR proteins Tetratrico peptide repeats (TPR).

The tetratrico peptide repeat (TPR) is a structural motif present in a wide range of natural proteins. It is mainly responsible for protein-protein interactions and the assembly of multi protein complexes. The TPR motif consists of 3-16 tandem-repeats made of 34 amino acids residues. These proteins are interesting because of their folding characteristics, modular architecture and range of binding specificities. TPR motifs have been identified in various different organisms, ranging from bacteria to humans (ref-SM00028-SMART*). Proteins containing TPRs are involved in a range of biological processes, such as cell cycle regulation, transcriptional control, mitochondrial and peroxisomal protein transport, neurogenesis and protein folding. [22] The X-ray structure of a domain containing three TPRs from protein *phosphatase 5* revealed that TPR adopts a helix-turn-helix arrangement, with adjacent TPR motifs packing in a parallel fashion, resulting in a spiral of repeating anti-parallel α-helices (*Fig IV.4*). [51] The packing angle between helix A and helix B is ~24^{o} within a single TPR and generates a right-handed super helical shape.[22] Helix A interacts with helix B and with helix A` of the next TPR. Two protein surfaces are generated: the inner concave surface is

composed of residue from helices A and the other surface presents residues from both helices A and B. The consensus sequence of a TPR is defined by a pattern of small and large hydrophobic amino acids since no positions are completely invariant. The uniform secondary structure, regular tertiary structure and stability of TPR domains make them of particular interest for specific binding interactions. The successful design of full consensus tetratricopeptide (TPR) repeats has been described and discussed in references. [52] [53]

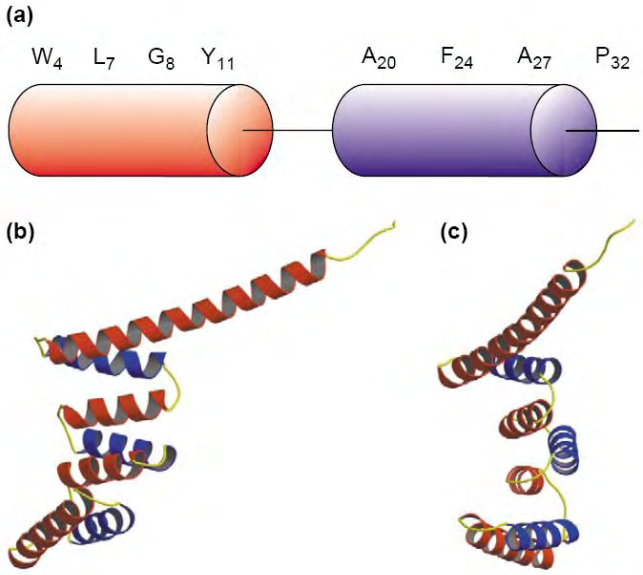

Fig IV.4: *A tetratrico peptide repeat (TPR) motif. (a) Schematic of the secondary structure arrangement of 34 amino acids in a TPR motif. Helix A, helix B and the loop region are shown in red, blue and black, respectively. The original consensus sequence is shown.*[54] *(b) Front and (c) perpendicular views of the three TPRs of protein phosphatase 5* [51] *showing the extra helix present at the C terminus; secondary structure elements are colored as (a), except for the loop regions, which are displayed in yellow. Image taken from the reference.*[22]

Leucine Rich repeats (LRRs).

Leucine-rich repeat proteins (LRR) are short sequence structural motifs that forms a α/β horseshoe fold.[20] It is composed of 20-30 amino acid repeating stretches that are remarkably rich in the hydrophobic amino acid leucine. The known structures of LRR proteins containing 4–17 repeats have revealed that each repeat unit has a beta strand-turn-alpha helix* structure. Many repeats in LRR proteins have a horseshoe shape with an interior parallel beta sheet and an exterior array of helices (*Fig IV.1d*). One face of the beta sheet and one side of the helix array are exposed to solvent and are therefore dominated by hydrophilic residues. The region between the helices and sheets is the hydrophobic core of protein and is tightly sterically

packed with leucine residues. Leucine-rich repeat motifs have been identified in a large number of functionally unrelated proteins.[55] [56] One leucine-rich repeat variant domain (LRV) has a novel repetitive structural motif consisting of alternating alpha- and 3(10)-helices arranged in a right-handed super helix, with the absence of the beta-sheets that one present in other leucine-rich repeats.[57]Natural LRR proteins participate in many protein-protein interactions and also involved in various signal transduction and cell adhesion processes.[58]

Ankyrin repeats.

Ankyrin repeats were first found, the human erythrocyte protein.[59] Each repeat contains approximately 33 residues and forms an L-shaped structure consisting of two antiparallel α-helices followed by a β-hairpin*. The hairpins of different repeats pack tightly together forming an anti-parallel β-sheet (*Fig IV.5*). Hydrophobic residues in the α-helices form complementary non polar surfaces that assemble forming an extended helical bundle. Additional hydrogen bonds between residues of adjacent repeats contribute to further stabilization of the ensemble. The smaller sizes of the side chains lining the inner α-helices, and the left-handed twist of the stacking, produce a characteristic solvent-accessible groove. These repeat proteins were the first successful family that generated consensus designed new artificial proteins.[40]The ankyrin-repeat sequence motif has been studied using multiple sequence alignment to determine which conserved amino acid residues are critical for folding and stability.[34] The residues that appear on the wide lateral surface of ankyrin repeat structures are variable, often hydrophobic, and involved mainly in mediating protein-protein interactions.[60]

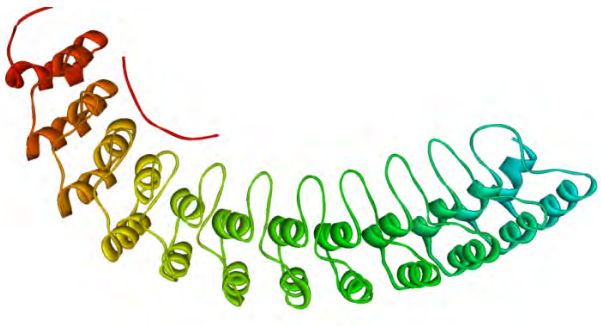

Fig IV.5: *Ribbon diagram of a fragment of the membrane-binding domain of ankyrin*[27].

DARPins (designed ankyrin repeat proteins) derived from natural ankyrin repeat proteins, feature protein architecture in which varying number of structural motifs (repeats) stack to

form the repeat protein domain. To take advantage of ankyrin repeat proteins as alternatives to antibody-based scaffolds, DARPins libraries were engineered in 2006 by a consensus design approach[61]. These DARPins show some of the highest expression levels reported for soluble, functional proteins in *E. coli*. Because of the absence of cysteines and low aggregation tendencies, they seem optimally suited not only for novel fusions and conjugates and extracellular targeting use, but also for intracellular applications.

HEAT repeats.

HEAT repeats derive their name from four diverse eukaryotic proteins in which they were first identified: ***h***untingtin (involved in Huntington's disease), ***e***longation factor 3, PR65/***A*** subunit of protein phosphatase A, and the ***T***OR (target of rapamycin).[62] They were first identified in eukaryotic proteins but were later found as common motifs in prokaryotes as well [63]. The biological functions of these proteins are very diverse, but HEAT repeats are often involved in protein-protein interactions. These proteins are folded as a succession of α helix pairs forming a right-handed superhelix. Compared to other repeat proteins, HEAT repeats show several interesting features. These repeat proteins are folded as a succession of α-helix pairs forming right handed super helix. The side by side arrangement of helices results in the evolution of extended surfaces which can be effectively used for target binding sites. In some cases, the curvature and local flexibility of the elongated solenoid allow HEAT repeats to wrap around their protein partners. The HEAT repeat proteins have highly divergent repeat sequences and at least three different subgroups have been classified.

Recently the group of Ph.Minard (IBBMC Orsay) has selected a specific subtype of HEAT repeat proteins[64] for their high thermal stability and from modified consensus sequence a new protein library has been created. Mth187* a protein with currently unknown function, [21] from Methanobacterium thermoautotrophicum was taken as the starting point for the alignment. This structure has one clear C-cap* domain, but since the N-cap* is not folded, a new N-cap was designed. After library construction, unselected variants with varying repeat numbers showed that the proteins were stable, well expressed and generally monomeric. Below, we explain in detail the validation of the consensus sequence, the library design with purification and characterization of these artificial HEAT repeat proteins, which we then used as a template for morphosynthesis of inorganic materials as well as for self assembly of nanoparticles.

4.4. Alpha-helicoidal repeat (α Rep) proteins.

4.4.1. Design of α-repeat sequence.

The strategy to obtain fully synthetic consensus sequence for alpha-helicoidal repeat (α Rep) proteins follows method **A'** *Fig IV.2* described in section 4.2.6. This method is advantageous to generate the sequence alignment in order to have a particular combination of repeat domains which helps to create functionally related set of protein. This could be desirable when possible differences between internal and external (capping) repeats are taken into account. Here PSI-BLAST is used to generate the multiple sequence alignments and thus allows control over the search criteria and many options for output format.

HEAT repeats are rather long (37 – 47 amino acids) and variable motifs compared to those from other repeat families. This highly divergent character complicates the design of the consensus sequence. Any sequence feature incorporated incorrectly into an artificial motif would be repeated in the resulting protein and could consequently have severe cumulative destabilizing effects. Therefore, if the consensus is defined from a widely divergent sequence family such as HEAT repeats, the risk is high of incorporating features originating from several subfamilies that are no longer mutually compatible into a single consensus. The design was therefore focused on a specific class of repeat proteins classified as PBS HEAT-like repeat* SMART* (SM00567) and Pfam* (PF03130), named from phycobylinsynthase accessory protein, in which it was first identified. This repeat sub-type was chosen for several reasons. First, these repeats are commonly found in thermophile Archaea (*Methanobacterium thermoautotrophicum)* and consequently could provide a stable protein platform. Second, compared to other HEAT repeat subgroups, repeats from this group are shorter and appears to be more homogeneous in length and sequence than classical HEAT repeats. The 3D structure of one protein from this group, named Mth187, has been solved (PDB* code 1TE4). In order to define completely the sequence features associated with this protein subgroup, sequence analysis was done, starting with the known structure of Mth187 as a guide.

In a first step (diversification), Urvoas et.al explored if a subgroup of non-redundant proteins with similar motifs could be identified. Mth187 is made by a succession of three pairs of α-helices and a disordered N-terminal extremity. A family of proteins was identified by a PSI-Blast* search, using a query sequence, which is obtained by the sequence of the first two repeats of the folded part of Mth181. The last motif differs from internal motifs because one

of its faces is exposed to the solvent and therefore was not incorporated in the query sequence. This search yielded 81 Aligned protein sequences (*Fig IV.2*).

In the second step (selection) a more diverse collection of related proteins was assembled using a Blast search with a longer query sequence made by five repetition of the previously defined consensus. The 100 best "penta-consensus" (consensus which repeated 5 times) similar sequences were collected. This search procedure efficiently identifies consecutive repeats which are closely related to the consensus of the Mth187 repeats structure. These repeat sequences were then split into sequence modules to calculate frequency of each amino acid residue at each particular position (*Fig IV.6)*.

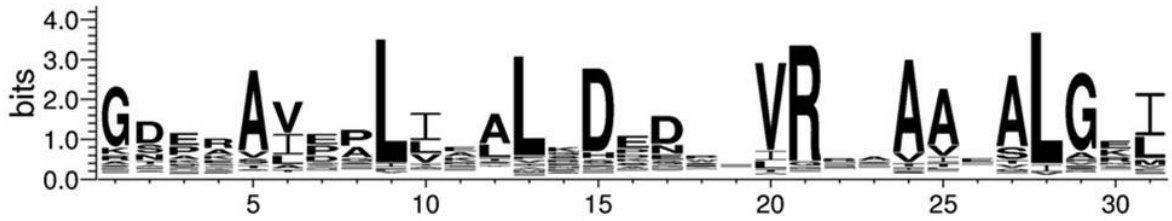

Fig IV.6: *Design of the αRep motif. A sequence Logo computed from the distribution of amino acids in multiple sequence alignments of natural Mth187 like repeats. Large letter corresponds to amino acids highly conserved in the repeat family.*

Although this collection of repeats was created using similarity to a fully defined idealized penta-consensus 1, the sequence variability in the aligned repeats is not uniform, it is much higher in some positions than in others. When mapped on the known structure of Mth187, the highly conserved positions (5,6,9,13,15,20,21,24,25,27,28,29) correspond to side chains oriented either between the two helices of each repeat or between consecutive repeats. The side chains located on the outside surface of helices is more variable. The most variable positions (18, 19, 22, 23, 26) (small letters *Fig IV.6*) are located on the outside surface of the second helix of each repeat. As the second helices of consecutive repeats are parallel one to the other, the variable amino acids are all oriented toward the same face of the protein and while the general architecture is the same, these variable side chains creates a macro surface on each protein of the family, with a unique chemical composition.

Design of N and C caps.

The external repeats at each end of most repeat proteins are referred to as N- and C-cap repeats. Capping repeats can have an overall fold similar to internal repeats but must differ at several sequence positions as one side of the cap, the exoface, will be exposed to the solvent, whereas the equivalent positions in the internal repeats are part of the inter-repeat contacts.

The structure of Mth187 has one clear C-cap motif, folded as a pair of α helices. Urvoas et.al directly used this sequence as a C-cap. The N-terminal part of this protein (residues 1–23) is not folded, and therefore cannot be used as an N-cap. Another N-cap was identified from sequence data base. A protein was identified (UniProtKB identifier* A0B7C6 (A0B7C6_METTP)) with a very clear Mth187-like consensus preceded by a 34 amino acid residues N-terminal extension, the length of which is expected for a two helices repeat (31 residues). Additionally, this putative N-cap sequence had characteristic features of the Mth187 HEAT-like repeat: LXDXXXXVRXXAAXALGXI suggesting this peptide forms an N-cap made by two helices. This 34 residues N terminal extension of A0B7C6 was retained as an N-cap.[64]

4.4.2. Construction of α-repeat proteins: Homorepeat.

αRep proteins used in this thesis work are artificial proteins expressed from synthetic genes. The sequences of all αRep follows the general scheme: Ncap-(internal modules)$_n$-Ccap (*Table IV.4*).The simplest group of αRep is called “homorepeats”. Proteins in this group have one N and one C cap plus a variable number of internal modules, but all these internal repeats have exactly the same sequence (*Table IV.4*). The sequence of this repeated motif is a full consensus, each residue is the most commonly found amino acids at this position in the database of natural proteins. There must be at least 1 internal module per αRep, and the longest protein studied so far has 18 internal repeats. In the context of this work, these homorepeats can be viewed as reference proteins to explore the influence of these αRep structures on the protein-gold interface but are not expected to have specific interaction for any other target protein.[64]The gene coding for homorepeats αRep were assembled by homo-polymerization of a microgene coding exactly for one module, in between the N and the C cap sequences previously cloned in an expression vector (*Fig IV.7*).[64] The repeat microgenes were synthesized by coding α-Rep motif by two oligonucleotides (O14-31) and (O1-13) which were annealed at their extremities with complementary bridging oligonucleotides Ob13-14 and Ob1-31 to make DNA circles coding exactly for one repeat (*Fig IV.7*). the stars in each motifs represents the diversity in the hyper variables positions and corresponds to amino acid positions 18, 19, 22, 23, 26 and 30. This resulted in a collection of clones with variable number of repeats. The number of repeats of each clone is experimentally determined by the size of the restriction fragment corresponding to the coding sequence (each module contributes to 93 nucleotides to the sequence) or by direct sequencing.

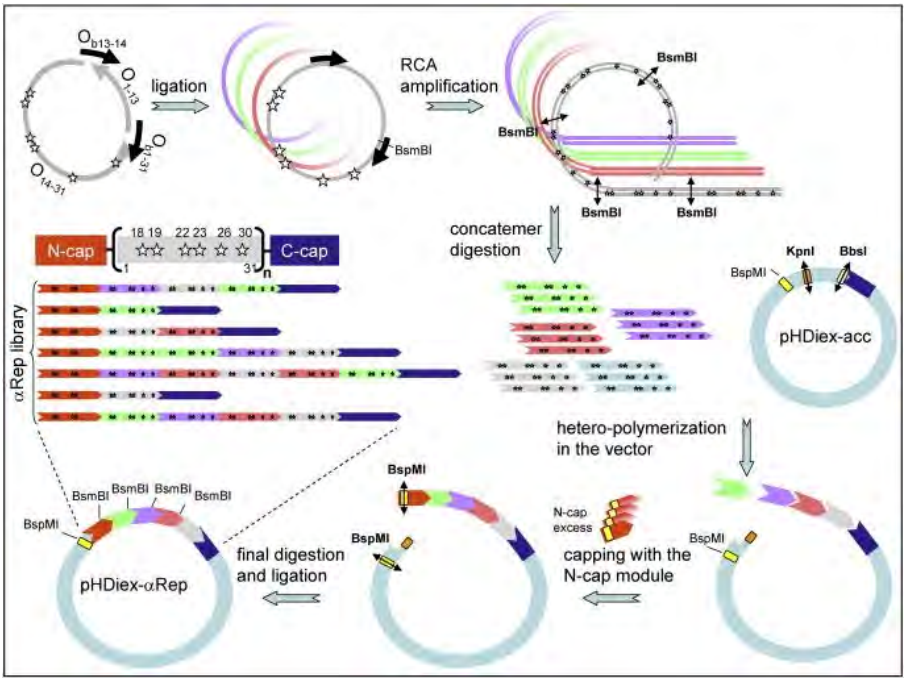

Fig IV.7: *Schematic diagram illustrating the α-Rep protein library construction. The 31 amino acid αRep motif was coded by different oligonucleotides and annealed with short bridging primers. Two primers are then ligated to form DNA circles and these circles are used for CA amplification to give double-stranded homopolymers of repeats. The repeats were heteropolymerized in the C-cap and polymerization was capped by ligation with an excess of the N-cap variable module re circularized by intramolecular ligation. Fig extracted from the reference.* [64]

Protein	Number of amino acids	Molecular weight (kDa)	Theoretical pI	Ext. coefficient assuming all pairs of Cys residues form cystines ($M^{-1}.cm^{-1}$)
α-Rep-N9(n=9)	356	38.56	5.00	8480
α-Rep -N10(n=10)	387	41.80	5.11	8480
α-Rep -N11(n=11)	418	45.30	5.07	9970

N-cap
MPLRADPEKVEMYIKNLQDDSXXVRXXAAXALGXI

C-cap
GGERVRAAMEKLAETGTGFARKVAVNYLETH

Variable Internal repeats
GDERAVEPLIKALKDEDXXVRXXAAXALGXI

Sequence: α-Rep-N9	*Sequence: α-Rep -N10*	*Sequence: α-Rep -N11*
HHHHHHTDPEKVEMYIKNLQDDSWQVRRAAAEALGKI	HHHHHHTDPEKVEMYIKNLQDDSWQVRRAAAEALGKI	HHHHHHTDPEKVEMYIKNLQDDSWQVRRAAAEALGKI
GDERA VEPLI KALKD EDSDV RRAAA EALGK I	GDERA VEPLI KALKD EDSDV RRAAA EALGK I	GDERA VEPLI KALKD EDSDV RRAAA EALGK I
GDERA VEPLI KALKD EDSDV RRAAA EALGK I	GDERA VEPLI KALKD EDSDV RRAAA EALGK I	GDERA VEPLI KALKD EDSDV RRAAA EALGK I
GDERA VEPLI KALKD EDSDV RRAAA EALGK I	GDERA VEPLI KALKD EDSDV RRAAA EALGK I	GDERA VEPLI KALKD EDSDV RRAAA EALGK I
GDERA VEPLI KALKD EDSDV RRAAA EALGK I	GDERA VEPLI KALKD EDSDV RRAAA EALGK I	GDERA VEPLI KALKD EDSDV RRAAA EALGK I
GDERA VEPLI KALKD EDSDV RRAAA EALGK I	GDERA VEPLI KALKD EDSDV RRAAA EALGK I	GDERA VEPLI KALKD EDSDV RRAAA EALGK I
GDERA VEPLI KALKD EDSDV RRAAA EALGK I	GDERA VEPLI KALKD EDSDV RRAAA EALGK I	GDERA VEPLI KALKD EDSDV RRAAA EALGK I
GDERA VEPLI KALKD EDSDV RRAAA EALGK I	GDERA VEPLI KALKD EDSDV RRAAA EALGK I	GDERA VEPLI KALKD EDSDV RRAAA EALGK I
GDERA VEPLI KALKD EDSDV RRAAA EALGK I	GDERA VEPLI KALKD EDSDV RRAAA EALGK I	GDERA VEPLI KALKD EDSDV RRAAA EALGK I
GGERVRAAMEKLAETGTGFARKVAVNYLETHKSLIS*	GGERVRAAMEKLAETGTGFARKVAVNYLETHKSLIS*	GGERVRAAMEKLAETGTGFARKVAVNYLETHKSLIS*

Table.IV.4: *Table summarizing amino acid sequence and general information of α-Rep N9,α-Rep N10, α-Rep N11 protein.*

Our study detailed in chapters 5 and 6 focuses on three homorepeat proteins N9, N10 and N11 containing respectively 9, 10 and 11 internal repeats (*Table IV.4*). Sequence analysis showed that the motif is not strictly repeated. This indicates that mutations were introduced during the gene construction, probably in the polymerization step. The mass spectra of the purified proteins corresponded to the theoretical masses calculated from the experimental DNA sequences.

4.4.3 Construction of library of αRep proteins.

Libraries of αRep proteins with variable binding surfaces were also produced by our colleagues in IBBMC (Ph.Minard, A.Urvoas et.al). In these proteins, the number of modules between the N and C cap is variable and each internal module has 6 partially randomized positions (18, 19, 22, 23, 26, 30) corresponding to the most variable positions in the database of natural proteins. The N cap can also have some variability in the position structurally equivalent to the variable positions of internal modules. Two different libraries were produced.

The first library[64] was initially designed to test experimentally the properties of proteins made following the αRep design. In this first library (1.0) the variable amino acids were partially randomized so as to exclude destabilizing residues such as proline within alpha helices and to include amino acids with very different characters (size, polarity, charge). The size distribution in this library is from 1 to more than 10 repeats. Sequencing of randomly picked clones indicated that only 65% of the modules had the expected sequence while approximately one third of the modules have a sequence error resulting in frame shift of the proteins in which these modules were incorporated. As a consequence, genes taken from this first library are less likely to have a correct sequence when the number of inserted modules increases. Therefore a large fraction of fully correct coding genes have three internal modules or less.

A second library was then produced with a more complete randomization scheme at variable positions. The randomization scheme was adjusted to mimic the statistical distribution of amino acid computed from the database, at each randomized position. Furthermore, this library (2.0) was produced by polymerization of randomized modules using a pool of modules previously selected to have the expected correct coding sequences. Therefore the proportion of coding sequences is higher in lib 2.0 than in lib 1.0 especially for proteins with many internal modules.

4.4.4. Biophysical characterization of αRep proteins.

Proteins with a randomized repeat surface

Alpha-Rep proteins produced in E. coli by a set of clones containing 1 to 6 internal repeats from the library 1.0 were purified and characterized. These proteins are very efficiently expressed and highly soluble. Far UV Circular Dichroism (CD) spectra indicate that these proteins are folded with a large fraction of alpha helices, as expected[64]. The Differential Scanning Calorimetry (DSC) and thermal unfolding experiments indicate that these proteins are cooperatively folded, and are extremely resistant to denaturation[64]. The stability increases with the number of modules suggesting that every repeat contribute to the overall stability.[64]

These proteins are monomeric with the exception of one protein with 4 internal modules. This protein, named αRep-N4 (also nick named A3) appears by gel filtration and SAXS to be a homodimer. This particular protein was chosen for crystallization trials. Crystals were obtained and the crystal structure confirmed that this protein is effectively a homodimer stabilized by interaction between C cap and variable N cap surface (*Fig IV.8*). All the studied proteins are efficiently expressed and have a very stable fold whatever is the side chain combination on the variable surface.[64]

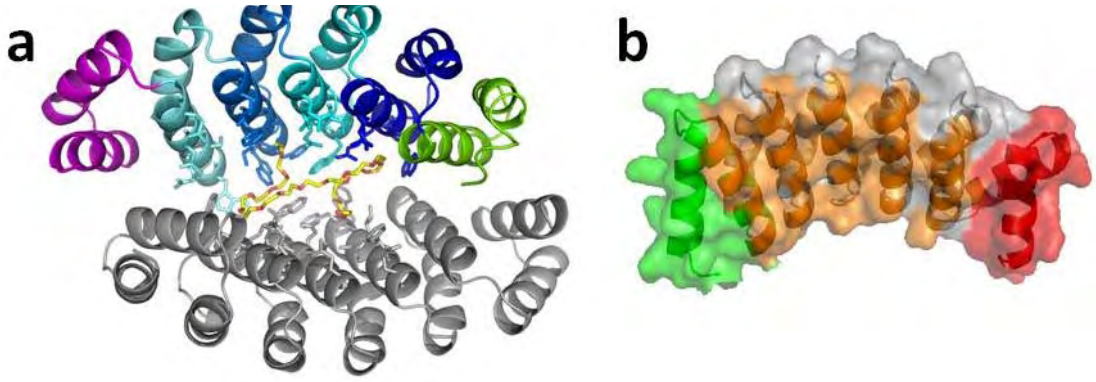

Fig IV.8: *Crystal structure of the protein α-Rep-n4 (also named aRep-A3. (a) Structure of the PEG-bound dimer. The protein is shown in ribbon representation. The first monomer is colored gray. For the second monomer, the N-cap is colored green, the C-cap in purple and each internal repeat in orange. Side chains of the randomized residues are displayed as sticks representation and are located at the dimer interface. The bound PEG molecule found in the crystal structure is in yellow. (b) Molecular surface representation of a monomer. The surface formed by constant residues is indicated in grey; the randomized residues form a continuous surface and N-cap indicated in orange. Courtesy of Ph.Minard.*

α- Rep-N4 protein could be crystallized and its structure was solved to better than 2 Å resolution (*Fig IV.8*). This protein has four repeats in its sequence and the crystal structure

shows that αRep-n4-a associates as a dimer. Each monomer is folded as a succession of α helix pairs stacking on each other (Fig IV.8a). The succession of repeats forms a flattened right-handed superhelix. The structures of the internal repeats are almost identical, with the exception of the variable side chains. Two different conformations (one obtained without, and one with bound PEG used as a precipitant in crystallization) indicated some flexibility within this scaffold and at the interface between monomers. The convex face is made by helix 1 of successive repeats and the concave face of the protein is made by the succession of the external surfaces of helices 2. The variable side chains are clustered together and create a continuous surface located on the concave face of the protein (*Fig IV.8b*) this shows the variable chemical environment on the surface of the protein.

4.4.5. Homorepeat proteins with a conserved repeat surface.

To study the biophysical properties of longer proteins (N>6 repeat), we considered homorepeat proteins containing 9, 10 and 11 internal repeats. The secondary structure content of the characterized proteins was analyzed by far-UV CD. For each α-Rep protein, the far-UV CD spectra were recorded at 25°C under identical conditions (*Fig IV.9a*). All spectra were superimposable and displayed the characteristic signal of an all α protein with a maximum absorbance at 192 nm and minima at 209 nm and 222 nm.

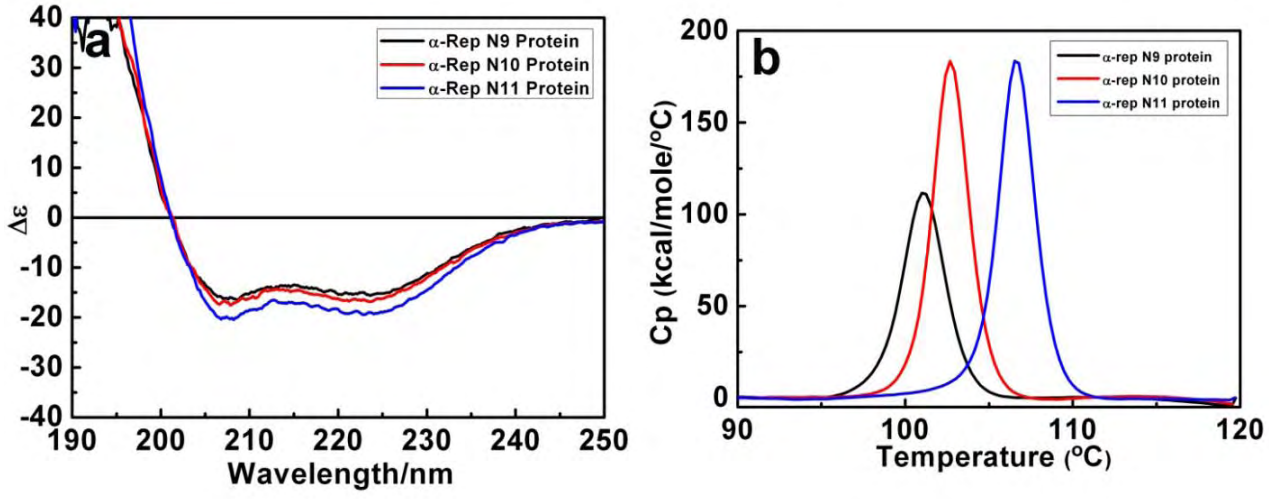

Fig IV.9: *a) CD spectra of α-Rep-N9, α-Rep-N10, and α-RepN11. Each spectrum was measured with 10 μM protein concentration at 25°C. b) DSC thermograms of αRep-N9, αRep-N10, and αRep-N11.*

A quantitative comparison showed that all characterized proteins have the same ellipticity on a per residues basis, this clearly suggested that the helicoidal content was correlated directly

with the length of the protein and that all the repeats of longer proteins are folded. The CD spectra recorded before and after denaturation were identical. These data indicated that thermal unfolding of secondary structure in these proteins was reversible.

The Differential Scanning Calorimetry and thermal unfolding experiments indicated that these proteins were cooperatively folded, and extremely resistant to denaturation. The stability was increased with the number of modules suggesting that every repeat contribute to the overall stability. The thermal unfolding of all 3 proteins was first monitored by following the change in CD signal at 220 nm in the temperature range of 35-95 °C. This experiment showed that the stability of repeat proteins increased with the number of repeats but it was not possible to evaluate their transition midpoint (Tm) because the proteins were too stable. The thermal unfolding behavior of αRep proteins was also evaluated by differential scanning microcalorimetry (DSC) in the temperature range of 35-120°C (*Fig IV.9b*). The αRep-N9 transition displays a midpoint Tm of 96.05(±0.01) °C. αRep-N10 and αRep-N11 exhibit slightly higher Tm values (98.05 (±0.01) °C and 102.2 (±0.1) °C, respectively. *Table IV.5* summaries the data obtained by CD and DSC experiments' on homorepeats.

	Thermal denaturation (No salt)		**Thermal denaturation(200 mM NaCl)**	
Protein	**Tm (°C)**	**ΔH (kcal. mol^{-1})**	**Tm (°C)**	**ΔH (kcal. mol^{-1})**
HR-N9	**96.05± 0.01**	**40.2 ± 2.5**	**101.1 ± 0.01**	**378 ± 2**
HR-N10	**98.05± 0.02**	**37.0 ± 0.7**	**102.7 ± 0.01**	**525 ± 2**
HR-N11	**102.2± 0.01**	**510 ± 2**	**106.6 ± 0.01**	**535 ± 3**

Table.IV.5: *Table summarizing the DSC analysis of αRep proteins in the presence and in the absence of NaCl salt.*

Analytical size exclusion chromatography suggested that, in the absence of salt (NaCl), these proteins tend to oligomerize in solution. Complementary SAXS experiments were performed and indicated that in addition to the presence or absence of salt, the protein concentration is an important parameter controlling oligomerisation of these long homorepeat proteins. In the presence of 200mM NaCl and at low concentrations (< 0,3 mg/mL) the 3 proteins (N9, N10 and N11) are monomeric while at higher concentrations (> 1 mg/mL) N10 and N11 oligomeric forms are observed.

These experimental findings provide a promising starting point for the use of these proteins for morphosynthesis of inorganic materials. Also the nature of the surface with distinct character from the variation of some amino acids combined with a stable 3 dimensional structure can serve as a very good template for shape directing synthesis of nanomaterials. Although the crystal structures of these proteins are not known, SAXS data, CD, and DSC characterization showed they have stable 3D structure with high thermal stability. Hence αRepA3, αRep-N9, αRep-N10 and αRep-N11 proteins are used as a template for anisotropic crystal growth of Au, as we will explore in chapter 5.

4.4.6. Selection of interacting protein pairs

For the selection of αRep protein pairs, Ph.Minard, A. Urvoas, M .Valerio-Lepiniec have selected αRep-A3 binders from the libraries (1) and (2) by phage display. In this case, the highly conserved residues implicated in the folding of the motif were constant and the highly non-conserved residues at variable positions (18, 19, 22, 23, 26 and 30) were randomized which resulted in proteins with different amino acid sequence in their repeats. Hence with this procedure two proteins, αRep-2 and αRep-17 were selected as αRep-A3 binders. αRep-2 was found to have a higher affinity for αRep-A3 than αRep-17 protein. The detailed selection procedure and biophysical characterization of protein pairs are described in chapter 6 prior to their use as Au NP self assembly agents.

4.5. Applications of Artificial proteins.

The affinity of artificial proteins was demonstrated for different targets, ranging from low molecular weight compounds to large proteins since their affinities and specificities can be achieved that are comparable to those of natural binding molecules. Therefore artificial proteins are gradually entering the areas of classical antibody applications and are currently being evaluated. At the same time, favorable properties of the parent scaffold can be conserved that enable high yield production and high physicochemical stability. In this regard we postulate that the use of artificial proteins can be extended towards material chemistry where it can also be utilized as a stable template for the synthesis of inorganic nanomaterials.

4.5.1. Therapeutic applications of binding proteins.

Artificial protein scaffolds are in many aspects well-suited for biotechnology applications. In general, high biophysical stability, long shelf-life and convenient expression at high yields

and efficient production of engineered affinity proteins, makes them effective candidates when compared to conventional antibodies.

A new generation of therapeutic drugs that has evolved in the last few decades involving protein-protein interaction show better potential in competition with small molecule drugs.[65] Affinity proteins are group of therapeutic proteins with targeting activity and they function specifically recognizing and binding to target biomolecules in the body. By binding, they can interfere or block functions, target molecules or organisms for destruction, or stimulate a signaling pathway. They can also be used as vehicles for delivery of other proteins or compounds to a specific site. More recently, an attempt has been made to use engineered affinity proteins based on non-immunoglobulin scaffolds used as an alternative for targeting therapeutically relevant molecules.[12] The applicability of an artificial binding protein in a therapeutic scenario is to a large extent dependent on the properties of the protein scaffold and the intended mechanism of action.

4.5.2. Separation of ligands and crystallographic structure determinations.

Engineered affinity proteins can capture agents in affinity matrices. In affinity chromatography, the affinity ligands have to be stable enough to withstand harsh Cleaning-In-Place (CIP) procedures and long-term storage without affecting the efficiency. Since small scaffold proteins have favorable properties in terms of stability and robustness, convenient protein engineering of scaffold proteins allows for introduction of amino acid residues suitable for site-specific directed coupling to a matrix, for example cysteine. Affibody molecules that have been extensively used as affinity ligand for immunoglobulins were considered early on for bio separation purposes. These molecules were coupled to affinity resins and were demonstrated to specifically capture their target in complex samples such as fermentation medium, bacterial lysate, and human body fluids.[66]

Proteins are large biomolecules and it is very difficult to solve their structure by X-ray crystallography in addition they provide great challenge due to intrinsic properties such as high flexibility or inadequate degree of hydrophilicity compared to small molecules. Hence simple protein structure determinations can contribute with invaluable knowledge about biological function and protein interactions. Affinity proteins, by specific binding can stabilize the protein and increase the overall hydrophilicity and thereby increase the changes of yielding crystals and enabling high resolution determinations. Several DARPins have successfully been used in X-ray structure determinations in complex with their target proteins.[67, 68]

4.5.3. Material design using genetically engineered proteins.

As we mentioned earlier, the morphological, structural and functional complexity in inorganic materials can be achieved by bioinspired and biomineralization approaches which mainly involve specific interaction between inorganic materials and biological scaffold. DNA,[69] Polypeptides,[70] Virus[71, 72] and natural proteins[73] have been used as a template on which growth of metal nanostructures were executed. In addition successful modulation of existing scaffold (peptide) for metal binding sites has also been achieved.[74]To some extent, these biomolecules have their limitation towards inorganic material design and hence there is a still large room for improvement for better functioning of these biomolecules.

In this prospect here we propose a novel application of artificial repeats proteins for morphosynthesis and self assembly of plasmonic nanostructures as they possess specific features in terms of structure and function compare to the other biological scaffolds. αRep proteins show high thermal stability with well folded 3D topology that can be simply modulated by increasing the number of repeats. In addition it provides an option for successful modulation of the sequence on their surface to have an affinity with specific crystallographic face of a metal. Further, new affinity pairs of proteins can be generated with high affinity, by using combinatorial approaches well established in biology and we can use these pairs for controlled nanoparticle self assembly. With this objective, we have worked on αRep proteins along with Au as an inorganic interface to obtain anisotropic nanostructures and also we worked on self assembly of preformed metal nanoparticles by using αRep protein pairs which is detailed in the coming chapters.

References:

(1) Boersma, Y. L.; Plueckthun, A. *Current Opinion in Biotechnology* **2011**, *22*, 849-857.

(2) Lamla, T.; Erdmann, V. A. *Protein Expression and Purification* **2004**, *33*, 39-47.

(3) Wikman, M.; Steffen, A. C.; Gunneriusson, E.; Tolmachev, V.; Adams, G. P.; Carlsson, J.; Stahl, S. *Protein Engineering Design & Selection* **2004**, *17*, 455-462.

(4) Amstutz, P.; Binz, H. K.; Parizek, P.; Stumpp, M. T.; Kohl, A.; Grutter, M. G.; Forrer, P.; Pluckthun, C. *Journal of Biological Chemistry* **2005**, *280*, 24715-24722.

(5) Heyd, B.; Pecorari, F.; Collinet, B.; Adjadj, E.; Desmadril, M.; Minard, P. *Biochemistry* **2003**, *42*, 5674-5683.

(6) Nicaise, M.; Valerio-Lepiniec, M.; Minard, P.; Desmadril, M. *Protein Science* **2004**, *13*, 1882-1891.

(7) Binz, H. K.; Amstutz, P.; Pluckthun, A. *Nature Biotechnology* **2005**, *23*, 1257-1268.

(8) Skerra, A. *Journal of Molecular Recognition* **2000**, *13*, 167-187.

(9) Nygren, P. A.; Uhlen, M. *Current Opinion in Structural Biology* **1997**, *7*, 463-469.

(10) Hosse, R. J.; Rothe, A.; Power, B. E. *Protein Science* **2006**, *15*, 14-27.

(11) Skerra, A. *Current Opinion in Biotechnology* **2007**, *18*, 295-304.

(12) Hey, T.; Fiedler, E.; Rudolph, R.; Fiedler, M. *Trends in Biotechnology* **2005**, *23*, 514-522.

(13) Nygren, P.-A. *Febs Journal* **2008**, *275*, 2668-2676.

(14) Nilsson, B.; Moks, T.; Jansson, B.; Abrahmsen, L.; Elmblad, A.; Holmgren, E.; Henrichson, C.; Jones, T. A.; Uhlen, M. *Protein Engineering* **1987**, *1*, 107-113.

(15) Jansson, B.; Uhlen, M.; Nygren, P. A. *Fems Immunology and Medical Microbiology* **1998**, *20*, 69-78.

(16) Koide, A.; Koide, S. *Methods in molecular biology (Clifton, N.J.)* **2007**, *352*, 95-109.

(17) Skerra, A. *Febs Journal* **2008**, *275*, 2677-2683.

(18) Schlehuber, S.; Skerra, A. *Drug Discovery Today* **2005**, *10*, 23-33.

(19) Stumpp, M. T.; Forrer, P.; Binz, H. K.; Pluckthun, A. *Journal of Molecular Biology* **2003**, *332*, 471-487.

(20) Enkhbayar, P.; Kamiya, M.; Osaki, M.; Matsumoto, T.; Matsushima, N. *Proteins-Structure Function and Genetics* **2004**, *54*, 394-403.

(21) Julien, O.; Gignac, I.; Hutton, A.; Yee, A.; Arrowsmith, C. H.; Gagne, S. M. *Journal of Biomolecular Nmr* **2006**, *35*, 149-154.

(22) D'Andrea, L. D. R., L. *Trends in Biochemical Sciences* **2003**, *28*, 655-662.

(23) Kim, Y.; Ho, S. O.; Gassman, N. R.; Korlann, Y.; Landorf, E. V.; Collart, F. R.; Weiss, S. *Bioconjugate Chemistry* **2008**, *19*, 786-791.

(24) Kobe, B.; Deisenhofer, J. *Nature* **1995**, *374*, 183-186.

(25) Schubert, W. D.; Urbanke, C.; Ziehm, T.; Beier, V.; Machner, M. P.; Domann, E.; Wehland, J.; Chakraborty, T.; Heinz, D. W. *Cell* **2002**, *111*, 825-836.

(26) Jacobs, M. D.; Harrison, S. C. *Cell* **1998**, *95*, 749-758.

(27) Michaely, P.; Tomchick, D. R.; Machius, M.; Anderson, R. G. W. *Embo Journal* **2002**, *21*, 6387-6396.

(28) Lapouge, K.; Smith, S. J. M.; Walker, P. A.; Gamblin, S. J.; Smerdon, S. J.; Rittinger, K. *Molecular Cell* **2000**, *6*, 899-907.

(29) Taylor, P.; Dornan, J.; Carrello, A.; Minchin, R. F.; Ratajczak, T.; Walkinshaw, M. D. *Structure* **2001**, *9*, 431-438.

(30) Huber, A. H.; Weis, W. I. *Cell* **2001**, *105*, 391-402.

(31) Vetter, I. R.; Arndt, A.; Kutay, U.; Gorlich, D.; Wittinghofer, A. *Cell* **1999**, *97*, 635-646.

(32) Forrer, P.; Stumpp, M. T.; Binz, H. K.; Pluckthun, A. *Febs Letters* **2003**, *539*, 2-6.

(33) Houghten, R. A.; Pinilla, C.; Blondelle, S. E.; Appel, J. R.; Dooley, C. T.; Cuervo, J. H. *Nature* **1991**, *354*, 84-86.

(34) Mosavi, L. K.; Minor, D. L.; Peng, Z. Y. *Proceedings of the National Academy of Sciences of the United States of America* **2002**, *99*, 16029-16034.

(35) Schultz, J.; Milpetz, F.; Bork, P.; Ponting, C. P. *Proceedings of the National Academy of Sciences of the United States of America* **1998**, *95*, 5857-5864.

(36) Bateman, A.; Birney, E.; Cerruti, L.; Durbin, R.; Etwiller, L.; Eddy, S. R.; Griffiths-Jones, S.; Howe, K. L.; Marshall, M.; Sonnhammer, E. L. L. *Nucleic Acids Research* **2002**, *30*, 276-280.

(37) Altschul, S. F.; Madden, T. L.; Schaffer, A. A.; Zhang, J. H.; Zhang, Z.; Miller, W.; Lipman, D. J. *Nucleic Acids Research* **1997**, *25*, 3389-3402.

(38) Virnekas, B.; Ge, L. M.; Pluckthun, A.; Schneider, K. C.; Wellnhofer, G.; Moroney, S. E. *Nucleic Acids Research* **1994**, *22*, 5600-5607.

(39) Nord, K.; Nilsson, J.; Nilsson, B.; Uhlen, M.; Nygren, P. A. *Protein Engineering* **1995**, *8*, 601-608.

(40) Binz, H. K.; Stumpp, M. T.; Forrer, P.; Amstutz, P.; Pluckthun, A. *Journal of Molecular Biology* **2003**, *332*, 489-503.

(41) Barbas III, C. F., Burton, D.R., Scott, J.K., Silverman, G.J., *Phage Display: A Laboratory Manual.* ; Cold Spring Harbor Laboratory Press, Cold Spring Harbor, NY., 2001.

(42) Gronwall, C.; Stahl, S. *Journal of Biotechnology* **2009**, *140*, 254-269.

(43) Holler, P. D.; Holman, P. O.; Shusta, E. V.; O'Herrin, S.; Wittrup, K. D.; Kranz, D. M. *Proceedings of the National Academy of Sciences of the United States of America* **2000**, *97*, 5387-5392.

(44) Kieke, M. C.; Shusta, E. V.; Boder, E. T.; Teyton, L.; Wittrup, K. D.; Kranz, D. M. *Proceedings of the National Academy of Sciences of the United States of America* **1999**, *96*, 5651-5656.

(45) Schaffitzel, C.; Hanes, J.; Jermutus, L.; Pluckthun, A. *Journal of Immunological Methods* **1999**, *231*, 119-135.

(46) Lipovsek, D.; Pluckthun, A. *Journal of Immunological Methods* **2004**, *290*, 51-67.

(47) Hanes, J.; Pluckthun, A. *Proceedings of the National Academy of Sciences of the United States of America* **1997**, *94*, 4937-4942.

(48) Jawad, Z.; Paoli, M. *Structure* **2002**, *10*, 447-454.

(49) Lehmann, M.; Wyss, M. *Current Opinion in Biotechnology* **2001**, *12*, 371-375.

(50) van den Burg, B.; Eijsink, V. G. H. *Current Opinion in Biotechnology* **2002**, *13*, 333-337.

(51) Das, A. K.; Cohen, P. T. W.; Barford, D. *Embo Journal* **1998**, *17*, 1192-1199.

(52) Main, E. R. G.; Lowe, A. R.; Mochrie, S. G. J.; Jackson, S. E.; Regan, L. *Current Opinion in Structural Biology* **2005**, *15*, 464-471.

(53) Main, E. R. G.; Jackson, S. E.; Regan, L. *Current Opinion in Structural Biology* **2003**, *13*, 482-489.

(54) Sikorski, R. S.; Boguski, M. S.; Goebl, M.; Hieter, P. *Cell* **1990**, *60*, 307-317.

(55) Rothberg, J. M.; Jacobs, J. R.; Goodman, C. S.; Artavanistsakonas, S. *Genes & Development* **1990**, *4*, 2169-2187.

(56) Kobe, B.; Deisenhofer, J. *Nature* **1993**, *366*, 751-756.

(57) Peters, J. W.; Stowell, H. B.; Rees, D. C. *Nature Structural Biology* **1996**, *3*, 991-994.

(58) Buchanan, S. G. S.; Gay, N. J. *Progress in Biophysics & Molecular Biology* **1996**, *65*, 1-44.

(59) Lux, S. E.; John, K. M.; Bennett, V. *Nature* **1990**, *344*, 36-42.

(60) Mosavi, L. K.; Cammett, T. J.; Desrosiers, D. C.; Peng, Z. Y. *Protein Science* **2004**, *13*, 1435-1448.

(61) Kajander, T.; Cortajarena, A. L.; Regan, L. *Methods in molecular biology (Clifton, N.J.)* **2006**, *340*, 151-170.

(62) Andrade, M. A.; Bork, P. *Nature Genetics* **1995**, *11*, 115-116.

(63) Andrade, M. A.; Petosa, C.; O'Donoghue, S. I.; Muller, C. W.; Bork, P. *Journal of Molecular Biology* **2001**, *309*, 1-18.

(64) Urvoas, A.; Guellouz, A.; Valerio-Lepiniec, M.; Graille, M.; Durand, D.; Desravines, D. C.; van Tilbeurgh, H.; Desmadril, M.; Minard, P. *Journal of Molecular Biology* **2010**, *404*, 307-327.

(65) Walsh, G. *Trends in Biotechnology* **2005**, *23*, 553-558.

(66) Nord, K.; Gunneriusson, E.; Ringdahl, J.; Stahl, S.; Uhlen, M.; Nygren, P. A. *Nature Biotechnology* **1997**, *15*, 772-777.

(67) Binz, H. K.; Amstutz, P.; Kohl, A.; Stumpp, M. T.; Briand, C.; Forrer, P.; Grutter, M. G.; Pluckthun, A. *Nature Biotechnology* **2004**, *22*, 575-582.

(68) Bandeiras, T. M.; Hillig, R. C.; Matias, P. M.; Eberspaecher, U.; Fanghaenel, J.; Thomaz, M.; Miranda, S.; Crusius, K.; Puetter, V.; Amstutz, P.; Gulotti-Georgieva, M.; Binz, H. K.; Holz, C.; Schmitz, A. A. P.; Lang, C.; Donner, P.; Egner, U.; Carrondo, M. A.; Mueller-Tiemann, B. *Acta Crystallographica Section D-Biological Crystallography* **2008**, *64*, 339-353.

(69) Cheng, B.; Cai, W. Q.; Yu, J. G. *Journal of Colloid and Interface Science*, *352*, 43-49.

(70) Shaw .P.Christopher , M. A. D., Volk Martin and Levy Raphae¨ l . *Acs Nano* **2012**, *6 ’* 1416-1426.

(71) Dujardin, E.; Peet, C.; Stubbs, G.; Culver, J. N.; Mann, S. *Nano Letters* **2003**, *3*, 413-417.

(72) Lee, S. W.; Mao, C. B.; Flynn, C. E.; Belcher, A. M. *Science* **2002**, *296*, 892-895.

(73) Shenton, W.; Pum, D.; Sleytr, U. B.; Mann, S. *Nature* **1997**, *389*, 585-587.

(74) Kasotakis, E.; Mossou, E.; Adler-Abramovich, L.; Mitchell, E. P.; Forsyth, V. T.; Gazit, E.; Mitraki, A. *Biopolymers* **2009**, *92*, 164-172.

CHAPITRE 5
PROTÉINES ARTIFICIELLES COMME INDUCTEURS DE MORPHOSYNTHESE

Résumé

Dans ce chapitre, nous exposerons comment les protéines α-Rep peuvent être utilisées pour modifier la morphologie de nanostructures métalliques. Les protéines α-Rep présente en premier lieu, une topologie 3D avec une haute stabilité thermique jusqu'à plus de 100°C dans l'eau, confirmée dichroïsme circulaire et calorimétrie (figures IV.9 et IV.10). Deuxièmement, l'augmentation du nombre de motifs répétés de séquence identique dans les protéines α-Rep dites "homorepeat" (α-Rep N9, N10 α-Rep et α-Rep N11) induit un changement systématique dans la structure 3D de la protéine (figure V.1) vers la formation d'une super-hélice. Troisièmement, parmi les protéines α-Rep disponibles de structure et de séquence connues, la protéine α-Rep A3 possèdent des motifs répétés de séquences d'acides aminés différentes entre elles et de celle des protéines *homorepeat* (figure V.1a). Par conséquent, ce jeu de protéines sera donc testé comme matrice pour la morphosynthèse de nanostructures métalliques. Par conséquent, notre objectif spécifique dans ce travail est d'exploiter les protéines α-Rep pour étudier comment la forme des protéines peut influer sur la forme des

nanostructures métalliques lorsque la protéine est utilisée comme moule (*template*) lors de la réaction. Par ailleurs, nous allons examiner l'influence de changements modéré de séquence. Pour les premières tentatives, nous avons utilisé des protéines α-Rep A3, α-RepN9, α-RepN10 et α-RepN11 qui sont représentés dans la figure V.1, comme agents de contrôle de la croissance des nanostructures Au.

Dans notre méthodologie expérimentale, nous avons fait varier plusieurs paramètres spécifiques tout en étudiant la variation morphologique des nanostructures. Les acides aminés qui composent les protéines peuvent être cationiques, anioniques ou neutres en fonction du pH de la solution. Le pH est un paramètre important que nous avons décidé de maintenir au cours de notre réaction. Généralement, la taille et la forme de la nanoparticule sont dépendent de la concentration et du rapport molaire entre le réducteur et le sel précurseur ainsi que de ceux relatif à l'agent stabilisant utilisé dans la réaction. Ainsi, le rapport molaire du sel d'or à la protéine est un paramètre que nous avons considéré dans notre réaction. Enfin, nous avons étudié l'influence de la présence d'agents co-réducteurs sur la morphologie des nanostructures en conservant aux protéines le seul rôle d'agent stabilisant.

Dans une première expérience, une concentration élevée de précurseur, de protéines et de sel d'or ont été mélangées et la réaction a été effectuée avec chauffage à trois pH différents à savoir : pH 4, pH 7 et pH 11. La réaction à pH 4 ne montrent aucun changement spécifique dans la couleur de la solution ainsi qu'aucun objet a été trouvé dans l'analyse par MET. La réaction à pH 7 montre un changement dans la couleur de la solution et l'analyse des échantillons TEM montrent clairement la formation de nanoparticules sphériques avec des nanobâtonnets. Toutes les protéines testées réduisent Au (III) en Au (0). Lorsque la même réaction a été effectuée à un pH plus élevé (pH 11), un grand nombre d'objets a été trouvé et il apparait que la réaction à pH 11 augmente le taux de réduction. Des nanoparticules sphériques très monodisperses de 15 nm de taille moyenne ainsi qu'un petit nombre de nanobâtonnets sont formés lorsque l'α-protéine Rep A3 a été utilisé comme agent de morphosynthèse (figure V.5). Cependant un grand nombre de nanobâtonnets de longueur variable a été obtenue en présence de la protéine α-Rep N9 (figure V.6). Les protéines α-Rep N10 et N11 réduisent l'or en formant respectivement des nanoparticules sphériques et un mélange de sphères et de nanobâtonnets (figure V.7). Enfin, des petites nanoparticules de taille 2-6 nm ont été observées dans toutes les réactions.

Des échantillons purs de protéines en solution à cette concentration ont été soumis une l'analyse TEM. La protéine α-Rep N9 présente une structure supramoléculaire en tubes cylindriques qui semble confirmés par des données SAXS en cours d'analyse. La comparaison des tubes protéiniques individuels avec les nanobâtonnets d'or montre qu'ils possèdent des longueurs comparables et que la largeur des nanobâtonnets est d'environ le tiers de celui des tubes protéiniques. Nous proposons donc que la formation de nanotubes Au s'effectue à l'intérieur de la cavité de la superstructure protéinique qui agit comme une matrice pour la croissance de nanobâtonnets unidimensionnels. La formation de nanobâtonnets beaucoup plus rares et moins uniformes a également été observée lorsque la protéine α-Rep A3 a été utilisé comme agent réducteur. Cependant, aucune superstructure n'a été observée quand la protéine pure a été analysée par TEM, au contraire, des protéines très isolées ont été imagées. La séquence d'acides aminés de la protéine α-Rep A3, fournie par analyse de sa structure cristallographique aux rayons X, montre que le tryptophane, la tyrosine, l'acide aspartique et la glycine sont présents en abondance. Ces acides aminés ont déjà démontré leur capacité à se lier à l’or et à le réduire. On interprète que la présence de nanobâtonnets résulte de la formation de graines maclées qui, en présence de la protéine α-Rep A3 qui induit une inhibition de la croissance de certaines facettes, croissent de manière anisotrope et conduisent à la formation de nanotubes. De même, lorsque la protéine α-Rep N10 a été analysée par TEM, au lieu de la longue structure cylindrique, une structure globulaire de protéines individuelles est obtenue qui abouti à la formation de petites nanoparticules d'or sphériques.

Dans une deuxième procédure, nous avons graduellement diminué la concentration de la protéine et fait varier le rapport molaire entre la protéine et l'or (1:10 et 1:100). Lorsque la protéine est utilisée dans ces conditions, la formation de particules sphériques, de nanoparticules de taille variable a été observée à pH 11. Il est intéressant que la réaction à pH réduit (pH 7) conduise à la formation de nanoparticules hexagonales et triangulaires (figures V.14 et V.15). Ce comportement est particulièrement évident dans le cas des protéines α-Rep N9 et α-Rep N11. L'analyse MET des échantillons de protéines pures à cette concentration montre une structure globulaire indiquant l'absence d'assemblages supramoléculaires tubulaires qui ne peuvent plus servir de template pour la croissance des nanobâtonnets. Toutefois, les protéines conservent une activité d'inhibiteur de croissance moléculaire et limitent la croissance des faces denses en atomes d'or {111} et permettre la croissance des faces {100} uniquement, ce qui conduit à la formation de nanoprismes triangulaires et

hexagonales (figure V.18d). L'analyse par CD et DSC révèle que les protéines ont perdu une part significative de leur structure tertiaire, mais ont conservé leur structure secondaire.

Dans la dernière partie, nous avons suivi l'effet d'agents co-réducteurs sur la morphologie des nanoparticules. Deux types d'expériences ont été effectués lorsque l'on utilise à la fois un fort agent de réduction tel que le borohydrure de sodium ($NaBH_4$) ou un agent réducteur faible, TCEP (tris (2-carboxyéthyl) phosphine) ou de l'acide ascorbique avec des protéines pour la réduction de l'or. La réaction de Au (III) et des protéines α-Rep avec $NaBH_4$ conduit toujours à une réduction rapide de l'or et à la formation de nanoparticules sphériques. TCEP est souvent utilisé comme agent réducteur pour briser une liaison disulfure quand elles sont présentes dans ou entre les protéines comme une étape préparatoire pour l'électrophorèse sur gel. Il possède trois groupes acide carboxyliques similaires à l'acide citrique qui peuvent réduire efficacement sel d'or. La réaction du sel d'or avec des protéines et TCEP donne des nanostructures en forme de chaînes ou de rubans dont la longueur varie de 0,5-1μm et de largeur 6-10nm en moyenne (figure V.20). Une fine couche de protéines d'une épaisseur de 2 nm est visible sur ces rubans. Les spectres d'absorption des échantillons montrent une bande transversale à 560 nm et une faible absorption à 965nm. Il est intéressant de signaler que lorsque l'acide ascorbique est utilisé comme agent de co-réduction aucune absorption de plasmon n'a été observée, mais on observe cependant des particules petites taille ~ 5nm par MET (figure V.23). Les spectres de fluorescence de ces échantillons lorsqu'ils sont excités à 415nm montrent une émission spectrale bleu à 485 nm et qui ne montre aucun signe de blanchiment sur une période de temps prolongée.

La morphologie des nanostructures peut être substantiellement affectée par la modification des conditions de réaction, tels que le pH et le rapport molaire entre la protéine précurseur et Au et la concentration de la solution de précurseur. La modification de ces paramètres conduits à la production de particules d'or de formes diverses (nanobâtonnets, nanoparticules hexagonales, triangulaires, y compris des agrégats de petite taille) avec différentes tailles (de quelques nanomètres à près de 1 μm). Toutefois, la variation de morphologie est aussi liée à la séquence et à la forme des protéines utilisées, ce que la librairie des protéines α-Rep nous permettra d'étudier en détail à l'avenir.

Bien que les protéines utilisées dans ce travail n'ont pas été sélectionnés pour leur reconnaissance spécifique des faces cristallographiques d'Au, elles montrent une forte

capacité à produire des nanostructures anisotropes. Les résultats de ces études indiquent que cet effet synergique de la structure des protéines et des différentes séquences d'acides aminés peut être utilisé avec succès pour moduler la taille et la forme des nanostructures d'Au. Ainsi les protéines α-Rep peuvent servir de meilleure matrice pour la synthèse de nanostructures plasmoniques anisotropes.

CHAPTER 5
ARTIFICIAL PROTEINS AS MORPHOSYNTHETIC AGENTS.

5.1. Synthesis of noble metal nanostructures by using α-Rep proteins as a template.

In section 4.4 we have described the selection and structural characterization of α-Rep proteins performed by our collaborators, in Prof. Ph.Minard's group. In this chapter we will expose how these α-Rep proteins can be used to tune the shape of metal nanostructures.

5.1.1 Objective.

α-Rep proteins show well folded 3D topology with high thermal resistance confirmed by CD and DSC analysis (*Fig IV.9* and *Fig IV.10*). In addition, as the numbers of repeats increases in α-Rep homorepeat proteins, they induce a systematic change in the 3D structure (*Fig V.1*) of the protein (α-Rep N9, α-Rep N10 and α-Rep N11). Moreover among the available α-Rep proteins of known structure and sequence, α-Rep A3 protein possess different amino acid

sequence (*Fig V.1a*) compared to the homo repeat proteins. Therefore, for the morphosynthesis of plasmonic metal nanostructures, these proteins can serve as a better template. Hence, our specific objective in this work exploiting α-Rep proteins is to study how shape of the proteins can effectively influence the shape of the metal nanostructure when the protein is used as a template during the reaction. Incidentally, we will examine the influence of moderate sequence change. For the first attempts in this rational approach, we have used α-Rep A3, α-RepN9, α-RepN10 and α-RepN11 proteins that are represented in *Fig V.1* as a template for Au nanostructure growth.

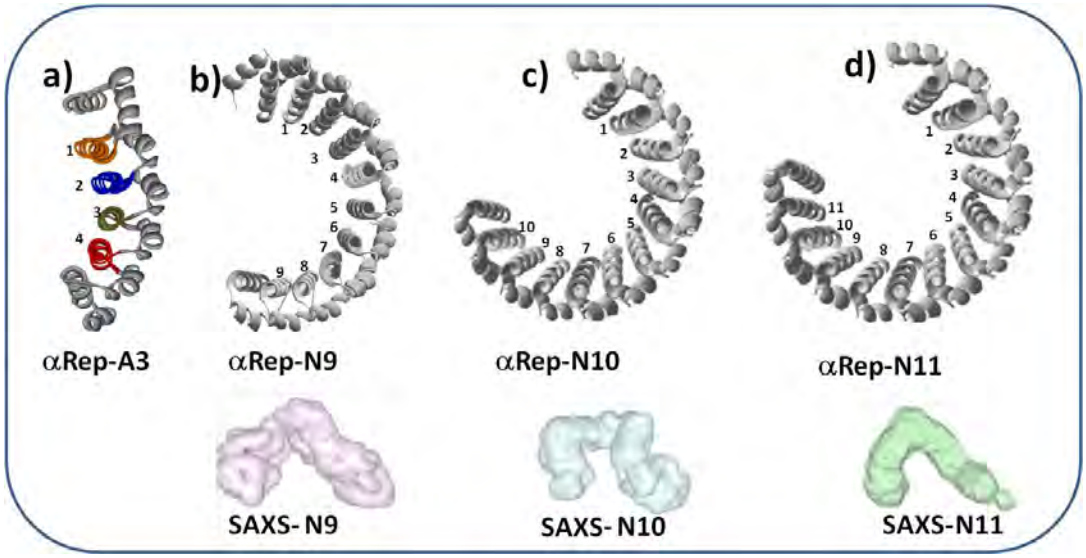

Fig V.1*: a) X-ray crystallographic structure of α-Rep A3 protein. b, c, d) Model diagram and SAXS structure of a) b) α-Rep N9, c) α- Rep N10 and d) α- Rep N11proteins.Courstey of D.Durand and Ph.Minard IBBMC Orsay.*

5.1.2 Methodology.

There are very few reports on the morphosynthesis of plasmonic nanoparticles by using proteins.[1-3] Most reported studies lead to spherical or pseudo spherical nanoparticles, isolated or delusively but randomly packed. Thus it is difficult to assume at what conditions nanoparticles with different morphology could be generated. In order to use α-Rep proteins as morphosynthetic agents, we considered a few specific parameters to vary while monitoring if control over the shape of the nanostructures could be achieved. It is well-known that the amino acids that make up proteins may be positive, negative, neutral, or polar or hydrophobic in nature, and this together gives a protein its overall charge. At a pH below their Isoelectric point (pI), proteins carry a net positive charge, pH above their pI they carry a net negative

charge. Hence pH was one important parameter which we decided to maintain during our reaction. The pI of A3, N9, N10 and N11 α-Rep proteins were calculated theoretically and found to have a value 5.43, 5.00, 5.11, and 5.07 respectively (*Table IV.4*). Hence at physiological pH these proteins are slightly acidic in nature. Generally, size and shape of the nanoparticle is mainly dependent on the concentration of reducing as well as stabilizing agent used in the reaction. Thus molar ratio of gold to protein was also one other parameter which we considered in our reaction.

Finally, we have studied the influence of the presence of co-reducing agents on the morphology of nanostructures by using protein as a stabilizing agent. Initially, we performed reaction with very low volume but with high concentration of α-Rep proteins, mainly at pH4, pH7 and pH11. In the later experiments we have subsequently reduced the protein as well as gold concentration and also we have introduced co reducing agents in the reaction mixtures.

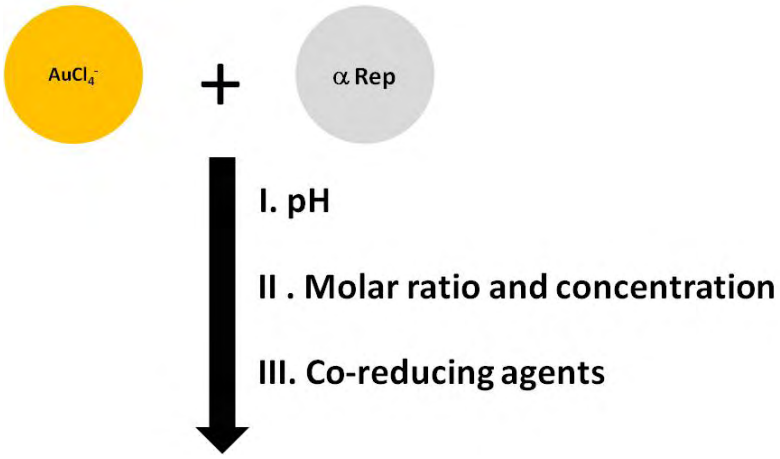

Fig V.2: *Schematic diagram illustrating the 3 main experimental parameters that have been considered for the morphosynthesis of Au in the course of this work.*

5.2. Effect of pH on the shape of nanoparticles

In the first method, the reaction pH was maintained at pH4, pH7 and pH11 by using 0.1M HCl and Nap Buffer of concentration 50mM.

5.2.1. Procedure.

The reaction was performed in 500µL microtubules. 25µL of protein (230µM for α-Rep A3, 70 µM for α-RepN9, 40 µM for α-Rep N10 and 40 µM for α-Rep N10) solution were treated

with 25µL of aqueous $HAuCl_4$ solution of 100mM. Later, about 50µL 0.1M HCl were added to bring the pH of the solution to pH4. For the reaction at pH7 and pH11, the same volume of protein and Au (III) solutions were mixed together and 50 µL of sodium phosphate buffer solution of pH 7 and pH 11 was added. The concentration of Au (100mM) was always kept high and the molar ratio between Au and protein was different for different protein, namely 1:500 for α-RepA3, 1:1500 for α-RepN9, 1:2500 for α-RepN10 and α-RepN11. The reaction medium was heated at 50^{o}C for 12 hour and then the reaction was allowed to stand at room temperature for 24 hour. Interestingly no change in the color of the solution was observed when the reaction of α-Rep proteins with the Au (III) precursor was performed at acidic pH. The TEM analysis of the samples never yielded any object and confirmed that no reaction occurred between Au (III) and protein at pH4. On the contrary a color change was observed for reactions at pH7 and pH11.The samples were characterized mainly by TEM.

5.2.2. TEM characterization.

When α-Rep A3 protein was reacted with Au (III) solution at pH7, the color of the solution transformed from yellow to pale pink. TEM analysis of the sample clearly showed the formation of spherical nanoparticles as well as nanorods with little irregularity in shape (*FigV.3*).The length and width of the of the nanorods were not uniform but they were found to be crystalline, confirmed by electron diffraction analysis (*Fig V.3e*).

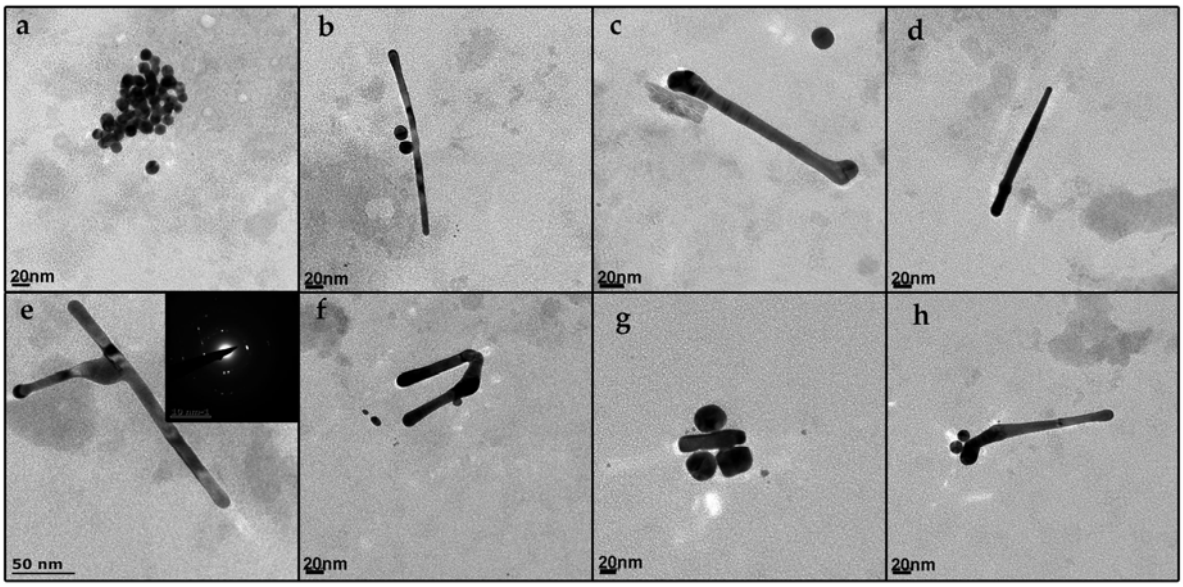

Fig V.3: *TEM images of α-Rep A3 protein reduced Au nanostructures at pH 7. Nanorods and spherical nanoparticles were found. Scale bar a), b), c), d), f), h) - 20nm g) 10nm and e) 50 nm.*

When Au (III) solution was reduced at pH7 with α-Rep N9 proteins, change in the color was observed from yellow to pale pink. TEM images revealed the formation of very small nanoparticles of size 2-4nm (*Fig V.4a*) along with bigger spherical nanostructures of diameter 15-22 nm in small amount (*Fig V.4b*). It appears that, these small nanoparticles (2-4nm) were formed specifically in the small cavity of the proteins where proteins act as a stable template for the growth of these nanoclusters. Very small amount of nanorods were also found along with spherical nanoparticles in TEM (*Fig V.4c*).The size distribution measurement confirmed that many more small particles were present in the sample compared to 22nm sized particles.

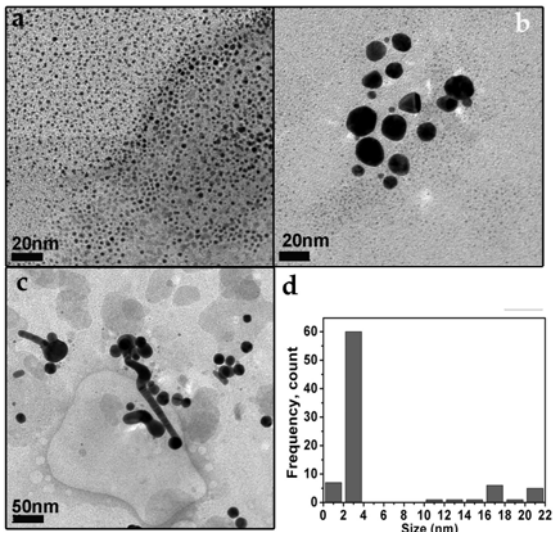

Fig V.4: *a,b,c) TEM images of α-Rep N9 protein reduced Au nanostructures at pH 7.d) Size distribution analysis showed spherical nanoparticles of size15-22nm along with 2-4nm small nanoclusters.*

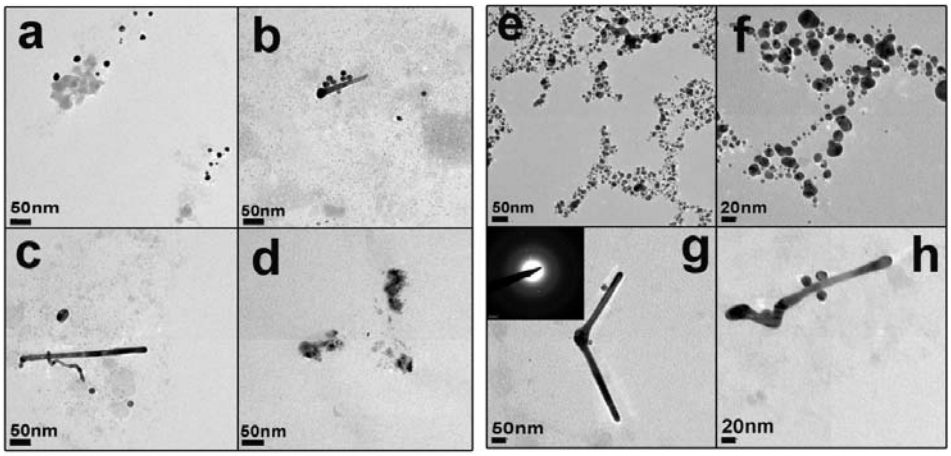

Fig V.5: *a), b), c), d)TEM images of α-Rep N10 protein reduced Au nanostructures at pH 7 and e), f), g), h)α- Rep N11 protein reduced Au nanostructures at pH 7.*

Following the same protocol, when α-Rep N10 protein was used as a reducing agent for Au (III) solution at pH 7, formation of spherical nanoparticles along with very rare number of nanorods were observed (*Fig V.5 a, b, c*). We have also observed small amount of precipitate or a solid mass on the grid, probably due to the excess of buffer salt in the reaction mixture. TEM images of α-Rep N11 protein reduced Au (III) at pH 7, showed nanoparticles of varying size and shape *(Fig V.5 e, f)*. Very small numbers of crystalline nanorods were also observed (*Fig V.5g, h*).

Thus reaction at pH7 with α-Rep proteins and Au (III) precursor showed uncontrolled effect and not seem to be more reliable. This could be an effect of the amino acid lysine (Lys) which is present in large number at convex surface of the proteins. At pH7, protonation of amine group of lysine along with adsorption of $AuCl_4^-$ takes place, but the pH needs to be high enough to release $AuCl_4^-$ towards another facet of protein where most of the reducing amino acids are present.[1, 3] Hence less number of objects were observed in TEM because of the low diffusion of Au (III) which in turn reduced at concave face. Hence in our next protocol we maintained the solution pH at 11 in order to increase the reduction of Au (III) by α-Rep proteins.

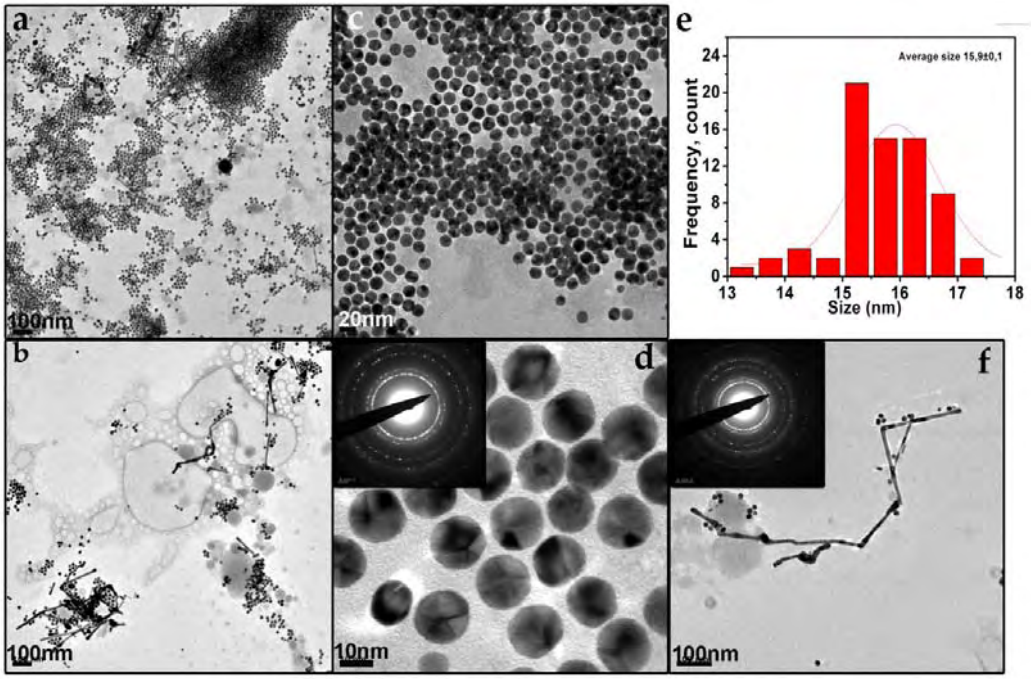

Fig V.6: *TEM images of α-Rep A3 protein reduced Au nanostructures at pH 11.Size distribution analysis showed average size of spherical nanoparticle as 15.9nm.*

The reaction of α-Rep A3 protein with Au (III) solution at pH 11 resulted in color change from yellow to dark pink. The TEM analysis of the sample revealed the presence of large

number of spherical nanoparticles with fewer numbers of nanorods (*Fig V.6*).Statistical size distribution analysis on these images showed average particle diameter of the spherical nanoparticles were 15nm (*Fig V.6e*), and they were highly crystalline as confirmed by electron diffraction patterns (*Fig V.6d*). The obtained nanorods or nanowires were highly distorted and found to have a length in a range 300-600nm. Electron diffraction pattern showed these nanorods were highly crystalline (*Fig V.6f*).

Similarly a deep black color solution was obtained when α-Rep N9 protein was used as a reducing agent at pH11. The corresponding TEM images showed a large number of nanorods as well as nanowires (*Fig V.7*). Similar with the previous result, these nanorods vary to a large extent in length (300-600nm) and width (7-20nm) (*Fig V.7 c, d, e, and f*). Spherical nanoparticles of diameter 28±2 nm as well as small nanoclusters were also observed along with nanorods (*Fig V.7b*).

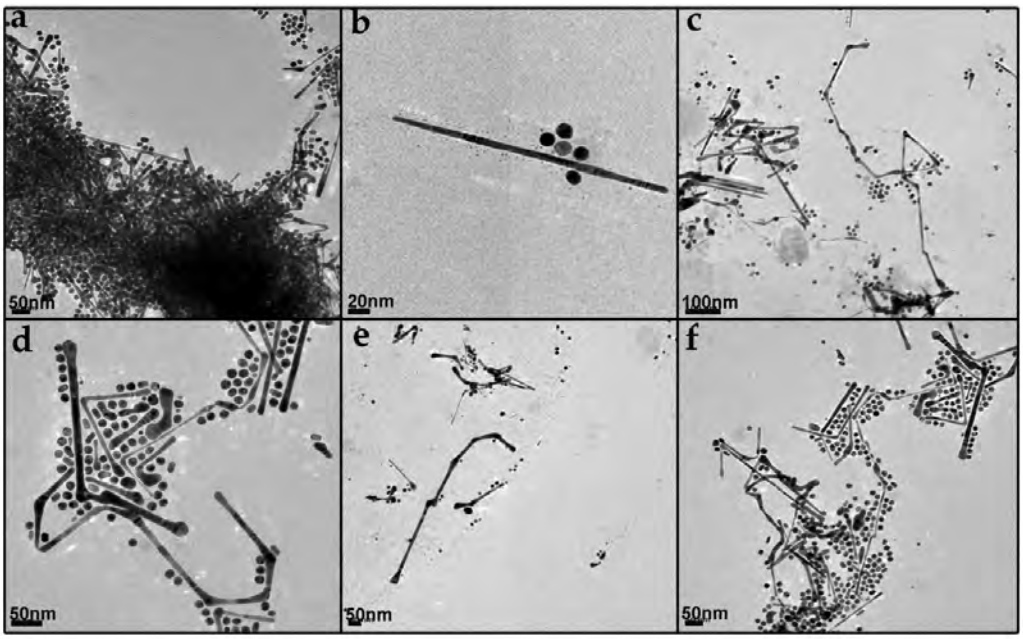

Fig V.7: *TEM images of α-Rep N9 protein reduced Au nanostructures at pH 11. Spherical nanoparticles along with nanorods and nanowires were found.*

Au (III) reduction in the presence α-Rep N10 protein at pH11 resulted in the formation of very small nanoclusters along with spherical nanoparticles of size varying from 15to30nm. These nanoparticles were found aggregate systematically. In case of α-Rep N10 protein the change in the pH of the reaction from pH 7 to pH 11 does not improve the morphology or yield of the products.

Reaction of α-Rep N11 protein with Au (III) at pH 11 showed color change from yellow to dark pink. Spherical nanoparticles (*Fig V.8g*) of average diameter 15±2nm along with nanorods of varied length (*Fig V.8 f, h*) were observed in TEM images. Nanoclusters of size 2-5 nm (*Fig V.8e*) were also found in TEM.

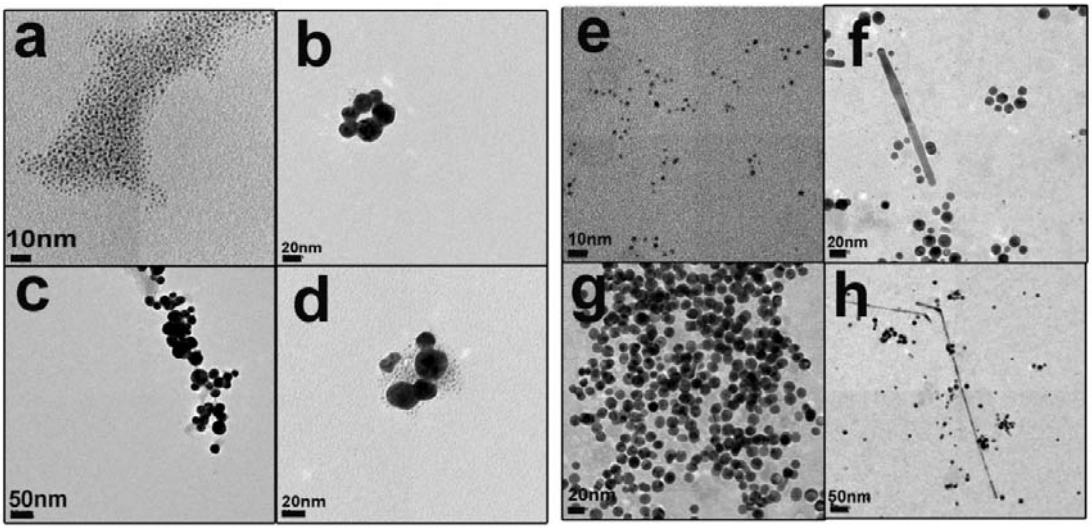

Fig V.8: *a, b, c, d) TEM image of α-Rep N10 protein reduced Au nanostructures at pH 11. e, f, g, h) α-Rep N11 protein reduced Au nanostructures at pH 11.Scale bar a) 10nm, b) 50nm, c), d) 20nm, e), h) 20nm, f) 50nm, g) 10nm.*

In order to get a better understanding in the phenomena involved in the formation of these structures, we examined the X-ray crystallographic structure of α-Rep A3 protein (*Fig V.9d*). It contains four repeats, each of them were different from their amino acid sequence (*Table VI.1*). The amino acids such as Tryptophan (Trp), Aspartic acid (Asp), Glycine (Gly) which were present in the concave face of α-Rep A3 *(Fig V.9d)* have previously been shown to have a large affinity for metallic gold.[4-7] The sequence analysis of homorepeats (α-Rep N9,α-Rep N10 and α-Rep N11) also showed the presence of Trp, Asp, Gly in their repeats (*Table IV.4*). The reaction at pH4 corresponds to the condition where $AuCl_4^-$ can be better selected by Lysine (Lys) onto α-Rep proteins. Yet no reduction was observed. This could be due to the weak reducing action at low pH. The experiments showed that α-Rep proteins acquire good reducing ability at pH7 and pH11. At higher pH, Asp, Trp and Tyrosine (Tyr) can better reduce the Au(III), which can better diffuse towards concave facets because it is less sequestered electrostatically.

The size of the nanorods formed by the reduction of Au (III) with α-rep N9 proteins has sizes similar to the protein superstructure (*Fig V.9b).* If we closely examine the model structure of

α-rep N9, it has a semi circular shapes which can self assemble in a coiled shape with inter protein-protein interaction to form rod like superstructure with a cavity in side (*Fig V.9e).*

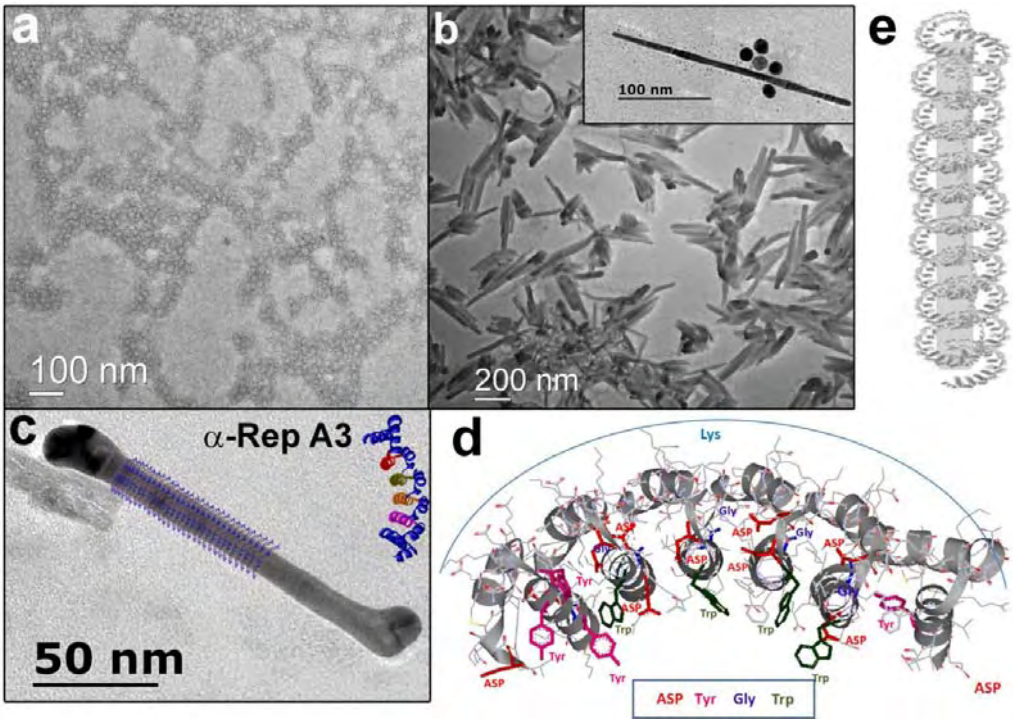

Fig V.9: *TEM images of negatively stained a) α-Rep N10 protein, b) α-Rep N9 protein, inset show the image of Au nanorod formed by the reduction of α-rep N9 protein at pH 11. c) Illustration of growth inhibition process by α-rep A3 protein for the formation of Au NRs and d) crystal structure of α-Rep A3 showing active amino acids responsible for the formation of Au nanostructures. e) Schematic diagram representing Au nanorod formation in a cavity of α-Rep N9protein superstructure.*

The formation of Au nanorods can take place by controlled growth of Au in self assembled protein templates. The nucleation of Au can occur specifically in these cavities at specific pH because of the reducing Trp and Tyr amino acids present in these cavities and hence resulting in the formation of Au nanorod. It is therefore possible that $AuCl_4^-$ precursor is sequestered by the outer Lys-rich surface but slow diffusion across the protein wall, the gold salt is efficiently reduced by the Trp and Tyr amino acid. This scenario is drawn in analogy with the previous work done by Bittner and colleagues, where the sequestration of nickel inside the cavity of tobacco mosaic virus (TMV)[8, 9] was combined with the adsorption of Pt on the outer side and therefore the redox reaction took place across the protein wall and resulted in the formation of nanowires. In our case these templates are not visible after the formation of Au nanorods because they are probably unfolded during the redox process. The overall TEM analysis

showed that the formation of nanorods was more in case of α-Rep N9 and α-Rep A3. It is also possible that these α-rep proteins acts as a growth inhibitor at particular crystallographic face during the growth of nanostructures. As described in *Fig V.9c*,α-Rep A3 proteins can restrict the growth at {111} face , and in this case only {100} face can grow which lead to the formation of Au nanorods. Small numbers of nanorods and low yield of nanoparticles were also found with the reduction of Au (III) by α-rep N11 and α-rep N10 respectively. From the SAXS results, we know that oligomerisation of these proteins has a destabilizing effect on the global protein folding process. Hence there is a possibility that larger folding of α-*R*ep N10 compared to other α-*R*ep proteins has limited the efficient functioning of amino acid (*Fig V.1c*). Monodispersed spherical nanoparticles were also formed with the controlled nucleation of Au by α-*R*ep proteins.The above reaction with protein and gold was performed at very low volume and at high concentration of the protein and Au precursors. But this protocol consumes large amount of proteins for the reaction with Au (III). Hence we have modified our procedure by subsequently lower the concentration of proteins. Hence we can study the effect of concentration on the morphology of nanostructure formed.

5.3. Effect of concentration on nanoparticle morphology.

Fresh experiments were performed with artificial proteins and gold solution by maintaining two molar ratio (protein: Au) namely at 1:10 and 1:100 and at two different pH, pH7 and pH11 with reduced concentration of proteins. The temperature was maintained at 40^0C in a thermo mixer and reactions were performed in a 2mL eppendorf tube. The Au(III) concentration was varied from 100μM to 10μM in order to see the effect on growth process under the influence of proteins.

5.3.1. Procedure.

500uL of 10μM protein was mixed in 2ml eppendorf tube with 500uL of 100μM gold solution (Protein: Au, 1:10). This solution was brought to pH7 or pH11 by adding 1mL of NaP buffer of concentration 50mM. The above solution was heated at 40deg for 24hour in a thermo mixer. Change in the color of the solution was observed and the temperature was cooled down and samples were analyzed by TEM and absorption spectroscopy. The same reaction was performed by adding 500uL of 10μM protein to 500uL of 1mM gold solution at pH 7 and pH 11 (Protein:Au,1:100).

5.3.2. UV-Vis spectroscopy and TEM analysis of samples (pH 11)

The reaction at pH 11 at two different concentration of the Au precursor (Protein: gold, 1:10 and 1:100) showed no change in the color of the solution except for α-*R*ep N9 protein, which turned to pale pink (1:100) (*Fig V.10b*).

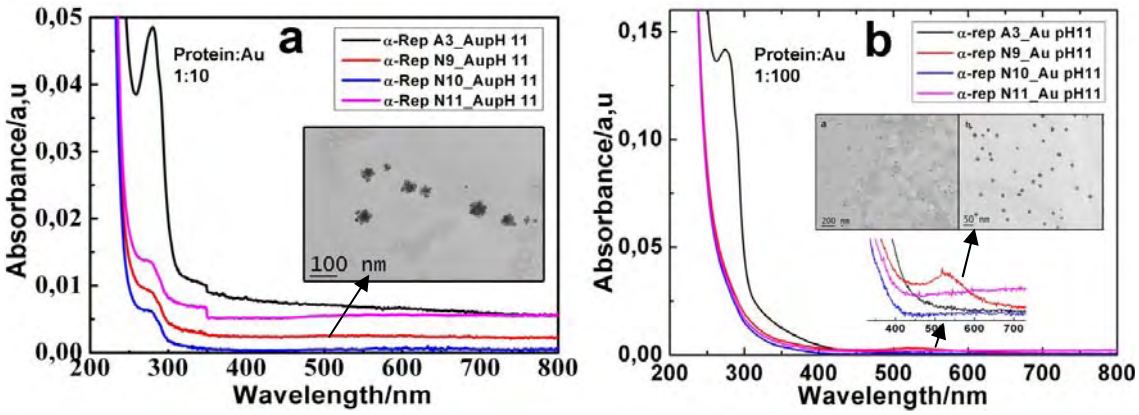

Fig V.10: *UV-Vis spectra of α-Rep protein reduced Au nanostructures at pH11 at two molar ratios and inset show corresponding TEM image of α-Rep N9 reduced Au nanostructures at pH 11.*

UV-Vis spectra of the sample (1:10) showed no plasmon band of absorption in α-*R*ep protein reduced Au solution (*Fig V.10a*). The protein peak at 280nm was observed in all the cases with different intensity. When these colorless samples were analyzed by TEM, no particles were found except in case of α-*R*epN9-Au which showed aggregated nanoparticles of size ~60nm (*Fig V.10a*). When the molar ratio between the protein and Au precursors was increased to 1:100, very small intensity plasmon band at 528nm was observed for α-*R*epN9 protein reduced Au solution (*Fig V.10b red*). The TEM analysis of α-*R*epN9-Au sample showed homogeneous particles of size 25-30nm (*Fig V.10b*). Although no plasmon peak was observed in α-*R*epN10-Au and α-*R*ep N11-Au samples, TEM analysis revealed the presence of a very small number of spherical nanoparticles.

We analyzed the α-*R*epN9-Au sample by DSC and CD to determine the integrity of proteins after the reaction with Au (III). DSC spectra clearly showed a signal at least 10 times lower than the pure protein signal (*Fig V.11a*). The Tm shift was observed from 96.05°C (apo) to 107.69°C (gold) suggesting protein stabilization for α-*R*epN9-Au reduced sample. The CD analysis of α-*R*epN9-Au showed some differences in signal (*Fig V.11b*) which supports the DSC, but further work is needed to clearly determine the exact mechanism.

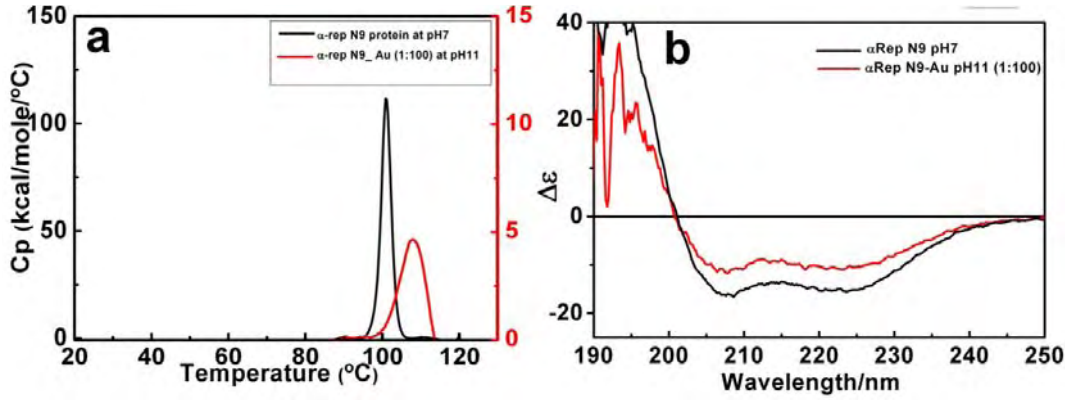

Fig V.11: *a) DSC and b) CD spectra of α-RepN9-Au sample at pH 11 (red) compared with pure α-RepN9 protein sample (black) (pH 7).*

This observation clearly suggested that the protein had lost its tertiary as well as secondary structure after the reaction with gold at pH11. Similar results were obtained with the other α-Rep proteins when they were used as a reducing agent for Au (III) at pH 11. Hence reaction at pH 11, mostly denature the proteins which in turn fail to affect on the morphology of the nanostructure.

5.3.3. UV-Vis spectroscopy and TEM analysis of samples (pH7, 1:100).

The reduction of Au (III) with α-*R*ep proteins at pH7 showed change in the color of the solution from colorless to pale pink except for α-*R*ep A3-Au where no change in the color was observed. UV-Vis absorption spectra showed 535nm plasmon absorption band for samples prepared in the presence of α-*R*ep N9, and α-rep N11 reduced Au, and a slightly increased absorption band at 540nm for the α-rep N10-Au sample.

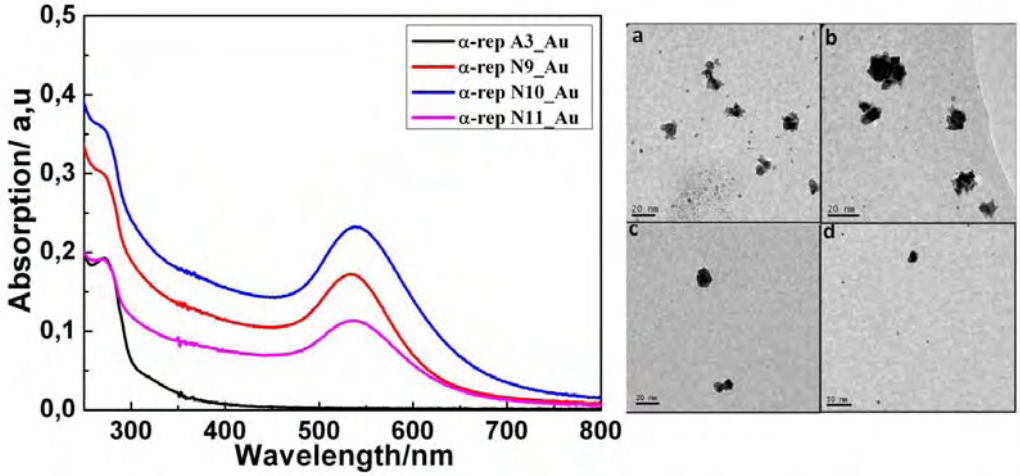

Fig V.12: *UV-Vis spectra of α-Rep protein reduced Au at pH 7 with Protein: Au, 1:100 and TEM images of a, b) α-RepN9 reduced and b, c)α- RepN11reducued Au samples.*

The intensity of plasmon absorption was different for the samples prepared with different proteins. No plasmon absorption band was visible in case of α-*R*ep A3-Au (*Fig V.12*).We observed the absorption band for protein at 280nm in all the cases.The TEM observation revealed that nanoparticles formed in case of α-*R*ep N9 reduction were spherical but tended to grow and form cluster like structures (*Fig V.12a, b*).These clusters were 20-25 nm in size. When performed with α-*R*ep N10 and α-*R*ep N11 proteins as a reducing agent, spherical nanoparticles were obtained with size ranging from 15-20nm (*Fig V.12c, d)*. The TEM analysis of α-*R*ep A3 reduced Au sample did not show any particles. Hence reaction at pH 7 show the reduction of Au (III) but no specific control on the morphology was observed, probably because of the high concentration of Au (1:100) lead to an uncontrolled nucleation in presence of proteins.

5.3.4. TEM analysis and UV-Vis spectroscopy of samples (pH7, 1:10)

The outcome of the reaction was slightly different when the molar concentration of Au (III) was reduced consistently at pH 7. The change in the color of the solution from colorless to pale pink was observed in case of α-*R*epA3, α-*R*ep N9 and α-*R*ep N11 reduced Au solution, whereas α-*R*epN10-Au solution showed no change in the color of the solution. This behavior was different when compared to the previous case where all the homorepeats showed reduction ability except α-*R*ep A3. Small spherical nanoparticles of size 30-50nm were found in TEM in case of α -*R*ep A3 protein reduced Au nanostructures (*Fig V.13)*.

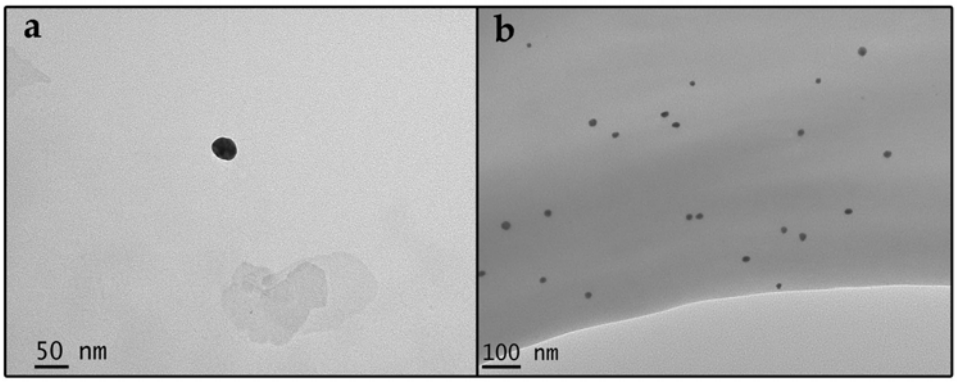

Fig V.13: *TEM images of α -Rep A3 protein reduced Au nanostructures at pH 7.*

The TEM analysis of α-*R*ep N9 protein reduced Au solution exposed the formation of anisotropic nanostructures. Very small numbers of particles were observed in TEM but the observed particles were mostly hexagonal and triangular in shape (*Fig V.14*). These particles

were found to have a size in range of 40-50nm. Closer view by TEM analysis revealed the presence of thin layer of protein around these particles and they can be visible even without staining (*Fig V.14a*).

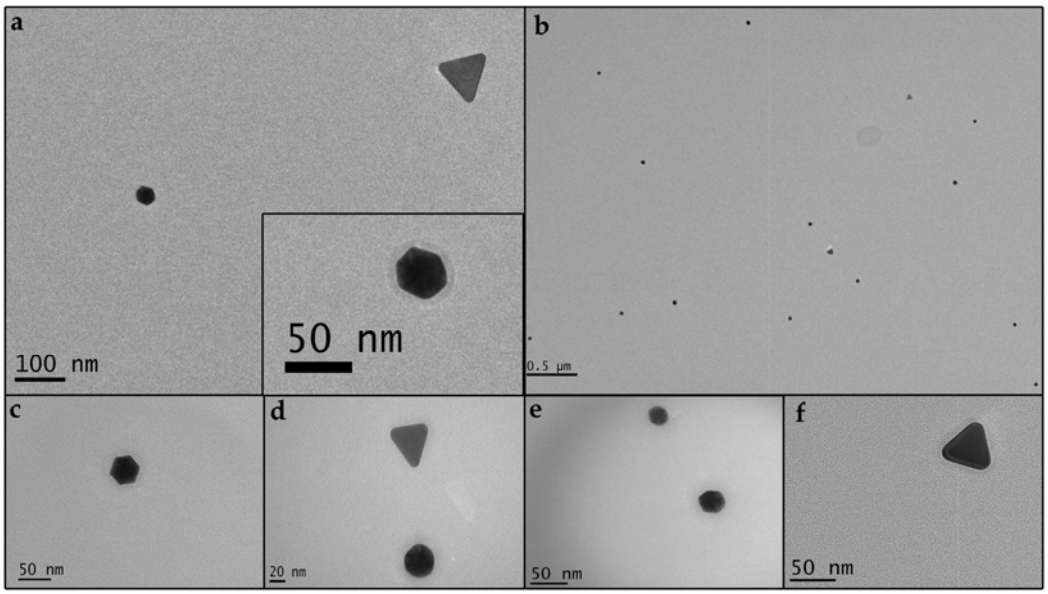

Fig V.14: *TEM images of α-Rep N9 reduced Au nanostructures at pH 7.formation of hexagonal and spherical nanoparticles can be seen.*

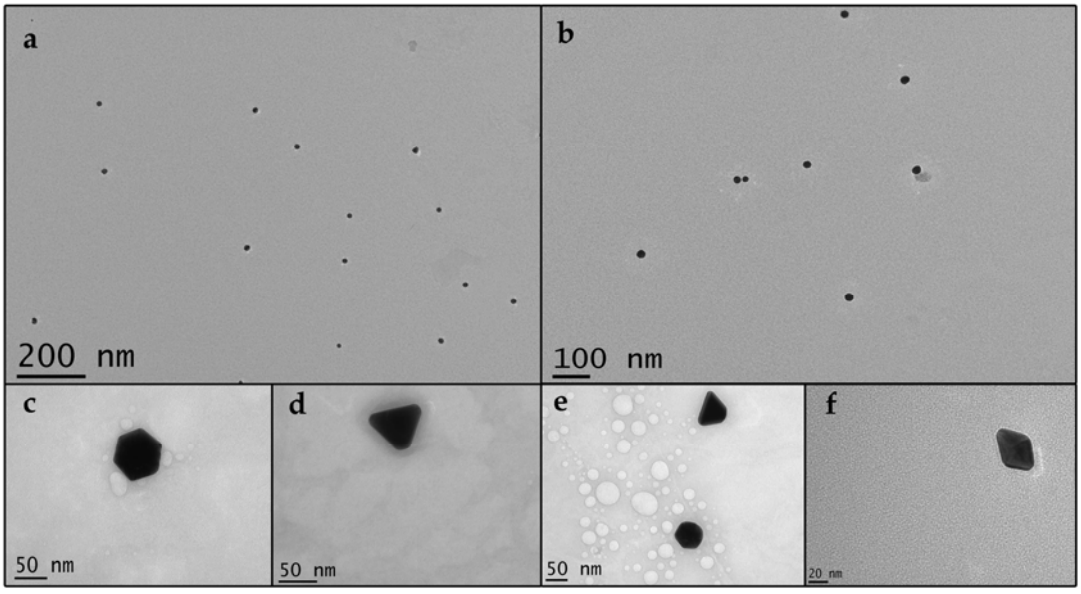

Fig V.15: *TEM images of α-Rep N11 reduced Au nanostructures at pH 7.Hexagonal and triangular nanoparticles of size 40-50nm was found.*

Similarly in case of α-*R*ep N11, we obtained hexagonal and triangular nanoparticles with minimum number of spherical nanoparticles **(***Fig V.15*). The sizes of the triangular as well as hexagonal nanoparticles were similar as found in the previous case, i.e. 40-50nm, moreover

thin protein layer can also be visible around these particles **(***Fig V.15d*). It is interesting to note that the decrease in concentration of protein never yielded any nanorods or nanowires instead it influenced for the formation of hexagonal and triangular nanoparticles. This reveals the absence of penta twined seeds and the preferential attachment of protein to {111} facets. Here again α-*R*ep N10 protein showed no specific activity in presence of Au (III) precursor.

UV-Vis spectra of Au nanostructures obtained with the assistance of proteins (1:10) at pH7 is shown in *Fig V.16* with closer view of the same spectrum. Small plasmon band of absorption was found at 520nm in case of α-*R*ep A3, α-*R*ep N9 and α-*R*ep N11 protein reduced Au sample followed with small absorption peak at 650nm. Protein absorption band at 280nm is also present in these samples whereas α-*R*ep N10-Au showed no plasmon absorption band.

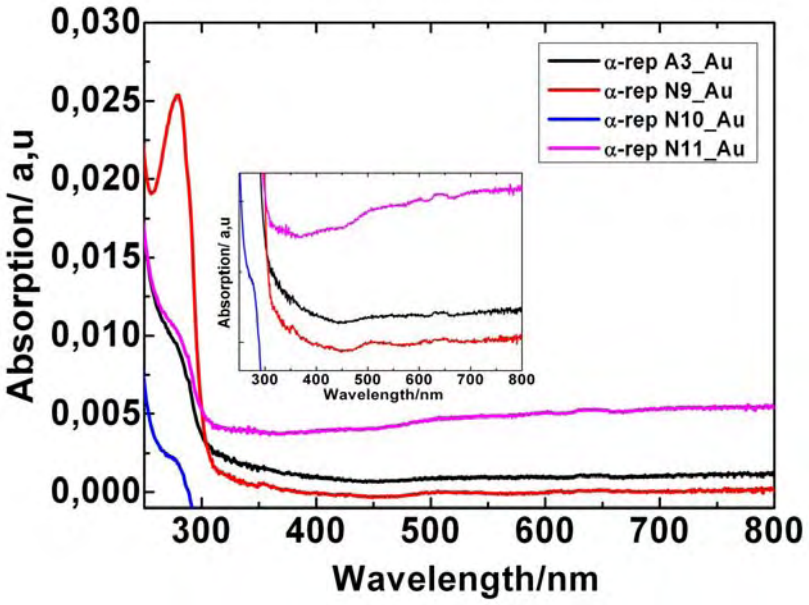

Fig V.16: *UV-Vis spectra of protein reduced Au nanostructures at molar concentration protein: Au, 1:10 and at pH 7. Inset shows enlarged spectra of the same.*

The Thermal analyses of these samples were performed in order to investigate whether *α-Rep* proteins were still intact with their stable structure after the reaction with Au (III).

5.3.5. DSC and CD analysis.

Clearly, in all the cases the DSC signal was lost upon gold particles growth. A small peak was preserved at the normal Tm shift in all cases revealing that some proteins were intact but a most of them had been oxidatively unfolded. Concerning the remaining folded proteins, a Tm shift was observed for N9 from 100.7°C (apo) to 104.1°C (gold) suggesting protein

stabilization (*Fig V.17a*). The same effect was not observed for N11 protein (*Fig V.17b*). In both the cases a small and broad signal appearing at lower temperature was probably due to unfolded proteins. A similar behavior was found in DSC spectra of α-Rep A3 and α-Rep N10 reduced Au samples. The summary of the DSC analysis is given in the *Table V. 1.*

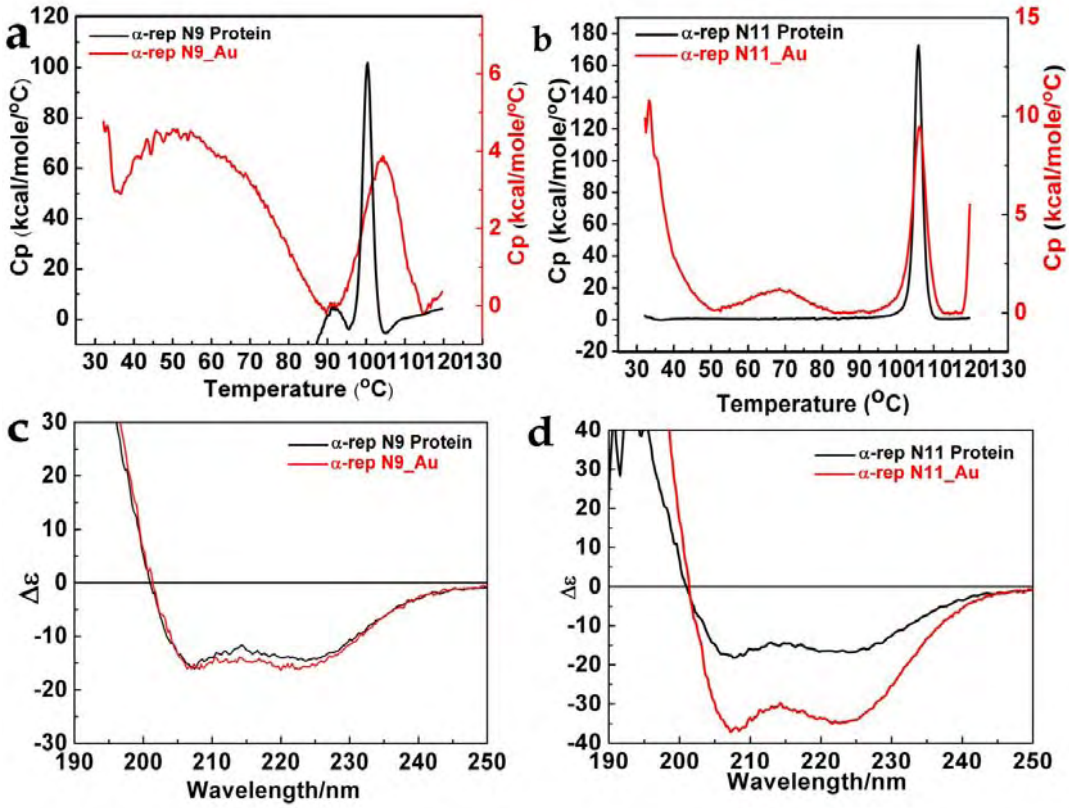

Fig V.17: *Differential Scanning Calorimetry (DSC) spectra of a) α-RepN9 b) α-Rep N11 and CD spectra of c) α- Rep N9 and d) α-Rep N11 reduced Au nanostructures (red) at pH 7 in comparison with pure protein samples (black).*

Protein	Tm (apo) (°C)	Tm (gold) (°C)
α-Rep A3	80.82	89.1
α-Rep N9	100.7	104.1
α-Rep N10	98.05	102.3
α-Rep N11	105.1	106.1

Table V. 1: *Table summarizing DSC analysis of α-Rep pure proteins compared to protein reduced Au nanostructures.*

In order to know whether proteins have conserved their secondary structure, we have performed circular Dichroism analysis. All spectra of the protein reduced Au nanoparticles were superimposed with the spectra of pure proteins (*Fig V.17c, d*). The characteristic signal of all α-*R*ep proteins was observed with a maximum absorbance at 192 nm and minima at 209 nm and 222 nm (*Fig V.17 c, d*). The CD spectra of Au nanostructures (red) produced in presence of α-*R*ep proteins at pH 7, showed that the proteins still possessed their secondary structure and further experiments needs to be carried in order to understand the increase of intensity in CD signal ((*Fig V.17 d*).

These results obtained at pH7 are completely different when compared to the reaction at pH 11 where absorption tends to decrease after the reaction with Au (III) (*Fig V.10b).* Reaction at pH 11 at both the molar ratio of protein and Au (III) precursors (1:10 and 1:100), resulted in complete denaturation of the proteins. At pH 11, the proteins were highly de-stabilized as confirmed by DSC and CD experiments. Although some proteins still show reducing ability (α-*R*epN9-Au, α-*R*epN10-Au and α-*R*epN11-Au), because of the reducing ability of amino acids, but the control over the morphology of nanoparticles is almost in existent. Hence we obtained mostly spherical nanoparticles of different size. Au (III) reduction at pH 7 was quite interesting where we saw two different events. When the molar concentration of the protein and Au (III) was maintained at 1:100 molar ratios, formation of spherical as well as aggregates of nanoparticles were observed. The size of these particles and nanoparticle-aggregates were found similar with triangular and hexagonal nanoparticles. This could be due to the uncontrolled nucleation because of the large amount of Au ions present in the solution and hence proteins were unable to control the reaction, lead to the growth of irregular or simple morphology of the particles.

When the same reaction are performed with reduced Au concentration at pH7 and molar ratio (1:10), controlled crystal growth of Au occurred with the influence of partially stable proteins which resulted in the formation of triangular and hexagonal nanoparticles. A quantitative comparison of CD data of these samples with pure protein samples showed that all characterized proteins samples have the same ellipticity as per residue basis. This clearly suggests that protein has conserved its secondary structure even after the reaction with gold and indicates that thermal unfolding of secondary structure in these proteins were reversible.

Hence, performing reaction at pH 7, could able to conserve secondary structure of the protein which results in anisotropic growth of Au nanostructure.

In order to get further insight on the possible pre organization of the protein in such diluted conditions, we performed TEM analysis of the diluted protein samples by staining with Phosphotungstic acid. The images obtained from TEM showed a change in the morphology of proteins assembly when compared to the previous case of concentrated solutions. Interestingly no super structure was observed in case of α-*R*ep N9, but spherical particles of size 3-5nm was found (*Fig V.18a)*. Whereas α-*R*ep N10 proteins showed similar kind of spherical particles as observed before (*Fig V.18b).*

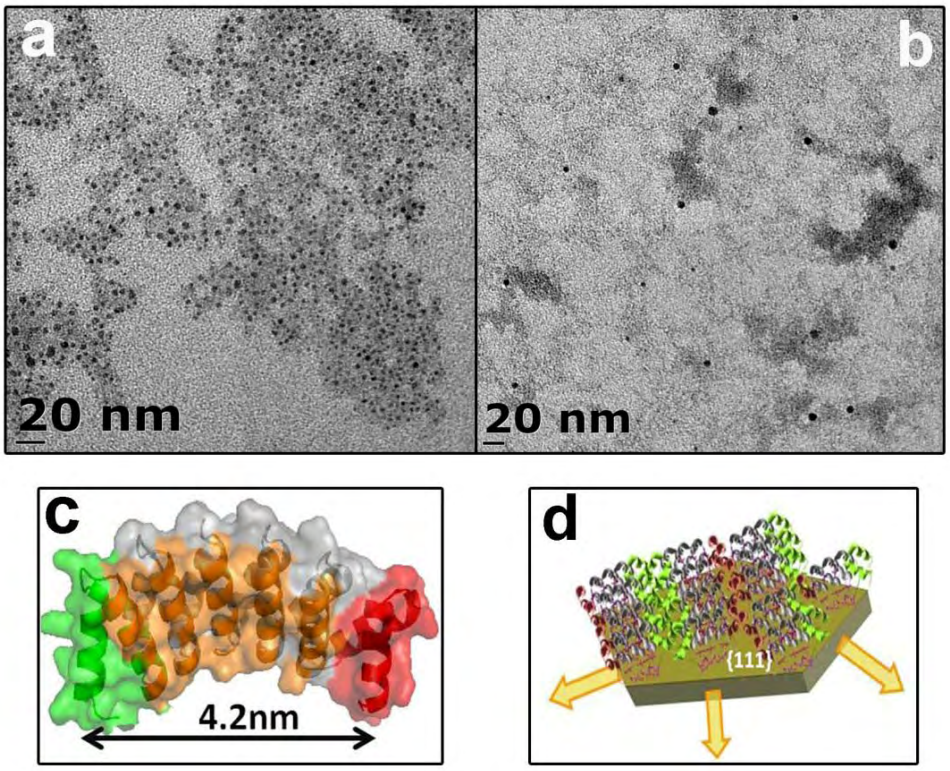

Fig V.18: *Phosphotungstic acid stained TEM image of a) α-Rep N9 and b) α-Rep N10 proteins at low protein concentration. c) Crystal structure of α-Rep A3 proteins with a measured the distance between N-cap and C-cap. d) Schematic diagram explaining the possible mechanism involved in the formation of hexagonal nanoparticles.*

Hence decrease in the concentration of the proteins resulted in the collapse of α-*R*ep N9 superstructure and hence no longer serves as a preorganized template for nanorod growth. Instead they can act as a molecular growth inhibitor by limiting the growth at {111} face and allow maturation of only {100} face and results in the formation of triangular and hexagonal nanoparticles (*Fig V.18d)*.

In contrast, proteins can still act effectively at pH 11 when their molar concentration was consequently high and resulted in the formation of nano rods and monodispersed spherical nanoparticles (*Fig V.5 and Fig V.6).* But when the concentration was lowered, at pH 11 most of the proteins are denatured. The partial loss of 3D structure of the α-*R*ep protein at pH 7 could be due to the fact that protein was oxidized during the reduction of Au (III) to Au (0).Hence in our next procedure we introduced co reducing agent along with α-*R*ep proteins.

5.4 Effect on morphology of gold with co-reducing agent.

In order to keep protein intact, we consider here the use of co reducing agent so that the role of the protein is limited as a stabilizing agent. We have performed 2 types of experiments, where either strong reducing agent sodium borohydride ($NaBH_4$) or a weak reducing agent, TCEP (*tris* (2-carboxyethyl) phosphine) or ascorbic acid were used along with proteins for the reduction of the gold. Reaction of Au (III) and α-*R*ep protein along with $NaBH_4$ always lead to a fast reduction of gold and resulted in the formation of spherical nanoparticles. Hence we excluded the use of $NaBH_4$ in our future experiments.

TCEP is often used as a reducing agent to break disulfide bond when they present within and between proteins as a preparatory step for gel electrophoresis. Note that this is not the case of α-Rep proteins. To the best of our knowledge there is no report of using TCEP as a reducing agent for Au (III). TCEP is hydrophilic and more resistant to oxidation in air than Dithiothreitol **(**DTT). The measured pKa of TCEP is 7.6 and hence we designed a protocol to work at pH slightly higher than 7.6 in order to reduce Au (III). On the other hand we have also used ascorbic acid, which is vastly used during the synthesis of nanorods for the preparation of Au seeds.[10, 11] During the reaction the molar ratio was maintained in such a way so that the reduction of Au (III) should mainly occur by co reducing agent and protein should serve as a stabilizing or capping agent.

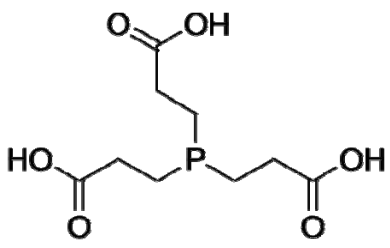

Fig V.19: *Molecular structure of TCEP (tris (2-carboxyethyl) phosphine).*

5.4.1. Synthetic protocol.

1mL of 2μM protein was added to 1mL of 10mM $HAuCl_4$ with stirring in 2 mL eppendorf tube. The stirring of the above solution was continued for 24 hr at 12^oC. The color of the solution changed from yellow to colorless showing the reduction of Au (III) to Au (I) and the pH of a solution measured as pH7. 200μL of 20mM TCEP in water was added to the above solution and the pH of the solution increased to pH 8 by the addition of NaP buffer. Temperature of the solution was raised from 12 deg to 40 deg for 8hr. The color was observed to change from colorless to deep black color. Precipitation of the solution was observed in case of α-*R*ep N10 protein. The solution was then brought to room temperature, cooled and characterized by and TEM and UV-Vis absorption spectroscopy.

5.4.2. TEM analysis and UV-Vis spectroscopy.

TEM analysis of the Au nanostructures reduced by TCEP in the presence of α-*R*epN9 or α-RepN11 showed extended networks of Au ribbons (*Fig V.20a,c,d*), the length of which varies from 0.5- 1μm. The width of these ribbons was 6-10nm on average. Once again α-*R*epN10 showed typical nanostructure mostly spherical nanoparticles with diameter were in the range of 5-30nm (*Fig V.20b*).

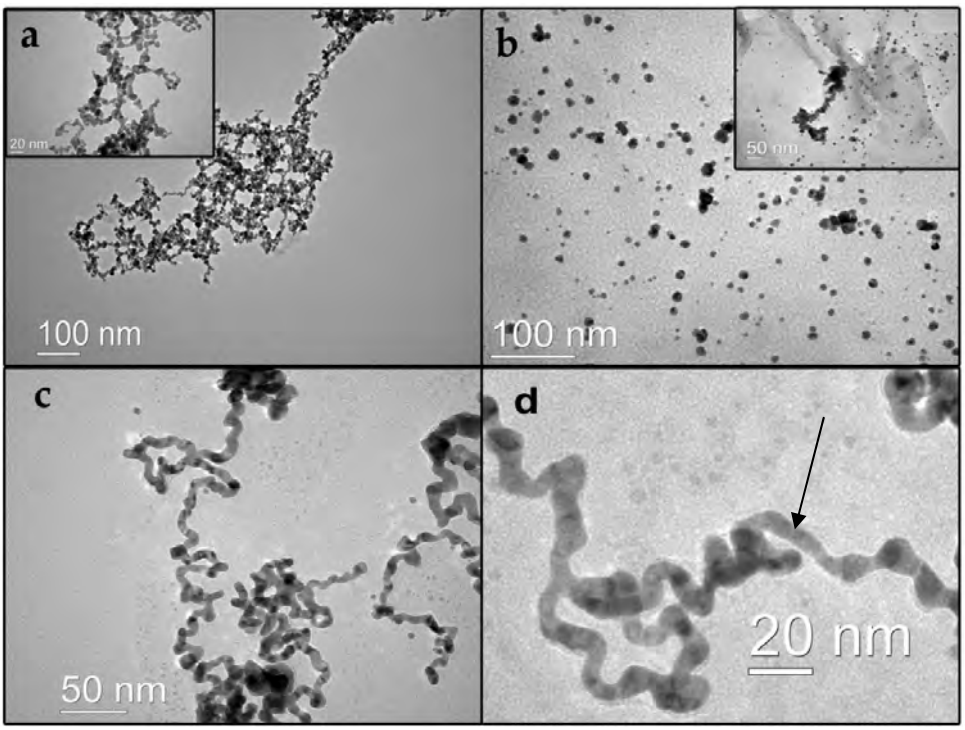

Fig V.20: *TEM images of a) α-RepN9 -TCEP, b) α-RepN10 -TCEP and c, d) α-RepN11 -TCEP reduced Au nanostructures.*

The closer inspection of these chains showed a thin organic layer probably protein, of thickness 2nm can be observed along the ribbon sides (*Fig V.20d*).

UV-Vis spectra of TCEP-assisted reduction of Au in presence of α-*R*ep proteins are displayed in *Fig V.21*. A broad plasmon absorption band was observed at 564nm in case of α-*R*ep N9-TCEP reduced Au sample, whereas α-*R*ep N10-TCEP and α-*R*ep N11-TCEP reduced Au sample showed absorption at 605 and 558nm respectively. In addition Au nanostructures reduced in the presence of α-*R*ep N11-TCEP and α-*R*ep N9-TCEP showed another absorption band at 965nm (*Fig V.21 black* and *blue*) that could be attributed to a longitudinal mode. The intensity of absorption was different for each sample.

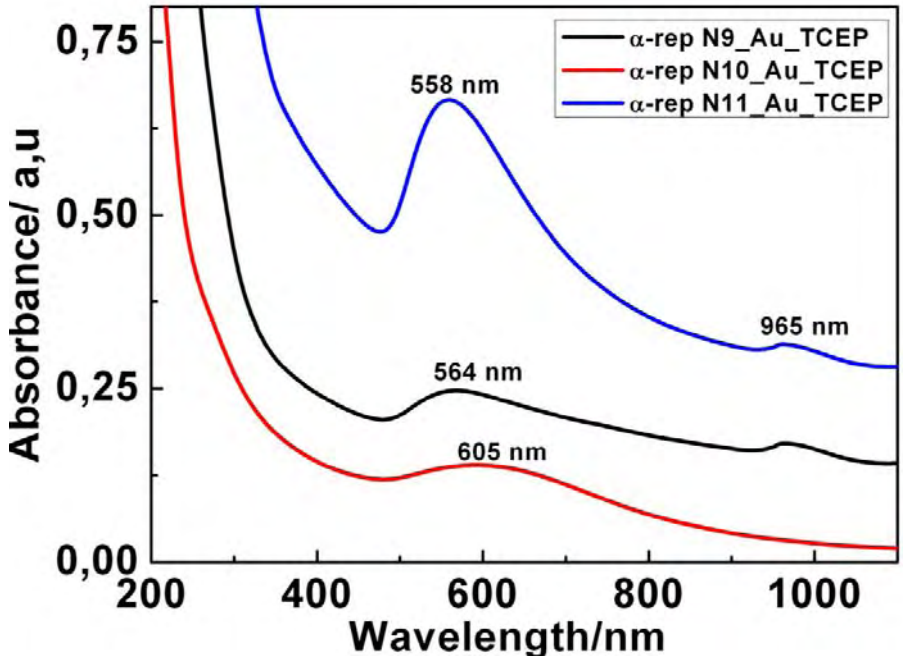

Fig V.21: *UV-Vis spectra of α-Rep protein-TCEP reduced Au nanostructures.*

Interestingly, in the case of gold reduced by TCEP in the presence α-*R*ep N9, no spherical particles could be found in TEM samples and similarly, only very few nanoparticles were formed in the sample produced with α-*R*ep N11. TCEP alone cannot produce these Au nano networks since the same reaction with TCEP in the absence of protein resulted in brown precipitation of the solution which showed no absorption in UV-Vis spectra.

This demonstrates that TCEP cannot stabilize the nanostructure but plays a major role in the reduction of Au (I) to Au (0). Hence both TCEP and proteins played a major role in the formation of these structures. The CD and DSC analysis on these samples are underway which could expose the conserved protein structure on these nanostructures. In the next

reaction we have used ascorbic acid as a mild reducing agent and nanostructures obtained here are completely different and hence we present this work in the next section.

5.3. Artificial protein directed synthesis of fluorescent nanoclusters.

Here we used ascorbic acid as a mild co-reducing agent in order to preserve proteins. Protein kept as intact as possible, may influence the growth of Au nanostructure with their preserved 3D topology. In this case, the procedure was slightly modified, where we introduced protein in the second step just after the addition of ascorbic acid so that protein can better influence the structure of the nanoparticles.

5.3.1. Synthetic protocol.

500 µL of 40mM ascorbic acid solution was added to 500 µL of 20 µM $HAuCl_4$ in 2mL eppendorf tube. The solution was heated for 30 min at 40^0C and 1mL of protein solution 20µM (pH8 NaP buffer 100mM) was added. After 2 hour the pH of the solution was increased to pH 8 by the addition of 0.1M NaP buffer and the solution was maintained at 40^0C under stirring for overnight. A change in the color of the solution was noticed from colorless to pale yellow. We used α-RepA3,α- RepN9, α- RepN10 and α-RepN11 proteins and in all the cases we saw the same color change.

5.3.2. TEM analysis and UV-Vis spectroscopy.

These samples were analyzed by TEM. In this case, unlike the formation of chains, nanorods, triangles or spherical nanoparticles, the formation of fine nanoclusters were observed. We discovered that the growth of these small clusters took place in all the cases (α-*R*ep A3, α-*R*ep N9, α-*R*ep N10 and α-*R*ep N11) and had size ranging from 3-5nm (*Fig V.22)*. Subtle difference in the organization of the cluster could be observed. For A3, small aggregates of cluster were found all over the TEM grid while these clusters formed in the presence of α-*R*ep N9, α- *R*ep N10 and α-*R*epN11 posses well separated nanoclusters on the TEM grids. It is found that the sizes of the clusters formed are nearly same in size of the pure proteins. These TEM images are well correlated with the absorption behavior of these samples. The UV-Vis spectra of all the samples show superposition of the 280nm of the proteins with slowly decreasing absorbance from 400 to 600nm. This behavior was typical for the particles of sub nanometer size ~5nm (*Fig V.23)*.

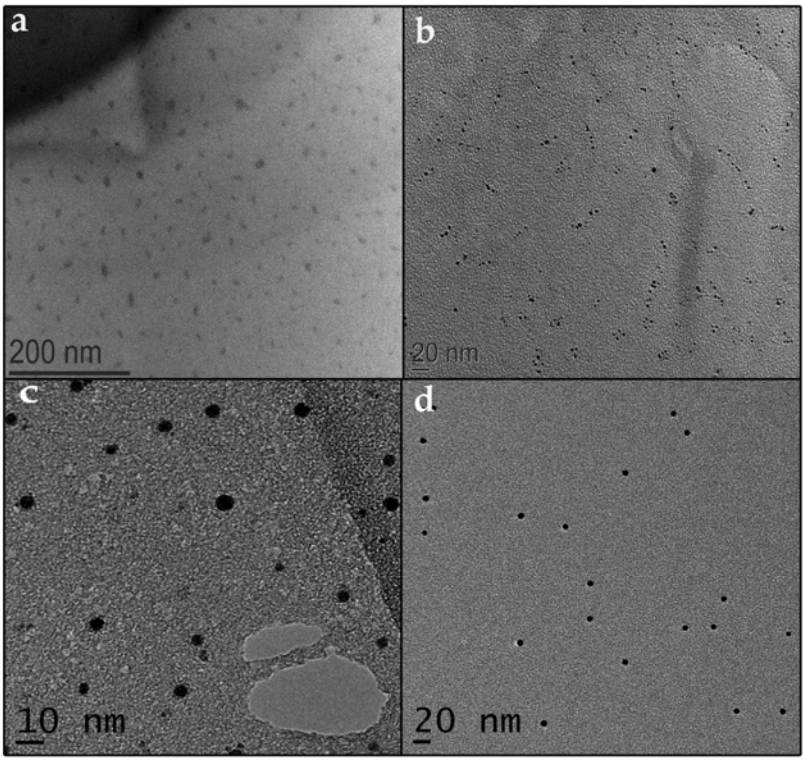

Fig V.22: *TEM images of a α-Rep A3, b) α-Rep N9, c,d)α-Rep N11 protein reduced Au nanoclusters. Size of these nanoclusters were found as 3-5nm.*

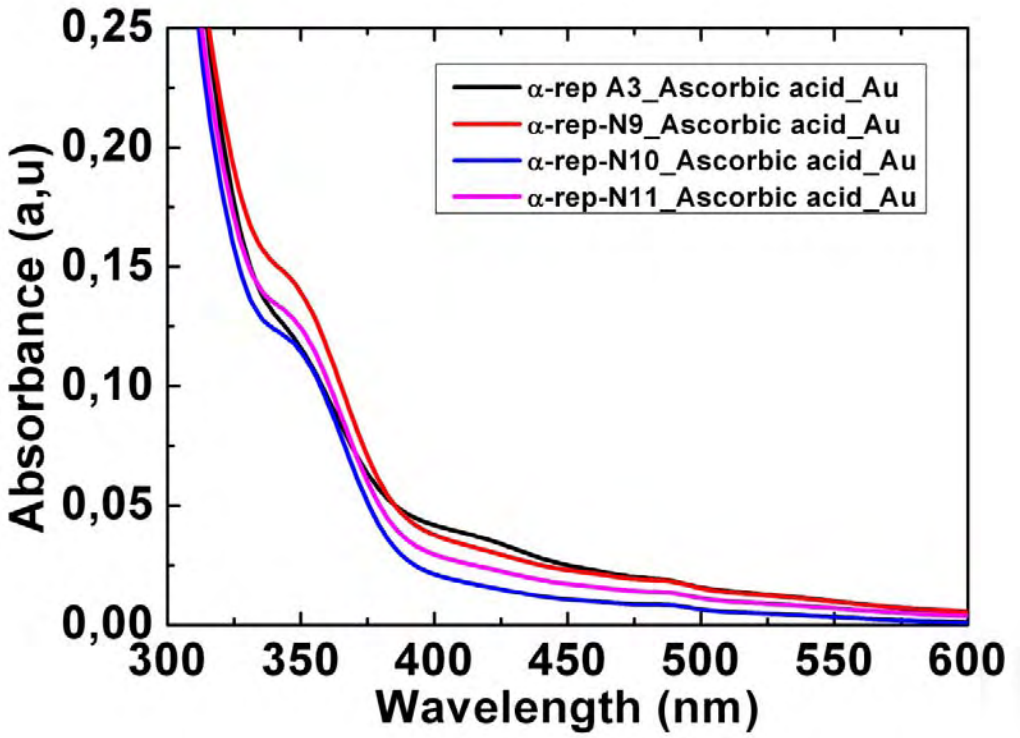

Fig V.23: *UV-Vis spectra of α-Rep protein reduced Au nanoclusters. Small absorption at 350nm and 415nm was observed.*

5.3.3. Fluorescence spectroscopy

It is known that small (~5nm) Au clusters can be fluorescent[12-14] and therefore we have investigated the emission property of the samples reduced by ascorbic acid. The fluorescence spectroscopy was performed at two excitation wavelengths namely, λ_{exc} 350 and 415 nm because of the presence of 2 features in the absorption spectra.

As expected our 3-5nm cluster showed an intense blue fluorescence which did not show any sign of bleaching with extended period of time. The yellow solutions, on excitation at 350nm give very small emission band at 485nm. Whereas emission spectra recorded for excitation wavelength 415nm is intense at the same emission wavelength (*Fig V.24*). The emission spectra are same in all the samples obtained after the reaction with different α-Rep protein and ascorbic acid solution. Interestingly, reaction at lower pH (< pH8) show no change in the color of the solution and hence it is necessary to maintain pH of the reaction minimum pH8 to obtain fluorescent nanoclusters. α-rep proteins were colorless and do not show emission when excited at 415nm.

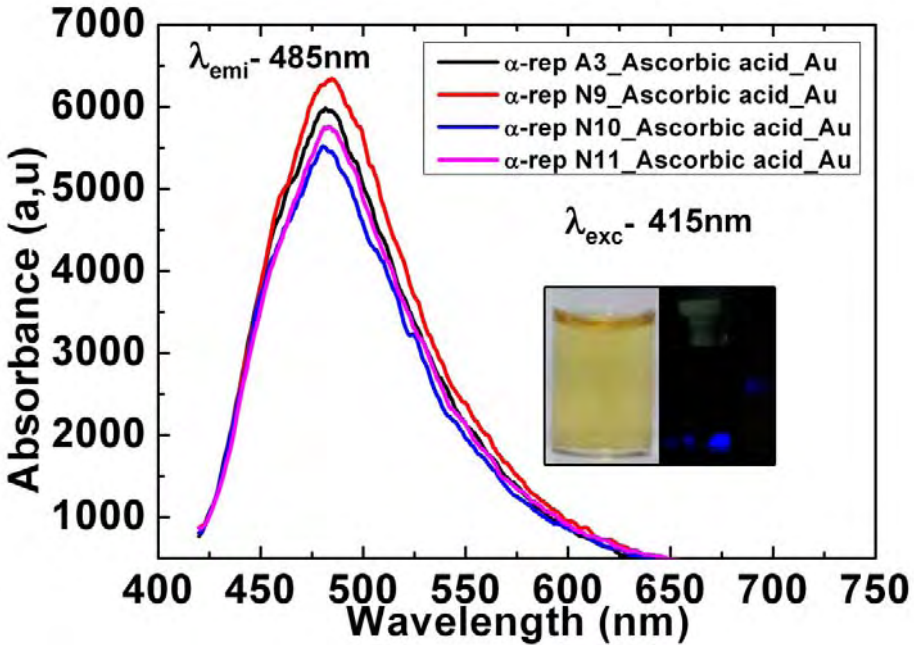

Fig V.24: *Fluorescence emission spectra of α-Rep protein reduced Au nanoclusters. Inset fig shows visible and fluorescent image of nanocluster solution.*

As reported by Xie et.al,[3] the reaction of bovine serum albumin (BSA) with Au (III) solution at physiological temperature (37°C) and at pH 11 produced fluorescent nanocrystals with red emission (λ_{em}640nm). The reaction was performed at pH 11, we know from our previous results that proteins were most probably destroyed during this reaction. In our method we

have performed reaction at lower pH (pH8) in addition with mild reducing agent, which gave a greater chance for protein to conserve its tertiary structure. Hence in order to know whether α-Rep proteins have conserved their 3D structure we have performed DSC analysis of the sample.

5.3.4. Differential scanning Calorimetry.

The DSC data obtained from α-*R*epN9-ascorbic acid reduced sample and α-*R*ep11-ascorbic acid reduced sample showed very weak signal in comparison with pure proteins (*Fig V.25*). In spite of the use of additional co reducing agent and reaction at pH8 resulted in the destruction of the 3D structure of the protein. We observed similar behavior with other samples. Hence during the growth process protein has been successively destroyed even in the presence of ascorbic acid and resulted in the loss of protein conformation.

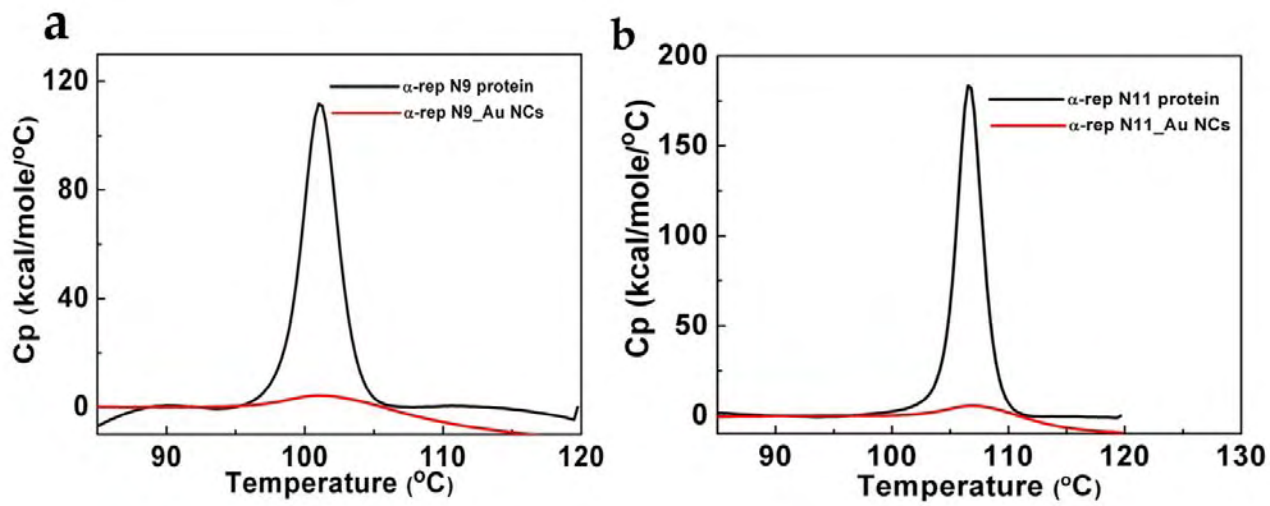

Fig V.25: *DSC spectra of α-RepN9 and α-Rep11 reduced Au nanoclusters (red) in comparison with original proteins (black).*

From the X-ray crystallographic structure of α-RepA3, we measured the distance of the concave part, i.e. from N-cap to C-cap and it was found as 4.2nm (*Fig V.18c*). This was in good correlation with the size of the proteins observed from TEM images *(Fig V.18a, b).* Therefore there is a possibility that the nucleation of Au has occurred specifically in these part resulting in the formation of small fluorescent nanoclusters in presence of ascorbic acid. No specific difference was observed in the asynthesised nanoclusters with different proteins, since, there is only a small difference in the sequence as well as number of repeats. Therefore we anticipate that, successive engineering in the variable position in these proteins to a large

extent by specifically incorporating amino acids which are active at low pH can help to synthesize fluorescent nanoclusters by conserving protein structure. Fluorescence emission at different wavelength can also be achieved by this method.

5.4. Conclusion and perspective.

The protein mediated change over size and shape of gold nanostructures can be substantially affected by changing the reaction conditions, such as pH and molar ratio between protein and Au precursor and concentration of the precursor solution. Alteration of these parameters was shown to result in the production of diverse shapes of gold particles (nanorods, hexagonal, triangular nanoparticles including small nanoclusters) with different sizes (from few nanometers to close to 1μm). Although these proteins were not selected with recognition on Au crystallographic faces, they still showed strong ability to produce anisotropic nanostructures. The initial results from these studies indicated that synergistic effect of the structure of proteins and different amino acid sequence can be successfully used to modulate the size and shape of Au nanostructures. Mixture of nanoparticles of different shape was obtained during the reaction, and the next step is to improve the yield of nanoparticles of specific shape by modulating the reaction parameters and protein structure. Interestingly, when protein was used as a stabilizing agent, formation of fluorescent nanoclusters as well as gold nanochains was observed where the effect of reducing agent as well as stabilizing agent can be clearly viewed. Thus α-Rep proteins can serve as a better template for the synthesis of anisotropic plasmonic nanostructures.

In general, the morphosynthesis of nanoparticles is a kinetically controlled process where the selective adsorption of capping molecules on the nuclei alters the relative growth rates of the crystalline facets and results in the emergence of shape anisotropy. Alternatively, anisotropic growth can also achieved by templating where a more rigid organic structure (assembled proteins) drives the formation of anisotropic nanostructures. In this case, a correlation can be observed between the shape of the nanostructure that of the template. The analysis of the sequence of α-*R*ep A3 proteins has shown that amino acids such as tryptophan, aspartic acid, tyrosine and glycine are present in the concave part of the protein. Whereas homorepeats exhibits especially glutamic acid and aspartic acid at positions 19 and 26, which consecutively repeats a number of times (9, 10, 11) giving particular recognition or reducing ability for Au. We believe that, anisotropic growth of Au nanostructures has been promoted by the

functionalities of the concave part, since most of the effective amino acids were present here especially tyrosine which has a strong ability for the reduction of Au (III) to Au (0).[4] The convex face of homorepeat proteins is rich in lysines which contribute to the local enrichment in $AuCl_4^-$ precursor.

Apart from this, the template effect of protein supramolecular structures greatly influence the morphology of nanostructures. This can be clearly viewed and differentiated in case of α-*R*epN9 and α-*R*epN10 protein. Pre-organized rod shaped template of α-*R*epN9 at high concentration results in the formation of gold nanorods whereas sphere shaped α-*R*epN10 proteins only able to form spherical gold nanoparticles.

We anticipate that future engineering at variable positions of α-*R*ep proteins with specific amino acid can help to improve the facet-specific binding and thus inhibition in order to generate nanostructures with desired shape and structure. The engineering of artificial proteins will also affect the supramolecular structure of the proteins, which in turn affects the precision and monodispersity of the templated growth of metallic nanostructures. The tunability of Au nanostructures can be achieved by imposing changes in the protein sequence and reaction conditions for constructing a variety of nano architectures and will find wide applications in the field of plasmonics. Moreover, nanostructures synthesized by this strategy will hardly show any limitation for post functionalization in contrast to surfactant-coated nanoparticles (e.g. CTAB-coated nanorods), since the surface of the proteins exposed to the solution can be classically derivatized. Finally, we have provided preliminary results that α-*R*ep proteins provide a unique chance for the synthesis of fluorescent nanoclusters with different emission wavelength according to the variable amino acids in their sequence. In addition post functionalization of these fluorescent nanoclusters has a specific advantage with an effective application in the field of bio imaging and nano plasmonics.

References:

(1) Basu, N.; Bhattacharya, R.; Mukherjee, P. *Biomedical Materials* **2008**, *3*.

(2) Brown, S.; Sarikaya, M.; Johnson, E. *Journal of Molecular Biology* **2000**, *299*, 725-735.

(3) Xie, J.; Zheng, Y.; Ying, J. Y. *J Am Chem Soc* **2009**.

(4) Tomczak, M. M.; Slocik, J. M.; Stone, M. D.; Naik, R. R. *Biochemical Society Transactions* **2007**, *35*, 512-515.

(5) Peelle, B. R.; Krauland, E. M.; Wittrup, K. D.; Belcher, A. M. *Langmuir* **2005**, *21*, 6929-6933.

(6) Iosin, M.; Baldeck, P.; Astilean, S. *Journal of Nanoparticle Research* **2010**, *12*, 2843-2849.

(7) Tan, Y. N.; Lee, J. Y.; Wang, D. I. C. *Journal of the American Chemical Society* **2010**, *132*, 5677-5686.

(8) Knez, M.; Sumser, M.; Bittner, A. M.; Wege, C.; Jeske, H.; Martin, T. P.; Kern, K. *Advanced Functional Materials* **2004**, *14*, 116-124.

(9) Knez, M.; Bittner, A. M.; Boes, F.; Wege, C.; Jeske, H.; Maiss, E.; Kern, K. *Nano Letters* **2003**, *3*, 1079-1082.

(10) Johnson, C. J.; Dujardin, E.; Davis, S. A.; Murphy, C. J.; Mann, S. *Journal of Materials Chemistry* **2002**, *12*, 1765-1770.

(11) Shao, Y. J., Yongdong Dong, Shaojun *Chemical Communications* **2004**, 1104-1105.

(12) Zhu, M.; Lanni, E.; Garg, N.; Bier, M. E.; Jin, R. *Journal of the American Chemical Society* **2008**, *130*, 1138-+.

(13) Yu, M.; Zhou, C.; Liu, J.; Hankins, J. D.; Zheng, J. *Journal of the American Chemical Society* **2011**, *133*, 11014-11017.

(14) Kawasaki, H.; Hamaguchi, K.; Osaka, I.; Arakawa, R. *Advanced Functional Materials* **2011**, *21*, 3508-3515.

CHAPITRE 6
AUTO-ASSEMBLAGE DE NANO-PARTICULES PAR APPARIEMENT DE PROTEINES ARTIFICIELLES.

Résumé

Poursuivant notre travail sur le contrôle plasmonique par des nanostructures, nous décrivons ici notre stratégie visant à utiliser des protéines αRep pour l'auto-assemblage de nanoparticules. Dans ce chapitre, la sélection de paires de protéines αRep à forte affinité mutuelle, leurs propriétés physico-chimiques et leur attachement à la surface de nanoparticules métalliques sont décrites. L'affinité de ces paires de protéines est ensuite exploitée pour induire l'assemblage des nanoparticules. La sélection et la caractérisation des paires de protéines ont été réalisées par Ph. Minnard et ses collègues au laboratoire IBBMC d'Orsay. La méthode du phage display (Figure VI.1), une technique commune de biologie, a été utilisée pour la sélection des paires de protéines et leur affinité a été confirmée par analyse calorimétrique isotherme (ITC).

La protéine α-Rep A3 avec quatre motifs répétés a été utilisée comme cible du phage display dont deux protéines antagonistes, α2 et α17 possédant respectivement 1 et 2 motifs répétés,

ont été sélectionné (Table.VI.1). Les constantes de dissociation (K_D) des paires A3-α2 et A3-α17 ont été mesurées et sont inférieures à 200 nM mais la protéine α17 semble avoir une affinité plus forte pour A3 que la protéine α2 (Figure VI.2). La paire A3-α2 a pu être cristallisée et la résolution de sa structure a montré que l'interaction protéinique se produit principalement à travers la partie concave hydrophobe de la protéine A3 et la partie C-cap de la protéine α2 (Figure VI.3). Afin de pouvoir greffer ces protéines sur des nanoparticules d'or, elles ont été munies d'une série de six cystéines (Cys_6) en extrémité de C-cap. L'analyse ITC a montré que ces paires de protéines modifiées présentent des valeurs de K_D peu altérées et que leur affinité a été préservée malgré l'insertion des cystéines (Figure VI.4).

Les deux paires de protéines sélectionnées ont été utilisés pour diriger l'assemblage de nanoparticules d'or afin de créer des superstructures d'ordre supérieur tel que des dimères, des chaînes et des réseaux. Dans notre travail, nous avons suivi un protocole déjà établi afin de conjuguer des protéines sur des nanoparticules d'or préformés et de diriger l'auto-assemblage. Les liaisons disulfures des séquences Cys_6 ont été préalablement réduites à l'aide de dithiothréitol (DTT). Par la fixation de ces protéines, via Cys_6, à des échantillons distincts de nanoparticules d'or confèrent à chaque population de nanoparticules une affinité pour une autre population de nanoparticules portant la protéine complémentaire (Figure VI .5). La fixation des protéines directement sur des nanoparticules d'or stabilisées par du citrate a été analysée par analyse DLS, spectroscopie UV-Vis et microscopie TEM. La conjugaison de la protéine A3Cys sur des nanoparticules d'or (à un rapport molaire Au: protéine de 1:5) montrent un petit décalage vers le rouge dans la bande plasmonique et une augmentation du rayon hydrodynamique (Figures VI.7 et VI.10). La stabilité des nanoparticules d'or conjugués avec des protéines a été confirmée dans une solution 0.1 M de NaCl. La conjugaison des protéines α2Cys et α17Cys à des nanoparticules dans les mêmes conditions a montré un important décalage vers le rouge des spectres d'absorption UV-visible, et une augmentation du taux de nanoparticules précipitées a été confirmée par TEM et analyse DLS (Figure VI.9). Ainsi la conjugaison directe des protéines des paires sélectionnées sur des nanoparticules n'est pas suffisamment stable et, par conséquent, nous avons modifié notre protocole.

Dans le second protocole, un court ligand peptidique thiolé a été attaché aux nanoparticules d'or, puis la protéine est introduite sur la surface des particules par échange de ligand. De cette manière, le revêtement bifonctionnel est conçu pour améliorer la stabilité des particules et préserver la capacité de fixation des protéines. Deux types de peptides, chargés négativement

et partiellement chargés positivement, ont été utilisés afin d'optimiser l'échange avec les protéines. La conjugaison du peptide sur des nanoparticules d'or montre une légère augmentation du rayon hydrodynamique et l'échange correspondant avec des protéines montre une nouvelle augmentation de la taille. L'analyse par microscopie TEM de l'échantillon coloré à l'acide phosphotungstique permet d'observer une fine couche de protéines autour des nanoparticules (Figure VI.16). Les spectres d'absorption des nanoparticules peptidiques conjugués et des échantillons de protéines échangés montrent la stabilité de la solution par un faible décalage vers le rouge sans perte d'intensité.

Lorsque deux suspension de nanoparticules complémentaires conjuguées avec des protéines (en présence de ligand peptidique) ont été mélangées en rapport volumique isomolaire de 1:1, l'intensité de la bande d'absorption du plasmon nanoparticules du mélange ne varie pas et aucun changement dans la forme de la bande de plasmons n'a été observé (Figure VI.18). Par conséquent, après le mélange de deux solutions complémentaires de nanoparticules, aucun signe d'appariement n'a été observé. L'analyse par microscopie MET de ces échantillons a montré exclusivement des particules individuelles isolées. Certaines structures en chaînes ont cependant été observées indiquant une faible interaction conduisant à la formation de grappes de petites chaînes contenant 3 à 6 nanoparticules en moyenne (Figure VI.19). Une raison possible de cette faible interaction est la dilution importante des suspensions de particules en cours de protocole. La baisse de la concentration diminue effectivement la valeur K_D et de sorte que la reconnaissance moléculaire ne se produise plus significativement. Par conséquent, dans notre prochain protocole, les suspensions de nanoparticules conjuguées à des protéines ont été concentrées cinq fois, ce qui correspondrait à une augmentation de 25 fois de la concentration en duplex.

Les suspensions concentrées de nanoparticules conjuguées à des protéines ont été contrôlées par électrophorèse sur gel d'agarose. Les échantillons de protéines, de particules conjuguées aux protéines et les mélanges des particules portant les deux paires complémentaires migrent en fonction de leur charge de surface dans un gel immergé dans une solution tampon lorsqu'une tension est appliquée. Des différences de migration ont été observées entre les nanoparticules d'or initiales, les nanoparticules d'or couvertes de peptides et les nanoparticules d'or fonctionnalisées avec les protéines suivant leur taille et état de charge de surface. Lorsque deux paires de particules stabilisées par le peptide négatif et rendues complémentaires par

A3Cys et α2Cys ont été mélangées, on observe deux bandes distinctes alignées avec celles des particules seules portant les différentes protéines (Figure VI.20). A l'inverse, dans le mélange Au-A3Cys-Au-α17Cys deux bandes distinctes qui ne sont pas strictement alignées avec les échantillons individuels sont visibles. L'image TEM de l'échantillon Au-A3Cys-Au-α2Cys montre de très petit nombre de nanostructures assemblées (figure VI.21). Une fine couche de protéines est visible même sans coloration, et un grand nombre de nanoparticules isolées ont été trouvées avec de très petits nombres de dimères, des chaînes de longueur courte. L'image TEM de l'échantillon Au-A3Cys-Au-α17Cys a montré un comportement différent : une monocouche uniforme de nanoparticules d'or étendue sur plusieurs micromètres a été observée. Les images MEB confirment cette observation.

Le spectre d'absorption UV-Vis montre une grande diminution de l'intensité de la bande de plasmon de la solution mixte par rapport à la solution initiale (figure VI.26). Le même comportement a été observé lorsque deux autres populations de Au-αRepA3Cys et Au-α17Cys conjugués sont mélangées. L'absence de décalage spectral ou de bande plasmon à plus faible énergie indique que seules les particules individuelles sont restées en suspension tandis que le précipité observé en microscopie électronique n'a pas pu être analysé en spectroscopie UV-Visible.

De la même façon, l'analyse par électrophorèse sur gel d'agarose des mélanges complémentaires montrent une bande unique au lieu de deux bandes distinctes des populations de départ (Figure VI.27). Il s'agit d'une indication forte que l'interaction entre les paires de protéines conduit à un assemblage de nanoparticules. Les images TEM correspondantes des échantillons ont montré l'agrégation de grandes nanoparticules à la fois sur les échantillons au-A3Cys-Au-α2Cys et Au-A3Cys-Au-α17Cys et en particulier dans le dernier cas (figure VI.28). Cependant, les spectres d'absorption UV-Vis ont montré une très légère baisse dans l'intensité des spectres plasmons sans changement ou déplacement de la bande d'absorption longitudinale (figure VI.29). Les expériences d'ITC sont en cours afin d’avoir une meilleure connaissance sur le processus en cours d'auto-assemblage.

En conclusion, des paires de protéines artificielles à forte affinité ont pu être produites par nos collaborateurs et pour la première fois, elles ont été utilisées pour conduire l'auto-assemblage de nanoparticules. La méthode d'échange de ligand a un avantage sur la conjugaison directe de protéines sur des nanoparticules, car elle assure la stabilité colloïdale des particules modifiées. Les résultats expérimentaux ont montré que la protéine α17Cys a une plus grande

affinité avec la protéine A3Cys et fonctionne mieux quand il a été échangé avec un ligand neutre ou partiellement chargé positivement. Le principal avantage de notre approche est que l'on peut désassembler des nanoparticules en introduisant une autre protéine qui a une affinité supérieure au premier interactant, impliqué dans le processus d'assemblage initial. En outre, la fixation de paires de protéines différentes ouvre la voie à l'assemblage orthogonal de nanoparticules. Également une meilleure conception de la superstructure peut être obtenue en contrôlant la stœchiométrie protéine:particule. La structure 3D de la protéine-protéine donne un nouvel atout qui est le contrôle 3D de la topologie des assemblages de nanoparticules.

CHAPTER 6
ARTIFICIAL PROTEIN DRIVEN NANOPARTICLE ASSEMBLY.

6.1. α-Rep protein pair selection and characterization.

Continuing our work on plasmonic control with nanostructures here we describe our strategy to use αRep proteins for the self assembly of nanoparticles. In this chapter, we describe the selection and properties of αRep protein pairs and their attachment to metal nanoparticles surfaces. We then use these pairs of proteins to induce the assembly of the nanoparticles.

6.1.1. Selection of interacting protein pairs.

The selection and characterization of protein pairs were performed by Ph. Minnard and colleagues in IBBMC, Orsay. For the selection of protein pairs, αRep proteins were selected from the libraries for their specific affinity for a target protein chosen beforehand. The proteins to be displayed were expressed as fusion with the phage coat protein pIII. The αRep

* Terms are explained briefly in symbols and abbreviations.

libraries were assembled in a phage display phagemid vector[1]. In this construction, the αRep coding sequence was fused to the C terminal part of protein pIII from capsid of M13 filamentous bacteriophage. This fusion protein αRep-pIII was expressed using a SRP-dependant signal sequence (dsbA)* adapted to the secretion of very stable proteins in the periplasm.[2]

The affinity selection of phage library was performed on an immobilized target in Elisa plate. In the first step, the phage library was exposed to the target (*Fig VI.1a*). Phages which show high affinity for the target were captured whereas non-binding phage washed off (*Fig VI.1b*). The bound phages were then eluted and amplified by infection in *E.coli* cells. When co-infected with a helper phage and αRep expressing phagemid, each bacterial cell produces phage particles with the phagemid included in the phage particle and the associated protein (αRep) displayed at the bacteriophage surface. The amplified phage population can be subject to the next round of selection/amplification. This cyclic process of selective enrichment and amplification allows obtaining a pool of phage potentially able to bind the target (*Fig VI.1e*). It is therefore possible to select αRep proteins from these libraries, interacting specifically for any given protein targets (*Fig VI.1*).

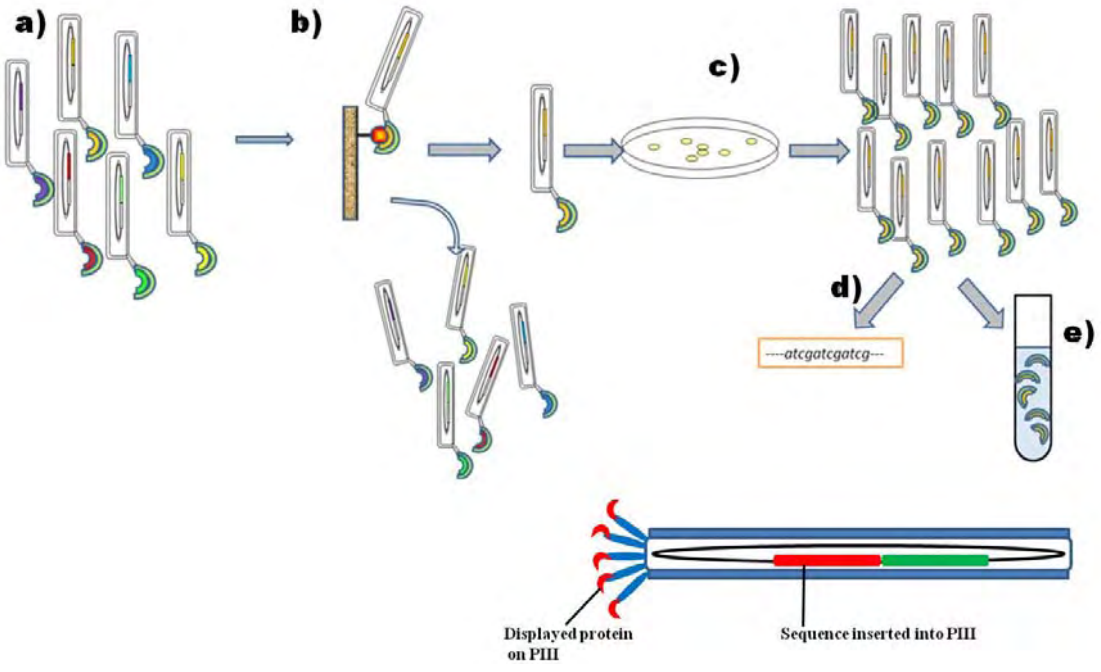

Fig VI.1: *Schematic diagram describing different steps involved in Phage-display selection procedure for the selection of protein pairs and schematic representation of a filamentous phage.*

Hence, this method offers an opportunity to create pairs of specific binding proteins. If a chosen αRep (αRep A) is used as a target protein for the selection, it should be possible to select new antiA αRep proteins that interact specifically with the binding surface of αRep A. Both αRep A and antiA will then have the favorable properties (stability, solubility) of αRep scaffold. In principle, this should be possible with any arbitrarily chosen αRep B or C and a range of independent proteins pairs A-antiA; B-antiB could possibly be created. A first demonstration in this direction was made by using αRep-n4 (A3) as a target for selection. After three rounds of selection using Lib1.0 and lib 2.0 as described in the section 4.4.3, two different binders named αRep2 and αRep17 were selected and amplified. These two proteins have different sequences but interact specifically with the target protein αRep A3 (*Table.VI.1*).

a)

Protein	Number of amino acids	Molecular weight (Da)	Theoretical pI	Ext. coefficient assuming all pairs of Cys residues form cystines	Ext. coefficient assuming all Cys residues are reduce
α-Rep A3(n=4)	206	22585.5	5.43	29575 $M^{-1}.cm^{-1}$	29450 $M^{-1}.cm^{-1}$
α-Rep-2 (n = 1)	113	12322.0	7.05	8605 $M^{-1}.cm^{-1}$	8480 $M^{-1}.cm^{-1}$
α-Rep-17 (n = 2)	144	15873.2	8.46	8605 $M^{-1}.cm^{-1}$,	8480 $M^{-1}.cm^{-1}$,

b)

Sequence: α-Rep A3(n=4)

N-cap

MRGSHHHHHHTDPEKVEMYIKNLQDDSYYVRRAAAYALGKI
GDERAVEPLIKALKDEDAWVRRAAADALGQI
GDERAVEPLIKALKDEDGWVRQSAAVALGQI
GDERAVEPLIKALKDEDWFVRIAAAFALGEI
GDERAVEPLIKALKDEDGWVRQSAADALGEI
GGERVRAAMEKLAETGTGFARKVAVNYLETHKSLIS C-cap

Sequence: α-Rep-2 (n = 1)

N-cap

MRGSHHHHHHTDPEKVEMYIKNLQDDSSVVRKAAAVALGEI
GDERAVEPLIKALKDEDQFVRIAAAWALGKI
GGERVRAAMEKLAETGTGFARKVAVNYLETHKSLIS C-cap

Sequence α-Rep-17 (n = 2)

N-cap

MRGSHHHHHHTDPEKVEMYIKNLQDDSWQVRRVVAEALGKI
GDERAVEPLIKALKDEDLAVRRNAALALGKI
GDERAVEPLIKALKDEDPFVRRVAAQALGKI
GGERVRAAMEKLAETGTGFARKVAVNYLETHKSLIS* C-cap

Table.VI.1: *Table summarizing general information and amino acid sequence of α-Rep A3, α-Rep-2, α-Rep-17 proteins. Green color showing sequence of N-cap and red color showing sequence of C-cap and orange color show variable positions in the amino acids sequence.*

6.1.2. Analysis of binding affinity of protein pairs.

The binding parameters of αRep2 and αRep17 for A3 were determined by Isothermal Calorimetry (ITC) (*Fig VI.2*) in IBBMC, Orsay. During the ITC experiment, a protein was titrated with its binding partner in a cell that was coupled with a sensitive thermophile and change in the temperature was measured during the titration. The heat released upon their interaction was monitored over time, which allows determining binding constants (K_B), reaction stoichiometry (N), enthalpy (ΔH) and entropy (ΔS).

Since $K_B = \frac{1}{K_D}$ **(I)**

Hence the dissociation constant (K_D) can be calculated from this equation (I). Of all the techniques that are currently available to measure binding of two proteins, isothermal titration calorimetry is the only one capable of measuring the magnitude of the binding affinity and also the magnitude of the two thermodynamic terms that define the binding affinity: the enthalpy (ΔH) and entropy (ΔS) changes. While measuring the K_D of protein pairs, although the concentrations of the two proteins were not equal but the approximate binding affinity of protein was still large showing the protein pair interaction.

In this experiment, lower concentration of target was injected to a cell and higher concentration of the binder was injected through a syringe carefully. Titration consists in 20 consecutive injections of 2mL of binder (350µM) in the cell containing the target (~30µM) until saturation of the binding site on the target was achieved. The molar ratio N is the number of binder per target. When it was around 1 as below it means that there is one binder per target.

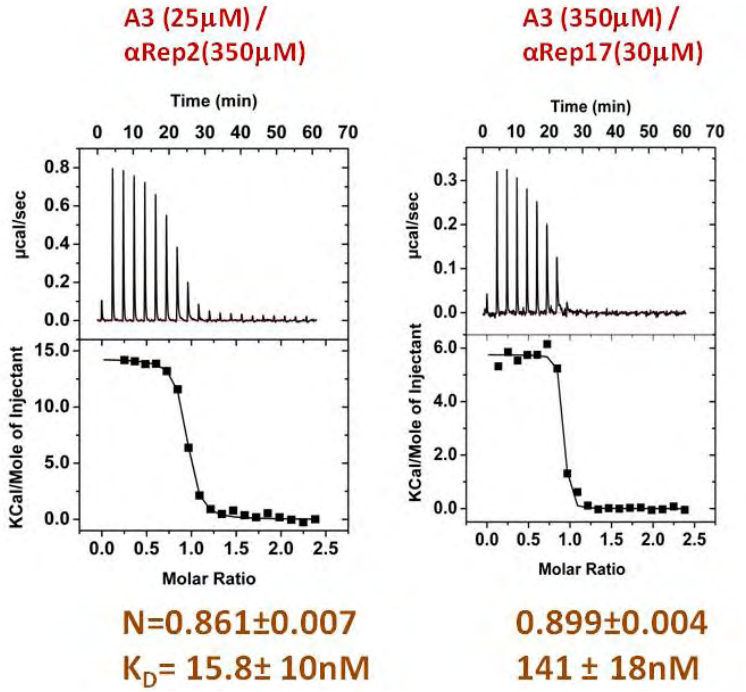

Fig VI.2: *Binding activity of αRep-2 and αRep-17 towards A3 analyzed by microcalorimetry (ITC): The parameters of each binding reaction, K_D and stoichiometry (N) are shown under the corresponding panel.*

Each peak (*Fig VI.2)* represents a heat change associated with the injection of a small volume of sample into the ITC reaction cell. Successive amounts of the protein was titrated into the

ITC cell, the quantity of heat absorbed or released is in direct proportion to the amount of binding. As the system reaches saturation, the heat signal diminishes until only heats of dilution are observed. A binding curve was then obtained from a plot of the heats from each injection against the ratio of protein and binding partner in the cell. The binding curve was analyzed with the appropriate binding model to determine K_B, N and ΔH. Titration of increasing amounts of the binders αRep2 or αRep17 into sample cell containing purified target A3 protein gave the value of 15.8 nM and 141 nM respectively, for the dissociation constant (K_D).

The stoichiometry (N) of the interacting proteins in the complex was found to be 0,861 for A3/αRep2 and 0,899 for A3/αRep17 corresponding approximately to 1-to-1 binary complex.

The binding affinity has also been confirmed by the resolution of the structure of the A3/αRep2 complex by X-ray crystallography. After the formation of the complex an important conformational change in the cleaved C-cap of αRep2 was observed. The crystal structure of the complex A3- αRep2 is determined at 2.15 Å resolutions. The crystal structure of the two proteins showed that the characteristics of Heat-repeat motif fold are well maintained and this structure display globally a well-conserved backbone structure (*Fig VI.3*).

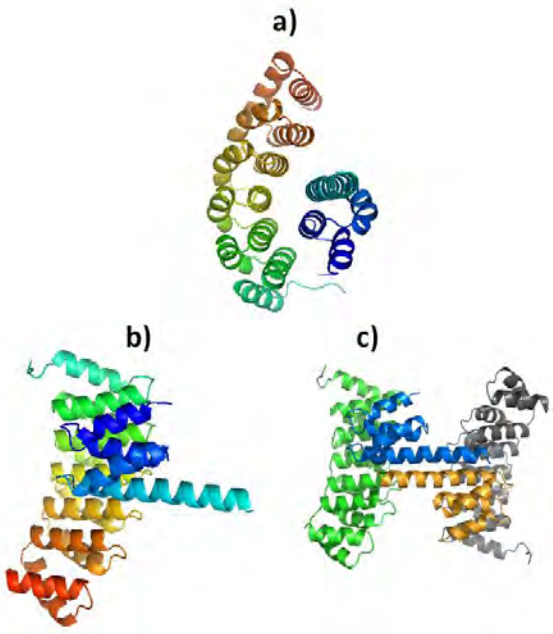

Fig VI.3: *Figure showing the X-ray crystallographic structure of the A3/αRep2 complex. The protein pair interaction occurring through randomized surface (hydrophobic part) of the protein is displayed.*

Further observations of crystal structure show that the αRep2 C-cap is cleaved allowing the opening of the C-cap alpha helix and therefore exposes the surface, which can dimerize as it is

presented in (*Fig VI.3c*). Two complexes A3- αRep2 are compiled by the interaction of C-cap of αRep2. The A3- αRep2 binding interface involves the randomized surface in the concave interface of each protein (*Fig VI.3a*). It is found that the interaction of protein pairs occur on hydrophobic part of the protein structure. Crystallographic data highlights the main information on protein-protein interaction by taking into account of overall protein structure.

In order to use these protein pairs, A3/αRep2 and A3/αRep17 as directing agents for self assembly, we need to graft these proteins on Au nanoparticles. Hence the next step, a cystine tag (CGCGCGS) was inserted at the C-terminal at the end of each of proteins as cystine can bind covalently with Au nanoparticles[3,4]. The αRep genes were sub-cloned into a new vector encoding the corresponding Cys-tag in phase with the αRep genes. The corresponding "αRep-Cys" were produced and purified under reducing conditions (1 mM DTT) in order to break the disulphide bond between cystines. For the last purification step by size exclusion chromatography, DTT was removed and protein samples were frozen to be reduced and coupled with gold nanoparticles (see section 6.2).

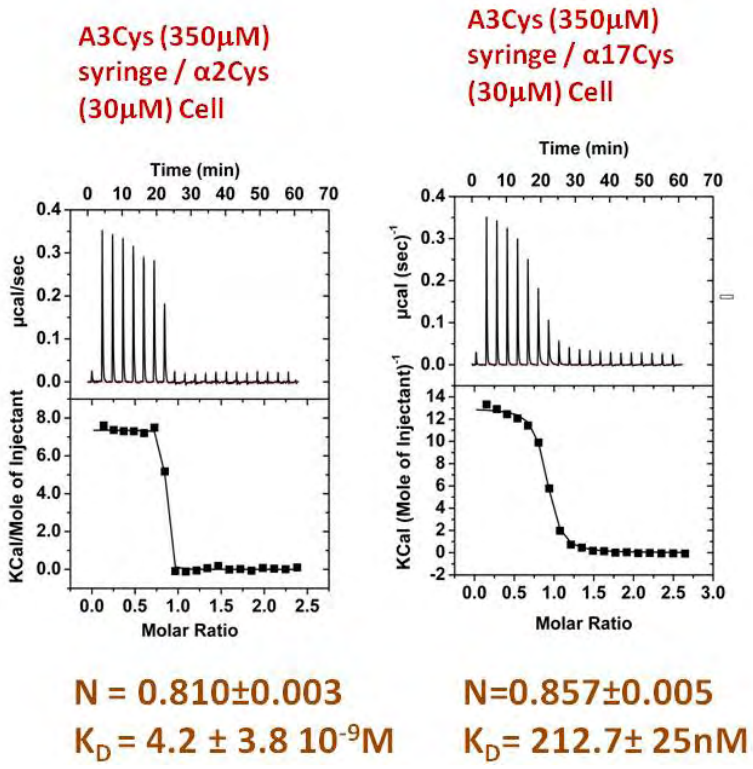

Fig VI.4: *Binding activity of αRep2Cys and αRep17Cys towards αRepA3Cys protein analyzed by microcalorimetry (ITC): The parameters of each binding reaction, K_D and stoichiometry (N) are shown under the corresponding panel.*

After the insertion of cystine tag, it is important to know whether the binding capacity of the protein is still retained. Hence, micro calorimetric analyses were carried out on cystine-tagged proteins. An ITC experiment showed that the Cys-tag did not interfere with protein binding as the affinities were similar to those obtained with the non-modified proteins (*Fig VI.4*). Titration of increasing amounts of the binders αRep2cys or αRep17cys into sample cell containing purified target A3cys protein gave slightly different K_D values 4.2 ± 3.8nM and 212 ± 25nM but still showed that these proteins retained their affinity even after the insertion of Cys-tag.

6.1.3. Thermodynamic stability characterization of protein pairs.

DSC analyses of protein pairs have been performed in IBBMC Orsay, in order to know the thermal stability of these binders. Prior to the DSC experiments, samples were treated with DTT for disulphide bond reduction (*Fig VI.6*) and desalted by using desalted column. The DSC analysis on protein pairs before and after the insertion of Cys-tag was compared. In table *Table.VI.2,* the insertion of Cys-tag in the protein pairs did not affect the transition midpoint Tm in the DSC spectra which showed that the proteins have retained their stability.

Protein	Protein Tm (°C)	Cys-tag protein Tm (°C)
αRep A3	82.95± 0.03	83.09 ± 1.0
αRep2	84.61± 0.03	82.86 ± 0.10
αRep17	75.9± 0.05	ND

Table.VI.2 *Table summarizing the DSC data showing thermal stability of αRep and αRep-Cys proteins.*

Thus, our colleagues from IBBMC Orsay have successfully synthesized new αRep protein pairs using αRep-n4 (A3) as a target for selection. Two proteins αRep2 and αRep17 have been identified as having strong affinity with αRep A3. The sequence analysis showed that αRep2 and αRep17 have one and two repeats respectively. While the target A3 is composed of four repeats. Also ITC experiments have shown that αRep17 has a stronger affinity with αRep A3 than αRep2. The crystallographic structure of the complex αRepA3-αRep2 demonstrated that the interaction of protein pair occurs at hydrophobic part of the protein surface. In addition, the insertion of Cys-tag on these proteins does not affect on the

interaction capability and stability of the proteins confirmed by ITC experiment and DSC analysis. In the next step, we use these protein pairs to induce self assembly of nanoparticles by attaching them to the nanoparticle surface.

6.2. Direct α-Rep protein conjugation to Au nanoparticles.

The selected protein pairs were used to direct the assembly of gold nanoparticles in order to create higher order superstructures such as dimers, chains and networks. The control of optical properties can be better achieved by this method with hybrid conjugates by tuning the protein: nanoparticle stoichiometry and exploiting orthogonal recognition between protein pairs. This section details the first attempts to produce α-Rep protein conjugates.

6.2.1. Method and Scheme description.

When mixed together A3cys and α-Rep-17cys or A3cys and α-Rep-2cys form strong conjugates. By the attachment of these proteins with gold nanoparticles separately through their cystine tag, the particles acquire the affinity to interact specifically with another population of nanoparticles bearing the complementary protein.

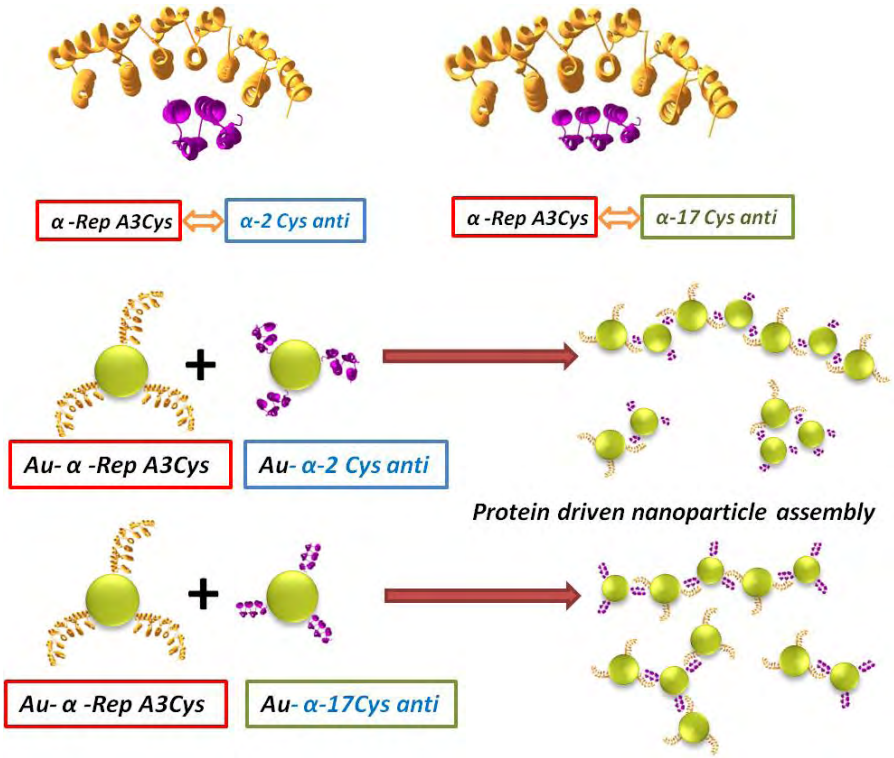

Fig VI.5: *Scheme describing protein driven self assembly of nanoparticles.*

After the attachment of protein on gold, the two complementary solutions are slowly mixed to induce the self assembly of the nanoparticles. For the protein-driven self-assembly of colloidal nanoparticles, we first attempted the direct attachment of the proteins on the surface of the nanoparticles (*Fig VI.5*). In this strategy, the calculated amount of protein was directly added to the known quantity of Au nanoparticles. The grafting efficiency of the particles on conjugation of proteins can be ascertained by the addition of 100mM NaCl.

The conjugation approach was similar with those reported by Mirkin et.al and Alivisatos [5,6] but one advantage of our approach is, we can disassemble nanoparticles by introducing another protein which has higher affinity than with the existing protein, which was involved in the primary assembly process. Moreover, the attachment of different protein pairs paves the way to orthogonal assembly of nanoparticles. Also a better design of the superstructure can be obtained by controlling the protein: particle stoichiometry (1:1, 2:1, 3:1 etc) (*Fig VI.5*). The 3D structure of protein-protein complex gives a new asset which is the 3D control of AuNP topology.

6.2.2. Experiemental procedure.

In order to conjugate protein to gold nanoparticles, it is first necessary to cleave intra and inter protein disulphide bonds formed between cystines. There are three cystine groups present in each protein, hence it is necessary to reduce them in order to engage thiol groups to gold nanoparticles surface. The usual method to reduce disulphide bond is to use Dithiothreitol **(**DTT) a common reducing agent in biology. DTT is a strong reducing agent, owing to its high conformational propensity to form a six-membered ring with an internal disulfide bond. It has a redox potential of -0.33 V at pH 7. The reduction of a typical disulfide bond proceeds by two sequential thiol-disulfide exchange reactions and is illustrated below (*Fig VI.6*).

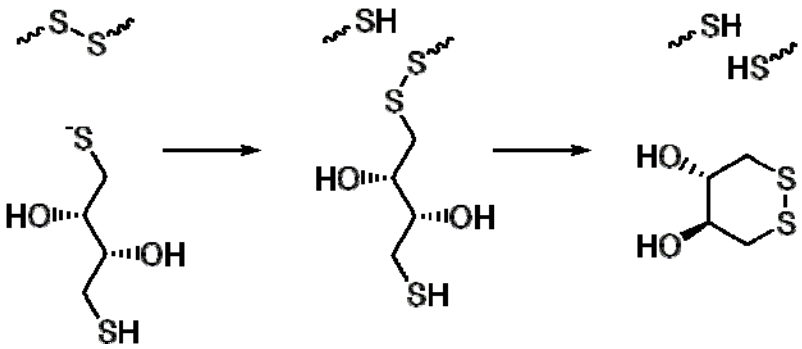

Fig VI.6: *Reaction describing the Mechanism involved in the cleavage of disulphide bond by TCEP.*

The intermediate mixed-disulfide state is unstable because the second thiol of DTT has a high propensity to close the six membered ring, forming oxidized DTT and leaving behind a reduced disulfide bond. The reducing power of DTT is limited to pH values above ~7, since only the negatively charged thiolate form $-S^-$ is reactive (the protonated thiol form -SH is not), the pKa of the thiol groups is 9.2 and 10.1.Excess DTT is removed by desalting columns.

6.2.3. Calculation of number of protein particles to conjugate on nanoparticles.

In order to induce self assembly, it was very important to maintain the stoichiometry of the two solutions. The concentration of the gold nanoparticles is calculated as mentioned in the section 2.1.4. The protein aliquots were collected in small quantity after several steps of purification and the concentration of the protein was assayed by UV-Vis spectroscopy. The extinction coefficient of the proteins calculated assuming all pairs of Cys residues form cystines. The molar concentration "C" which was defined as the amount of a constituent divided by the volume of the mixture. Hence, 6μM protein was passed through desalting column and collected in aliquots of 2μM concentration. Since the starting nanoparticle concentration was 22nM, we have investigated Au: protein molar ratio ranging from 1:200 to 1:40, 1: 20, 1:10 and 1:5 by diluting the protein sample using 50mM NAP buffer (pH7). The efficiency of the grafting as well as the stability of the protein-conjugated Au nanoparticle was monitored by UV-Vis spectroscopy and TEM analysis including after the addition of 100mM NaCl which is known to precipitate for non-functionalized, citrate-stabilized Au nanoparticles.

Procedure: Prior to each experiment, freshly reduced samples of proteins were prepared for gold nanoparticle conjugation. 1mL of 6μM protein was prepared from the concentrated solution of protein at pH 8 and about 100μL of DTT was added and incubated for 4 hours. The excess DTT was removed through desalting column by eluting with NaP buffer of concentration 50mM of pH 7 and collected with final volume with the concentration of 2μM. 1mL of 22nM of Au nanoparticles was then taken in 2mL eppendorf tube, fresh sample of 1mL of protein was added very slowly in the molar ratio 1:5, 1:10, 1: 20 and 1:40 of Au: protein, with slow stirring at 15 deg for overnight.. The above solution was then characterized through UV-Vis spectroscopy and TEM analysis.

6.2.4. UV-Vis absorption spectroscopy and TEM analysis.

In starting experiments the ratio of Au: protein was maintained at 1:200 ratio which resulted in a large aggregation of Au nanoparticles. Hence, we have reduced protein concentration subsequently. *Fig VI.7a* shows UV-Visible spectra of pure gold nanoparticles (black) and α-RepA3Cys protein conjugated gold nanoparticles (red) at Au: protein=1:5 molar ratios. The plasmon band of pure nanoparticles at 520nm appeared to have red shifted to 525nm on conjugation of proteins. Accordingly a slight change in the color of the solution was observed from pale pink to dark pink with the addition of protein to Au solution and with the course of the time this color remained the same. This shift can be associated with the increase in local refractive index by the formation of a protein shell. When the ionic strength of the solution was increased by the addition of 1mL of 100mM NaCl, the solution remains stable in time (*Fig VI.7a blue*) in contrast to citrate nanoparticles which immediately precipitated. We have analyzed the samples by through TEM after negative staining of the sample using Phosphotungstic acid (see section 2.4.1). A very thin layer of protein clearly visible in TEM with 2nm thickness (*Fig VI.7b*).

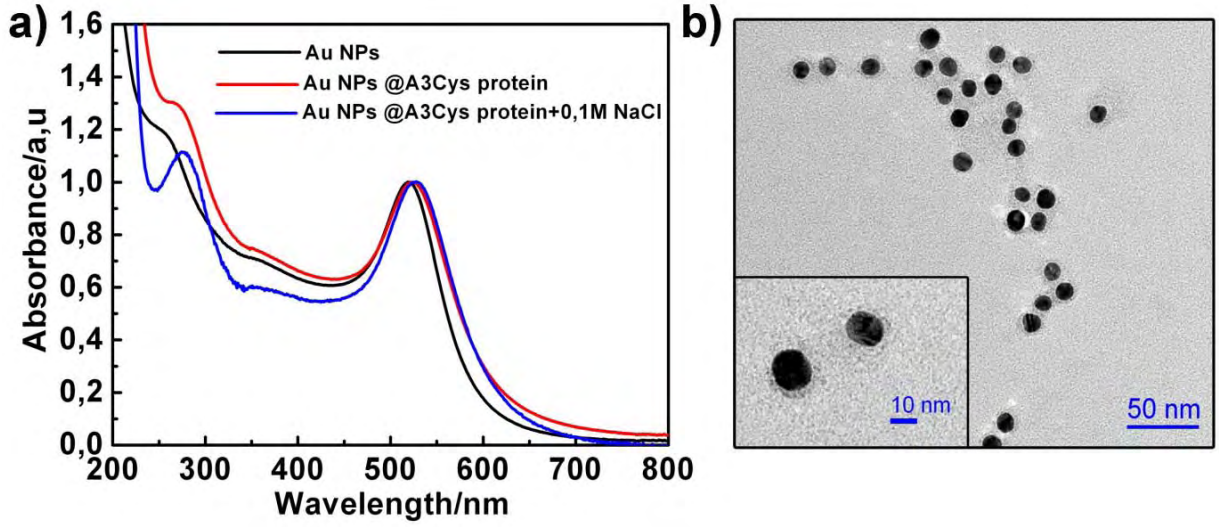

Fig VI.7: *a) Normalized UV-Vis spectra of α-Rep A3Cys coated Au nanoparticles with addition of NaCl solution (Au: protein, 1:5).b) Stained TEM image of protein coated Au nanoparticles.*

The functionalization of nanoparticles by α-2cys and α-17cys proteins, show transformation in the color of the solution from pale pink to dark pink and solution darkens with extended period of time (*Fig VI.8 inset*). The corresponding UV-Vis spectra show large red shift of plasmon band observed at 536 and 540 nm respectively (*Fig VI.8*). In addition, broadening of

the spectrum was observed in case of α-17cys protein conjugated Au nanoparticles (*Fig VI.8a)*. When the ratio of protein was increased from 1:5 to 1:10, 1:20, and 1:40, on gold nanoparticles, the red shift of 520nm plasmon band was even large for Au-α-2cys Au-α-17cys conjugates. Evolution of new bands at 607 and 612nm were observed in case of Au-α-2cys and Au-α-17cys conjugates (*Fig VI.8 b, c*). Very small shift was observed in case of Au-α-RepA3cys protein conjugates but precipitations of the samples are observed when the molar ratio is increased from 1:40 to 1:100 and 1:200. We have analyzed these samples by TEM.

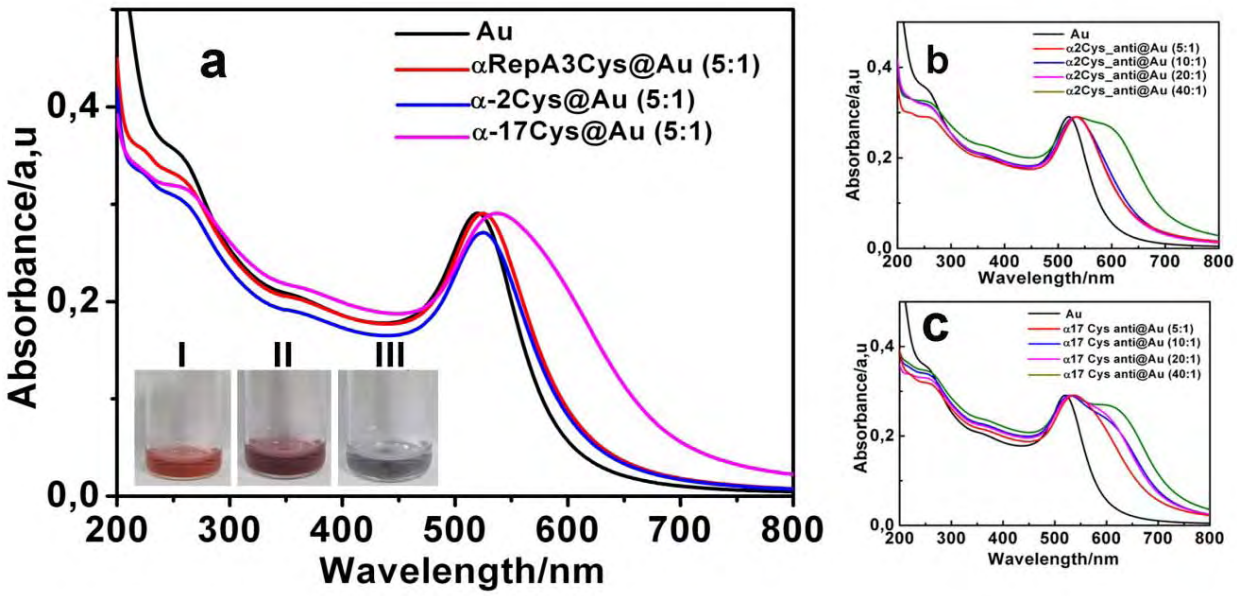

Fig VI.8: a) *Normalized UV-Vis spectra of Au nanoparticle and α-Rep A3Cys, α-2Cys, α-17Cys protein conjugated Au nanoparticles with molar ratio Au: protein, 1:5.In set fig shows change in the color of the solution after addition of protein. I-Au NPS, II-after addition of α-Rep A2Cys and α-Rep A17Cys protein, III-after 24 hour .b) and c) Normalized UV-Vis spectra of Au nanoparticles conjugated with α-2Cys and α-17Cys protein at different molar ratio. Evolution of longitudinal band was observed with increasing protein amount.*

6.2.5. TEM characterization and Dynamic light scattering experiment.

When αRep A3Cys protein was conjugated to Au nanoparticles, mono dispersed particles of Au (*Fig II.1*) tends to form small aggregated structures as observed in (*Fig VI.9a*). Whereas conjugation of α-2cys (*Fig VI.9b*) and α-17cys (*Fig VI.9 c)* proteins resulted in the formation of large aggregated structure along with massive nanoparticles networks. The statistical distribution on interparticle distance follows Gaussian distribution and measured at 1.1 ±0.2nm.

Dynamic light scattering (DLS) experiments were performed on these samples and we observed increase in the hydro dynamic radius on conjugation of protein. When α-Rep A3Cys protein is attached to Au nanoparticles the hydrodynamic radius was increased from 21 to 25 nm *(Fig VI.10)*. Whereas with the conjugation of α-Rep-2cys and α-Rep-17cys , the increase in size was quite large and observed as 36nm and 58 nm respectively.

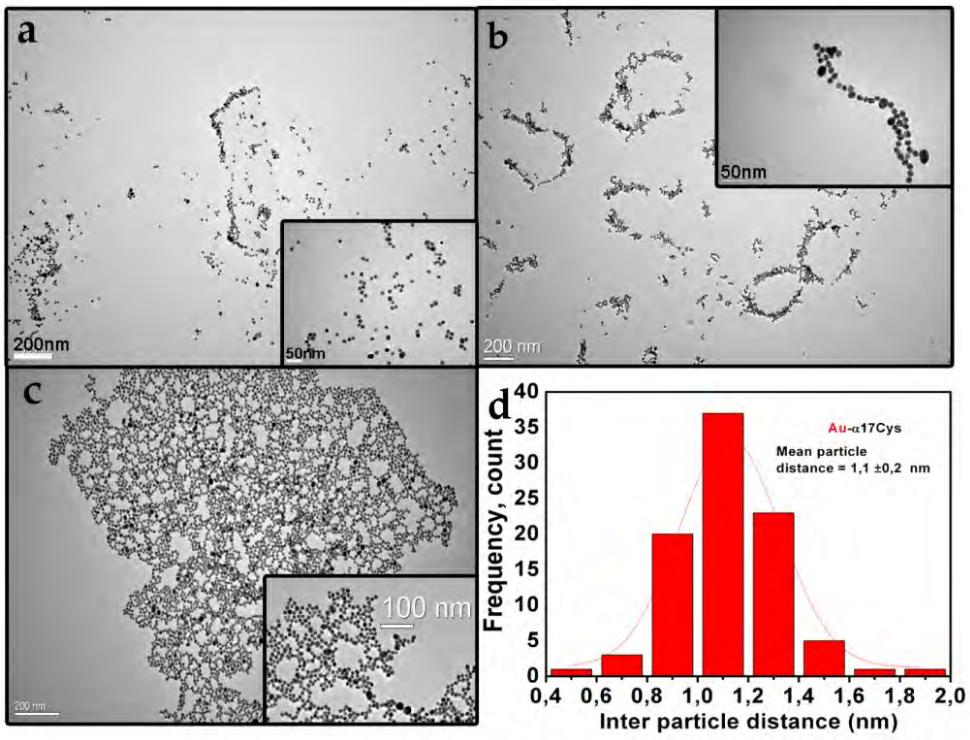

Fig VI.9: *TEM images of a) α-Rep A3Cys, b) α- 2Cys and c) α- 17Cys protein conjugated Au nanoparticles. Small numbers of aggregates were found in case of Au-α-Rep A3Cys whereas large numbers of nanoparticle chains were found in Au-α2Cys and Au-α17Cys conjugates.d) Statistical analysis of interparticle distance measured on the TEM images.*

The zeta potential measurements of pure protein samples showed large negative potential indicating that proteins are highly stable in solution (α-Rep A3cys -41.83, α-2cys -29.6 , and α-Rep-17cys -40.9). The measured zeta potential of pure Au nanoparticles (-24.3mV) tend to decrease (-19.1mV) when α-Rep A3cys protein was conjugated and a further decrease in zeta potential was observed (-18.2) with the conjugation of α-Rep-2cys and α-Rep-17cys protein. This correlates with DLS spectra and TEM analysis where conjugation of protein on Au nanoparticles resulted in large aggregation. This change was also evident from UV-Vis spectra which showed large red shift and arise of new longitudinal band with the conjugation of α-Rep proteins on Au NPs. This behavior can be illustrated by taking into account the

formation of Au nanochains with the addition of mercaptoethanol (section 1.3.1) [7,8].

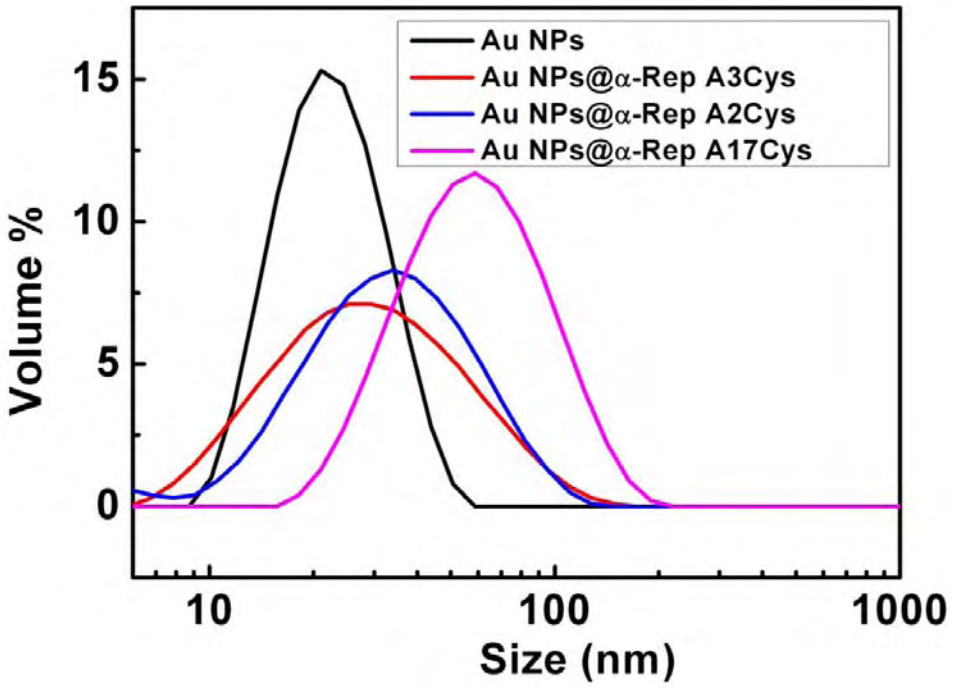

.

Fig VI.10: *Dynamic light scattering spectra of Au nanoparticles and Au nanoparticles conjugated with α-Rep A3cys, α–2cys and α- 17cys proteins.*

When α-Rep proteins were directly added to citrate stabilized Au nanoparticles at low protein concentration (Au: protein, 1:5), proteins displace citrate molecules and isotropic distribution of proteins on the surface of nanoparticles results in no change in the stability (*Fig VI.11c*). Whereas when proteins were added with increased molar ratio (1:50), the non uniform attachment of these proteins on the nanoparticle because of the protein-protein interaction leads to the formation of an induced dipole (*Fig VI.11b and Fig VI.8b, c*). Interacting dipole born by each nanoparticle will tend to align to other dipoles and form chain like structure to minimize energy. When extremely large excess of proteins (1:200) were added isotropic compact aggregates were formed and eventually precipitates (*Fig VI.11a*). The formation of nanoparticle networks was more pronounced in case of α-2Cys and α-17 Cys conjugated Au nanoparticles than with Au-α-RepA3Cys conjugates, probably because of the more inter protein interactions. Hence we observed the formation of nanoparticle chains in case of α-2Cys and α-17 Cys protein conjugation even at lower molar ratio between the Au and proteins. The interparticle distance was found at ~1nm and as the numbers of particles were increased in these chains, an increase in the red shift of plasmon band was observed. This result was in well correlation with the theoretical calculation performed on similar system.[9]

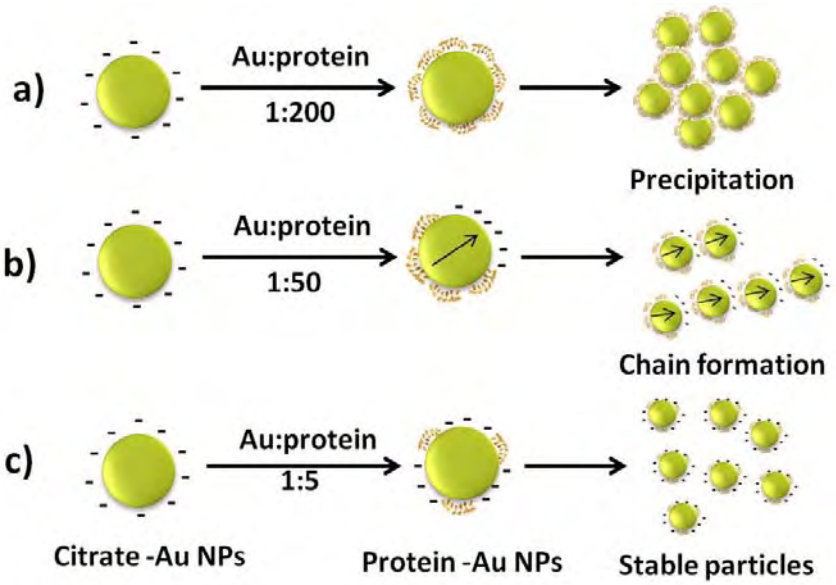

Fig VI.11: *Schematic diagram explaining the mechanism involved in the formation of Au nanochains and aggregation with the conjugation of proteins on Au nanoparticle surface.*

6.3. Protein conjugation by ligand exchange.

The direct grafting of α-Rep proteins onto nanoparticles leads to a moderately controlled the stability of the conjugates. To overcome this problem, we have modified our procedure by employing a two step method. First, we stabilize the nanoparticles with a short thiolated peptide ligand and then we proceed to a ligand exchange with our protein. In this manner, we expect the bifunctional coating to improve the particle stability and preserve the binding capacity of the proteins.

6.3.1. Method and scheme description.

In this modified method, the gold nanoparticles were first functionalized covalently with a negatively charged peptide ligand which was composed of three blocks: a 3- cystine tag, a 6-glycol spacer, an aspartate head group. C_3E_6Asp named as ***Cys-Cys-Cys-21-amino-4, 7, 10, 13, 16, 19-hexaoxaheneicosanoyl-Asp***, **C_3E_6 Asp**. The neutral peptide sequence was similar when compared to negatively charged peptide sequence except the end $–NH_2$ group i.e. ***Cys-Cys-Cys-21-amino-4, 7, 10, 13, 16, 19-hexaoxaheneicosanoyl-NH_2*, C_3E_6 NH_2.**

This C_3E_6Asp ligand binds to Au nanoparticles from the cystines and bears a negative charge at pH 7 by the presence of aspartic acid (pKa=4.0). Hence the large negative charge of the ligand with covalent binding on to the surface of nanoparticles was efficient to maintain their colloidal stability (*Fig VI.13-I*).

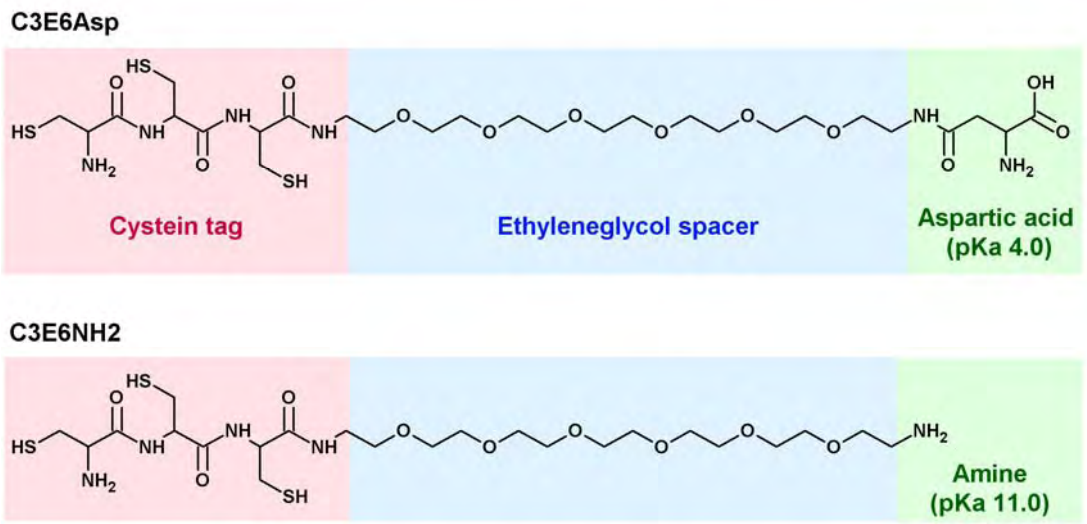

Fig VI.12: *Figure showing chemical structure of two ligands commercially obtained and used for conjugating Au nanoparticles.*

In the second step, α-Rep proteins were added to the peptide-conjugated nanoparticles to induce a controlled exchange of peptides with proteins (*Fig VI.13-II*). The same approach was followed by conjugating a neutral or partially positively charged peptide ligand in order to see the effect of the charge during the ligand exchange with peptide. ($C_3E_6NH_2$) was also obtained commercially and is also composed of three cystine and ethylene glycol spacer except that it carries an amine group at the end. This peptide ligand has a partial positive charge but very less compared to the negatively charged peptide which may favor exchange of proteins effectively on the nanoparticle surface in comparison with the previous peptide and also interact less with protein surface once bi functional sheath was formed.

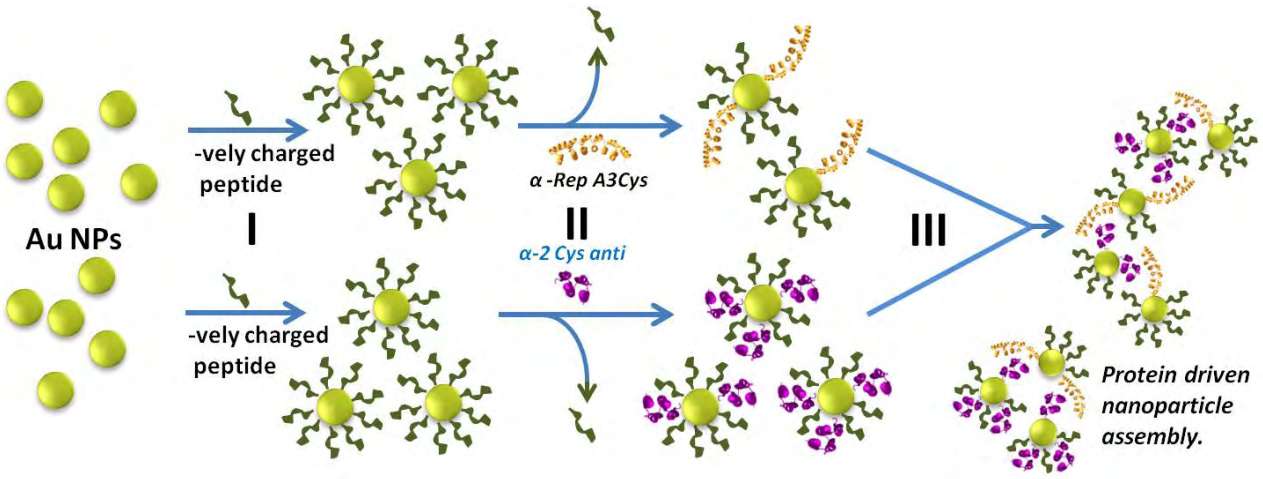

Fig VI.13: *Scheme describing two step conjugation of protein on Au nanoparticles and protein driven self assembly.*

6.3.2. Ligand exchange protocol.

1mL of 22nM Au nanoparticles was taken in a 2mL eppendorf tube and about 100µL of C_3E_6Asp or C_3 E_6 NH_2 solution of 2mM was added and incubated for four hours. This solution was centrifuged to remove the excess of ligand and the precipitate was redispersed in 1mL of 50mM NaP buffer at pH 7.The ligand exchange with protein was performed by the addition of 1mL protein with molar ratio, Au: protein, 1:200 to the peptide coated Au NP. The solution was then incubated for overnight and characterized by UV and DLS spectroscopy and TEM analysis. The pH and ionic strength of the protein-conjugated nanoparticles was maintained similar to that of pure protein samples in order to have recognition process alive when mixed with complementary conjugate solution.

6.3.3. UV-Vis absorption spectroscopy.

The stepwise functionalization of NP by either ligand followed by the exchange with the protein has been followed by UV-Vis spectroscopy (*Fig VI.14).* The surface conjugation with the C_3E_6Asp results in no major change of the spectrum. A very limited shift of the plasmon was observed from 522 to 523nm (Fig VI.14a).

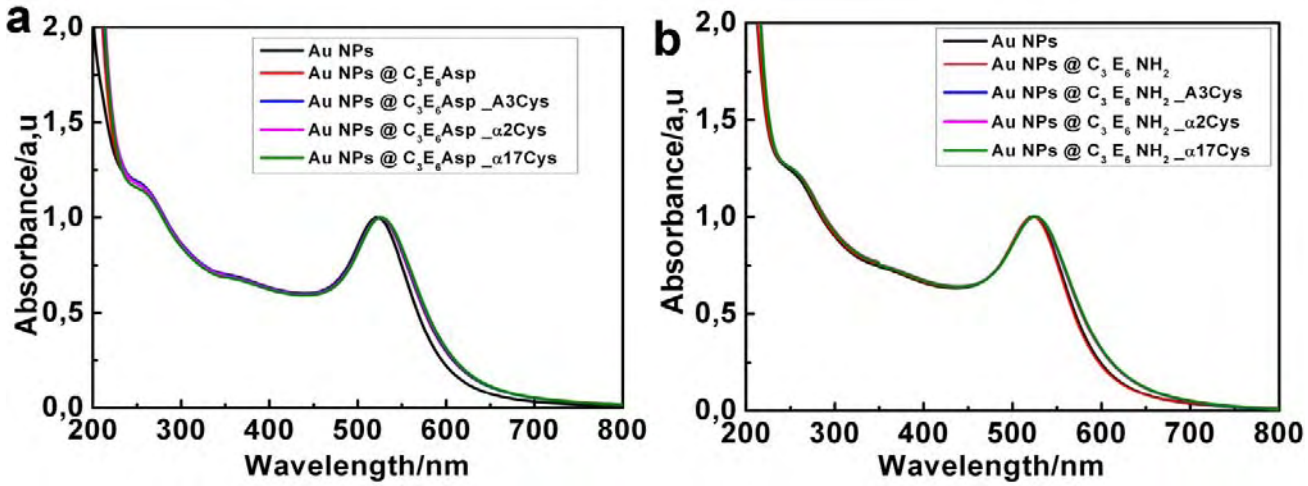

Fig VI.14: *Normalized UV-Visible spectra of Au nanoparticles conjugated with a) C_3E_6Asp ligand, b) C_3 E_6 NH_2 ligand and exchanged with α-Rep A3Cys, α-Rep-2cys or α-Rep-17cys protein.*

The exchange of C_3E_6Asp, with α-Rep A3Cys, α-Rep-2cys or α-Rep-17cys increases shift from 523 to 525 nm or 526 nm. **(***Fig VI.14a*). This very gradual and limited shift was consistent with the small increase of the local refraction index upon functionalization. Interestingly, no new longitudinal band has been observed on conjugation of proteins. The

similar experimental protocol was repeated by conjugation of $C_3E_6NH_2$ in order to limit the electrostatic interaction of the ligand shell with the protein binding site. UV-Visible spectroscopy performed after the conjugation of $C_3E_6NH_2$ and subsequent exchange with α-Rep proteins showed essentially the same feature. Indeed the NP plasmon band at 522nm is shifted by 1 nm on conjugation with $C_3E_6NH_2$ ligand (*Fig VI.14b*). When this solution is subjected to exchange with α-Rep A3Cys proteins, plasmon band shifts at 524nm (*Fig VI.14b*). No sign of longitudinal band was observed which signifies that there was no aggregation of nanoparticles.

6.3.4. Dynamic light scattering experiment.

DLS spectra were recorded at each setup in order to see the change in the hydrodynamic radius of Au nanoparticles after conjugation with either ligand and after exchange with proteins. Conjugation of C_3E_6Asp peptide ligand show an increase in hydrodynamic radius from 21nm to 28 nm (*Fig VI.15*). The partial exchange of this ligand with α-Rep A3Cys, *α-Rep-2cys* and *α-Rep-17cys* proteins showed a further increase of the hydrodynamic radius to 32nm (*Fig VI.15*).

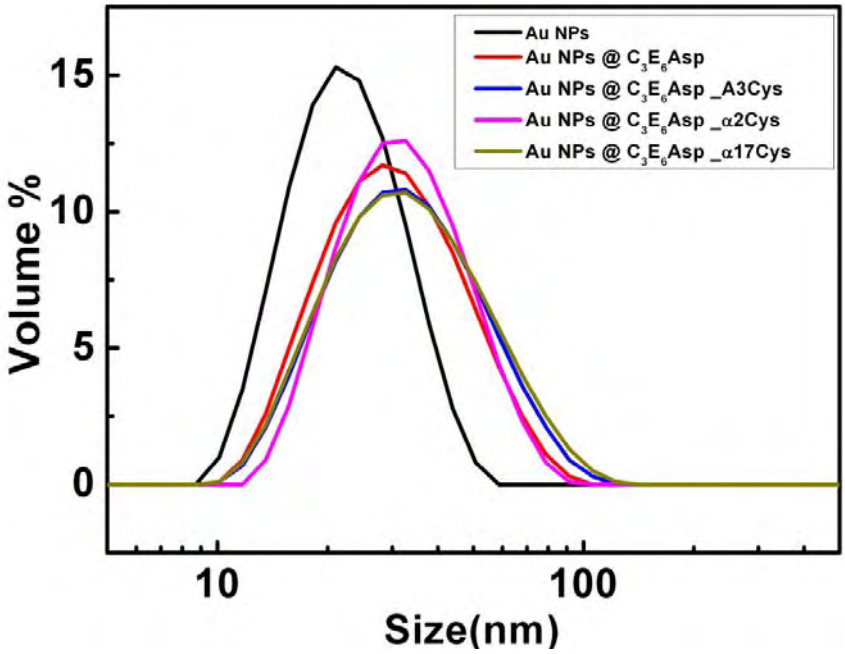

Fig VI.15: *DLS spectra of Au nanoparticles conjugated with C_3E_6Asp peptide and exchanged with α-Rep A3Cys, α- 2cys and α-17cys protein.*

No aggregation behavior was observed and this data confirms that protein is effectively exchanged with C_3E_6Asp peptide ligand onto nanoparticle surface without affecting the stability of nanoparticles. The size increase was consistent with the sizes of the peptide ligand

and proteins. A similar spectrum was obtained with neutral peptide exchanged Au-α-Rep protein samples.

6.3.5. TEM analysis.

TEM analysis of the functionalized nanoparticles was performed on stained and unstained samples. The conjugation of C_3E_6Asp peptide ligand on Au nanoparticles does not induce observable aggregation. Similarly protein exchange preserves the quality of the nanoparticles. The analysis of same samples 10days after the conjugation shows similar results. Negative staining on the samples showed a thin protein layer of sheath thickness of 2nm and it is not uniform all around the samples (*Fig VI.16 b, c, d*).

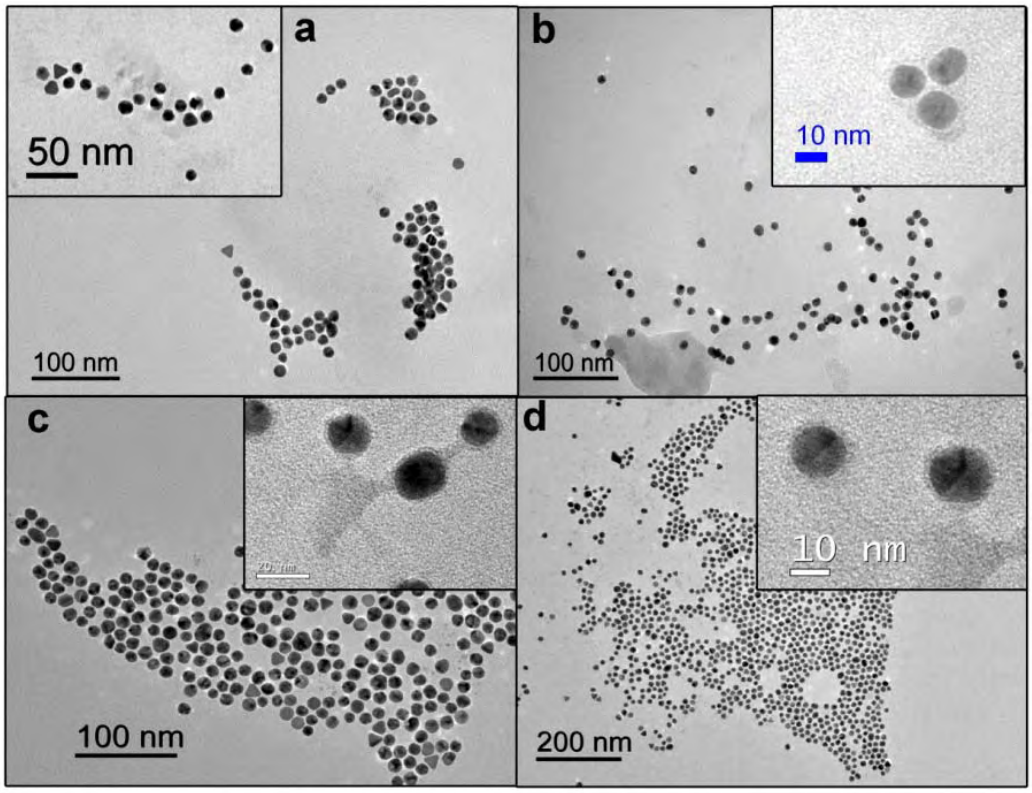

Fig VI.16: *TEM images of a) Au nanoparticles conjugated with C_3E_6Asp peptide and exchanged with b) α-Rep A3Cys, c) α- 2cys and d) α- 17cys protein.*

Similar behavior was observed in TEM images when nanoparticles were conjugated with C_3 E_6 NH_2 ligand (*Fig VI.17a*) and exchanged with α-Rep A3Cys (*Fig VI.17b*), α2cys (*Fig VI.17c*) and α17cys protein (*Fig VI.17d*). The stained TEM images of the sample show thin layer of protein surrounding nanoparticles. Hence stability of the nanoparticles was retained after the conjugation ligand and exchange with proteins.

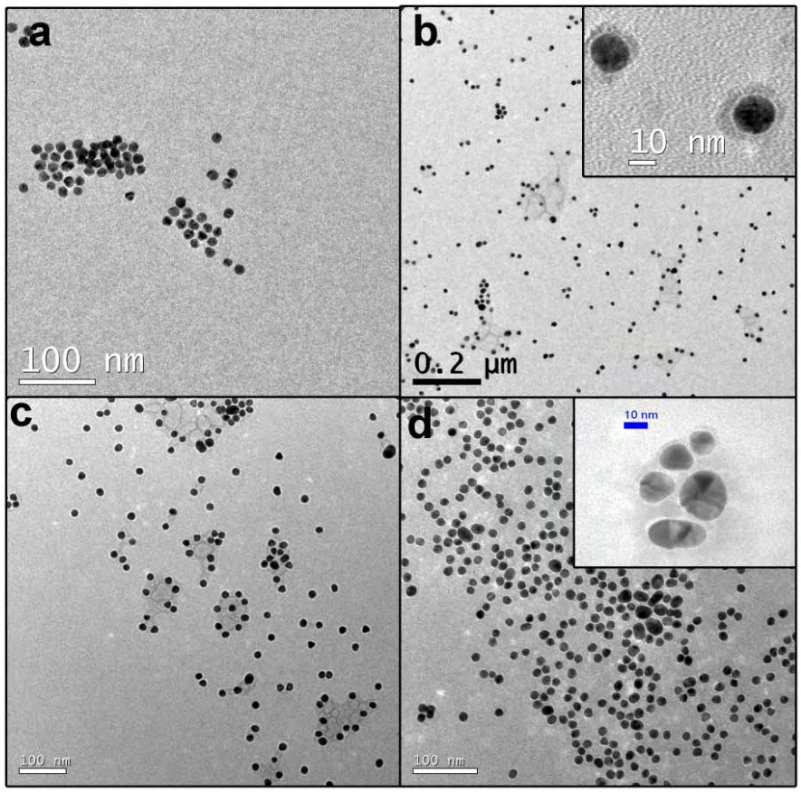

Fig VI.17: *TEM images of a) Au nanoparticles conjugated with $C_3E_6NH_2$ and exchanged with b) α-Rep A3Cys, c) α -2Cys and d) α- 17cys protein.*

Ligand exchange method described here appears to be more efficient than the direct conjugation of proteins. In addition the protein-conjugated nanoparticle solutions with the ligand exchange method were found to be stable with the course of the time. UV-Vis, TEM and DLS analysis showed similar results.

6.4. Artificial protein driven nanoparticle self assembly.

Following the scheme of *Fig VI.12*, we proceeded to step III by mixing nanoparticles conjugated with complementary proteins i.e. A3Cys-conjugated nanoparticles with α-2cys conjugated nanoparticles or α- 17cys conjugated nanoparticles

6.4.1. Experimental procedure of self assembly.

Protocol: 300µL of C_3 E_6 Asp -α-Rep A3Cys protein conjugated nanoparticle solution was mixed with 300µL of α-Rep A2Cys protein conjugated Au nanoparticles with 1:200, molar ratio. The solution was then incubated with stirring for 6 hour at 15deg and the solution was left undisturbed for 24 hours for interaction. The same procedure was repeated while mixing

Au nanoparticles conjugated with α-Rep A3Cys protein with Au nanoparticles conjugated with α-Rep A17Cys protein. In the second experiment the similar protocol was repeated with the samples conjugated with neutral peptide and exchanged with α-Rep proteins. The samples were then characterized with UV-Vis spectroscopy and TEM analysis.

6.4.2. UV-Vis spectroscopy and TEM analysis.

The UV-Visible spectra of nanoparticles conjugated to affinity pairs and their mixtures are shown in *Fig VI.18*. The intensity of the mixture varies when two nanoparticle solutions were mixed together. No shift in the plasmon peak is observed. This spectrum was similar when obtained with neutral peptide primed samples. Hence, no specific change in favor of self assembly of nanoparticles was observed in absorption spectra, after mixing two complementary nanoparticle solutions.

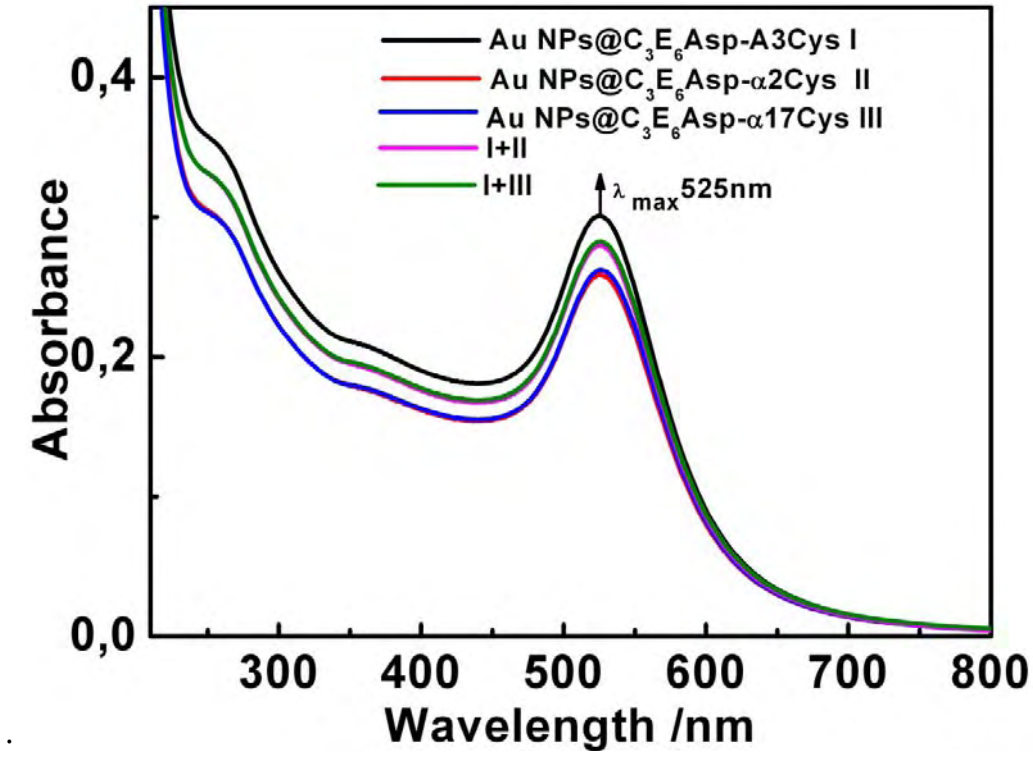

Fig VI.18: *UV-Visible spectra of Au nanoparticles conjugated with affinity α-Rep proteins, α-Rep A3Cys, α2 cys and α17 cys and their pair wise mixtures (I)+(II) and (I)+(III).*

We performed TEM analysis of the samples in order to get a direct insight. Very few chains and assembled particles were observed in TEM image , when Au -α-Rep A3Cys conjugates mixed with Au - α2Cys protein conjugate (*Fig VI.19a,b*). On the contrary, TEM images

showed almost exclusively isolated individual particles, when we mix Au -αRep A3Cys conjugate with Au - α17Cys conjugate. Some chain like structures were also observed indicated a weak interaction leading to the formation of small chain clusters containing 3 to 6 nanoparticles on average. However, in this case also, most of the nanoparticles were isolated. It therefore appears that weak or no specific interaction was conferred by the complementary proteins to the nanoparticles, although the grafting of proteins has been demonstrated successfully.

Similar results are obtained with the particles initially primed with neutral C_3 E_6 NH_2 ligand. One possible reason is that, our protein functionalization procedure results in a large dilution, so that the effective concentration of protein was lowered. The decrease in the concentration effectively modifies the strength of intermolecular interactions between protein-protein complexes.

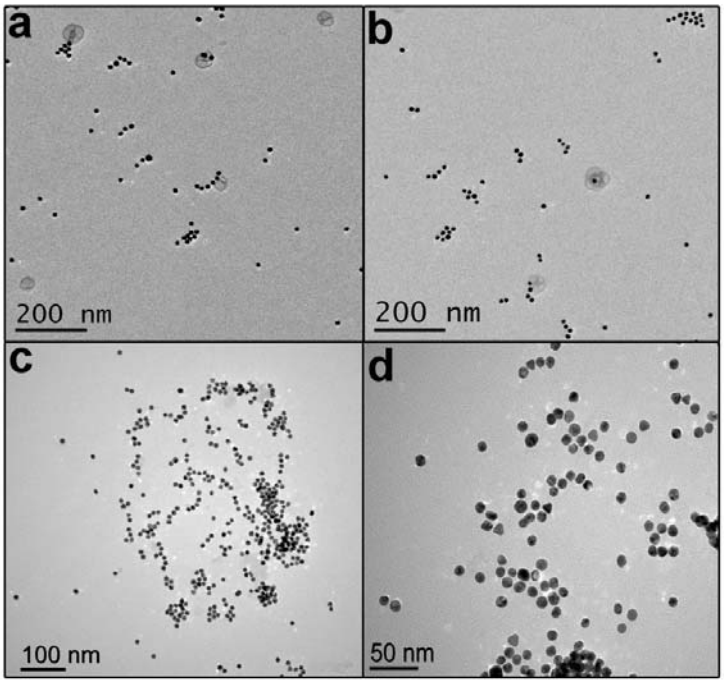

Fig VI.19:*TEM images of a, b) Au nanoparticles conjugated to α-Rep A3Cys mixed with Au nanoparticles conjugated to α 2Cys, c, d) Au nanoparticles conjugated to α-Rep A3Cys mixed with Au nanoparticles conjugated to α17Cys protein.*

The dissociation constant K_D of nanoparticle pairs formed by the mixture of Au-αRep A3Cys and with Au-α17Cys is given by

$$\boldsymbol{K_D = \frac{[\mathbf{Au-\alpha Rep\ A3Cys}][\mathbf{Au-\alpha 17\ Cys}]}{[\mathbf{Au-\alpha 17\ Cys-\alpha Rep\ A3Cys-Au}]}} \qquad (\boldsymbol{II})$$

where, **[Au-αRepA3Cys]**, **[Au-α17Cys]** and [**Au-αRepA3Cys - α17Cys-Au**] are the concentration of Au-αRep A3Cys, Au-α17Cys and the complex Au-αRep A3Cys- α17Cys-Au respectively. The measured dissociation constant K_D for pure protein complex **αRepA3Cys -α2Cys** and **αRepA3Cys-α17Cys** is 4.2 and 212.7nM with the initial concentration of target (αRepA3Cys) 350μM and binder (α17Cys or α2Cys) 30μM respectively. Therefore it is clearly visible that in our protocol, the concentration of the protein present in the solution or on the surface of the nanoparticles, are ~200 times lesser than the original protein concentration.

Moreover, considering the surface area of the nanoparticles, the above concentration of the protein is in large excess to cover the nanoparticle surface and may result in the precipitation of Au nanoparticles, with the increase in protein concentration. Therefore in order to get closer with these conditions, solutions of protein-conjugated nanoparticles were concentrated five times. This should result in a 25-fold increase of duplex concentration.

6.4.3 Assembly of concentrated protein-conjugated nanoparticles (with C_3E_6Asp primer).

Agarose gel electrophoresis.

Electrophoresis is a standard technique used for the separation, purification and analysis of protein solutions. It consists in forcing the migration of proteins in a gel by applying a high voltage. Protein mixtures and complexes can then be solved according to their molecular weight and charge. For α-Rep proteins, electrophoresis is more efficient when performed on an acrylamide gel (See section 2.3.5, Chapter 2). When α-Rep conjugated nanoparticles were applied in acrylamide gel, no migration was obtained due to the small pore size in the gel we therefore changed over agarose gel electrophoresis which is better suited for nanoparticles.

Protocol: 0.5% agarose gel was prepared in 0.2M Tris borate buffer at pH 7. About 100μL of sample (5X) solution was centrifuged and about 70μL of supernatant liquid was removed. 20 μL of 30% glycerol was added and loaded onto the Gel. 130V of electric field was applied between two electrodes for 30 min and the migrations of the sample were observed. *Fig VI.20* shows a typical example of simultaneous AGEP of samples with the red band indicating the position of the nanoparticles after applying voltage. Citrate-stabilized Au nanoparticles bear small charge which is only weakly bound, hence they will not migrate in the gel (track 1).

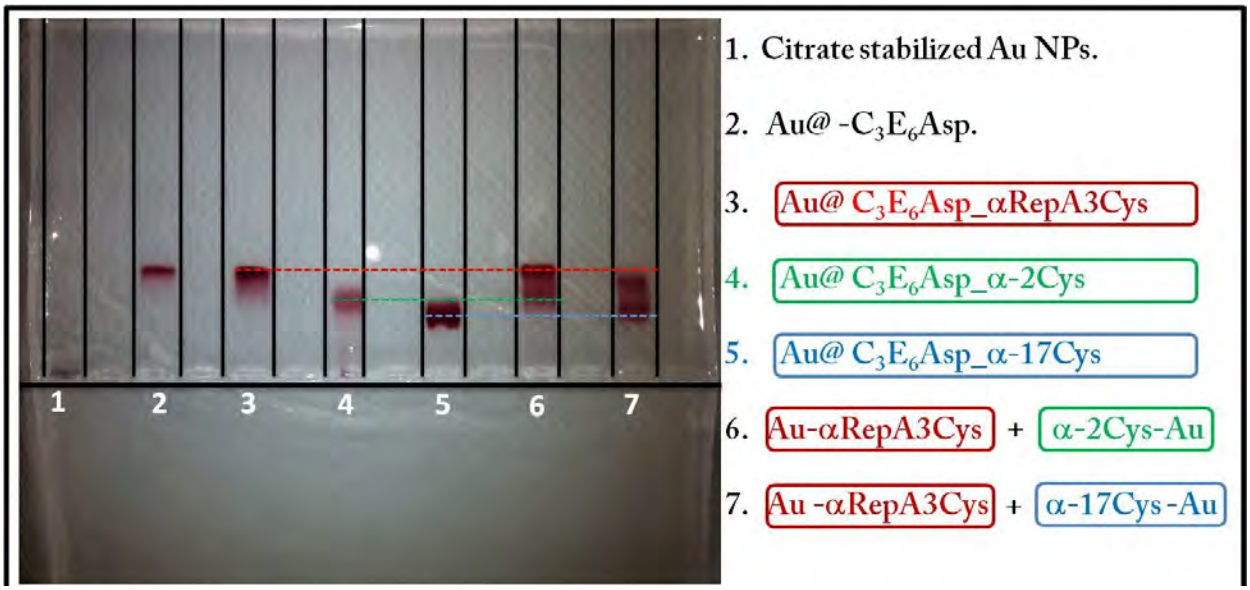

Fig VI.20: *Photograph of agarose electrophoresis gel of Au nanoparticles (1) primed with C_3E_6Asp (2) , after exchange with complementary α-Rep proteins pairs (3, 4, 5) and their mixture (6, 7).*

After their conjugation to negatively charged ligand C_3E_6Asp, the nanoparticles migrate substantially (*Fig VI.20 track 2*) and the ligand exchange with α-Rep A3Cys proteins shows a migration of nanoparticles that remains essentially same, but we can notice that part of the sample drags behind (*track 3*). This is probably because the addition of the protein increases the nanoparticle overall size with peptide but after the exchange the potential on the nanoparticle surface remains same because of the protein charge. The track-4 and 5 shows migration of Au-α2Cys and Au-α17Cys protein conjugates. While track 6 and 7 shows migration of these population mixed with Au-A3Cys protein conjugate.

During the exchange reaction, the ligands were only partially replaced by α-Rep proteins (*Fig VI.13 II*). Zeta potential measurement have shown that the net charge of α17Cys and α2Cys was much smaller than that of A3Cys, which accounts for the fact that the increased size is not complemented by an increased charge except for A3Cys. Two bands (*Fig VI.20 track 6*) exactly match the bands with the original Au-protein conjugate (*Fig VI.20 track 3 and track 4*). This indicates no or very weak interaction takes place between αRepA3Cys-Au and α2Cys Au protein conjugated nanoparticles. When conjugates of Au-αRepA3Cys are mixed with Au-α17Cys, similar result was observed. Yet the upper bands are not strictly aligned with the reference bands (*track 3 and track 5*). A small but visible decay on the Au-αRepA3Cys particles and acceleration on the Au-α17Cys band along with some significant

matter in between could indicate a recognition mechanism between the two populations. Since gel does not provide a complete proof of protein driven self assembly, the samples were analyzed by TEM.

TEM and SEM analysis.

TEM image of the mixture of Au-αRep A3Cys with Au- α2Cys showed very small number of assembled nanostructures (*Fig VI.21*). A thin layer of protein is visible even without staining, and large number of isolated nanoparticles were found along with very small numbers of dimers, short length chains in TEM.

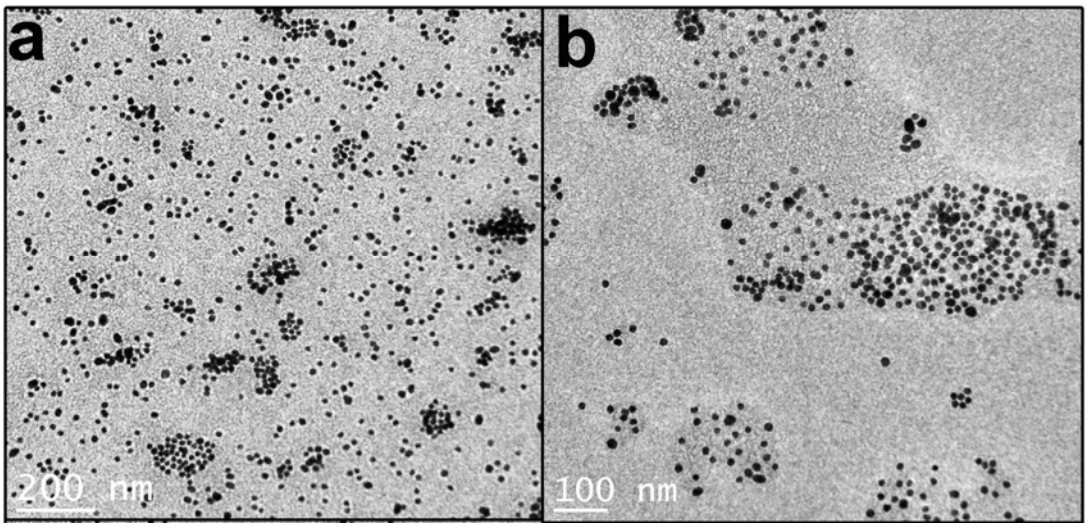

Fig VI.21: *TEM images of Au-α-RepA3Cys conjugates mixed with Au -α2Cys protein conjugates.*

When we mixed the Au-αRep A3Cys protein conjugate with Au- α17Cys protein conjugate, formation of very small amount of precipitate or filament was observed in the bottom of the eppendorf tube. Hence, we prepared samples for TEM and SEM analysis, by collecting samples from the major part of the samples (supernatant) as well as from the precipitate.

When the sample collected from the supernatant was analyzed by TEM, small numbers of chains composed of 2-3 nanoparticles were found (*Fig VI.22a, b)*. Whereas, when the filaments or precipitate obtained from the same solution were analyzed in TEM, massive monolayer of nanoparticles was observed (*Fig VI.23*). The edge of the monolayer showed no closer assembly of the particles compared to the rest part of the monolayer. Therefore drop drying artifacts during TEM preparation are unlikely to account for the monolayer formation. Moreover a very thin layer of protein is visible between the particles (*Fig VI.23d*).

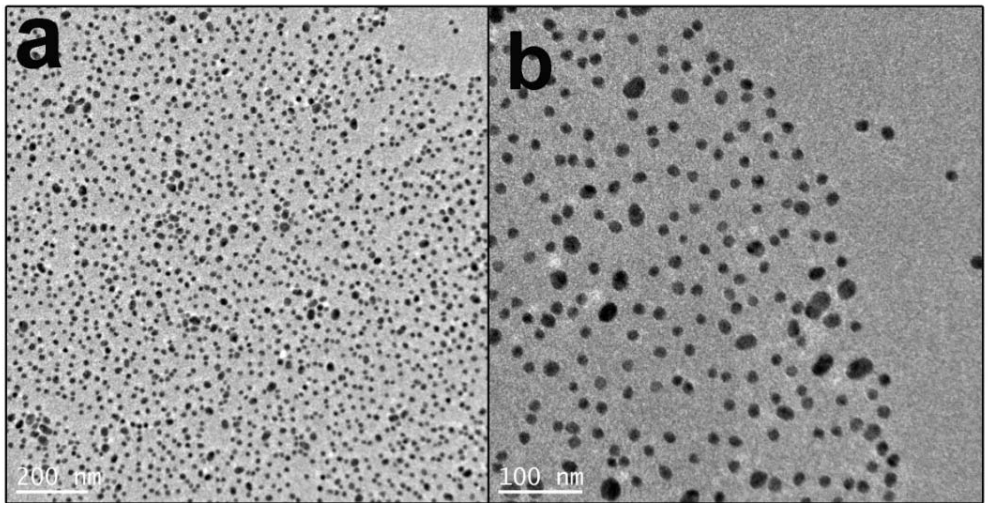

Fig VI.22: *TEM image of the Au-αRepA3Cys conjugate mixed with Au- α17Cys protein conjugate. Samples were collected from the supernatant and prepared for TEM analysis.*

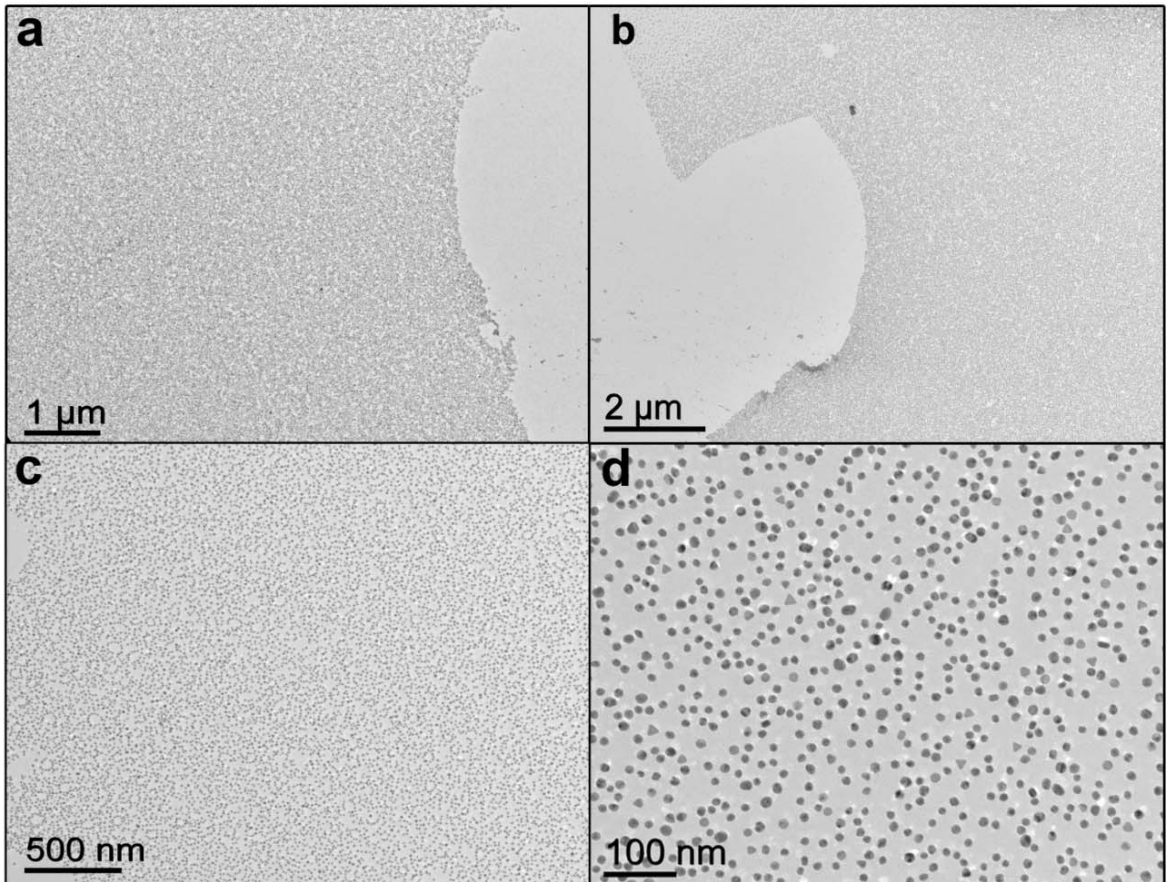

Fig VI.23: *TEM image of Au nanoparticle monolayer formed by the interaction of Au-α Rep A3Cys with Au -α17Cys protein conjugates. Samples are collected from the precipitate and prepared for TEM analysis.*

The SEM analysis of same sample showed the formation of uniform monolayer of nanoparticles as observed in TEM, which is of several tens of micrometer size (*Fig VI.24*).

We observed a more compact arrangement of these nanoparticles along with a formation of second monolayer at certain places (*Fig VI.24c*).

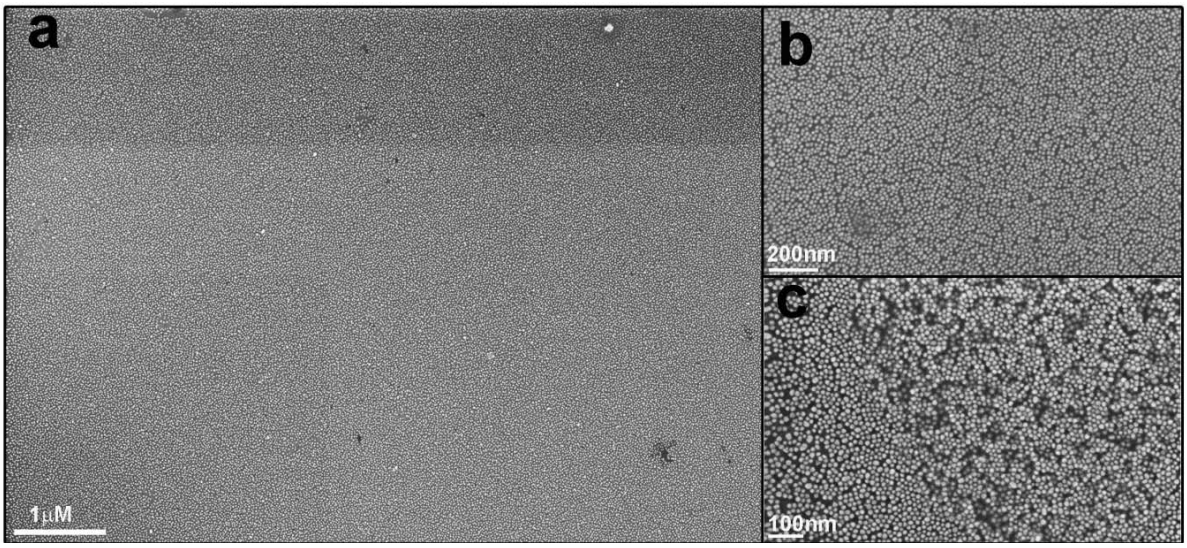

Fig VI.24: *SEM image of Au-αRepA3Cys conjugate mixed with Au- α-Rep A17Cys protein conjugate. a) Micrometer long monolayer of Au nanoparticles, b) closer view of the monolayer showing compact arrangement of nanoparticles and c) portion of bi-layer which were found in some places.*

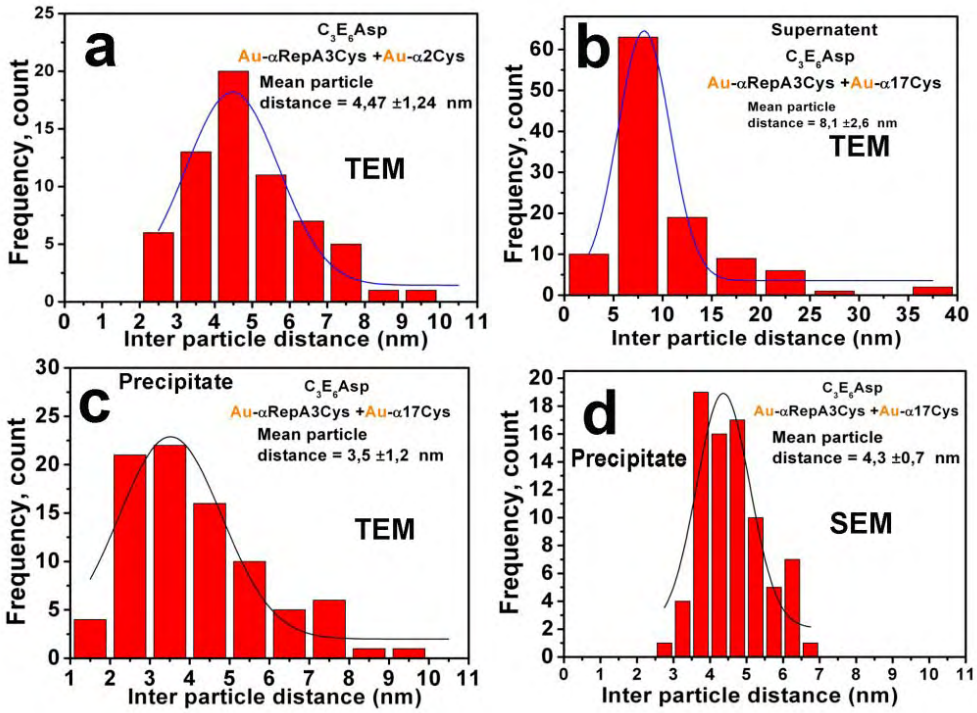

Fig VI.25: *Statistical distribution analysis on interparticle distance from TEM and SEM images. a) Duplex solution containing a mixture of Au-αRep A3Cys and Au-α2Cys and b, c,d) mixture of Au-αRep A3Cys and Au-α17Cys conjugates.*

The statistical distribution of inter particle distance has been measured from TEM and SEM images (*Fig VI.25)*. This follows Gaussian distribution, where the average interparticle distance of 4.4 ±1.2nm was found in case Au-α-RepA3Cys mixed with Au -α2Cys (*Fig VI.25a)* samples. Quite large interparticle distance 8.1± 2.6 nm (*Fig VI.25b)* was measured in case of Au-α-RepA3Cys mixed with Au -α17Cys supernatant samples. This comprises the larger portion of the sample. Whereas much smaller interparticle distance, 3.5 ±1.2nm (TEM) and 4.3±0.7nm (SEM) was found in case of compact monolayer obtained from the precipitate in the same solution (*Fig VI.25c, d*).

Analysis by UV-Vis Absorption spectroscopy.

The Au-α-Rep protein conjugate solutions were concentrated five times by centrifugation technique. These samples were analyzed by UV-Vis spectroscopy (*Fig VI.26)*. The UV-Vis spectra of all conjugates showed the expected increase in the intensity and no spectral shift which suggest that that this protocol did not induce any non specific aggregation of protein conjugated nanoparticle solution.

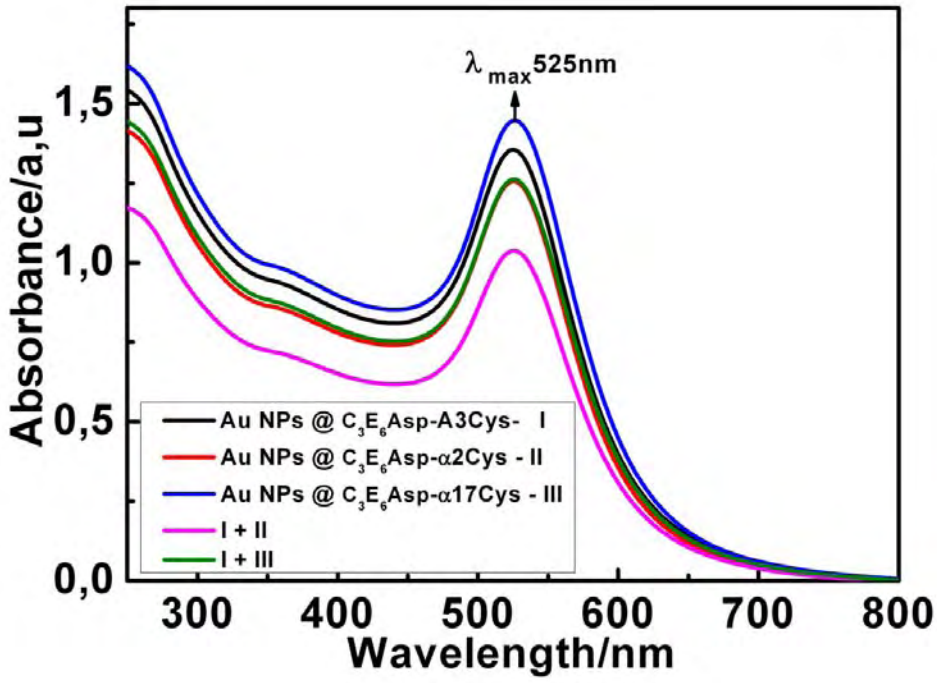

Fig VI.26: *UV-Visible spectra of concentrated Au nanoparticle-protein conjugates and mixture of two affinity pair (I) + (II) and (I) + (III).*

When Au-αRep A3Cys conjugates are mixed with Au-α2Cys no change in the spectrum was observed during 1 hour after the mixing. The solution was kept undisturbed for 48 hour and

the UV-Vis spectra were recorded again. We saw large decrease in the intensity of the plasmon band of the mixed solution compared to the original solution (*Fig VI.26 pink curve)*. The same behavior is observed when two populations of Au-αRepA3Cys and Au-α17Cys conjugates are mixed together (*Fig VI.26 a green curve*). There is no spectral shift or lower energy plasmon band is observed after mixing. In this case, although the large portion of the solution remained clear, very minute quantity of filaments were observed at the bottom of the eppendorf tube with increasing time. Presumably, indirect interaction involving un-folded proteins or concatenated proteins (due to N terminal interaction as C-terminal is involved in attachment on Au surface) could account for the formation monolayer of nanoparticles. Even if assembled by some protein mediated networks which were found in small amounts, the large distance prevents the effective surface plasmon coupling .Therefore the observations in UV-Vis spectra are consistent with a massive aggregation that reduces the amount of free nanoparticles (plasmon intensity) but without any spectral shift, since no coupling was stabilized. The interaction of Au-αRepA3Cys with Au-α17Cys is found to be stronger than Au-αRepA3Cys with Au-α2Cys, conferred by TEM and Gel electrophoresis.

6.4.4. Assembly of concentrated protein-conjugated nanoparticles (with $C_3E_6NH_2$ primer).

In the second system, the nanoparticles were first primed with the neutral ligand $C_3E_6NH_2$ - prior to protein exchange. Once prepared, the two complementary population was mixed and the evolution of the system was monitored by Gel electrophoresis, TEM and UV-Vis spectroscopy.

Agarose gel electrophoresis.

A full set of assembly experiments for the $C_3E_6NH_2$ primed nanoparticles was followed by GEP. The photograph of agarose gel is given in *Fig VI.27*. The citrate-stabilized gold nanoparticles (*track 1*) showed very little migration as observed in the previous case. When conjugated with neutral $C_3E_6NH_2$ ligand, the particles show small migration (*track 2*). Since the replacement of negatively charged citrate by neutral ligand bear very small net charge from ammonium groups, hence does not favor for the large migration in electrophoresis gel. Further, when nanoparticles primed with $C_3E_6NH_2$ ligand, were exchanged with αRepA3Cys protein, the migration was restored and even amplified (*track 3*). This was consistent with the replacement of the ligand by charged proteins which results in the marginal increase of overall size. Similarly when nanoparticles were exchanged with α2Cys and α17Cys proteins (*track 4 and 5*), the migration was greater than for nanoparticle bearing $C_3E_6NH_2$ alone. This

was again in consistent with the pI and zeta potential of α2Cys and α17Cys proteins which bear less charge than αRepA3Cys protein at neutral pH (*Table VI.1*). This was very comparable in the case of negative C3E6Asp primed nanoparticle.

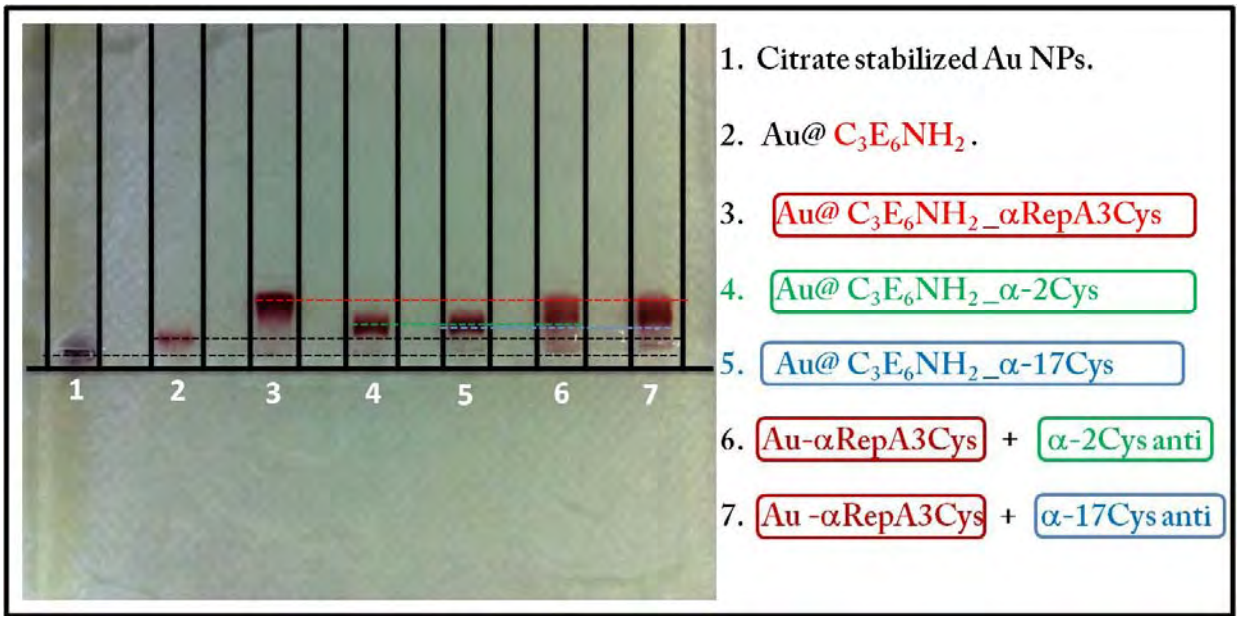

Fig VI.27: *Photograph of agarose electrophoresis gel of Au nanoparticles (1) primed with $C_3E_6NH_2$ (2), after exchange with complementary α-Rep proteins pairs (3, 4, 5) and their mixture (6, 7).*

When Au-αRepA3Cys was mixed with Au-α2 Cys conjugates, the sample migrated in the gel comprise of single band rather than two separate bands. Moreover the distance travelled by the sample was in between the original samples (*Fig VI.27 track 6*). A similar behavior was observed when we mixed Au-αRepA3Cys nanoparticle with Au-α17Cys particle samples. (*Fig VI.27 track 7*). This was a strong indication that interaction between the protein pairs drove nanoparticle assembly.

TEM analysis.

Fig VI.28 shows TEM analysis of the mixture of two complementary populations which were initially primed with C3E6NH2 ligand. Large numbers of chain like assembly of nanoparticles were found in the duplex solution containing the mixture of Au-αRepA3Cys and Au-α2Cys (*Fig VI.28a, b,*). Moreover statistical distribution of interparticle distance follows Gaussian distribution, which measures interparticle distance at 2.7nm (*Fig VI.28c*). When we mixed Au-αRepA3Cys with Au-α17Cys conjugates, a large aggregation of nanoparticles was observed by TEM images (*Fig VI.28 d, e)* and corresponding interparticle distance measurement in

certain places which follows lognormal distribution showed that particles were separated by 2nm distance. The interparticle distance measured in case of $C_3E_6NH_2$ primed nanoparticles was lesser than in a nanoparticle primed with C_3E_6AsP ligand. Hence the effect of ligand can be clearly observed on the protein mediated nanoparticle assembly.

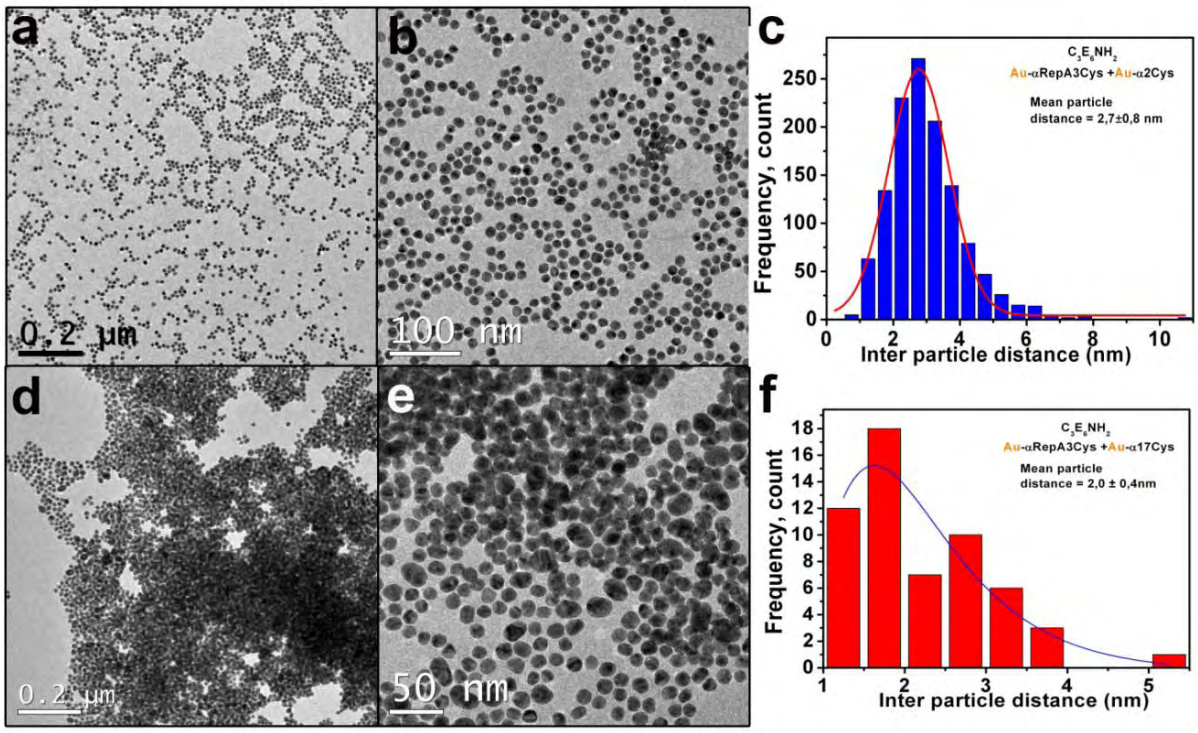

Fig VI.28: *a, b) TEM image of duplex solution containing Au-α-Rep A3Cys with Au-α2Cys protein, and c) corresponding interparticle distance analysis. d, e) TEM image of the duplex solution containing the mixture of Au-αRep A3Cys with Au-α17Cys protein and f) statistical distribution of interparticle distance in the corresponding image.*

Analysis by UV-Vis Absorption spectroscopy.

The UV-Vis absorption spectra after the mixing of Au-αRepA3Cys and Au-α2Cys conjugates showed very small decrease in the intensity of absorption (*Fig VI.29)*. Similar decrease in the intensity was observed in the sample of Au-α-RepA3Cys and Au-α17Cys mixture. Interestingly no red shift of plasmon band and no sign of longitudinal band were observed in UV-Vis spectra. Although the interparticle distance measured from TEM analysis was 2-3nm, this could not able to bring efficient coupling of surface plasmon in Au nanoparticles chain. The decrease in the plasmon band can be accounted as a result of aggregation of nanoparticles in the duplex solution, which is similar when compared to the self assembly of nanoparticles by polynucleotide reported by Mirkin et al[10].

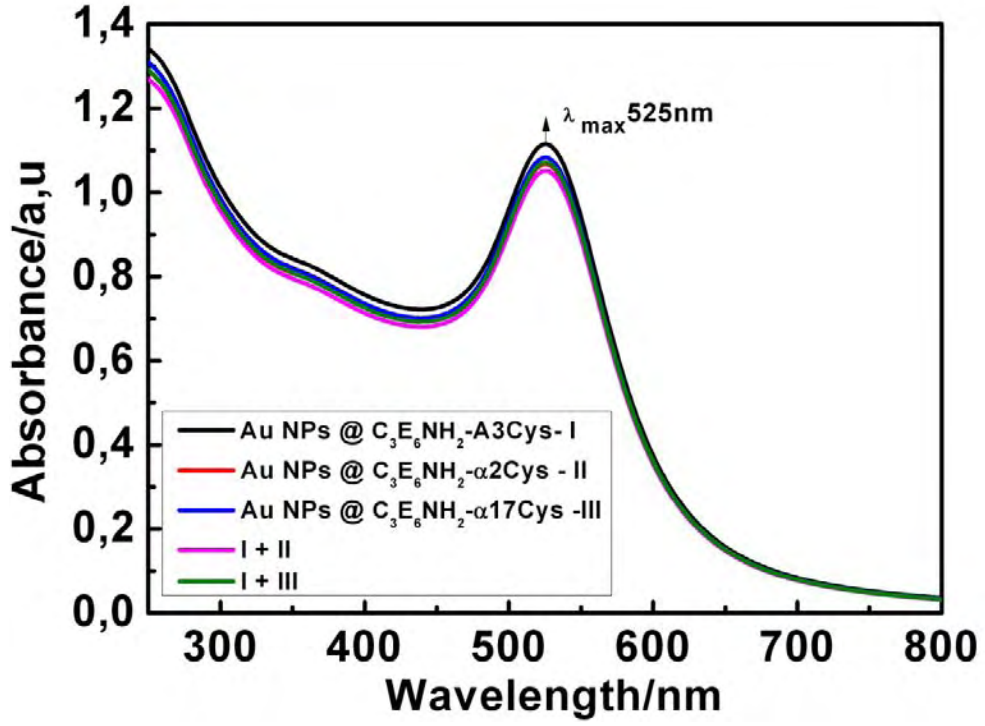

Fig VI.29: *UV-Visible spectra of concentrated Au nanoparticle-protein conjugates initially primed with $C_3E_6NH_2$ ligand and mixture of two affinity pair (I) + (II) and (I) + (III).*

Hence surface plasmon coupling was very sensitive and strictly depend on the distance between the two particles. Compared to our first result (*Fig VI.8 and Fig VI.9),* red shift of the plasmon band was observed when the interparticle distance was at ~1nm. Therefore the shift at 2-4nm probably too small moreover of size dispersion in the solution contribute large effect on plasmon band of Au. Nanoparticles primed with neutral ligand $C_3E_6NH_2$ showed better performance than the nanoparticles primed with negatively charged ligand C_3E_6Asp which offer small resistance for an effective protein exchange.

6.5. Conclusion and Perspective.

Artificial protein pairs were successfully created by our collaborators in IBBMC Orsay, by using phage display technique. These proteins have well-defined 3D structure and are protected by N and C-cap and they showed strong binding affinity with counter protein pairs. Micro calorimetric analysis (ITC) of protein pairs showed that the binding affinity of αRepA3-αRep17 was larger than that of αRepA3-αRep2. Insertion of cysteine tag in the protein pairs was successfully achieved while conserving the original nature as well as recognition ability of the protein pairs. In addition, the high thermal stability of proteins was evidenced by DSC analysis. With the

successful creation of protein pairs, we started using these proteins for inducing self-assembly of Au nanoparticles. The direct conjugation of binders (α2Cys and α17Cys) with Au nanoparticles resulted in the formation of small dimers followed by large number of chains and finally precipitation with the increase of protein amount. Hence, the ligand exchange method proved to be efficient for the preparation of stable nanoparticle-protein conjugates. Weak interaction was found when two complementary solutions were mixed, since the K_D was not adequate for the effective interaction of two proteins conjugates. The concentration of the proteins in pure protein-protein interaction experiments is consistently large in comparison with gold conjugated protein pair experiment. Thus we attempted to equate these conditions by concentrating the conjugate solution and mixing two complementary conjugate pairs.

Self-assembly experiments carried with this method contributed for the increase in K_D value and resulted in the formation of large number of nanoparticle assembly. Moreover the effect of two different ligand was clearly visible, where $C_3E_6NH_2$ primed nanoparticles showed better performance in comparison with the C_3E_6ASP primed nanoparticles. Statistical analysis of interparticle distance on TEM images showed decrease in the distance from 4.4nm to 2.7nm in case of Au-α-RepA3Cys and Au-α-2Cys mixture, and from 3.5nm to 2.0nm when Au-αRepA3Cys mixed with Au-α17Cys conjugates. Large affinity of Au-α-RepA3Cys with Au-α17Cys was confirmed by TEM and Electrophoresis Gel experiments.

In our series of nanoparticle self-assembly, we have shown that artificial protein pairs could be grafted onto distinct populations of nanoparticles and then drive their organization into large scale assembly. In particular, we have evidenced that the recognition activity of the protein partner is strongly dependent on the co-grafted molecules that prime the nanoparticle surface. We have been able to incorporate new and stronger binders of the target (α-RepA3Cys) and show recognition ability without the deformation in their structure.

Our future goal is to demonstrate the reversibility of the self assembly by performing competition tests in which the assembled nanoparticles are put in competition with free proteins that can disassemble the tethered protein pair by pure entropic effect. In the medium to long term, this self-assembly process could allow to control the stoichiometry in the assembly experiments or the orthogonal self assembly of plasmonic nanoparticles.

Such a degree of control is still out of reach of most current chemistry strategies. and would results in better controlled optical properties that will likely find applications in nano electronics and optical devices.

References:

(1) Urvoas, A.; Guellouz, A.; Valerio-Lepiniec, M.; Graille, M.; Durand, D.; Desravines, D. C.; van Tilbeurgh, H.; Desmadril, M.; Minard, P. *Journal of Molecular Biology* 2010, *404*, 307-327.

(2) Steiner, D.; Forrer, P.; Stumpp, M. T.; Pluckthun, A. *Nature Biotechnology* 2006, *24*, 823-831.

(3) Mocanu, A.; Cernica, I.; Tomoaia, G.; Bobos, L.-D.; Horovitz, O.; Tomoaia-Cotisel, M. *Colloids and Surfaces a-Physicochemical and Engineering Aspects* 2009, *338*, 93-101.

(4) Estevez-Hernandez, O.; Molina-Trinidad, E. M.; Santiago-Jacinto, P.; Rendon, L.; Reguera, E. *Journal of Colloid and Interface Science* 2010, *350*, 161-167.

(5) Alivisatos, A. P.; Johnsson, K. P.; Peng, X. G.; Wilson, T. E.; Loweth, C. J.; Bruchez, M. P.; Schultz, P. G. *Nature* 1996, *382*, 609-611.

(6) Mirkin, C. A.; Letsinger, R. L.; Mucic, R. C.; Storhoff, J. J. *Nature* 1996, *382*, 607-609.

(7) Li, M. J., Sara Guo, Hongtao Dujardin, Erik Mann, Stephen *Advanced Functional Materials* 2011, *21*, 851-859.

(8) Lin, S.; Li, M.; Dujardin, E.; Girard, C.; Mann, S. *Advanced Materials* 2005, *17*, 2553-+.

(9) *Handbook of Nanophysics*; Sattler , K., Ed.; Taylor & Francis: London, 2010; Vol. Vol. 3 , Chp. 27, 29pp.

(10) Storhoff, J. J.; Elghanian, R.; Mucic, R. C.; Mirkin, C. A.; Letsinger, R. L. *Journal of the American Chemical Society* 1998, *120*, 1959-1964.

CONCLUSION.

Le contexte de ce travail de thèse est la recherche actuelle de systèmes plasmoniques plus performants dans leurs fonctions confinement, exaltation, propagation et couplage des champs lumineux à l'échelle du nanomètre. Il a récemment été démontré que les nanoparticules métalliques sont moins dissipatifs que les dispositifs métalliques standards faits par lithographie. Pourtant, le défi majeur qui leur est associé est le contrôle de la forme et la cristallinité des nanoparticules métalliques, ainsi que leur organisation dans l'espace et leur couplage à des fluorophores. Ceci est, dans une large mesure, liées à leur chimie de surface. Alors que quelques approches de chimie colloïdales découvertes récemment ont atteint certains de ces objectifs, nombre de ces défis doivent encore être résolus.

Nos objectifs étaient donc de contribuer à l'exploration de nouvelles approches ascendantes de la mise en forme et du couplage de nanoparticules plasmoniques dans le but de mieux contrôler les propriétés optiques à l'échelle nanométrique. Nous nous sommes concentrés principalement sur trois aspects: le contrôle de la structure et de la morphologie des

nanoparticules, leur intégration par auto-assemblage dans des architectures colloïdales d'ordre supérieur, et le couplage de nanoparticules métalliques avec des structures moléculaires optiquement actives.

Pour étudier l'interface plasmon / molécule et éventuellement trouver des moyens pour amplifier le signal de fluorescence, nous avons appliqué avec succès une approche par minéralisation directe d'assemblages supramoléculaires de fluorophores qui jouent aussi le rôle de template pour la croissance in-situ d'un espaceur diélectrique et qui, par la suite, permet d'accrocher des nanoparticules métalliques à leur surface.

Les propriétés de fluorescence d'ensemble finis et ordonnés de porphyrines, appelés agrégats J, a été modulée par leur encapsulation dans une coque de silice d'épaisseur contrôlée entre 2 ± 1 nm et 12 ± 1 nm et par sa décoration avec des nanoparticules d'Au et Ag pré-formées. Les agrégats J de porphyrines agissent comme un template pour la condensation de la silice. La coquille minérale renforce la tenue mécanique de l'agrégat supramoléculaire et devient également un substrat pour l'adsorption spécifique de nanoparticules d'Au ou d'Ag avec un espacement diélectrique ajusté pour optimiser le couplage exciton-plasmons. L'encapsulation a pu être contrôlée dans la gamme des très faibles épaisseurs, ce qui nous a permis de sonder le régime de couplage fort entre les agrégats J encapsulés et les nanoparticules plasmoniques. La fluorescence exaltée des J-agrégats encapsulés a pu être optimisée de plus de 400% et 200% lors la conjugaison des nanoparticules d'Ag et d'Au respectivement.
De telles constructions pourraient contribuer à la conception de sondes optiques pour des applications en détection ou imagerie, mais aussi à une meilleure intégration d'absorbeurs ou émetteurs moléculaires dans des dispositifs plasmoniques pour le traitement optique de l'information, qui nécessitent un ajustement fin du régime de couplage fort entre les fluorophores et des nanostructures métalliques.

Dans la deuxième partie, nous avons exploré de nouvelles méthodes pour contrôler la morphologie des nanoparticules métalliques, et leur auto-assemblage en utilisant des protéines artificielles appelé α-Rep. Les principaux avantages de ces protéines artificielles sont leur grande stabilité thermique et leur structure 3D bien définie et robuste, qui peut être modulée par la concaténation d'une partie de la séquence, tout en préservant une certaine variabilité pour certains sites d'acides aminés. La réaction chimique directe, à forte concentration, de ces protéines α-Rep avec une solution de sel d'or résulte dans les particules

de morphologie sphérique, cylindrique ou filiforme pour lesquelles les protéines ou les architectures auto-assemblées de protéines agissent comme des template pour la formation de ces structures anisotropes. A faible concentration de protéines et à un pH physiologique, la même réaction conduit à la formation de nanoparticules triangulaires et hexagonale. A pH élevé, la réaction de la protéine avec la solution d'Au(III) résulte en la dénaturation des protéines, ce que nous avons confirmés par des expériences DSC et CD. La formation de nanostructures en ruban et de nanoclusters d'Au fluorescents de taille 2-6 nm a été observées lorsque les protéines α-Rep sont utilisées en tant que stabilisants de surface tandis que l'acide ascorbique ou le TCEP servent d'agent réducteur. Le mécanisme exact de la formation de ces structures anisotropes n'est pas connu. Cependant, nos expériences suggèrent que le paramètre ayant un impact le plus important sur la morphologie résultante des nanostructures est la concentration de protéines. Ainsi nous avons pu montrer que les protéines α-Rep étaient capables de générer des particules anisotropes ou des agrégats métalliques fluorescent en un réaction en une étape à partir de précurseur d'or. Ceci est un résultat innovant dans le domaine de la synthèse de nanoparticules en présence de protéines.

Enfin, des paires de protéines α-Rep ayant une affinité mutuelle ont été sélectionnés par "phage display" et conjuguée à des populations différentes de nanoparticule d'or. Un auto-assemblage massif et spontané a été déclenché par le mélange de ces deux populations de particules portant des protéines complémentaires. La conjugaison directe des protéines sur les nanoparticules est instable et résulte dans l'agrégation des nanoparticules. Un procédé d'échange de ligands a donc été développé qui produit une dispersion stable de nanoparticules d'or fonctionnalisées par les protéines. En dépit de constantes de dissociation K_D atteignant 10 ou 150 nM, une telle affinité semble être insuffisante pour l'auto-assemblage de nanoparticules à faible concentration. A des concentrations plus élevées, le mélange de populations de particules complémentaires induit l'agrégation et la formation d'une monocouche étendue de nanoparticules ainsi que des chaînes. Des caractérisations par électrophorèse sur gel, microscopie électronique et spectroscopies suggèrent que l'auto-assemblage est provoqué par la reconnaissance entre protéines. Pourtant, la configuration moléculaire semble inefficace à produire un régime de couplage fort plasmonique. Cela sera une prochaine cible.

Ces résultats constituent les premières étapes de l'élaboration d'une boîte à outils biomoléculaires polyvalente dans laquelle les protéines artificielles peuvent être conçues pour

contrôler la morphologie des nanoparticules plasmoniques ou induire leur couplage spécifique à d'autres nanoparticules fonctionnelles permettant ainsi la construction d'architectures colloïdales plasmoniques.

Grâce à notre travail, il est maintenant possible d'envisager l'expansion des stratégies basées sur des protéines artificielles à des systèmes mieux contrôlés. Par exemple, l'application de la sélection par "phage display" à des faces cristallines d'or permettrait de sélectionner une séquence α-Rep ayant une affinité spécifique pour l'or voire pour certaines facettes cristallographiquement orientées. L'incorporation d'une telle séquence dans les homopolymères de divers degrés de polymérisation permettrait de combiner l'effet template chimique et le confinement par la forme des protéines pour accroitre le contrôle morphologique.

En outre, l'auto-assemblage de protéines homopolymériques en superstructures tubulaires / hélicoïdale a été évoqué comme une explication possible pour la formation de nanobâtonnets d'or. Cette organisation supra-protéine peut être provoquée intentionnellement par la création d'homopolymères de degré plus important, qui adopteront sans doute une conformation en pas d'hélice avec une tendance naturelle à s'auto-organiser sous forme de tubes. La conjonction d'une séquence spécifique pour l'or et de l'assemblage supramoléculaire de protéines pourraient élargir le contrôle morphologique des particules.
En ce qui concerne l'auto-assemblage de nanoparticules induit par les paires α–Rep, il faut sûrement produire des paires de plus grande stabilité et d'affinité accrue. La recherche de partenaires ayant à la fois au moins 4 monomères est la prochaine étape évidente. Il sera également important d'affiner la conjugaison des particules de protéines afin de favoriser le couplage plasmon à moins de 5 nm.

Enfin, on pourrait envisager d'exploiter les paires de protéines pour induire le couplage entre nanoparticules plasmoniques et fluorophores, telles que les agrégats d'or fluorescents rapportés dans le chapitre 5 ou, plus classiquement, des nanoparticules semi-conductrices. Il apparaît donc que nos résultats ouvrent la voie de nouveaux systèmes dans lesquels des colloïdes plasmoniques peuvent être façonnés et interfacés, ce qui pourrait avoir des répercussions dans la conception de systèmes sensibles pour capteurs, l'imagerie par fluorescence ou même le traitement optique de l'information à l'échelle nanométrique par l'approche plasmonique.

Conclusion

Je tiens également à souligner, pour finir, que mon travail de recherche sur l'application des protéines α Rep à la science des matériaux a été rendu possible par le fort soutien et l'implication des biologistes Philippe Minard, Agathe Urvoas et Marielle Lepinec qui ont produit ces nano-objets biologiques atypiques que j'ai exploités à l'interface avec les nanomatériaux.

Résumé *:*

Le confinement et le guidage de l'énergie lumineuse à l'échelle nanométrique dans des composants colloïdaux requiert le contrôle précis (i) de la morphologie des nanoparticules, (ii) de leur agencement spatial dans des architectures d'ordre supérieur et (iii) du couplage entre structures plasmoniques et molécules photoactives. Ce travail de thèse explore des approches nouvelles de synthèse, essentiellement bio-inspirées, de ces trois défis.
Dans un premier temps, nous avons utilisé les principes de biominéralisation pour ajuster le couplage entre plasmon et fluorophore et ainsi contrôler l'exaltation de fluorescence. La fluorescence d'ensembles finis et organisés de fluorophores (porphyrines) appelé agrégats J est modulée par leur encapsulation dans une fine couche de silice d'épaisseur contrôlée (entre 2 ± 1 nm et 12 ± 1 nm) produite par minéralisation, suivie de l'accrochage de nanoparticules d'or ou d'argent. Les agrégats J servent de template à la minéralisation silicée qui renforce alors leur stabilité mécanique, permet d'adsorption spécifique de nanoparticules métalliques et joue le rôle d'espaceur diélectrique permettant une optimisation du couplage exciton-plasmon. L'exaltation de fluorescence par les plasmons a ainsi pu être optimisée à plus de 400% et 200% par conjugaison de particules d'argent et d'or respectivement sur les agrégats J minéralisés. Notre approche colloïdale ascendante pourrait contribuer à la conception de sondes optiques pour des applications capteurs ou en imagerie mais s'inscrit aussi dans la recherche de systèmes efficaces pour le traitement de l'information optique par intégrations de structures plasmoniques cristallines et d'absorbeurs /émetteurs moléculaires.

Dans un deuxième temps, nous avons exploré de nouvelles méthodes de contrôle de la morphologie de nanoparticules métalliques et de leur auto-assemblage en utilisant des protéines artificielles appelées a-Repins. Le principal avantage de ces protéines artificielles est leur grande stabilité thermique et leur structure tridimensionnelle robuste et modulable par concaténation de portions de séquence tout en permettant une variabilité de certains acides aminés. Pour la première fois, ces protéines ont été utilisées comme agents directeurs de croissance de nanoparticules d'or, ce qui nous a permis de produire des particules sphériques, prismatiques triangulaires, des nanobâtonnets par effet template des protéines de formes différentes. Dans des conditions particulières, nous avons aussi pu produire des nanoparticules fluorescentes d'or de 2-6 nm de diamètre. Par ailleurs, des paires de protéines a-Repins, sélectionnées par évolution dirigée pour leur affinité mutuelle, ont été conjuguées à des populations différentes de nanoparticules. L'auto-assemblage massif et spontané des nanoparticules est alors induit lors du mélange de population portant des protéines complémentaires.
Ces résultats constituent la première étape de la construction d'une approche généralisation dans laquelle des protéines artificielles peuvent être conçues et produites pour contrôler la structure cristalline et la morphologie de particules plasmoniques ou bien induire leur couplage spécifique avec d'autres particules fonctionnelles permettant ainsi d'envisager la construction d'architectures colloïdales plasmoniques complexes.

Mots clés :

exaltation de fluorescence,	**metal-enhanced fluorescence,**
minéralisation,	**mineralization**
protéines artificielles,	**artificial proteins**
morphosynthèse de nanoparticules,	**nanoparticle morphosynthesis**
auto-assemblage,	**self-assembly**
plasmoniques colloïdale.	**colloidal plasmonics**

Summary:

Confinement and guiding of light energy at nanoscale in devices composed of colloidal building blocks, requires a precise control of (i) the morphology of the nanoparticles, (ii) their spatial organization into larger scale architectures and (iii) the coupling between plasmonic colloid and optically active. This thesis work explores new synthetic approaches, including bio-inspired ones, of these three challenges.
As a first insight, we have employed biomineralization principles to tune the plasmon-fluorophore coupling in order to control the fluorescence enhancement. The fluorescence properties of a well-organized, finite ensemble of porphyrins called J-aggregates is modulated by the templated encapsulation of silica of controlled thickness, in the range of 2 ± 1 nm to 12 ± 1 nm, and its decoration with Au and Ag nanoparticles. Porphyrin J-aggregates act as templates for the silica mineralization, while the inorganic shell first provides a mechanical stability and also becomes a template for the specific binding Au or Ag nanoparticles with a dielectric spacing for optimal exciton-plasmon coupling. The metal-enhanced fluorescence can be optimized exceeding 400% and about 200% with the conjugation of Ag and Au nanoparticles on templated J-aggregates respectively. Such bottom-up templated constructions could contribute to the design of optical probes for sensing and imaging applications but also to the efficient integration of molecular absorbers and emitters into plasmonic devices for optical information processing.

In the second part we explored new methods to control the morphology of metallic nanoparticles, and their self-assembly using artificial proteins called α-Repins. The main advantages of these artificial proteins are there high thermal stability and their well-defined and robust 3D structure, which can be modulated by concatenation of a portion of the sequence while preserving some variability for some amino acid positions. The direct chemical reaction of these α-Rep proteins with Au sol results in the particles of spherical triangular, rod and wire shaped morphology where proteins acts as a template. Also fluorescent nanoclusters of size 2-6nm has been obtained when α-Rep proteins are used as a stabilizing agents. Finally, pairs of α-Rep proteins with mutual affinity have been selected by phage display and conjugated with different population of nanoparticles. Massive and spontaneous self-assembly was triggered by mixing these two particle particles populations bearing complementary proteins.
These results are the first steps of the development of a versatile biomolecular toolbox in which artificial proteins can be fully designed to either control the crystallographic structure and morphology of plasmonic nanoparticles or induce their specific coupling to other functional nanoparticles therefore allowing to construct plasmonic and metamaterials colloidal architectures.